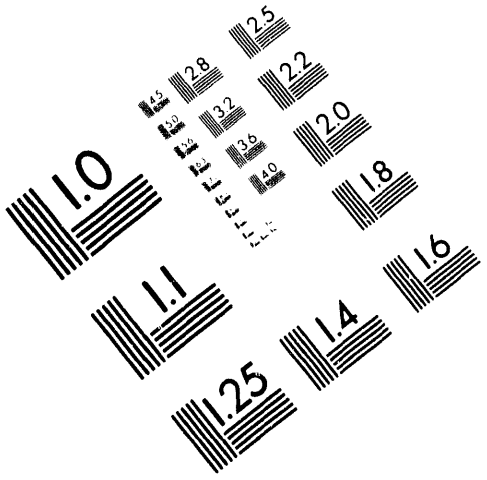

Association for Information and Image Management

1100 Wayne Avenue, Suite 1100
Silver Spring, Maryland 20910

301/587-8202

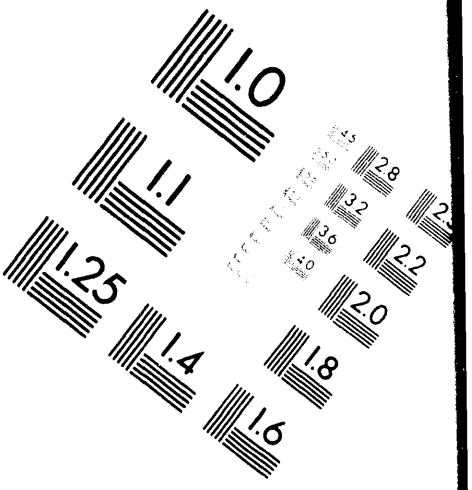

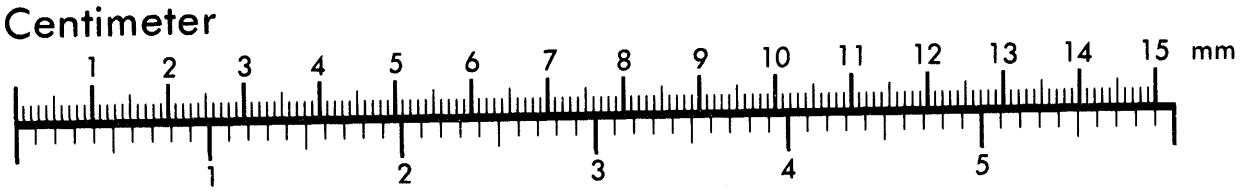

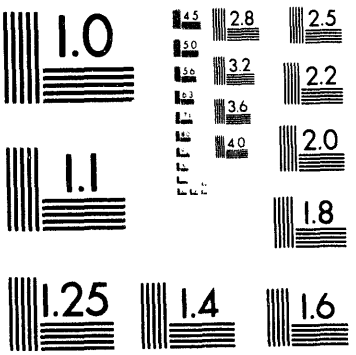

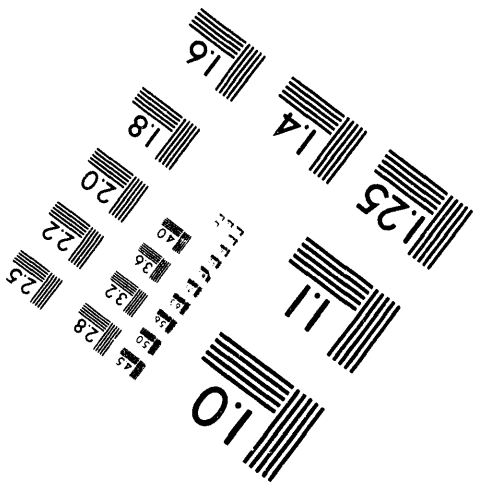

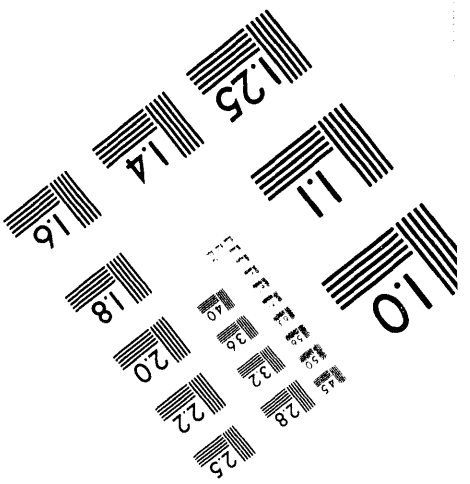

1 of 3

CONF-9306361--
DOE/ER/61578--1

DEPARTMENT OF ATMOSPHERIC
AND OCEANIC SCIENCES
McGILL UNIVERSITY, MONTRÉAL

THE ROLE OF LARGE-SCALE, EXTRATROPICAL DYNAMICS IN CLIMATE CHANGE

Proceedings of the Seventeenth Stanstead Seminar held at Bishop's University, Lennoxville, Québec, Canada June 13 – 18, 1993

T.G. Shepherd, Editor

Seminar Co-Chairmen
Jacques Derome and William J. Gutowski

February 1994

Summary

The climate modeling community has focused recently on improving our understanding of certain processes, such as cloud feedbacks and ocean circulation, that are deemed critical to climate-change prediction. Although attention to such processes is warranted, emphasis on these areas has diminished a general appreciation of the role played by the large-scale dynamics of the extratropical atmosphere. Lack of interest in extratropical dynamics may reflect the assumption that these dynamical processes are a non-problem as far as climate modeling is concerned, since general circulation models (GCMs) calculate motions on this scale from (almost) first principles. Nevertheless, serious shortcomings in our ability to understand and simulate large-scale dynamics exist. For example, GCM simulations of atmospheric poleward heat transport by large-scale eddies differ from observations and from model to model by up to 50% (Stone and Risbey, 1990). Furthermore, eddies in GCMs tend to transport momentum too efficiently compared to observations (Boer and Lazare, 1988; Boville, 1991). Partly due to a paucity of standard GCM diagnostic calculations of large-scale motions and their transports of heat, momentum, potential vorticity, and moisture, a comprehensive understanding of the role of large-scale dynamics in GCM climate simulations has not been developed. Substantial uncertainties thus remain in our understanding and simulation of large-scale extratropical dynamics and their interaction with other climatic processes, such as cloud feedbacks, large-scale ocean circulation, moist convection, air-sea interaction and land-surface processes.

To address some of these issues, the 17th Stanstead Seminar was convened on June 13-18, 1993 at Bishop's University in Lennoxville, Québec. The purpose of the Seminar was to promote discussion of the role of large-scale extratropical dynamics in global climate change. Abstracts of nearly all the talks are included in this volume. On the basis of these talks, several key issues emerged concerning large-scale extratropical dynamics and their climatic role:

I. A Hierarchy of Models is Needed

The Seminar participants endorsed Isaac Held's recommendation that climate research must rely on models of various levels of complexity. While attempting to offer a complete picture of the climate system, GCMs are often so complicated that feedbacks within the models are not easily identified or understood. Rather, our knowledge of atmospheric dynamics is much more fully expressed in a *hierarchy of models*, ranging from highly complex GCMs to relatively simple conceptual models. For example, GCMs simulate the quasi-geostrophic behavior of large-scale extratropical dynamics, but it is our ability to construct acceptable quasi-geostrophic models that demonstrates our understanding of the behavior.

To investigate climatic mechanisms and feedbacks, simpler models have the advantages of more extensive and varied experimentation, easier interpretation, and greater accessibility by the broad research community than is possible with computationally intensive GCMs. Simple models can be used to increase our understanding of dynamical and physical processes that occur within nature and more complex models. Closer cooperation between scientists working with simple models and scientists working in GCM groups is needed.

II. GCM Resolution of Dynamics is Limited

The supposed superiority of GCM simulations of extratropical dynamics is undermined by *limitations in spatial resolution*. Current GCMs are still unable to resolve details of extratropical dynamics. Until climate simulations by GCMs reach the high resolution of numerical weather prediction models, GCMs are unlikely to provide details on climatic alterations in storm tracks, intense cyclogenesis, frontal dynamics, cyclone-scale moisture processes, regional and local climate, and persistent circulation anomalies (e.g. atmospheric blocking). Furthermore, successful modeling of motions on scales smaller than planetary zonal wavenumber 15 or so will depend on the interaction of these motions with subgrid-scale processes. Increased vertical resolution, which is often overlooked, may also be needed to properly simulate the interaction of the planetary boundary layer with large-scale dynamics. As noted by George Boer, increases in model resolution must be accompanied by substantial improvements in subgrid-scale parameterizations.

III. Interactive Links Must be Simulated Accurately

Even with high resolution simulations, successful modeling of the climate system must involve an understanding of the interaction of various processes. This goal cannot be achieved by focusing on individual processes in isolation from all other mechanisms. Large-scale extratropical dynamics have important *interactive links* (or feedbacks) with many other processes in the climate system. For example, if a model incorrectly represents subgrid-scale processes such as moist convection or boundary layer fluxes, the model is likely to make errors in simulating the climatic feedbacks of large-scale eddies whose amplitudes, life cycles, and time-mean transports are affected by the subgrid-scale processes. These errors may spread to other parts of the model. For example, Peter Stone noted that coupled atmosphere-ocean GCMs typically overestimate atmospheric heat transports, which may lead to unrealistically weak oceanic transports. The resultant error in oceanic heat transports leads to the necessity of introducing surface heat flux corrections into the air-sea interaction component of the model. The heat flux corrections then cast doubt on the model's ability to simulate the climate system's response to anthropogenic or natural perturbations. Stone also cited an example of strong feedbacks between large- and small-scale processes within a GCM, in which the choice of a model's moist convection scheme

V. Climatic Extremes are Critical Tests

Experimentation with various climate models often includes simulations of known, extreme climatic changes as manifested in paleoclimatic variations and the seasonal cycle. These experiments should be examined further to reveal the sensitivity of extratropical dynamics to climate change. Such experimentation will be useful in model validation. Moreover, experiments that explore extreme climatic perturbations or a wide range of model parameters allow modelers to identify which parts of the models are critical to successful climate simulation of extratropical dynamics.

A number of special subtopics emerged from the Seminar presentations that represent areas meriting additional focus, among them:

VI. The Hydrological Cycle

The relationship between the hydrological cycle and large-scale dynamics is a critical component in future climate research. Four of the invited speakers addressed the importance of, and uncertainties in, observing and modeling water vapor concentrations, transports, and processes. Not only does the amount and distribution of water in its three phases affect radiative processes, it also influences the behavior of large-scale eddies and mean circulations. In turn, the large-scale dynamics influence moisture processes. As mentioned by Ray Pierrehumbert, little is known about the large-scale distribution of water vapor in the upper and middle troposphere and the mixing in this region between the tropics and extratropics. Analysis of water vapor from the perspective of isentropic surfaces and potential-vorticity mixing may be a useful approach to this issue.

VII. Low-Frequency Variability

Several speakers, especially Jacques Derome, discussed the behavior of the climate system's low-frequency signals that range from a few weeks to decades. These phenomena, which involve large-scale extratropical dynamics, strongly influence regional weather and climate over a range of spatial and temporal scales. More attention needs to be given to how these low-frequency phenomena might change in a warmer world, or if changes in these phenomena can be indicators of global climate change.

VIII. Mixing and Transport Mechanisms

Improved understanding of the basic mechanisms of mixing and transport by large-scale dynamics is needed. On global scales, should the transport of heat by large-scale eddies be viewed as a diffusion process or as an adjustment mechanism that drives the

influenced the relative proportions of vertical heat flux accomplished by large-scale eddies and moist convection. The distribution of vertical heat flux between the resolved and unresolved dynamics may affect the model's response to a perturbation in radiative forcing such as greenhouse gas enhancement. Several other examples were provided by Stone and other speakers.

Furthermore, interaction of large-scale atmospheric dynamics with other parts of the climate system may amplify climate sensitivity in ways that are presently unidentified or poorly understood. An example is the potentially dramatic feedback between atmospheric and oceanic transports mentioned by Stone in one of his presentations. Feedbacks within the system must be thoroughly explored in the context of theory, observations, and climate models, including both GCMs and simpler models.

IV. Diagnostic Validation is Limited

Simulations of extratropical dynamics in GCMs suffer from *inadequate diagnostic validation*, leading to overconfidence in the quality of these simulations. Comparisons of GCM simulations between models and with observations are made difficult by the lack of standardized diagnostic output from the models. Diagnostics from many GCMs focus on first-order statistics such as zonal mean temperature or on output related to specific modeling questions, such as how a change in a cloud parameterization alters time-mean cloudiness in a GCM. The impact of changing a physical parameterization, such as the cloud scheme, on the transports by large-scale eddies is often overlooked, even though the change may alter the sensitivity of the large-scale eddy transports to climatic perturbations.

Feedbacks of large-scale dynamics and their links to other processes in the models can only be evaluated and understood if more comprehensive diagnostics are developed and made available to the general scientific community. Furthermore, new and innovative methods of analysis, such as principal oscillation patterns and diagnostics related to potential vorticity dynamics and isentropic transport, need to be employed so that GCM diagnostics can be evaluated and compared with results from simpler models, observations, and theory. Availability of standard diagnostic output will foster cooperation among theoreticians, observationalists, and GCM research groups. In order to complement more comprehensive diagnostics from GCMs, better observational studies of higher-order dynamical quantities and feedbacks are required. For example, more information is needed on how large-scale eddies transport water vapor and influence cloud processes. One must also recognize, of course, that observational data itself is subject to accuracy limitations that can limit its usefulness for model validation.

mean circulation toward neutral stability? How does one model the additional complexity that emerges when low-frequency fluctuations are distinguished? For example, synoptic-scale eddies are known to dissipate the temperature field of intra-seasonal fluctuations, but maximum dissipation may occur downstream from maximum temperature anomalies. The interaction is thus complex and probably cannot be adequately modeled by a simple diffusion process. Resolution of these issues will influence our understanding of how the temperature and moisture structure of the troposphere will be altered in a warmer world.

The large-scale dynamics of the extratropical atmosphere play a crucial role in many components of the climate system, as the papers in this volume will attest. Large-scale dynamics are important in cloud formation and dissipation, evaporation and precipitation, transport and mixing processes, and regional phenomena. They also influence low-frequency variability within the coupled atmosphere-ocean system. As indicated by the issues above, successful evaluation and simulation of global climate change is impossible without a comprehensive understanding of large-scale dynamics and their feedbacks with other processes.

References

Boer, G.J., and M. Lazare, 1988: Some results concerning the effect of horizontal resolution and gravity-wave drag on simulated climate. *J.Climate*, **1**, 789–806.

Boville, B.A., 1991: Sensitivity of simulated climate to model resolution. *J.Climate*, **4**, 469–485.

Stone, P.H., and J.S. Risbey, 1990: On the limitations of general circulation climate models. *Geophys.Res.Letters*, **17**, 2173–2176.

L.E. Branscome
W.J. Gutowski

Acknowledgments

The Seminar was supported by a Conference Grant from the Natural Sciences and Engineering Research Council of Canada, and by U.S. National Science Foundation grant ATM–9221206 to Iowa State University. This latter grant contained funds pooled from three U.S. Federal agencies: the National Science Foundation (Large-Scale Atmospheric Dynamics Program), the Department of Energy (Office of Health and Environmental Research), and the National Oceanic and Atmospheric Administration (Climate and Global Change Program).

We are also grateful to Michel Béland of RPN for providing logistical support prior to the Seminar, and to M. Guerrera of McGill University for her clerical support.

Organizing Committee:

L.E. Branscome
J. Derome
W.J. Gutowski
C.A. Lin
T.G. Shepherd

PROGRAM

SUNDAY, 13 JUNE 1993

2:00 - 8:00 pm Registration - Entrance to Dewhurst Dining Hall
8:00 - 10:30 pm Reception - Outside Inn, Memorial House. Participants and families.

MONDAY, 14 JUNE 1993

8:45 INVITED SPEAKER *(Chair: J. Derome)*

THE ROLE OF EDDY TRANSPORTS IN CLIMATE CHANGE
Peter H. Stone, MIT

10:00 COFFEE BREAK

10:30 LATE MORNING SESSION *(Chair: J. Derome)*

HYDROLOGIC AND RADIATIVE FEEDBACKS ON EXTRATROPICAL TRANSIENT EDDIES: IMPLICATIONS OF GLOBAL WARMING
William J. Gutowski, Iowa State U., and Lee E. Branscome, Environmental Dynamics Res. Inc.

THE ROLE OF DYNAMIC TRANSPORT IN A TWO-DIMENSIONAL ENERGY BALANCE MODEL
Douglas Chan and Kaz Higuchi, CCC/AES, and Charles A. Lin, McGill U.

MERIDIONAL ENERGY FLUXES: CONSISTENCY OF RECENT ECMWF AND NMC ANALYSES
David Keith, NCAR

12 NOON LUNCH

1:15 EARLY AFTERNOON SESSION *(Chair: C.A. Lin)*

DETERMINING THE SENSITIVITY OF TRANSIENT AND STATIONARY WAVES TO FORCING BY APPLICATION OF ADJOINT ANALYSIS
Brian F. Farrell, Harvard U., and Petros J. Ioannou, MIT

CLIMATIC FEEDBACKS BETWEEN STATIONARY AND TRANSIENT EDDIES
Lee E. Branscome, Environmental Dynamics Research, Inc.

TRANSIENT AND STATIONARY EDDIES IN DIFFERING GCM CLIMATE SIMULATIONS
Nicholas Hall and P.J. Valdes, U. Reading

2:45 BREAK

3:00 LATE AFTERNOON SESSION *(Chair: C.A. Lin)*

THE IMPORTANCE OF RESOLUTION ON THE RESPONSE OF MID-LATITUDE TRANSIENTS TO ENHANCED CO_2
C.A. Senior, Hadley Centre for Climate Prediction and Research

THE ENHANCED GREENHOUSE EFFECT AND WINTER CYCLONE FREQUENCIES
Steven J. Lambert, CCC/AES

HEAT FLUXES IN A COUPLED ATMOSPHERE-ATLANTIC OCEAN MODEL IN RESPONSE TO VARIATIONS IN IMPOSED TEMPERATURE GRADIENTS
Enda O'Brien and Eric Chassignet, U. Miami

4:30 END OF MONDAY'S SESSIONS

TUESDAY, 15 JUNE 1993

8:45 INVITED SPEAKER *(Chair: W.J. Gutowski)*

IDEALIZED MODELS OF BAROCLINIC EDDIES AND GLOBAL CLIMATE CHANGE
Isaac M. Held, GFDL

10:00 COFFEE BREAK

10:30 LATE MORNING SESSION *(Chair: W.J. Gutowski)*

WAVE-MEAN FLOW INTERACTION AND THE BAROCLINIC ADJUSTMENT HYPOTHESIS
Murray D. MacKay and G.W. Kent Moore, U. Toronto

SCALING OF SATURATION AMPLITUDES IN BAROCLINIC INSTABILITY
Theodore G. Shepherd, U. Toronto

DIAGNOSES OF BALANCED AND UNBALANCED MOTIONS IN SYNOPTIC EDDY LIFECYCLES FOR OCEANIC AND ATMOSPHERIC JETS
Andrew B.G. Bush and James C. McWilliams, NCAR, and W.R. Peltier, U. Toronto

12 NOON LUNCH

1:15 EARLY AFTERNOON SESSION *(Chair: L.E. Branscome)*

POTENTIAL VORTICITY DYNAMICS IN THE CANADIAN CLIMATE CENTRE GCM
John N. Koshyk and Norman McFarlane, CCC/AES

POTENTIAL VORTICITY DYNAMICS FOR GLOBAL SCALE CIRCULATIONS
Chungu Lu, Colorado State U.

AN EPV VIEW OF THE ZONAL MEAN DISTRIBUTION OF TEMPERATURE AND WIND IN THE EXTRATROPICAL TROPOSPHERE
De-Zheng Sun, Princeton U., and Richard S. Lindzen, MIT

2:45 BREAK

3:00 LATE AFTERNOON SESSION *(Chair: L.E. Branscome)*

ATLANTIC INTERDECADAL OCEAN-ATMOSPHERE INTERACTION
Yochanan Kushnir, Lamont-Doherty Earth Observatory of Columbia U.

NORTHERN HEMISPHERIC RESPONSE TO LARGE VOLCANIC ERUPTIONS IN RELATION TO EL NINO - WINTER CASE STUDIES
Ingo Kirchner, Max Planck Institute for Meteorology

4:00 END OF TUESDAY'S SESSIONS

WEDNESDAY, 16 JUNE 1993

8:45 EARLY MORNING SESSION *(Chair: T.G. Shepherd)*

AN OBSERVATIONAL STUDY OF THE INTERACTION BETWEEN THE SYNOPTIC-SCALE EDDIES AND THE INTRA-SEASONAL FLUCTUATIONS
Jacques Derome, J. Sheng, H. Lin, and M. Klasa, McGill U.

10:00 COFFEE BREAK

10:30 LATE MORNING SESSION *(Chair: T.G. Shepherd)*

SYNOPTIC EDDY FEEDBACK AND LOW-FREQUENCY VARIABILITY
Walter A. Robinson, U. Illinois at Urbana-Champaign

ON THE INTRA-SEASONAL VARIABILITY WITHIN THE EXTRA-TROPICS IN A GENERAL CIRCULATION MODEL AND OBSERVATIONAL DATA
Wilhelm May and Lennart Bengtsson, Max Planck Institute for Meteorology

LOW-FREQUENCY ANOMALIES IN THE NMC MRF MODEL AND REALITY
Wilbur Y. Chen, Climate Analysis Center, NMC

12 NOON LUNCH

1:30 EARLY AFTERNOON SESSION *(Chair: W.J. Gutowski)*

INTRASEASONAL OSCILLATIONS AND THE STABILITY OF A SEASONALLY-FORCED BAROTROPIC MODEL
Christopher Strong, UCLA, Fei-fei Jin, U. Hawaii at Manoa, and Michael Ghil, UCLA

LOW-FREQUENCY VARIABILITY INDUCED BY BAROCLINIC INSTABILITY
Ming Cai, U. Maryland

2:30 BREAK

3:00 LATE AFTERNOON SESSION *(Chair: L.E. Branscome)*

MAINTENANCE OF EXTRATROPICAL LOW-FREQUENCY VARIABILITY IN THE ATMOSPHERE
Mingfang Ting, U. Illinois at Urbana-Champaign

PRINCIPAL OSCILLATION PATTERN ANALYSIS OF OBSERVED AND SIMULATED TROPICAL SUMMERTIME SYNOPTIC SCALE DISTURBANCES
John C. Fyfe, CCC/AES

4:00 END OF WEDNESDAY'S SESSIONS

THURSDAY, 17 JUNE 1993

8:45 INVITED SPEAKER *(Chair: T.G. Shepherd)*

VENTILATION OF MIDDLEWORLD -- DETERMINATION OF MIDLATITUDE MOISTURE AND POTENTIAL VORTICITY
Raymond T. Pierrehumbert, U. Chicago

10:00 COFFEE BREAK

10:30 LATE MORNING SESSION *(Chair: T.G. Shepherd)*

ROSSBY WAVE PROPAGATION AND TELECONNECTIONS FOR THE NORTHERN HEMISPHERE SUMMER FLOW
Tercio Ambrizzi and Brian J. Hoskins, U. Reading

FLUCTUATIONS IN THE LARGE-SCALE ATMOSPHERIC CIRCULATION AND OCEAN CONDITIONS ASSOCIATED WITH THE DOMINANT MODES OF WINTERTIME PRECIPITATION VARIABILITY FOR THE CONTIGUOUS UNITED STATES
Todd P. Mitchell, USRA, NASA, and Warren Blier, UCLA

PREDICTABILITY OF BLOCKING
Ennio Tosi, U. Bologna, S. Tibaldi, U. Camerino, P. Ruti, U. Bologna, and F. D'Andrea, U. Milano

12 NOON LUNCH

1:30 EARLY AFTERNOON SESSION *(Chair: L.E. Branscome)*

MIDLATITUDE FLOW REGIMES IN GCMS AND SIMPLE MODELS
Anthony R. Hansen, Augsburg College, Minneapolis, and Alfonso Sutera, U. of Camerino

CLIMATOLOGICAL FEATURES OF BLOCKING ANTICYCLONES
Anthony R. Lupo, Phillip J. Smith, and Robert J. Oglesby, Purdue U.

2:30 BREAK

3:00 LATE AFTERNOON SESSION *(Chair: L.E. Branscome)*

ON THE DIFFERENCES BETWEEN EARLY AND LATE WINTER ATMOSPHERIC RESPONSE TO THE SEA SURFACE TEMPERATURE ANOMALIES IN THE NORTHWEST ATLANTIC
Shiling Peng and L. Mysak, McGill U., H. Ritchie, RPN, J. Derome, McGill U., and B. Dugas, RPN

MODELING AIR-SEA INTERACTION IN THE NORTH ATLANTIC OCEAN
Uma Bhatt, U. Wisconsin, Madison

4:00 END OF THURSDAY'S SESSIONS

FRIDAY, 18 JUNE 1993

8:45 INVITED SPEAKER *(Chair: W.J. Gutowski)*

BUDGETS AND BALANCES IN A WARMER WORLD
George J. Boer, CCC/AES

10:00 COFFEE BREAK

10:30 LATE MORNING SESSION

Panel Discussion by Invited Speakers. *Moderator: W.J. Gutowski*

12 NOON END OF MEETING

Acronyms

AES	Atmospheric Environment Service of Canada
CCC	Canadian Climate Centre
GFDL	Geophysical Fluid Dynamics Laboratory
NCAR	National Center for Atmospheric Research
RPN	Recherche en prévision numérique
UQAM	Université du Québec à Montréal

Participants

Dr. Thomas Agnew
CCC/AES
4905 Dufferin
Downsview, ON

Mr. Tércio Ambrizzi
Dept. of Meteorology
University of Reading
2 Early Gate, Whiteknights
Reading, Berks RG6 2AU, UK

Ms. Christiane Beaudoin
RPN/ AES
2121 Trans Canada
Dorval, Qc. H9P 1J3

Mr. Guy Bergeron
Dép. de physique
UQAM, C.P. 8888, succ. A
Montréal, Qc. H3C 3P8

Ms. Uma Bhatt
Dept. Atm. & Ocean. Sci
University of Wisconsin at Madison
1225 West Dayton St
Madison, Wisconsin 53706 USA

Dr. George J. Boer
CCC/AES
4905 Dufferin St.
Downsview, ON M3H 5T4

Mr. Onno Bokhove
Dept. of Physics
University of Toronto
60 St. George St.
Toronto, ON. M5S 1A7

Dr. Lee Branscome
Environmental Dynamics Res. Inc.
7338 155 Place North
Palm Beach Gardens
FL 33418 USA

Mr. Andrew Bush
Oceanography section
NCAR
P.O. Box 3000
Boulder, Colorado
80307-3000 USA

Dr. Ming Cai
CICS, Dept. of Meteorology
Univ. of Maryland
College Park, MD 20742 USA

Mr. Daniel Caya
Dép. de physique
UQAM, C.P. 8888, succ. A
Montréal, Qc. H3C 3P8

Dr. Douglas Chan
ARQM/AES
4905 Dufferin St.
Downsview, ON M3H 5T4

Dr. Edmond Chan
CCC/AES
4905 Dufferin St.
Downsview, ON M3H-5T4

Dr. Wilbur Y. Chen
Clim. Analysis Center
W/NMC52, Room 605
World Weather Bldg
5200 Auth Road
Washington, DC 20233 USA

Dr. Xinhua Cheng
JISAO, GJ-40
University of Washington
Seattle, WA 98195 USA

Dr. John H.E. Clark
513 Walker St.
University Park, PA 16802 USA

Ms. Hélène Côté
Dép. de physique
UQAM, C.P. 8888, succ.A
Montréal, Qc. H3C 3P8

Timothy M. Del Sole
29 Oxford St.
Pierce Hall, 107H
Harvard University
Cambridge, MA 02138 USA

Mr. Bertrand Denis
Dép. de physique
UQAM, C.P. 8888, succ. A
Montréal, Qc. H3C 3P8

Dr. Jacques Derome
Dept. of Atm. & Ocn. Sci.
McGill University
805 Sherbrooke St. W.
Montreal, Qc. H3A 2K6

Dr. Bernard Dugas
RPN/AES
2121 Trans Canada
Dorval, Qc. H9P 1J3

Dr. Brian F. Farrell
Dept. of Earth & Planetary Sciences
Pierce Hall
Harvard University
Cambridge, MA 02138 USA

Mr. Emanuel B. Fishbein
140 - 72 Burpen Crescent
Briarwood, NY 11435 USA

Dr. John C. Fyfe
CCCC/AES
4905 Dufferin St.
Downsview, ON. M3H 5T4

Mr. Stéphane Gaument-Guay
Dép. de physique
UQAM, C.P. 8888, succ. A
Montréal, Qc. H3C 3P8

Mr. Michel Giguère
Dép. de physique
UQAM, C.P. 8888, succ. A
Montréal, Qc. H3C 3P8

Mr. Éric Girard
Dép. de physique
UQAM, C.P. 8888, succ. A
Montréal, Qc. H3C 3P8

Mr. Stéphane Goyette
Dép. de physique
UQAM, C.P. 8888, succ. A
Montréal, Qc. H3C 3P8

Dr. Sylvie Gravel
RPN/AES
2121 Trans Canada
Dorval, Qc. H9P 1J3

Dr. William J. Gutowski Jr.
Dept. of Earth Sciences
3010 Agronomy Building
Iowa State University
Ames, Iowa 50011 USA

Dr. Nicholas Hall
Dept. of Meteorology
University of Reading
2 Early Gate, Whiteknight
Reading, Berks,
ENGLAND RG6 2AU

Dr. Tony Hansen
Augsburg College
731 21st Avenue South
Minneapolis, MN 55454 USA

Dr. Isaac M. Held
Geophysical Fluid Dynamics Laboratory
Princeton University
P.O. Box 308
Princeton, New Jersey 08542 USA

Ms. Fiona Horsfall
MPO/RSMAS, University of Miami
4600 Rickenbacker Causeway
Miami, Florida 3349 USA

Dr. James Hurrell
NCACR, ML 202A
P.O. Box 3000
Boulder, CO 80307 USA

Dr. Petros Ioannou
Cent. for Met. & Phy. Ocean.,
M.I.T.
Cambridge, MA 02139 USA

Mr. Weidong Jiang
Dept. of Earth Sciences
3010 Agronomy Building
Iowa State University
Ames, Iowa 50011 USA

Dr. David Keith
NCAR
P.O. Box 3000
Boulder, CO 80307-3000 USA

Mr. Ingo Kirchner
Max Plank Institute
Bundesstrasse 55
2000 Hamburg 15
Germany

Mr. Marc Klasa
Dept. of Atm. & Ocn. Sci.
McGill University
805 Sherbrooke St. W.
Montreal, Qc. H3A 2K6

Dr. Kenndoff Klauss
Meteorologisches Institut Müchen
Theresienstrasse 37
0 - 8000 Müchen 2
Germany

Dr. John Koshyk
CCC/AES
4905 Dufferin St.
Downsview, ON. M3H 5T4

Mr. Paul Kushner
Dept. of Physics
University of Toronto
60 St. George St.
Toronto, ON. M5S 1A7

Dr. Yochanan Kushnir
Lamont-Doherty Earth Observatory
Columbia University
Palisades, NY 10964 USA

Dr. Stephen Lambert
CCC/AES
4905 Dufferin St.
Downsview, ON. M3H 5T4

Dr. René Laprise
Département de physique
UQAM, C.P. 8888, succ. A
Montréal, Qc. H3C 3P8

Mr. Marc Larocque
Dép. de physique
UQAM, C.P. 8888, succ. A
Montréal, Qc. H3C 3P8

Mr. Yvan Larocque
Dép. de physique
UQAM, C.P. 8888, succ. A
Montréal, Qc. H3C 3P8

Dr. Charles A. Lin
Dept. of Atm. & Ocn. Sci.
McGill University
805 Sherbrooke St. W.
Montreal, Qc. H3A 2K6

Mr. Hai Lin
Dept. of Atm. & Ocn. Sci.
McGill University
805 Sherbrooke St. W.
Montreal, Qc. H3A 2K6

Dr. Damin Liu
CCC/AES
4905 Dufferin St.
Downsview, ON M3H-5T4

Dr. C. Lu
Dept. Atm. Sciences
Colorado State U.
Fort Collins, CO 80523 USA

Mr. Anthony Lupo
Dept. Earth & Atmos. Sci.
Purdue University
West Lafayette
IN 47907-1397 USA

Dr. Norman McFarlane
CCC/AES
4905 Dufferin St.
Downsview, ON. M3H 5T4

Mr. Murray D. MacKay
Dept. of Physics
University of Toronto
60 St George St
Toronto, ON, M5S 1A7

Mr. Wilhelm May
Max-Planck Institute for Meteorology
Bundesstrasse 55
2000 Hamburg 13
Germany

Mr. Sylvain Ménard
Dép. de physique
UQAM, C.P. 8888, succ. A
Montréal, Qc. H3C 3P8

Mr. Douglas G. Mercer
6583 Quinpool Rd.
Halifax, NS B3L 1B6

Dr. Mu Mu
Dept. of Physics
University of Toronto
60 St. George St.
Toronto, ON. M5S 1A7

Dr. Todd P. Mitchell
Joint Inst. for the Study of
the Atmos. & Ocean, GJ-40
University of Washington
Seattle, WA 98195 USA

Mr. Keith Ngan
Dept. of Physics
University of Toronto
60 St. George St.
Toronto, ON. M5S 1A7

Mr. Gregor Nitsche
Dept. Atmospheric Sciences AK-40
University of Washington
Seattle, WA 98195 USA

Dr. Enda O'Brien
RSMAS/MPO
University of Miami
46000 Rickenbacker Cswy.
Miami, FL 33149 USA

Ms. Ge Peng
8600 S.W. 67 Ave. #905
Miami, Florida 33143 USA

Ms. Shiling Peng
Dept. of Atm. & Ocn. Sci.
McGill University
805 Sherbrooke St. W.
Montreal, Qc. H3A 2K6

Dr. Raymond Pierrehumbert
Dept. Geophysical Sciences
University of Chicago
5734 S. Ellis Ave.
Chicago. Ill 60637 USA

Dr. Harold Ritchie
RPN/AES
2121 Trans Canada
Dorval, Qc. H9P 1J3

Dr. Chantal Rivest
RPN/AES
2121 Trans Canada
Dorval, Qc. H9P 1J3

Dr. Walter Robinson
Dept. of Atmospheric Sciences
University of Illinois
at Urbana-Champaign
105 South Gregory Avenue
Urbana, Illinois 61801 USA

Mr. Kirill Semeniuk
Dept. of Physics
University of Toronto
60 St. George St.
Toronto, ON. M5S 1A7

Dr. Catherine A. Senior
Hadley C. for Clim. Prediction & Res.
Meteorological Office
London Road, Bracknell
Berks, RG12 2SY, UK

Mr. Hubert Shen
Dept. of Physics
University of Toronto
60 St. George St.
Toronto, ON. M5S 1A7

Dr. Jian Sheng
CCC/AES
4905 Dufferin St.
Downsview, ON. M3H 5T4

Dr. Theodore G. Shepherd
Dept. of Physics
University of Toronto
60 St George St
Toronto, ON. M5S 1A7

Dr. Phillip J. Smith
Dept. of Earth & Atm. Sciences
Purdue University
1397 Civil Eng. Bldg.
West Lafayette, Indiana
47907-1397 USA

Dr. Peter H. Stone
Room 54-1718
Mass. Inst. Tech.
Cambridge, MA 02139 USA

Mr. Christopher M. Strong
Dept. Atmospheric Sciences
UCLA
405 Hilgard Ave.
Los Angeles
CA 90024-1565 USA

Dr. De-Zheng Sun
GFDL/NOAA
Princeton University
US Route 1, Forrestal Campus
New Jersey, 08542 USA

Dr. K. Szilder
Meteorology Division
Dept. of Geography
University of Alberta
Edmonton, Alta T6G 2H4

Dr. Monique Tanguay
RPN/AES
2121 Trans Canada
Dorval, Qc. H9P 1J3

Ms. Danielle Therrien
Dép. de physique
UQAM, C.P. 8888, succ. A
Montréal, Qc. H3C 3P8

Mr. Christian Thurre
Dép. de physique
UQAM, C.P. 8888, succ. A
Montréal, Qc. H3C 3P8

Dr. Mingfang Ting
Dept. of Atmospheric Sciences
University of Illinois
at Urbana-Champaign
105 South Gregory Avenue
Urbana
Illinois 61801-3070 USA

Dr. Ennio Tosi
ADGB- Atmospheric Dynamics Group
Dept. of Physics
University of Bologna
Via Irnerio 46,40126 Bologna
Italy

Mr. Dinh Hai Tran
Dept. of Atm. & Ocn. Sci.
McGill University
805 Sherbrooke St. W.
Montreal, Qc. H3A 2K6

Dr. E. Yakimiw
RPN/AES
2121 Trans Canada
Dorval, Qc. H9P 1J3

Dr. Zuojun Zhang
Dept. of Atmospheric Sciences
UCLA
Los Angeles
CA 90024-1565 USA

Budgets and Balances in a Warmer World

G. J. Boer
Canadian Climate Centre
Downsview, Ont.

Potential climate warming is studied by performing the "first standard CO2 experiment" which consists of coupling a comparatively sophisticated atmospheric general circulation model to a thermodynamically, but not dynamically, active ocean/ice model. The differences in the equilibrium climates simulated for the current or 1xCO2 case and for the new equilibrium climate that results with twice that amount of CO2 are investigated. Experiments of this general kind are reviewed in Houghton et al. (1990,1992) and in many individual references. The results for the Canadian Climate Centre (CCC) general circulation model are discussed in that reference and, in more detail, in Boer et al. (1993) and Boer (1993).

The version of the model used for the experiment has a number of modestly unique features including: (1) increased resolution at T32L10, (2) interactive clouds and interactive cloud optical properties, (3) a soil hydrology scheme incorporating variable soil moisture capacity and evapotranspiration depending on soil and vegetation type, (4) more sophisticated radiative transfer calculations, (5) an interactive "slab" ocean incorporating a specification of the effects of ocean transport, and (6) an interactive thermodynamic ice model incorporating a parameterization of leads.

Results for December-February are analyzed as the season representing the (northern hemisphere) middle-latitude meteorological paradigm. Radiative forcing is strong and this results in large pole-to-equator temperature differences and land-ocean contrasts. The dynamics of the atmosphere and ocean act to reduce the temperature gradients which would otherwise exist by transporting energy poleward and continentward. This is associated with the conversion of internal forms of energy to the kinetic energy of the motions that accomplish the transports. The nature of the poleward energy transport and the associated rate of working of the atmospheric *heat-engine* are basic features of the climate system.

The thermodynamic aspects of simulated climate change are usually given most attention. As shown in Boer et al. (1993), the statistical significance of the simulated temperature change is very much higher than that of the other surface (and upper air) variables. The simulated temperature change shown in Figure 1 for December-February is certainly statistically significant. The change is such as to *reduce* temperature gradients both in the north/south and between land and ocean in the lower troposphere. In the upper troposphere however, the pole-to-equator temperature gradient increases.

Although doubling CO2 directly and indirectly affects the radiative forcing of the system, the change in overall forcing is remarkably small as shown in Figure 25 of Boer et al. (1993). Oceanic energy transports do not change in the simplified ocean treatment used here so the change in atmospheric energy transport must also be small. In other words, the atmosphere's dynamics must operate in a somewhat different fashion in the 2xCO2 case since the forcing and hence the poleward energy transport remains essentially the same but the thermodynamic structure of the atmosphere differs considerably.

The differences in middle latitude dynamics may be characterized in an over-simplified way by stating that the flow structures operate *more efficiently* in the 2xCO2 case since they transport essentially the *same* amount of energy poleward but are themselves *weaker*. Figure 2 shows the *decrease* in the poleward transport of internal and potential energy that might be expected given the decreased temperature gradients of Figure 1. This is accompanied by an *increase* in latent energy transport so that the *net* transport, which is the sum of the two, changes very little. Figure 2 also shows the *decrease* in the poleward transport of angular momentum accompanying the weaker transport of internal and potential energy associated with a less vigorous middle latitude dynamical regime.

The change in the atmospheric energy cycle is shown in Figure 3. The overall rate of working of the atmospheric heat engine decreases by about 10% in the warmer world as do the zonal and eddy available potential energies. The eddy kinetic energy decreases slightly indicating a weakening of the eddies while the zonal kinetic energy actually increases slightly. Intriguing differences are inferred for the

generation and dissipation terms. The generation of eddy available potential energy actually increases while the remaining terms decrease. The rate of dissipation of zonal kinetic energy decreases even though the kinetic energy itself increases.

In summary, although the dynamical consequences of greenhouse gas warming are not as marked nor statistically significant as the thermodynamical changes, they display an intriguing rearrangement of flow structures which take advantage, so to say, of the altered thermodynamic structures in the atmosphere that occur. Since the overall forcing does not change appreciably, the poleward transport of energy remains the same but this is accomplished by an increase in latent energy transport associated with a warmer and moister lower troposphere which balances a decrease in internal and potential energy transport associated with weaker temperature gradients in this region. The overall rate of working of the atmospheric heat engine decreases. The simulated atmosphere has balanced its basically unchanged top-of-the-atmosphere radiative forcing with somewhat weaker eddies and a weaker energy cycle by transporting energy poleward more efficiently in the form of latent energy in the warmer and moister 2xCO2 world. A more detailed investigation of these changes is underway.

References

Houghton, J.T., G.T. Jenkins and J.J. Ephraums (eds), 1990: *Climate Change: the IPCC Scientific Assessment.* Cambridge University Press, 364pp.

Houghton, J.T., B.A. Callander and S.K. Varney (eds), 1992: *Climate Change 1992: the supplementary report to the IPCC Scientific Assessment.* Cambridge University Press, 198pp.

Boer, G.J., N.A. McFarlane and M. Lazare, 1993: Greenhouse gas-induced climate change simulated with the CCC second-generation general circulation model. *J. Climate,* **5**, 1045-1077.

Boer, G.J., 1993: Climate change and the regulation of the surface moisture and energy budgets. *Climate Dynamics*, **8**, 225-239.

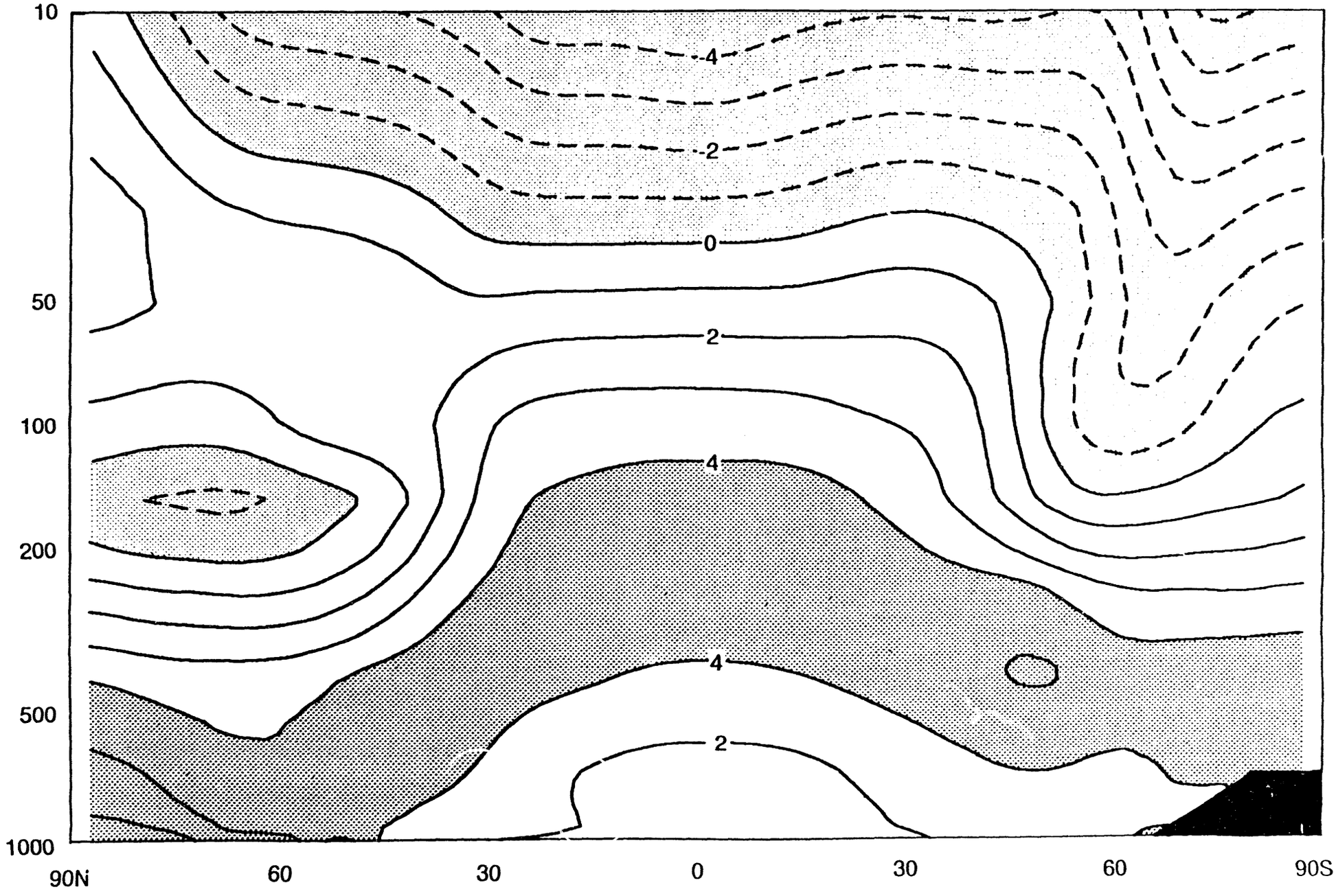

Figure 1. Simulated temperature change between 2xCO2 and 1xCO2 climates for December-February. Units °C

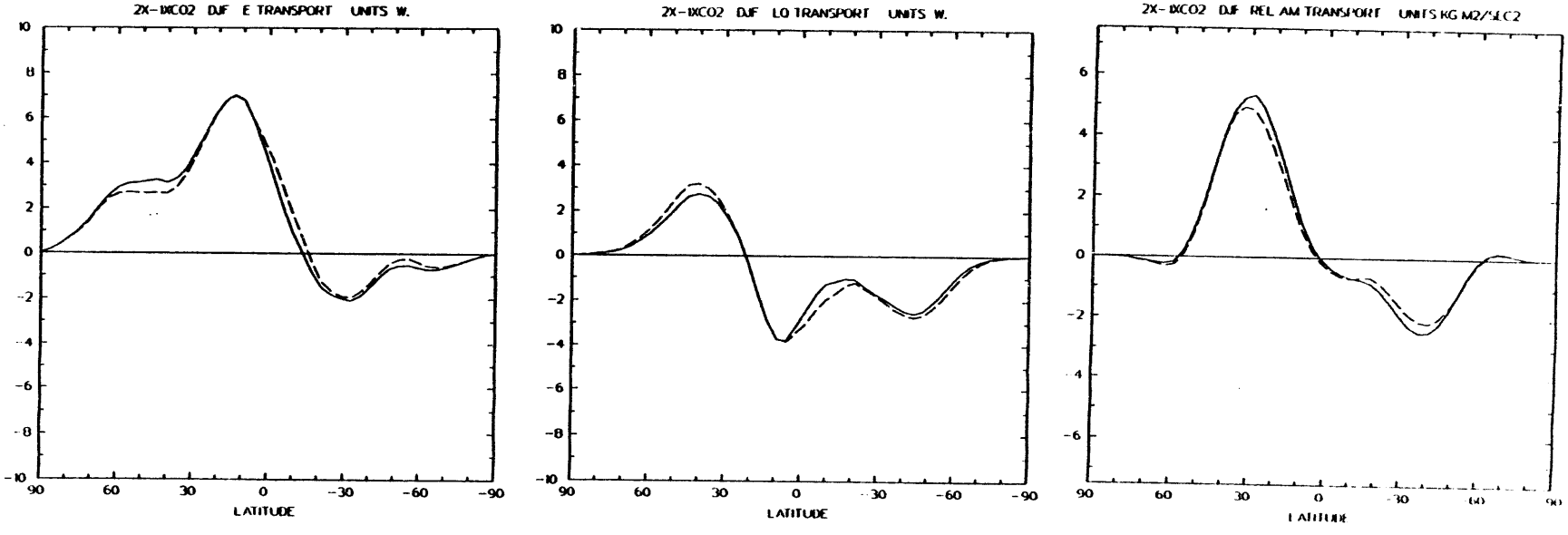

Figure 2. Energy and momentum transports (positive values imply northward transport) for the 1xCO2 climate (solid lines) and the 2xCO2 climate (dashed lines) for internal plus potential energy (left panel), latent energy (middle panel) and angular momentum (right panel). Energy transport units 10^{15} W, angular momentum transport units 10^{19} Kg m^2 s^{-2}.

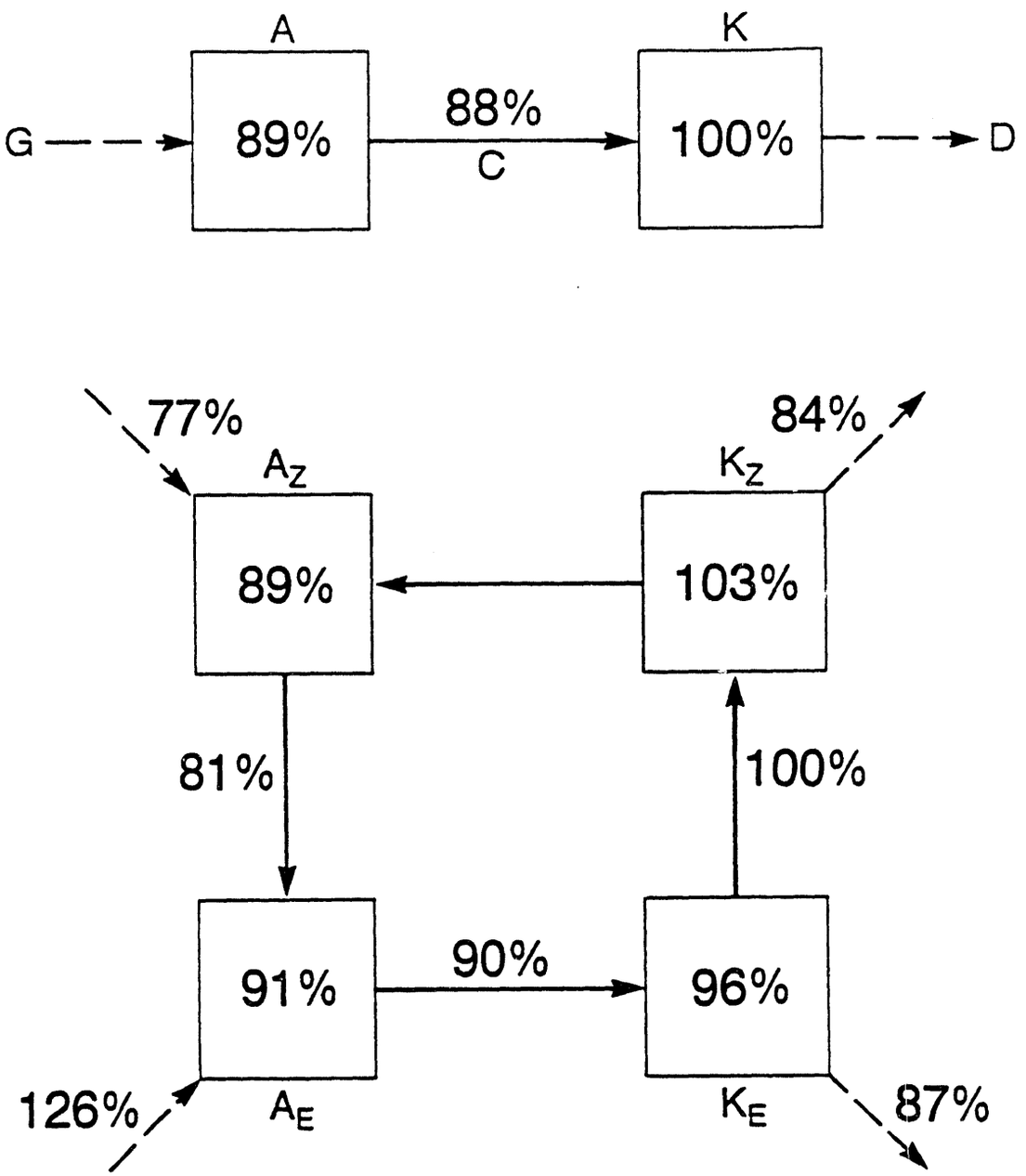

Figure 3. Simulated changes in the atmospheric energy cycle displayed as a ratio 2xCO2/1xCO2.

An Observational Study of the Interaction between the Synoptic-Scale Eddies and the Intra-Seasonal Fluctuations in the Atmosphere

Jacques Derome, Jian Sheng[1], Hai Lin and Marc Klasa

Department of Atmospheric and Oceanic Sciences, and
Centre for Climate and Global Change Research
McGill University

1. Introduction

It is clear from the kinetic energy spectrum published by Vinnichenko (1970) that the atmospheric fluctuations with periods between about 10 and 100 days form a very important part of the atmospheric flow. These oscillations, often called low-frequency or intra-seasonal fluctuations, could result from an instability of the time-mean flow, from an interaction with the oceans, or from a nonlinear transfer of energy from the faster synoptic-scale eddies. In the present study we concentrate on this last possibility and examine, with the help of atmospheric data and general circulation model (GCM) output, the extent to which the synoptic-scale eddies affect the low-frequency fluctuations.

2. Energetics of low-frequency fluctuations

Sheng and Derome (1991a) used ECMWF Northern Hemisphere analyses from 1980 through 1984 to study the energetics of the atmosphere. They expanded the data as a sum of three frequency classes, namely, (i) a seasonal mean (winter or summer), (ii) the intra-seasonal or low-frequency fluctuations, with periods between 10 and 90 days, and (iii) the synoptic-scale fluctuations, with periods between 2 and 10 days. The summer season results present a very systematic picture of the energetics. The available potential energy is transferred from the longer to the shorter time scales and for all three frequency classes it is converted to kinetic energy. The kinetic energy, on the other hand, is transferred from the faster to the slower time scales. In winter (Fig. 1) the energy transfers follow the same directions, except for one notable difference. During the cold season the time-mean flow transfers kinetic energy to the low-frequency flow, in agreement with the study of Simmons et al. (1983) who showed that the mean-January upper tropospheric flow is barotropically unstable to low-frequency oscillations. It is important to note, however, that the two main sources of kinetic energy for the low-frequency flow are the baroclinic conversion from the available potential energy (45%) and the transfer of kinetic energy from the synoptic-scale eddies (40%). There may well be episodes

---

[1] Now with the Canadian Climate Centre, Atmospheric Environment Service of Canada

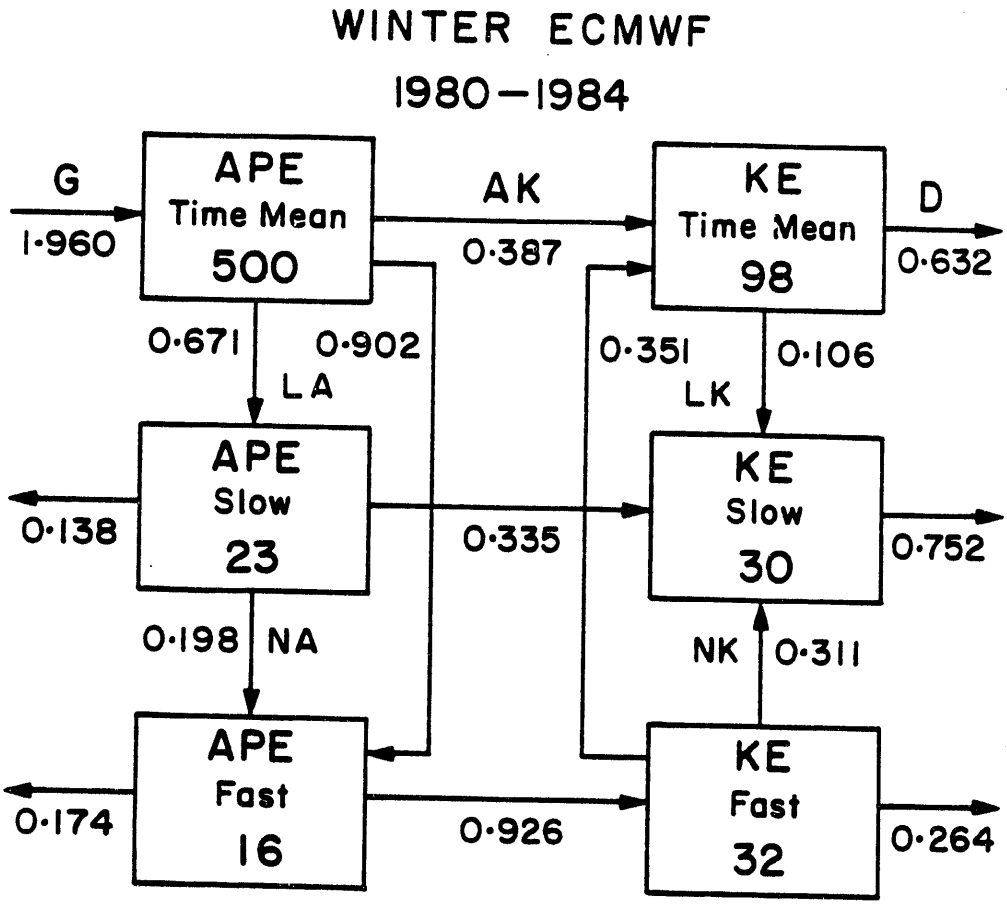

Fig. 1 Winter season energy levels, in units of 10^4 J/m^2, and conversions, in units of W/m^2, for the seasonal mean flow, the low-frequency fluctuations (periods 10 to 90 days) and the synoptic scale eddies (periods 2 to 10 days). From Sheng and Derome (1991a).

when the instability mechanism proposed by Simmons et al. is very important, but on average the other two sources of energy are much more important.

Sheng and Derome (1991b) performed similar calculations based on the output of a low resolution (T20) version of the Canadian Climate Centre GCM. They found that the energy transfers were all in the same direction as those of the atmosphere, for both the summer and winter seasons, but that the level of kinetic energy was too low for both the low-frequency flow and the synoptic-scale eddies, a common problem in GCMs.

3. Time evolution of low-frequency fluctuations

(a) Barotropic interactions with the synoptic-scale eddies

Sheng and Derome (1993) examined the time evolution of the low-frequency height field in the upper troposphere and compared it with that of the "forcing" by the synoptic-scale eddies. The latter was obtained by computing the vorticity flux divergence associated with the synoptic-scale flow, projecting the time series onto the low-frequency band, and applying the geostrophic relationship to convert the result to a height tendency. In an effort to determine whether the synoptic-scale eddies cause, or react to, changes in the low-frequency flow, the time series of the barotropic forcing was correlated with that of the low-frequency height field at various lags in time and in the zonal direction. The results (Fig. 2) indicate that in the region of maximum correlation over the eastern Atlantic, the low-frequency height field evolution is best correlated with the barotropic forcing about 20 degrees to the west, and about 12 hours earlier. As the time series that are being correlated with each other are associated with periods in the range 10 to 90 days, a time lag of 12 hours for the maximum correlation can be considered very small.

(b) Baroclinic interactions with the synoptic-scale eddies

Lin and Derome (1993) extended the above study by comparing the evolution of the low-frequency temperature field with the low-frequency projection of the temperature flux divergence by the synoptic-scale eddies. It was found that in the region of maximum correlation over eastern North America, the temperature flux convergence at a point is best correlated with the temperature field about 25 degrees to the west, about 1.5 days earlier (Fig. 3). It is important to note that the above correlation is negative, indicating that the synoptic-scale eddies have a damping effect on the low-frequency temperature wave, in agreement with the energetics of Fig. 1.

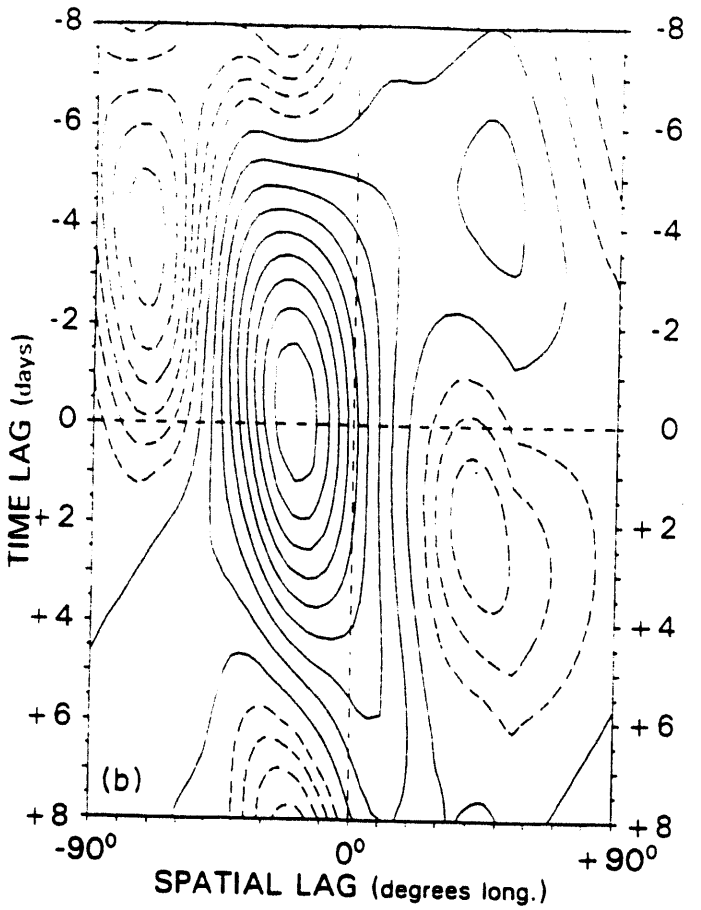

Fig. 2 Correlation coefficient between the barotropic eddy forcing and the low-frequency height field. Solid (dashed) contours represent a positive (negative) correlation; the contour interval is 0.05. A negative time or longitude lag indicates that the forcing is leading the low-frequency height. From Sheng and Derome (1993).

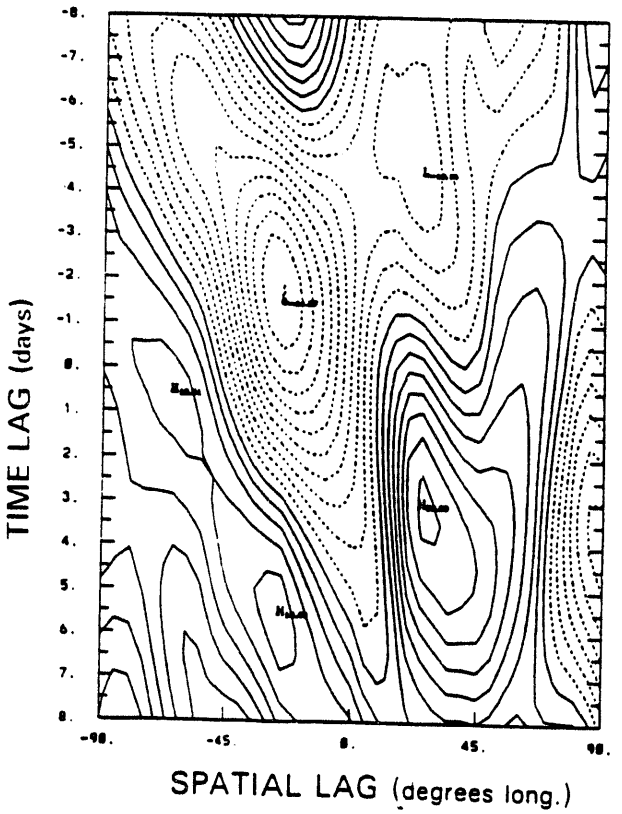

Fig. 3 Correlation coefficient between the baroclinic eddy forcing and the low-frequency temperature field. Solid (dashed) contours represent a positive (negative) correlation; the contour interval is 0.05. A negative time or longitude lag indicates that the low-frequency temperature is leading the eddy forcing.

4. The Pacific North American pattern and its interactions with the synoptic-scale eddies

The extent to which we will ever be able to predict atmospheric mean-monthly anomalies will depend to some extent on the importance of their interaction with the synoptic-scale eddies, which have a predictability period of less than one month. Klasa et al. (1992) have investigated the barotropic interaction between a special type of mean-monthly anomaly, namely, the Pacific North American Pattern (PNA), and the synoptic-scale eddies. Using the winter analyses from the U.S. National Meteorological Center for the period 1965 through 1989, the PNA index, as defined by Wallace and Gutzler (1981), was computed for each month. The 19 months with an index greater than 1 were grouped together to represent the positive phase of the PNA pattern, as were the 17 months with an index less than -1 for the negative phase. For each month in the two groups the mean-monthly vorticity flux convergence by the synoptic-scale eddies was computed at three levels over the Northern Hemisphere, and converted to a height tendency. Fig. 4 presents the composite anomaly pattern, and the composite height tendency at 250 hPa for both the positive and negative phases of the PNA pattern. The positive correlation between the height anomalies and the forcing fields is evident. Finally, a steady-state three-level global quasi-nondivergent model was developed to compute the response to the synoptic-scale eddy barotropic forcing. The model was linearized about a non-zonal mean flow obtained by averaging 23 winters. The results (not shown) indicate that in the positive phase of the PNA pattern the barotropic forcing leads to a low pressure centre south of the Aleutian islands and to a high pressure cell over north-eastern Canada and over Greenland, that is, somewhat downstream of the PNA pattern itself. The forced disturbance over the north-eastern Pacific has an amplitude of about 40% of the low pressure cell of the PNA pattern, but experiments remain to be done to determine the sensitivity of the results to the dissipation parameters. The current work on this modelling effort involves the calculation of the baroclinic forcing by the synoptic-scale eddies, and the computation of the model response to the combined barotropic-baroclinic forcing.

5. Conclusions

The main conclusions of the presentation are that:

a) About 40% the kinetic energy of the low-frequency oscillations comes from the synoptic-scale eddy kinetic energy.
b) The barotropic instability mechanism of Simmons et al. (1983) operates in winter, but provides relatively little energy, on average, to the low-frequency flow.
c) The low-frequency temperature field leads the temperature flux divergence by the synoptic-scale eddies.
d) The low-frequency height field lags very slightly the vorticity flux divergence by the synoptic-scale eddies.

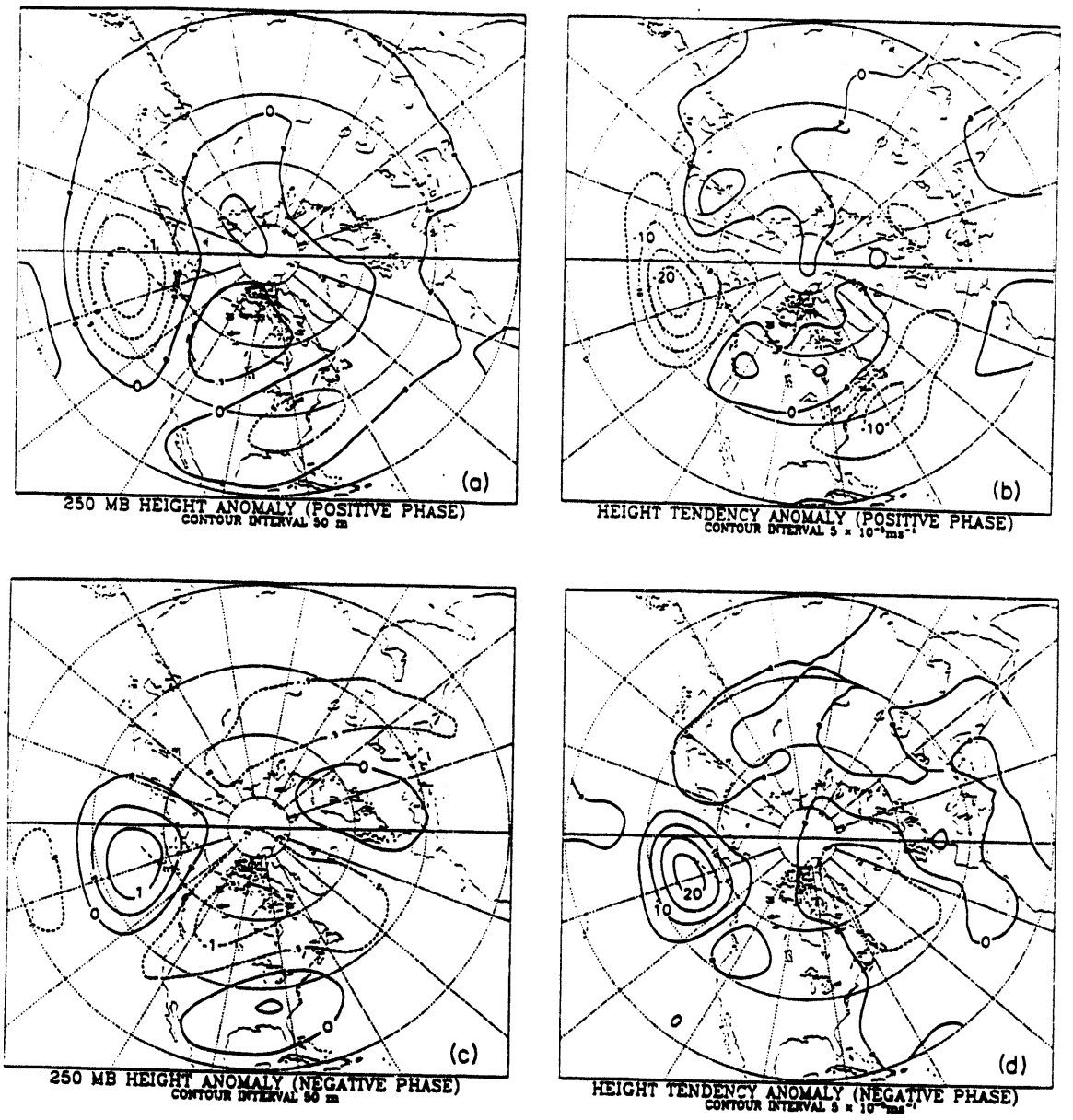

Fig. 4 250 hPa composites of the monthly mean height anomaly and barotropic eddy vorticity forcing anomaly expressed as a height tendency. Positive phase for (a) height and (b) height tendency. Negative phase for (c) height and (d) height tendency. The contour intervals are 50 m for (a) and (c) and 5×10^{-5} m/s for (b) and (d). From Klasa et al. (1992).

e) The mean-monthly barotropic forcing by the synoptic-scale eddies is spatially in phase with the PNA pattern itself. The linear response to the barotropic forcing is somewhat downstream of the PNA pattern.

References:

Klasa, M., J. Derome and J. Sheng, 1992: On the interaction between the synoptic-scale eddies and the PNA teleconnection pattern. *Contrib. Atmos. Phys. (Beitr. Phys. Atmos), 65/3*, 211-222.

Lin, Hai and J. Derome, 1993: Thermal forcing of slow transients by synoptic scale eddies in the atmosphere. Submitted for publication. Available as C²GCR report 93-10, from Department of Atmospheric and Oceanic Sciences, McGill University.

Sheng, J. and J. Derome, 1991a: An observational study of the interactions between the seasonal mean flow and the transient eddies. *Tellus*, **43A**, 128-144.

Sheng, J. and J. Derome, 1991b: On the interactions among flow components in different frequency bands in the Canadian Climate Centre general circulation model. *Atmosphere-Ocean*, **29**, 62-84.

Sheng, J. and J. Derome, 1993: The dynamic forcing of the slow transients by the synoptic scale eddies: an observational study. *J. Atmos. Sci.*, **50**, 757-771.

Simmons, A.J., J.M. Wallace and G.W. Branstator, 1983: Barotropic wave propagation and instability, and atmospheric teleconnection patterns. *J. Atmos. Sci.*, **40**, 1363-1392.

Vinnichenko, N.K., 1970: The kinetic energy spectrum in the free atmosphere - 1 second to 5 years. *Tellus*, **22**, 158-166.

Wallace, J.M. and D.S. Gutzler, 1981: Teleconnection in the geopotential height field during the Northern Hemisphere winter. *Mon. Wea. Rev.*, **109**, 784-812.

The Role of Eddy Transports in Climate Change

by Peter H. Stone

Massachusetts Institute of Technology

Abstract. Large-scale atmospheric eddies are the dominant transport mechanism in mid and high latitudes. Thus, climate models must simulate these eddies, their effects, and their feedbacks accurately. Getting the feedbacks right is particularly important since it is the feedbacks which affect climate sensitivity. Observational studies of these feedbacks are hindered by the lack of actual climate changes for which good data is available, and by the lack of data on vertical heat fluxes. General circulation model (GCM) studies are hindered by errors in GCM simulations of transports in the current climate; the dependence of GCM results on uncertain subgrid scale parameterizations; and large computational requirements.

A more promising approach for learning about eddy feedbacks and how they can be modelled is process model studies. So far these studies have only looked at the feedback between eddy sensible heat fluxes arising from baroclinic instability and the temperature structure. The results indicate that there is a very strong negative feedback between eddy fluxes and temperature structure, both meridional and vertical, with the fluxes themselves being sensitive to small changes in temperature structure. These studies need to be extended to higher vertical resolution, and to include the effects of moisture, stationary eddies, and coupling to the oceans.

1. Diagnostic Studies of the Current Climate

Diagnostic studies show that large-scale eddies are the dominant mechanism for transporting heat, moisture, and momentum from the subtropics to higher latitudes (Peixoto and Oort, 1992). Correspondingly, they play an important role in climate by making global temperatures more equable, drying out the subtropics, moistening higher latitudes, and forcing ocean circulations which in turn have important climatic effects (e.g., the Gulf Stream). The diagnostic studies also show that the meridional transports are associated primarily with transient eddies, but in the Northern Hemisphere in winter stationary eddies are quite important too.

Calculations of vertical eddy transports from observations are much more difficult and only give partial answers about the role of large-scale eddies. The total vertical eddy transports can be calculated as residuals (Hantel, 1976; Hantel and Hacker, 1978), but this does not distinguish between vertical transports by large-scale eddies and small-scale eddies, i.e., by moist convection. The residual calculations do show that vertical fluxes by eddies of all scales play an essential role in the heat and momentum balances at all latitudes. The only component of the vertical eddy fluxes that can be calculated directly from observations is that due to the large-scale stationary eddies (Oort and Rasmusson, 1971). Comparison of those results with the total eddy fluxes shows that the large-scale stationary eddies do not contribute significantly to the vertical eddy transport of heat (Stone, 1984) or momentum (Hantel and Hacker, 1978). Thus, diagnostic studies of vertical transports only tell us that large-scale transient eddies may be important in the heat and momentum balances in the extra-tropics. A similar ambiguity can be inferred concerning the role of vertical transports of moisture by large scale transient eddies.

By "large-scale" eddies we mean those eddies which make significant contributions to the global scale transports of heat, moisture, and momentum. The scales of these eddies can be determined from spectral decomposition of the eddy transports calculated from observations. Only very limited calculations of such spectra have been published and we therefore show in Figure 1 the results of an unpublished analysis of the eddy transports of sensible heat carried out by Amy Solomon, a student at MIT. The results show that most of the transport is accomplished by rather large-scale eddies, i.e., eddies with zonal wave

numbers ≤ 9, and very little by the synoptic-scale eddies associated with severe weather, i.e., those with wave numbers 10 to 20. Calculations of the spectral decomposition of the energy cycle (Kung, 1988) lead to a similar conclusion. Thus our discussion will implicitly be concerned with eddies with planetary wave numbers ≤ 9.

We will focus on the zonal mean state of the atmosphere and zonal mean eddy transports. This is not because zonal variations are unimportant -- they obviously are very important in determining regional climates. Rather it is because outside the tropics latitudinal variations are much stronger than longitudinal variations (Peixoto and Oort, 1992). Thus, in developing an understanding of climate and climate change outside the tropics we must first understand the zonal mean state. Diagnostic studies show that outside the tropics the meridional eddy momentum flux is not very important in forcing the zonal mean temperature and zonal wind fields (Edmon et al., 1980; Stone and Salustri, 1984), but very important in forcing the zonal mean meridional and vertical motions (Vernekar, 1967; Salustri and Stone, 1983). However, our understanding of how any of these fluxes or the zonal mean state would respond to climate change is still rudimentary. What we need to understand in particular is the feedbacks in the eddy fluxes, i.e., if climate changes, how will eddy transports change? Will the changes inhibit or magnify the climate changes, and how strongly will they do so? Given the importance of eddy transports in the extra-tropical atmosphere these changes will obviously play a crucial role in determining climate sensitivity.

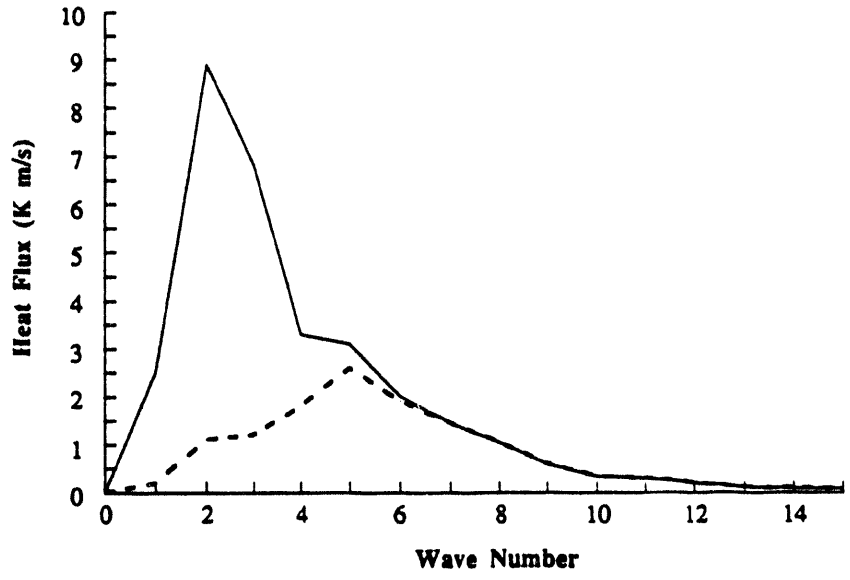

Fig. 1: Eddy fluxes of sensible heat at 51°N, 850 mb, vs. planetary wave number, calculated from ECMWF analyses for 10 Januarys (1979-1988). Solid line: total eddy flux; dashed line: transient eddy flux.

If we had observations of how eddy fluxes respond to actual climate changes we could attempt to deduce these feedbacks empirically. In practice the only example of such an observed change that we have is the seasonal change. Since this is only one possible kind of climate change it is not possible to use seasonal changes by themselves to determine

all the feedbacks. Nevertheless, observations of seasonal changes do provide an important constraint on models and theories of the feedbacks.

A prime example of such a constraint is the relationship between changes in the meridional eddy flux of sensible heat, $[\overline{v^*T^*}]$ and changes in the surface meridional temperature gradient, $\frac{\partial [T_s]}{\partial y}$. Stone and Miller (1980) considered an empirical relation of the form

$$[\overline{v^*T^*}] \propto -\left|\frac{\partial [T_s]}{\partial y}\right|^{n-1} \frac{\partial [T_s]}{\partial y}$$

and calculated n from observations of seasonal changes. They found that n varied from ~ 1.5 at 60N to ~ 3.5 at 30N. Allowing for errors in the observations, they concluded that these results were consistent with what one would expect if the eddy sensible heat flux was due to baroclinic instability. This is in fact the generally accepted explanation for why large-scale transient eddies form.

An equally noteworthy example of a potentially important feedback that cannot be studied using seasonal changes is the relation between large-scale vertical eddy heat fluxes and static stability. The former cannot be calculated directly from observations and the latter does not change appreciably in mid-latitudes during seasonal changes. Clearly at the present time observations give us only limited guidance and we must rely on model and theoretical studies to gain insights about feedbacks in eddy transports and how they affect climate sensitivity.

2. General Circulation Models

One possible approach for learning about eddy transports and feedbacks is to carry out experiments with numerical General Circulation Models (GCMs) of the atmosphere. One encouraging aspect of such an approach is that it appears that very high horizontal resolution is not necessary to simulate the eddy transports. This is implied by analyses like that shown in Figure 1 and also by numerical experiments with GCMs. The latter indicate that the most severe constraint is imposed by the need to resolve the eddy momentum flux. This flux is resolved reasonably well in the troposphere by a resolution of T31 (Boville, 1991). This resolution is readily obtained with current computers as long as the atmospheric GCM is not coupled to an ocean model requiring long time integrations.

A major problem with this approach is that the transports by the large-scale motions resolved in GCMs are sensitive to the sub-grid scale parameterizations (Stone and Risbey, 1990). These parameterizations are sufficiently uncertain that the meridional heat transports simulated by GCMs differ from each other and from observations by as much as a factor of two. Whether GCMs can simulate accurately vertical transports by large-scale eddies is completely unknown, because of the lack of observational analyses of these transports—and once again there are large differences between different GCMs (Stone and Risbey, 1990). A clear warning sign that GCMs may not be adequate for transport studies is that no coupled atmosphere-ocean GCM has yet been able to simulate the current climate without introducing large flux corrections at the interface between the atmosphere and the ocean (Washington and Meehl, 1989; Manabe et al., 1991; Cubasch et al., 1993). Consequently, simulations of eddy transports and feedbacks with GCMs are problematic and the results are likely to be model dependent. In addition, parametric studies of eddy transports and feedbacks with GCMs require large amounts of computer time. For all these reasons, studies of eddy transports and eddy feedbacks have not been carried out with GCMs.

3. Theoretical Studies

Theoretical studies of eddy transports and feedbacks can generally be thought of as "process" model studies, i.e., they use models which are more or less simplified compared to GCMs and the real world, and are designed to study how eddies interact with a limited number of physical processes. The simplifications necessarily mean that the models used in these studies cannot be thought of as true climate models. Nevertheless such studies can give valuable guidance as to what is necessary to simulate eddy transports and feedbacks accurately. Given the limitations of current observations and GCMs, process model studies may well be the most practical approach to improving our understanding of large scale eddy processes and how to represent them in climate models.

Theoretical studies have so far concentrated on the feedback between transient eddy sensible heat fluxes and temperature structure. This is natural, given that temperature is the primary climate variable and that the transient eddy sensible heat flux is the largest single contributor to the meridional heat transport in the atmosphere (Peixoto and Oort, 1992). However, it is not hard to think of many other interactions that also need to be studied. For example, these studies need to be extended to include transient eddy latent heat fluxes and stationary eddy sensible heat fluxes, since these are also important contributors to the heat transport in the extra-tropical atmosphere.

The studies of the feedback in the transient eddy sensible heat fluxes have generally relied on models in which the transient eddies owe their existence to normal-mode baroclinic instability. Farrell (1985) has suggested that in fact Ekman friction in the atmosphere is strong enough to eliminate baroclinic instability, and that the transient eddy heat fluxes are due to the nonmodal growth of forced perturbations. In response to this suggestion, Lin and Pierrehumbert (1988) carried out a thorough analysis of the effect of Ekman friction on baroclinic instability and concluded that normal mode instability would not be eliminated. However, this conclusion does depend on the poorly-known value of the eddy viscosity in the planetary boundary layer. Thus Farrell's suggestion is worth working out more fully to see if it is competitive with or complementary to baroclinic stability theory for explaining the observed properties of transient eddy fluxes.

4. The Interaction Between Baroclinic Instabilities and Temperature Structure

i) Unforced systems

The studies looking at eddy sensible heat fluxes arising from baroclinic instability fall into two groups, depending on whether the flow is forced or not. In the unforced case, an unstable initial state is perturbed, and the life-cycle of the growing perturbations and/or the manner in which they stabilize the initial state are analyzed. The most comprehensive study of this kind to date is that by Gutowski et al. (1989). They used a dry, primitive equation model, with a uniform lower boundary on a β-plane, and examined how a perturbation with a single zonal wave number grows and interacts with an initial flow similar to the mean flow in the atmosphere. Their most important result was that the stabilizing effect of the perturbations' vertical eddy sensible heat flux was just as important as the stabilizing effect of its meridional eddy heat flux.

This result shows that the question of the relative strength of vertical heat fluxes in the extra-tropics by large-scale eddies and by small-scale moist convection is an important one. The feedbacks associated with these two processes are quite different—e.g., the vertical eddy heat flux by large-scale eddies depends on the meridional temperature gradient, whereas that by moist convection does not—and one would anticipate that the response of the mid-latitude atmosphere to climate change would depend on the relative importance of these two fluxes. The small seasonal changes in the total vertical eddy heat flux found by Hantel (1976) in the extra-tropics suggest the vertical eddy heat fluxes are dominated by large-scale transient eddies in winter and by small-scale moist convection in summer. If the vertical heat fluxes by large-scale eddies are indeed important, then quasi-

geostrophic models are missing an important feedback mechanism and can give misleading results about eddy-mean flow interactions and climate sensitivity.

Another important result found by Gutowski et al. (1989) was that dissipative processes at the lower boundary significantly inhibited the stabilization of the initial state. This result is also implied by Lin and Pierrehumbert's (1988) analysis of the linearized baroclinic instability problem. Even if one accepts their conclusion as to what are typical values of the eddy viscosity (~ 3 m^2/s), these values are still sufficient to cut the maximum growth rates in half. It therefore appears that eddy transports and their feedbacks depend on small-scale dissipative processes. This is unfortunate from the point of view of modelling climate because these dissipative processes have to be parameterized, and how to parameterize them is uncertain.

Gutowski et al. (1989) also investigated what state the atmosphere would assume if it were adjusted to baroclinic neutrality. They concluded that the minimally adjusted state would have the meridional gradient of the quasi-geostrophic potential vorticity equal to zero in a layer next to the lower boundary. The adjusted state can be described rather simply in terms of the natural vertical scale that enters the baroclinic stability problem,

$$h = \frac{f^2 \frac{du}{dz}}{\beta N^2}$$

where f is the coriolis parameter, β is df/dy, y is the meridional coordinate, u the zonal wind, z the height, and N the Brunt-Vaisala frequency. h is just proportional to the isentropic slope, and in the minimally adjusted state

$$h = h_{adj} \equiv H\left(e^{z/H} - 1\right) \text{ for } z < z_a$$

where H is the scale height and z_a is the height at which the adjusted h equals the unadjusted h. In Gutowski et al.'s unforced model the initial state was in fact adjusted so that in the final state $h \equiv h_{adj}$ if dissipation is negligible. If it isn't, it is still adjusted towards h_{adj}, but h remains larger than h_{adj}.

ii) Forced systems

In forced systems baroclinic instabilities are being continually re-generated due to the destabilizing effect of the forcing. Thus one expects $h > h_{adj}$ in at least some layers of a forced system, even if dissipation is weak. Comparing the distribution of h in a model with that in the atmosphere is a useful way of assessing whether the model has a realistic simulation of baroclinic instability. Comparing these distributions in turn with h_{adj} can give useful insights as to whether baroclinic instability is playing an important role in adjusting the mean state in the model or in the atmosphere.

Figure 2 shows schematically what one would expect to find in a system where eddies arise due to baroclinic instability. As indicated in the figure one would expect the adjustment of h to be much weaker in the planetary boundary layer because dissipative effects and the boundary conditions suppress the eddy fluxes. If there is a strong baroclinic adjustment, then the distribution of h will be close to h_{adj}, and one would expect very strong feedback between the eddies and the temperature structure, i.e., the isentropic slope would be very insensitive to climate change. On the other hand, if the baroclinic adjustment is weak then h will be close to the unadjusted structure, h_e, the feedback in the eddy transports will be weak, and the isentropic slopes will be determined by the forcing.

Figure 3a shows h calculated for January conditions at 40N from observations and from the GCM of the Goddard Institute for Space Studies (GISS). (This is the GISS model II GCM with 4°x5° resolution described by Hansen et al., 1983.) Also shown is

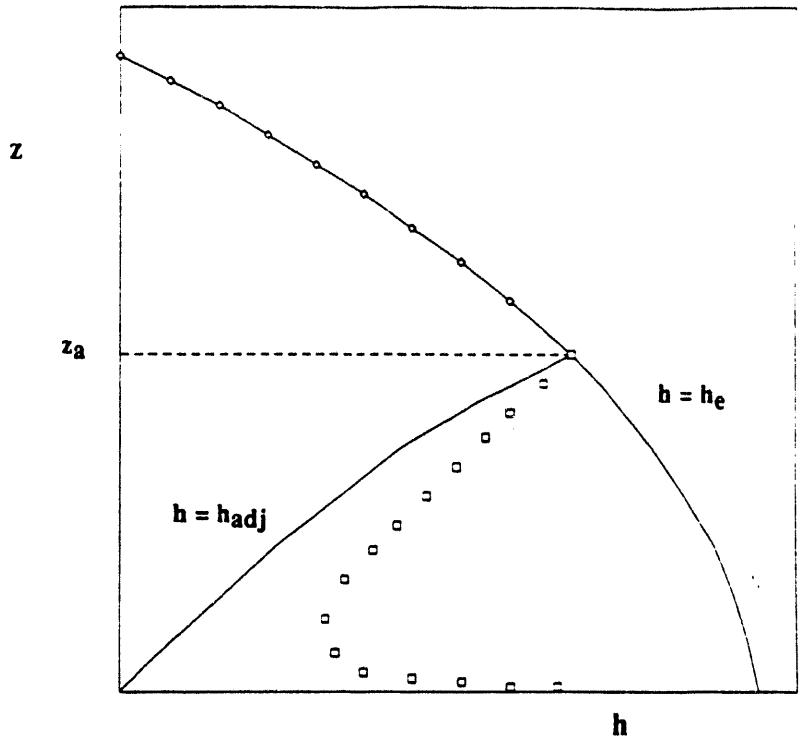

Fig. 2: Schematic diagram showing the variation of h with z in an atmosphere which is baroclinically unstable. The squares show the expected variation. The other quantities plotted are explained in the text.

h_{adj}. Both the model and the atmosphere appear to have a strong baroclinic adjustment in a layer 3 to 4 km deep, just above the planetary boundary layer. The increase of h with height in this layer is due to a decrease in the static stability, and as pointed out by Gutowski (1985) this is the characteristic signature of the stabilizing effect of the vertical eddy heat flux. This effect should be strongest at the steering level, and in fact the steering level does typically fall in the layer of apparently strong adjustment. Both the model and the atmosphere also show the effect of the lower boundary, i.e., near that boundary eddy fluxes are suppressed so h is farther from h_{adj}.

Figure 3a also shows a potentially important difference between the atmosphere and the GISS GCM, namely the GCM appears to be substantially more unstable in the lowest two km of the atmosphere. The larger values of h in this layer are due to smaller values of the static stability in the GCM. The GCM's overestimate of h in this layer may be the reason why the GISS GCM has too strong a poleward heat transport. The GCM's overestimate of the eddy heat flux (sensible plus latent heat) is illustrated in Figure 3b. In fact, the overestimate peaks in the lowest two km of the atmosphere.

Figures 3a and 3b supply another illustration of the potential importance of dissipative processes near the lower boundary in determining eddy fluxes and their feedbacks. The figures also suggest that vertical resolution higher than that in the GISS GCM may be necessary to simulate eddy processes accurately. The GISS model only has two layers in the planetary boundary layer and two in the layer where a strong baroclinic adjustment appears to occur. The questions of how many layers are necessary to simulate accurately dissipation in the planetary boundary layer, or to simulate accurately eddy-mean flow interactions near the steering level, deserve more attention than they have received.

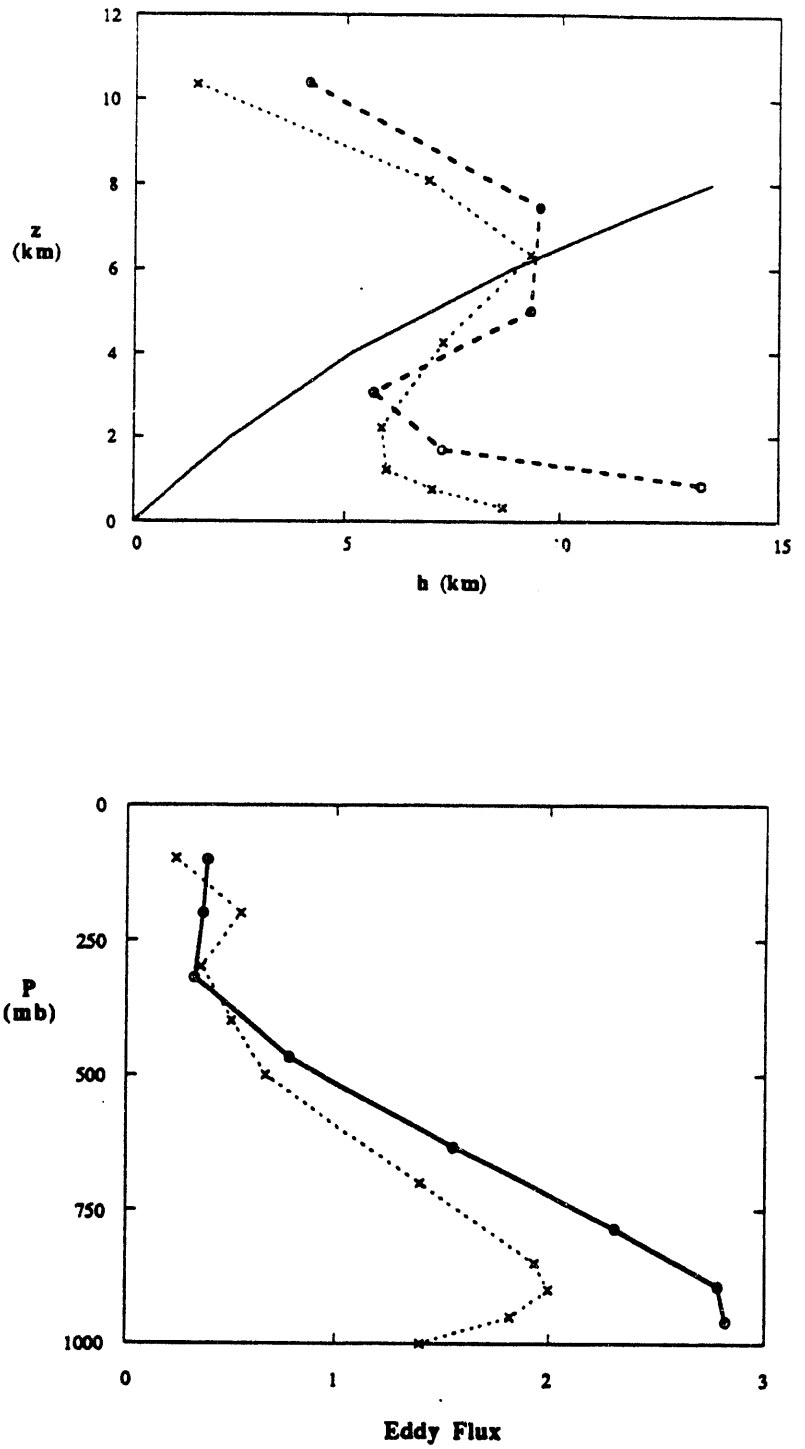

Fig. 3a, top: h as a function of height at 40°N in January. The solid curve is h_{adj}.

Fig. 3b, bottom: Eddy flux of heat as a function of pressure level at 40°N in January. Observations (Oort and Rasmusson, 1971) are indicated by x's and results from the GISS Model II GCM at 4°x5° resolution are indicated by o's.

Theoretical studies of forced systems are much more difficult than studies of unforced systems because they must integrate over many eddy life cycles in order to simulate the statistical equilibrium state, i.e., the climate. Parametric studies of eddy transports and feedbacks in forced systems to date have only been carried out with two-level models because of the computational requirements. Our discussion above makes it clear that two-level models may not be adequate for studying eddy processes as they occur in the atmosphere. However, they are the best studies available to date and do at least give guidance as to what one might look for in more sophisticated models.

The most realistic of these two-level model studies is that of Zhou and Stone (1993). They used a dry, balance equation model on a sphere with a uniform lower boundary. The model was forced by a Newtonian relaxation of the temperature structure towards a specified equilibrium state, the main dissipation outside the tropics was drag at the lower boundary, and the calculations were fully nonlinear. Two-level models only resolve a single value of h. For realistic parameter choices Zhou and Stone found that h was about twice h_{adj} and about three-quarters of h_e. Nevertheless, feedbacks in the eddy fluxes were very strong with the value of h being very insensitive to all the external parameters. They also confirmed the result found with unforced models, that the vertical eddy heat flux was an important part of the feedback.

The insensitivity of h to the forcing implies that the eddy heat fluxes are sensitive to the forcing. Indeed, Zhou and Stone found that the meridional eddy heat flux in midlatitudes in their model was proportional to the third or fourth power of the meridional temperature gradient. This result is in fact consistent with observed seasonal changes, if one identifies the temperature gradient in the two-level model with the mid-tropospheric temperature gradient. This gradient has smaller seasonal changes than the surface temperature gradient, and the empirical relationship between flux and temperature gradient is stronger, consistent with the two-level model result. In any case, in the model the temperature structure is very robust, but the heat fluxes are sensitive to the external parameters.

5. Interaction of Eddies with the Oceans

Another potentially very important role that eddies may play in climate change involves their interaction with ocean circulations. There is considerable paleoclimatic evidence that the thermohaline circulation (THC) in the North Atlantic is sensitive to small changes (e.g., Lehman and Keigwin, 1992) and modelling studies suggest that the THC is unstable to finite amplitude salinity perturbations (e.g., Marotzke and Willebrand, 1991). Since the THC is driven by fluxes of heat and moisture between the atmosphere and the oceans the sensitivity of the THC will depend on feedbacks between these surface fluxes and the THC, and changes in the surface fluxes in turn depend on feedbacks in eddy transports in the atmosphere. The surface moisture flux, and therefore the atmosphere's eddy moisture flux, are particularly important in determining the sensitivity of the THC (Marotzke and Willebrand, 1991).

Nakamura et al. (1993) have identified one particular feedback process that could be very important in determining the sensitivity of the THC. The process can be described by the following chain of events. A decrease in salinity of the high latitude oceans → a weaker THC → a decrease in poleward heat transport by the THC → a larger meridional temperature gradient → an increased poleward eddy moisture transport in the atmosphere → an increase in net precipitation in high latitudes → a further decrease in salinity of the high latitude oceans, etc. Thus this feedback is positive and enhances the sensitivity of the THC. Nakamura et al. tested its impact in a simple five-box model of the coupled atmosphere-ocean system and found that it decreased the salinity perturbation necessary to cause the THC to collapse by one-third.

Interactions like the above clearly need to be studied in more sophisticated models. Studies with GCMs, however, are again handicapped by their need for surface flux adjustments. In this case the fact that they require large adjustments in surface moisture fluxes implies that the GCMs are not simulating eddy moisture transports accurately. Such errors obviously compromise their ability to simulate accurately the feedback process identified by Nakamura et al. Given the relatively primitive state of our understanding of the coupled atmosphere-ocean system, there may also be other important feedbacks between the atmosphere and the oceans involving atmospheric eddy transports which have not yet been identified. There is a clear need for more process model studies of coupled atmosphere-ocean systems.

6. Summary

Our understanding of eddy transports and feedbacks and climate sensitivity is still very primitive. Answers to the following questions would advance our understanding significantly:

1. How important are vertical heat transports by large-scale transient eddies?

2. What are the sources of error in GCM simulations of eddy transports?

3. How is the interaction of baroclinic eddies with temperature structure affected by vertical resolution and dissipation?

4. How is the interaction affected by the presence of stationary eddies and/or moisture?

5. How is the sensitivity of the ocean circulations affected by their interaction with atmospheric transports?

References

Boville, Byron A., 1991: Sensitivity of simulated climate to model resolution. *J. Climate*, 4, 469-485.

Cubasch, U., K. Hasselmann, H. Höck, E. Maier-Reimer, U. Mikolajewicz, B. Santer, and R. Sausen, 1993: Time-dependent greenhouse warming computations with a coupled ocean-atmosphere model. *Clim. Dyn.*, 8, 55-69.

Edmon, Jr., H.J., B.J. Hoskins, and M.E. McIntyre, 1980: Eliassen-Palm cross sections for the troposphere. *J. Atmos. Sci.*, 37, 2600-2616.

Farrell, Brian, 1985: Transient growth of damped baroclinic waves. *J. Atmos. Sci.*, 42, 2718-2727.

Gutowski, W.J., Jr., 1985: A simple model for the interaction between vertical eddy heat fluxes and static stability. *J. Atmos. Sci.*, 42, 346-358.

Gutowski, W.J., L. Branscome, and D. Stewart, 1989: Mean flow adjustment during life cycles of baroclinic waves. *J. Atmos. Sci.*, 46, 1724-1737.

Hansen, J., G. Russell, D. Rind, P. Stone, A. Lacis, S. Lebedeff, R. Ruedy, and L. Travis, 1983: Efficient three-dimensional global models for climate studies: Models I and II. *Mon. Wea. Rev.*, 111(4), 609-662.

Hantel, M., 1976: On the vertical eddy transports in the northern atmosphere. 1. Vertical eddy heat transport for summer and winter. *J. Geophys. Res.*, 81, 1577-1588.

Hantel, M., and J.M. Hacker, 1978: On the vertical eddy transports in the northern atmosphere, 2. Vertical eddy momentum transport for summer and winter. *J. Geophys. Res.*, 83, 1305-1318.

Kung, Ernest C., 1988: Spectral energetics of the general circulation and time spectra of transient waves during the FGGE year. *J. Climate*, 1, 5-19.

Lehman, S.J., and L. Keigwin, 1992: Sudden changes in North Atlantic circulation during the last deglaciation. *Nature*, 356, 757-762.

Lin, S.-J., and R.T. Pierrehumbert, 1988: Does Ekman friction suppress baroclinic instability? *J. Atmos. Sci.*, 45, 2920-2933.

Manabe, S., R. Stouffer, M. Spelman, and K. Bryan, 1991: Transient responses of a coupled ocean-atmosphere model to gradual changes of atmospheric CO_2. *J. Climate*, 4, 785-817.

Marotzke, J., and J. Willebrand, 1991: Multiple equilibria of the global thermohaline circulation. *J. Phys. Ocean.*, 21, 1372-1385.

Nakamura, M., P.H. Stone, and J. Marotzke, 1993: Destabilization of the thermohaline circulation by atmospheric moisture transport. Submitted to *Science*.

Oort, A.H. and E.M. Rasmusson, 1971: Atmospheric circulation statistics. NOAA Prof. Paper No. 5, U.S. Dept. of Commerce, Washington, DC, 323 pp.

Peixoto, J.P. and A.H. Oort, 1992: Physics of Climate, Amer. Inst. of Physics, New York, 520 pp.

Salustri, G., and P.H. Stone, 1983: A diagnostic study of the forcing of the Ferrel Cell by eddies with latent heat effects included. *J. Atmos. Sci.*, 40, 1101-1109.

Stone, P.H., 1984: Feedbacks between dynamical heat fluxes and temperature structure in the atmosphere. Climate Processes and Climate Sensitivity (American Geophysical Union, Geophysical Monograph 29), 6-17.

Stone, P. H., and D. A. Miller, 1980: Empirical relations between seasonal changes in meridional temperature gradients and meridional fluxes of heat, *J. Atmos. Sci., 37*, 1708-1721.

Stone, P.H. and J.S. Risbey, 1990: On the limitations of general circulation climate models. *Geophys. Res. Lett.*, 17, 2173-2176.

Stone, P. H., and G. Salustri, 1984: Generalization of the quasi-geostrophic Eliassen-Palm flux to include eddy forcing of condensation heating. *J. Atmos. Sci., 41*, 3527-3536.

Vernekar, Anaudu D., 1967: On mean meridional circulations in the atmosphere. *Mon. Wea. Rev.*, 95, 705-721.

Washington, W.M. and G.A. Meehl, 1989: Climate sensitivity due to increased CO_2: experiments with a coupled atmosphere and ocean general circulation model. *Clim. Dyn.*, 4, 1-38.

Zhou, S. and P.H. Stone, 1993: The role of large-scale eddies in the climate equilibrium, Part II: Variable static stability. *J. Climate*, in press.

ROSSBY WAVE PROPAGATION AND TELECONNECTIONS FOR THE NORTHERN HEMISPHERE SUMMER FLOW

by

T. AMBRIZZI AND B. J. HOSKINS

1) INTRODUCTION

To produce more confident predictions of global climate change, we have first to understand the climate itself. One way to do this is to use a numerical model in order to simulate a specific aspect observed in the atmosphere in an attempt to gain an insight into its dynamics. Teleconnection analysis comprises a global view of atmospheric circulation where local phenomena act to influence remote regions in the atmosphere. They have been used mainly to study large-scale low frequency fluctuations in the atmosphere. Their importance for long range weather forecasting, for instance, is obvious. The theory of Rossby wave propagation can largely explain patterns of wavetrains obtained in observations and in the results of models.

The teleconnection patterns for the Northern Hemisphere winter flow have been extensively studied in the last decade. Many observational studies and numerical simulations have shown and confirmed their existence. However, for the global flow during the Northern Hemisphere summer the number of studies is comparatively small and they have tended to concentrate mostly on the Southern Hemisphere. One of the major purposes of the present work is to determine whether some of the observed teleconnection patterns can be simulated by imposing local forcing on a global barotropic model, linearized about a climatological mean corresponding to the N. H. summer time basic state.

In the next section, a brief review of the theoretical background will be given. Some details of the model are given in

Section 3. Section 4 discusses some aspects of the Jun-Aug 300 mb flow used and gives an overview of the experiments performed, together with a summary of the numerical results found. Conclusions are shown in Section 5.

2) THEORETICAL BACKGROUND

In this section, following Hoskins and Ambrizzi (1993) (hereafter referred to as HA), we discuss the features of Rossby wave propagation, concentrating on the behaviour of stationary waves. It will help us in the understanding of the remote response of the atmosphere. Only the basic ideas and main conclusions are given.

Starting from a linearized barotropic vorticity equation on a β-plane, HA have shown that the bending of the ray-paths is given by

$$\frac{d_g \alpha}{dt} = \frac{k}{K_s^2} c_g \frac{dK_s}{dy}, \qquad (2.1)$$

where $c_g = 2\bar{U}\cos\alpha$ is the local group velocity in the direction $\hat{K}$, which is the unit vector normal to the wave crests and troughs with a positive eastward component, α is the angle this vector makes with the eastward direction, k is the zonal wavenumber and $K_s = (\beta_e/\bar{U})^{1/2}$ is the total stationary wavenumber, with β_e equal to the northward absolute vorticity gradient.

From (2.1) we see that Rossby rays are always refracted towards latitudes with larger K_s. Defining the radius of curvature of the ray-path, r, to be positive if it is bending in an anti-clockwise manner, r is given by the simple expression

$$r = K_s^2 \Big/ \left[k \frac{dK_s}{dy} \right]. \qquad (2.2)$$

The curvature is clockwise if K_s increases towards the equator and anti-clockwise if it increases towards the pole.

It is useful to consider the schematic situations given in Fig.1. Fig.1a shows the refraction towards higher values of K_s. Fig.1b shows a ray reflected from a turning latitude, Y_{TL}, at which $K_s = k$ and $l = 0$. Extensions of the theory predict decay beyond this latitude. Fig.1c includes a latitude Y_B, at which β_*, and hence K_s, is zero. All rays must turn before this latitude. Fig.1d includes a critical latitude, Y_{CL}, at which $\bar{U}$ is zero and K_s becomes infinite. Rays are refracted normally into such a line but with the meridional scale and group velocity tending to zero. The theory is not valid very close to the critical line and study of such regions by Killworth and McIntyre (1985 and refs.) has suggested that they can become reflecting regions when non-linearity is fully taken account of. Finally, Fig.2e shows a local maximum in K_s. Waves with zonal wavenumber in the range K1 and K2 are trapped and such a K_s maximum provides a Rossby waveguide. This situation is particularly likely to occur in a strong westerly jet. Because of the curvature of the flow, β_* tends to have a larger relative maximum than does $\bar{U}$. Consequently, strong westerly jets can act as waveguides.

3) THE BAROTROPIC MODEL

The barotropic model used in this study is based on the damped barotropic vorticity equation, which is solved using the spectral - transform technique with a triangular truncation at wavenumber 21. Further details about the model itself and the size and shape of the forcing used in the many experiments performed can be found in HA.

4) BASIC FLOW AND THE NUMERICAL RESULTS

The basic flow used in this study is a six year 1979/85

Jun-Aug time mean 300 mb rotational flow derived from ECMWF analyses. Various aspects of this flow are shown in Fig.2.

Based on the zonal wind, $\bar{U}$ (Fig.2a) and the meridional absolute vorticity gradient, β_M (Fig.2b, defined by eq.2.12 in HA), the geographical distribution of K_s (defined by eq.2.13 in HA), for β_M and $\bar{U}$ positive, was plotted in Fig.2c. The zero wind line, $\bar{U} = 0$, is shown by a thickned contour and the zero β_M and K_s (but positive $\bar{U}$) line by dots. Each jet region contains quite uniform values of K_s bounded meridionally by lower values.

One important characteristic of the SH winter is the existence of a double jet in the troposphere. The presence of easterlies around the whole hemisphere in the equatorial regions is also an important aspect. In summary , the main features that can be deduced from Fig.2c (and Figs.2a and 2b) and the Rossby wave theory described in Section 2 are:

1) two strong waveguides parallel to each other in the SH; the first extending from Madagascar (east of Africa) to 45° east of Australia, about 20°S and with typical stationary wavenumber 7; and the second from south of Africa until southeast of the southern Pacific ocean, near the tip of South America, about 50°S and with typical stationary wavenumber 4.

2) a waveguide along the Asian jet from N. Africa to the eastern N. Pacific, around 40°N (poleward of its position for the DJF season), with typical stationary wavenumber 7-8.

3) a weak waveguide along the N. Atlantic jet from western N. Atlantic to northern Europe, with typical stationary wavenumber 6-7.

4) there are no favourable regions for cross-equatorial propagation.

Fig.3 shows some results performed using the barotropic model. All pictures are of the relative vorticity perturbation from

the initial Jun-Jul-Aug mean flow for day 12 of the integration. Figs.3a and 3b indicate that the energy tends to be trapped inside the SH sub-tropical and sub-polar jet streams respectively, which act as waveguides. Propagation escaping from one waveguide to another is also observed. With the forcing in the southern equatorial east Pacific (Fig.3c), we see that the wave follows an arc-like route pattern from the east Pacific to the equatorial Atlantic with a turning point about 45°S. Due to the similarity of this wave propagation pattern with the PNA pattern (Wallace and Gutlzer, 1981), it was called Pacific-South America pattern or PSA by Mo and Ghil (1987) who found a similar pattern in their data analysis. Figs.3d and 3e emphasize the role of the N. Atlantic and Asian jet streams as waveguides.

The results of all linear barotropic experiments performed are summarized in Fig.4. The background contours are some of the key ones from the basic flow stationary wave figure (Fig.2c). This picture shows the four waveguides found, the N. Africa - Asian jet, N. Atlantic - N. Europe region, the Australian jet and the mid-latitude Southern Hemisphere jet. The preferred propagation paths are also indicated. There is no evidence of teleconnection between hemispheres, which is not too surprising since the equatorial region is dominated by easterlies.

The extension of the Asian waveguide from the N. Africa to almost the west coast of N. America gives the impression of the existence of a weak waveguide belt near 40°N around the whole hemisphere. Indeed some of the experiments have shown this kind of behaviour, helped by the fact that the N. Atlantic waveguide is weak and has a connection with the Asian waveguide.

5) CONCLUSIONS

A number of experiments have been repeated with the linear barotropic model applied to the 150 mb flow and with a

non-linear barotropic model applied to the 300 mb flow. The differences found are generally quantitative rather than qualitative and the summary given in Fig.4 appears to be quite robust. Baroclinic model results, to be reported elsewhere, also generally support this picture.

In general, results from the simple model used here agree remarkably well with observations (e.g., Mo and Ghil, 1987; Berbery et al, 1992; and especially H.-H. Hsu, 1993, pers. comm.). Therefore, simple wave propagation ideas can provide a good qualitative interpretation of the results, though it must be said that the strict mathematical validity for the application of the theory is in doubt.

ACKNOWLEDGEMENT: One of us (TA) wish to acknowledge the Stanstead Seminar Committee for the student travel grant received.

REFERENCES

Berbery, E.H., J. Nogués-Paegle, and J.D. Horel, 1992: Wavelike Southern Hemisphere extratropical teleconnections. *J.Atmos. Sci.*, **49**, 155-177.

Hoskins, B.J., and T. Ambrizzi, 1993: Rossby wave propagation on a realistic longitudinally varying flow. *J.Atmos.Sci.*, **50**, 1661-1671.

Killworth, P.D., and M.E. McIntyre, 1985: Do Rossby wave critical layers absorb, reflect, or over-reflect?. *J.Fluid. Mech.*, **161**, 449-492.

Mo, K.C., and M. Ghil, 1987: Statistics and dynamics of persistent anomalies. *J.Atmos.Sci.*, **44**, 877-901.

Wallace, J.M., and D.S. Gutlzer, 1981: Teleconnections in the geopotential height field during the Northern Hemisphere winter. *Mon.Wea.Rev.*, **109**, 785-812.

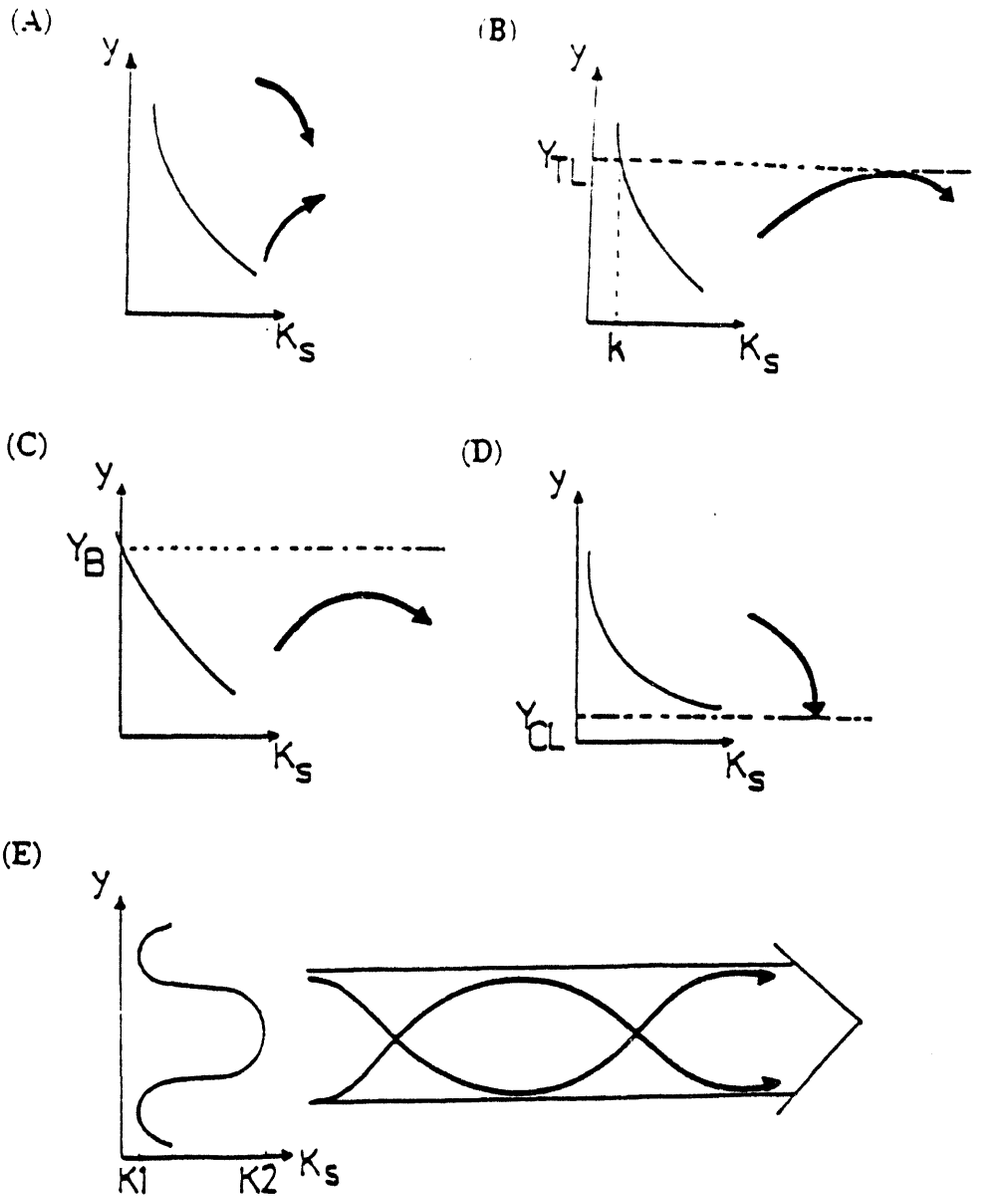

Fig.1: Schematic stationary Rossby wavenumber (K_s) profiles and ray path refraction. In each panel K_s is shown as a function of y and schemamtic ray paths are shown by heavy lines with arrow heads. (a) simple refraction; (b) reflection from a turning latitude Y_{TL}, at K_s = k; (c) reflection of all wavenumbers before a latitude Y_B at which β_e = 0; (d) refraction into a critical latitude Y_{CL}, at which $\bar{U}$ = 0; (e) waveguide effect of a K_s maximum. For more discussion see text. (After Hoskins and Ambrizzi, 1993).

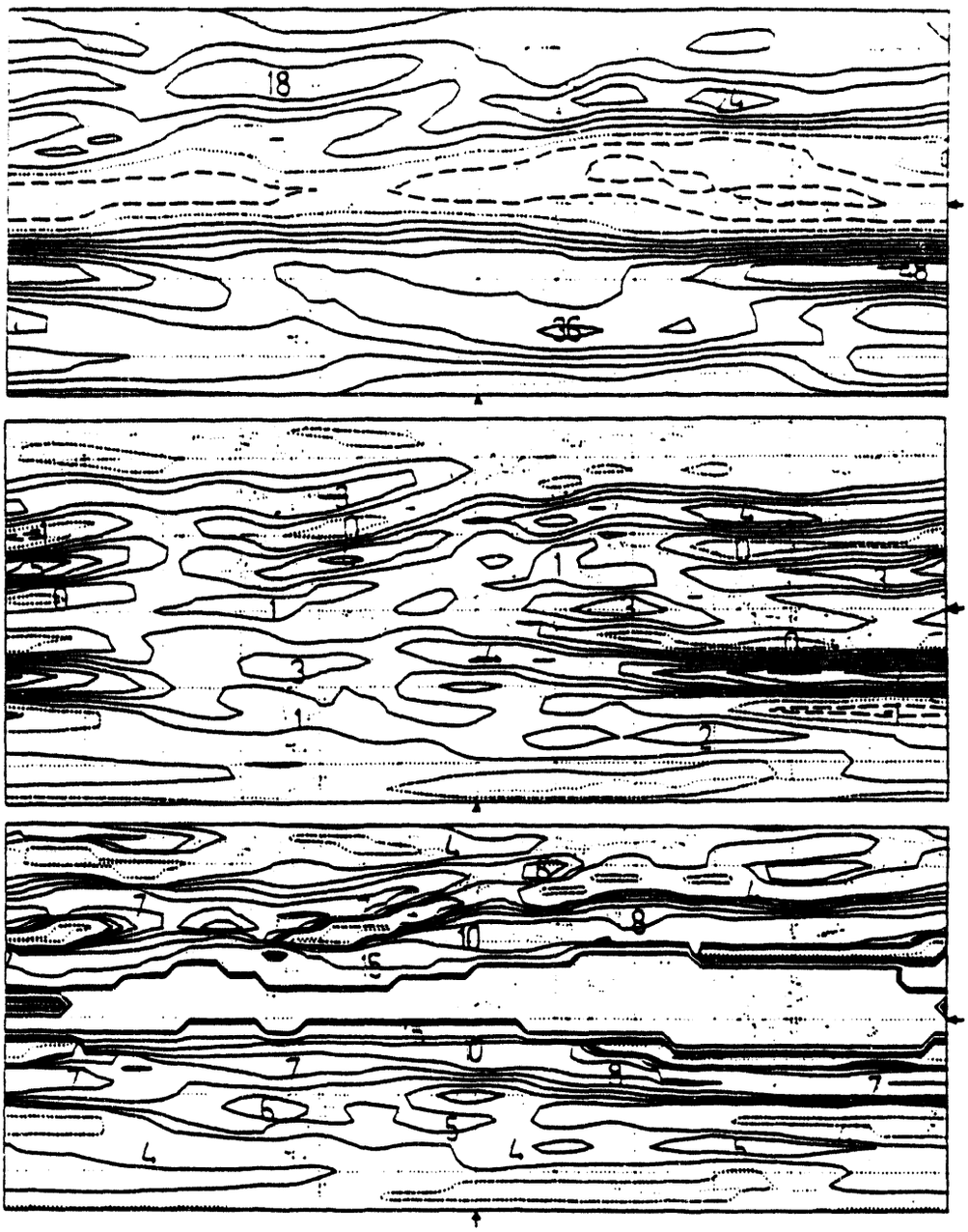

Fig.2: The climatological JJA 300 mb flow based on ECMWF data for the period 1979/85. (a) Westerly component of the wind, $\bar{U}$, contour interval 6 ms^{-1}. (b) Mercator coordinate meridional gradient of the absolute vorticity, β_M, (as defined in HA), contour interval $1.10^{-11} s^{-1} m^{-1}$. (c) Stationary wavenumber K_s, (as defined in HA), for β_M and $\bar{U}$ positive; contours at total wavenumbers 0,4,5,6,7,8,10 and 15, and also 25-30, producing a thickened contour indicating singular values of K_s. In all panels, negative contours are dashed and zero contours are dotted. Lines of latitude and longitude are drawn every 30° and arrows indicate 0° latitude and longitude.

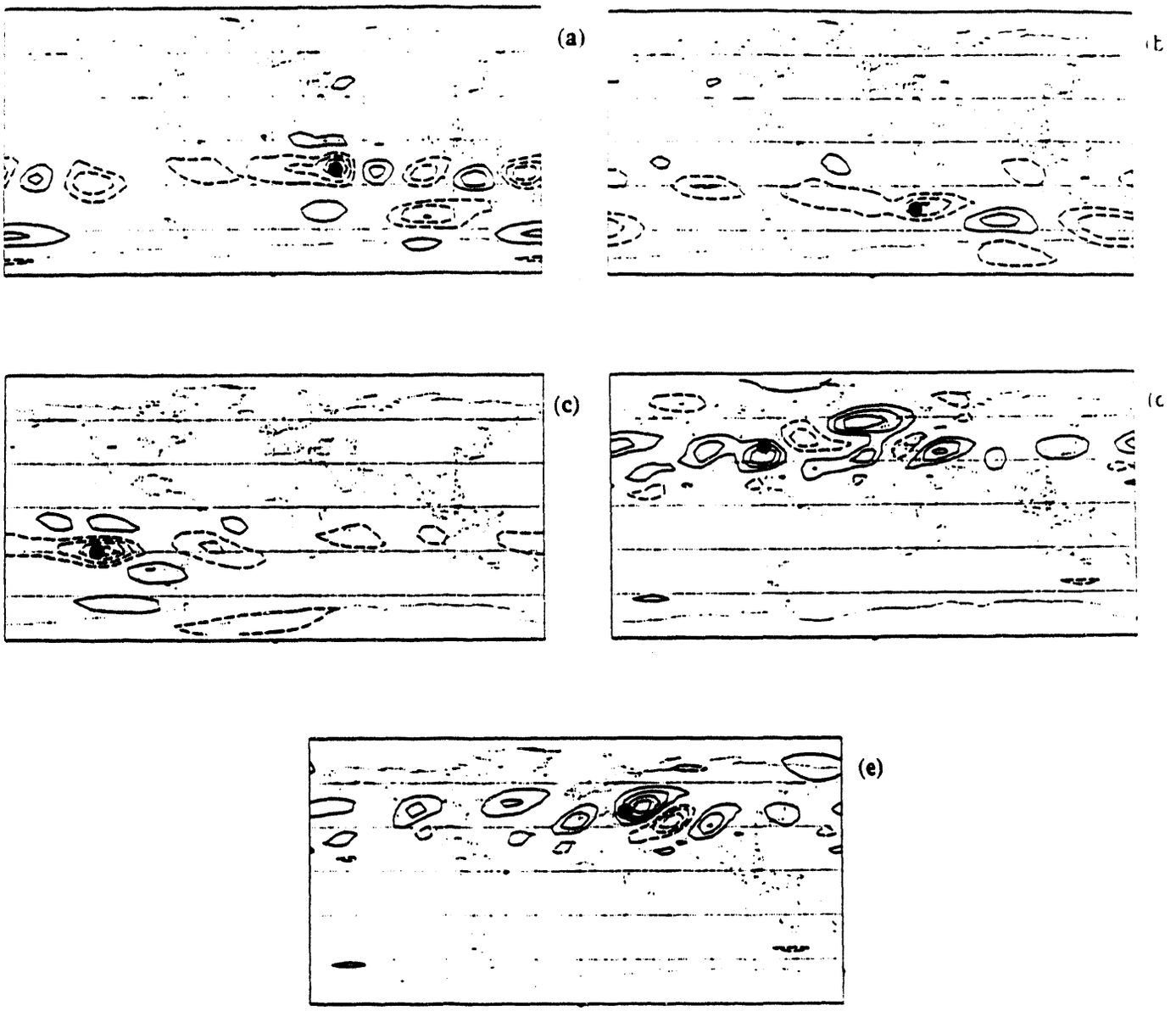

Fig.3: The model relative vorticity anomaly for the forcing centred at (a) (20°S, 40°E), (b) (45°S, 30°E), (c) (30°S, 120°W), (d) (40°N, 75°W) and (e) (40°N, 30°E) at day 12. The contour interval is 5.10^{-6} s^{-1}; negative values are dashed and the zero contour is not shown. The black circles indicate the forcing position.

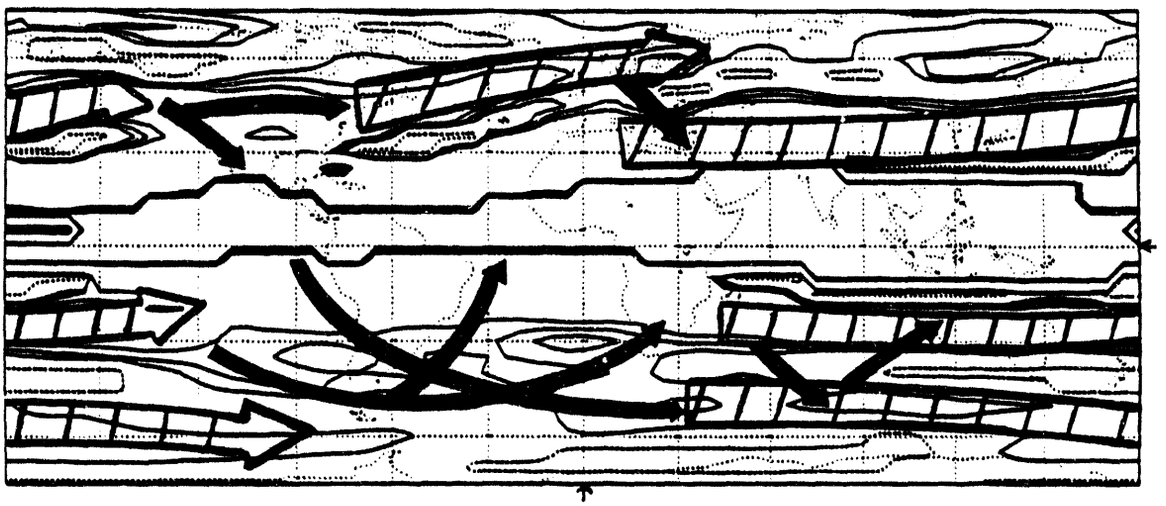

Fig.4: A schematic summary of the waveguides shown by the cross-hatched shafted arrows, and the preferred propagation patterns, indicated by the single-shafted arrows, deduced from the range of experiments done. The background contours are those for K_s equal to 0,4,5,6 and 25-30 taken from Fig.2c.

Interannual Variability of North Atlantic Sea Surface Temperatures

Uma S. Bhatt, Department of Atmospheric and Oceanic Sciences, University of Wisconsin-Madison
David S. Battisiti, Department of Atmospheric Sciences, University of Washington-Seattle
Michael A. Alexander, Cooperative Institute for Research in Environmental Studies, University of Colorado-Boulder

In the midlatitude north Atlantic Ocean the pattern of sea surface temperature anomalies (ssta) is characterized by a north - south dipole. Bjerknes (1964) was the first to propose that the banded structure was associated with the interannual variability. Recently, these patterns have been studied more extensively by Wallace and Jiang (1987), Kushnir (1993), and others. In this study the quantitative aspects of these patterns are examined through the use of a mixed-layer model (MLM) developed by Alexander (1990).

At first glance it would appear that these patterns are largely associated with changes in the Gulf Stream, but this does not appear to be the case. Firstly, the large-scale nature of the ssta patterns makes it unlikely that anomalies in the Gulf Stream are responsible for these patterns. Secondly, the atmospheric setting (Kushnir, 1993) indicates that anomalously warm (cold) water is associated with a decrease (increase) in wind magnitude directly over the anomaly, suggesting a coupling of the ocean - atmosphere through surface fluxes. Finally, the very large negative correlations (Cayan, 1992) between anomalous surface hear flux out of the ocean and the temperature tendency present strong evidence for the atmospheric forcing of the ocean. In light of this evidence, a mixed layer model of the ocean seems appropriate for first order studies of interannual variability in the North Atlantic.

Since the final goal of this work is to examine the feedback in a coupled study (MLM & CCM1) the MLM was tuned to the CCM1. Flux corrections were calculated and the model sensitivity was tested by forcing the model with observed atmospheric anomalies. A brief description of the experimental tools is followed by a discussion of the flux correction patterns and the results of the anomaly experiments.

The mixed layer model (MLM) is based on the classical formulation of Niiler and Kraus (1977) and uses the entrainment parameterization of Gaspar (1988). The processes considered in the MLM include surface energy flux, penetrating solar radiation, and entrainment due to buoyancy loss and wind mixing. The atmospheric model is the standard NCAR CCM1 (Williamson et al., 1987) with an R15 resolution, which translates into a 4.5° in latitude by 7.5° in longitude grid. The observations are from COADS (comprehensive Ocean-Atmosphere Data Set) (Woodruff et al., 1987).

Due to errors in both the atmosphere and ocean models, it is presently necessary to adjust for these errors and avoid climate drift in coupled modeling studies by using flux corrections (Sausen et al., 1988). The flux correction (Qcor) is the heat needed to match the model temperature tendency to the observed temperature tendency. Presently, flux corrections are necessary and will be needed until models are improved, but they can provide some insight into diagnosing model errors. Figure 1a presents a map of the annual average heat flux corrections and fig. 1b the annual average CCM1 net surface heat flux (shortwave - longwave - latent - sensible) into the north Atlantic Ocean. The similarity between the patterns in fig. 1a and 1b is remarkable, with the patterns having equal magnitudes but opposite signs. In

nature, if we assume a steady state then over the course of a year the oceanic heat that is lost or gained at the surface of the ocean is balanced by meridional transport. The flux correction pattern (fig. 1a) represents the heat transport an ocean would need when it is forced with CCM1 fluxes. Figure 1c displays the observed (Isemer and Hasse, 1987) net surface heat flux into the ocean. If the ocean and atmosphere models were perfect the flux corrections needed for an ocean model with no currents would resemble figure 1c, but be of the opposite sign. Errors in the CCM1 fluxes (compare fig. 1b and 1c) are particularly noticeable from 40-60 °N and can be largely attributed to known radiation errors in the model (Soden, 1992). The flux corrections represent the heat transport by the currents that are not represented in the model and they also represent errors in the models.

To test the sensitivity of the ocean model, observed anomalies (1950-88) of air temperature (tair), air moisture (qair), and wind magnitude (wind) were added onto the CCM1 forcing (mean tuned state) and the MLM was run for 39 years (repeating 5 years of CCM1 forcing). Using a method similar to Kushnir (1993), WARM (COLD) winter seasons were chosen if ssta were warm (cold) between 40-60 °N and cold (warm) between 20-40 °N. Anomalies were calculated by subtracting the corresponding year of the CONTROL experiment from the anomaly experiment. This method for calculating the anomaly was necessary because the natural variability in the CCM1 is similar to the observations, particularly in the North Atlantic. Table 1 lists the experiments performed with the varying atmospheric forcing. Correlation coefficients between the observed and modeled ocean temperatures for the winter months (nov. - april) are larger than .55 and significant at the .1 % level at 86 of the 89 gridpoints. Two of the problem gridpoints, located in the far north, had excessive mixed layer depths possibly due to no variations in salinity forcing during the 39-year simulation.

Table 1 List of experiments and anomalies applied in each experiment.

	CONTROL	TA	NT	NQ	NW
Tair	none	yes	no	yes	yes
qair	none	yes	yes	no	yes
wind	none	yes	yes	yes	no

Figure 2 presents the seven case composite for the WARM case of observed ssta (fig. 2a), model mixed-layer temperature anomaly (tmxa) (fig. 2b), and the model mixed layer depth anomaly (hmxa) (fig. 2c). The model does a reasonable job capturing the pattern and magnitude of the observed ocean temperature anomaly (fig. 2a), though the model magnitude is somewhat weaker. The model does not simulate the ssta as well in the far northern part of the domain. This may be due to the fact that at low temperatures salinity is more important than temperature in determining density and observed variations in precipitation and evaporation were not considered in these simulations. The anomalies in mixed layer depth (fig. 2c) indicate a shallowing (deepening) of the mixed layer in the regions of warming (cooling) of the ocean temperatures. This is consistent with the surface forcing that indicates weakened (strengthened) wind magnitudes and reduced (increased) heat loss by the ocean in regions of ocean warming (cooling). The total surface flux anomalies (not shown) of sensible plus latent heat are of the order 10-20 W/m2 averaged over the winter (nov. to april). Radiational flux anomalies were calculated from COADS, found to be considerably smaller than latent and sensible fluxes, and therefore were not included. The anomalies in heating due to entrainment (Qwe) were smaller than the surface forcing. The anomalous heating due to

entrainment, which depends on both the entrainment velocity and the temperature difference between the mixed layer and the layer below, acts to damp the ssta in the higher latitudes and acts to reinforce the anomaly in the southern part of the domain. In the northern part of the domain the anomalous temperature difference determines Qwe and in the southern part of the domain the enhanced entrainment determines Qwe. The results for the COLD case were similar.

Additional experiments were performed (see Table 1) to elucidate the role. each of the three atmospheric variables play in the formation of the anomalies. Figure 3 presents the mixed-layer temperatures for the NT (fig 3a), NQ (fig. 3b), and NW (fig. 3c) cases, where Taira, qaira, and winda are not added to the model mean state, respectively. Tmx is reduced the most in the NT case, followed by the NQ case, and the least in the NW case. In all three cases the mixed-layer temperature anomaly is reduced from the TA case (fig. 2b). It seems somewhat surprising that the wind effects were minimal and we are still analyzing this result. A more detailed explanation of these results is being prepared.

We tested the sensitivity of the ocean model to surface boundary conditions and have shown that given the air temperature, air moisture, and wind magnitude the ocean model produces reasonable mixed-layer temperatures characteristic of interannual timescales. In the next step we will perform coupled experiments to address the issue of feedback between the atmosphere and the ocean in the midlatitudes.

REFERENCES

Alexander, M., A., 1990: Simulation of the response of the north Pacific Ocean to the anomalous atmospheric circulation associated with EL Niño. *Climate Dyn.*, **5**, 53-65.

Alexander, R., C., Mobley, R., L.,1976: Monthly average sea-surface temperatures and ice-pack limits on a 1° global grid. *Mon. Wea. Rev.*, **104**, 143-148.

Bjerknes, J., 1964: Atlantic air-sea interaction. *Advances in Geophysics*, Academic Press, pp 1-82.

Cayan, D., 1992b: Latent and sensible heat flux anomalies over the northern oceans: the connection to monthly atmospheric circulation. *J. Climate*, **5**, 354-369.

Gaspar, Ph., 1988: Modeling the seasonal cycle of the upper ocean. *J. Phys. Ocean.*, **18**, 161-180.

Isemer, H., -J., Hasse, L., 1987: The Bunker climatic atlas of the North Atlantic, volume 2: air-sea interactions. Springer-Verlag, Berlin, 252 pp.

Kushnir, Y., 1993: Interdecadal variations in North Atlantic sea surface temperature and associated atmospheric conditions. Submitted to J. Climate.

Niiler, P., P., Kraus, E., B., 1977: Modeling and prediction of the upper layers of the ocean. *One-Dimensional models of the upper ocean*, Kraus, E., B., Ed., Pergamon Press, Oxford, 143-172.

Sausen, R., Barthel, K., Hasselmann, K., 1988: Coupled ocean-atmosphere models with flux correction. *Climate Dynamics*, **2**, 145-163.

Soden, B., J., 1992: Validation of cloud forcing simulated by the National Center for Atmospheric Research Community Climate Model using observations from the Earth Radiation Budget Experiment. *J. Geophys. Res.*, **97**, 18137-18159.

Wallace, J., M., Jiang, Q., -R., 1987: On the observed structure of the interannual variation of the atmosphere/ocean climate system. *Atmosphere and Oceanic Variability*, Cattle, H., Ed., Royal Meteorological Society, 17-43.

Williamson, D., L., Kiehl, J., T., Ramanathan, V., Dickinson, R., E., Hack, J., J., 1987: Description of NCAR Community Climate Model (CCM1). NCAR Technical Note NCAR/TN-224+STR, Boulder, Colorado.

Woodruff, S., D., Slutz, R., J., Jenne, R., L., Steurer, P., M., 1987: A comprehensive ocean-atmosphere data set. *Bull. Am. Meteorol. Soc.*, **68**, 521-527.

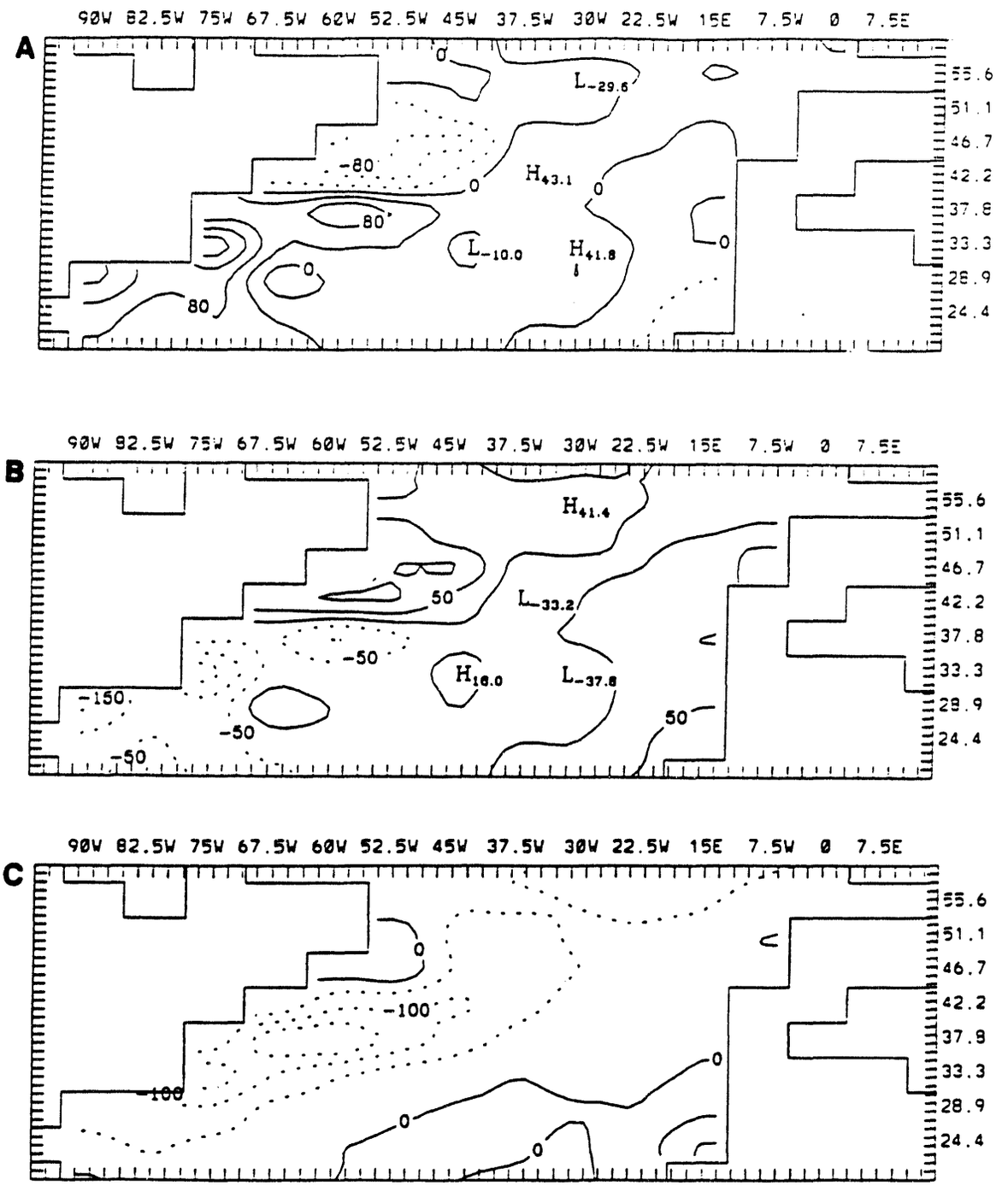

Figure 1 A) Annual average flux correction (Qcor) in W/m^2 B) annual average net heat flux into the ocean (Qtot) from the CCM1 in W/m^2 and C) observed annual average surface net heat flux into the ocean (Isemer and Hasse, 1987).

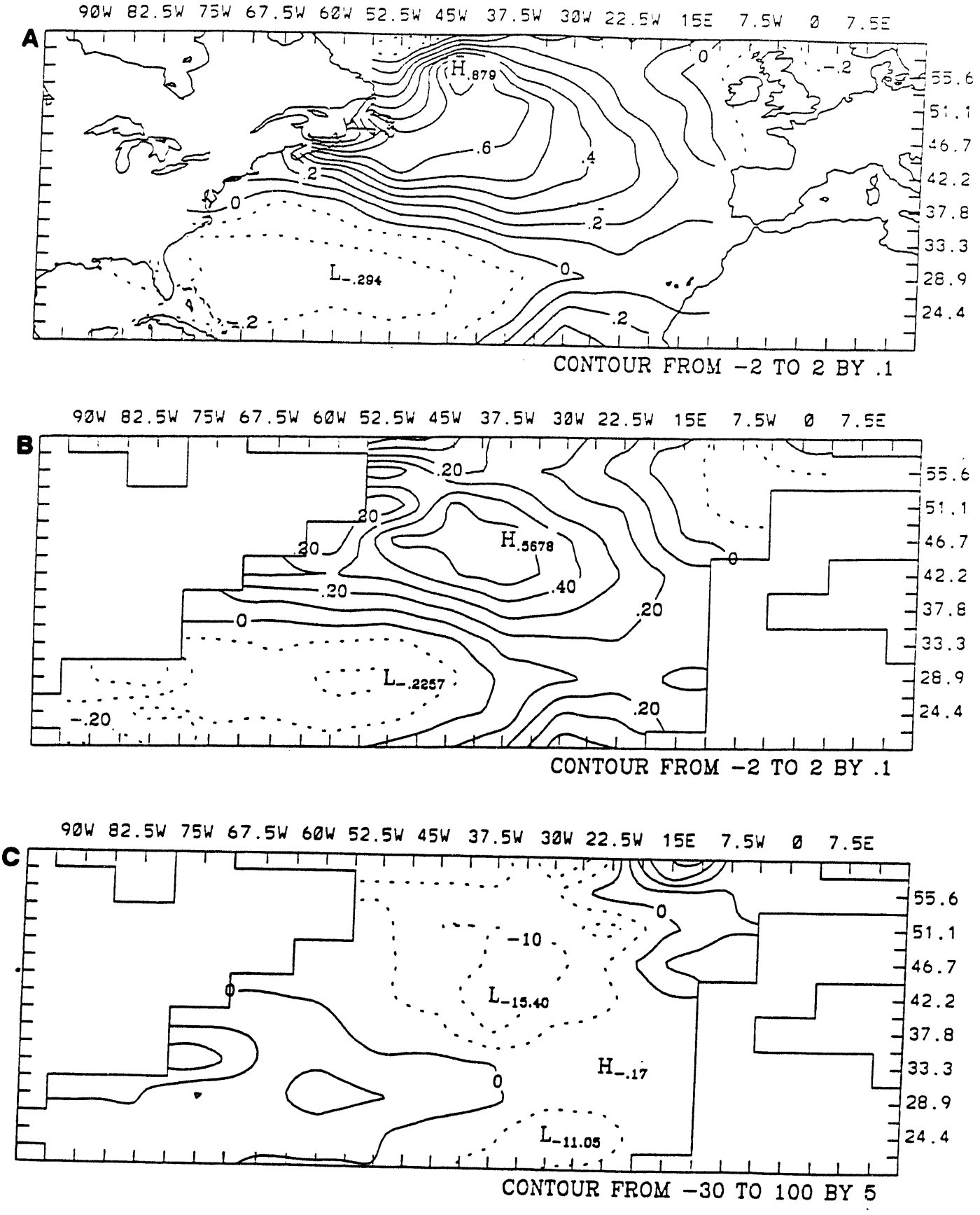

Figure 2 Total anomaly (TA) experiment A) observed SST (COADS) anomalies (°C), B) modeled Tmx anomalies (°C), and C) Hmx anomalies (meters) averaged from Nov.-April for the WARM case.

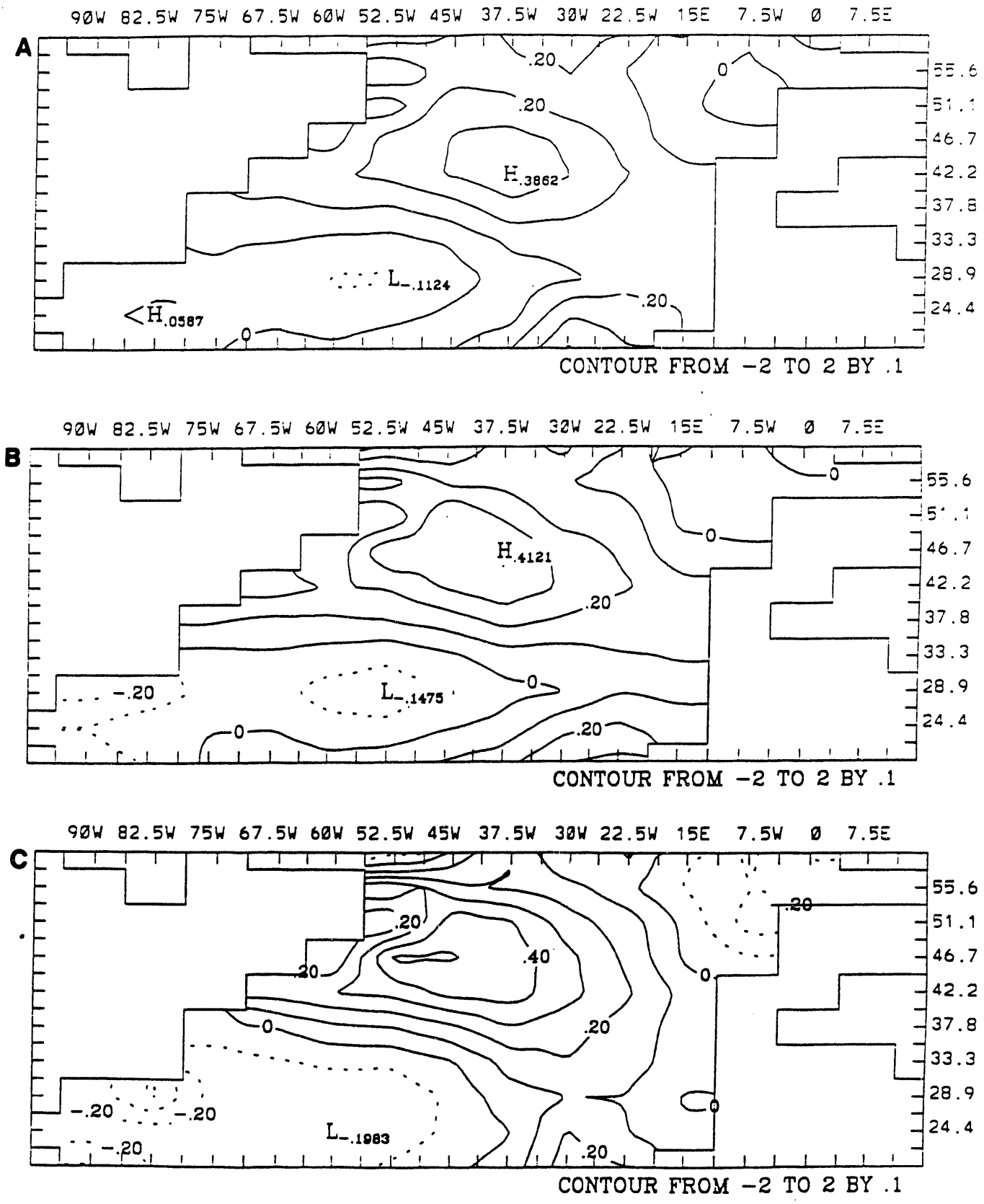

Figure 3 Mixed-layer temperature anomalies for the A) NT (no Air temperatuere anomaly), B) NQ (no Air moisture anomaly), and C) NW (no wind anomaly) cases in °C averaged from Nov.-April for the WARM case.

CLIMATIC FEEDBACKS BETWEEN STATIONARY AND TRANSIENT EDDIES

Lee E. Branscome
Environmental Dynamics Research, Inc.
7338 155th Place North
Palm Beach Gardens, Florida 33418

1. INTRODUCTION

Stationary eddies make a significant contribution to poleward heat transport during Northern Hemisphere winter, equaling the transport by transient eddies. On the other hand, stationary eddy transport during the summer is negligible. The effect of topography on time-mean stationary waves and low-frequency variability has been widely studied. In contrast, little attention has been given to the climatic feedbacks associated with stationary eddies. Furthermore, the relationship between stationary and transient eddies in the context of global and regional climate is not well understood. The response of the climate system to anthropogenic forcing is likely to have some dependence on stationary wave transport and its interaction with transient eddies. Some early GCM simulations and observational analyses indicate a strong feedback between the meridional heat fluxes of stationary and transient eddies (Manabe and Terpstra, 1974; Stone and Miller, 1980).

Feedbacks between stationary and transient eddies were examined in the context of a two-layer primitive-equation global spectral model. The responses of the meridional heat and momentum transports to changes in topographic and radiative forcing were investigated in model integrations that extended over several hundred days. Parameters such as radiative and dissipative time scales were varied in other experiments. The response of the model climate on global and regional scales to these parameter changes was examined in experiments with and without topography. In particular, we examined how the ratio of zonal-mean stationary to transient eddy heat flux varied with the externally specified parameters of the model. The main question was whether the stationary eddy fluxes were any more sensitive to changes in the radiative forcing than the transient eddy flux. The impact of topographic forcing on the baroclinic eddy adjustment of the zonal mean climate was also investigated.

2. MODEL AND EXPERIMENTS

We used a two-layer sigma-coordinate model with rhomboidal 15 truncation. The model atmosphere was dry with a parameterization of dry convection only. Linear damping of vorticity and divergence occurred in the lowest layer only with a standard damping time, t_f, of 7.5 days. Radiative heating was included in the form, $(T_e-T)/\tau$, where T_e was the radiative-convective equilibrium temperature and τ, the radiative time scale with a standard value of 15 days. "Realistic" topography was used, with no other zonal asymmetries. A similar version of the model has been used to study the dynamics of persistent anomalies (Stewart, 1993).

The principal parameters that were varied in our experiments were the equator-to-pole temperature difference (ΔT_e) and static stability (S_e) of the radiative-convective equilibrium, the radiative time scale (τ), and the frictional time scale (t_f). Some of the experiments were repeated with the topography removed, most commonly in experiments in which ΔT_e was varied. Here we focus on results from experiments with various ΔT_e and τ.

3. STANDARD SIMULATION

When ΔT_e was set to 50° C. in the Northern Hemisphere and 32° C. in the Southern Hemisphere for a standard "winter" experiment, the model's stationary eddy heat flux was similar in geographic distribution to the observed flux. As defined by $\bar{v}^*\bar{T}^*$ where * is the deviation from the zonal average and the overbar is the time mean, the stationary eddy flux had a primary maximum located just northwest of the Himalayas and weaker maxima located upstream and downstream of the Rockies and over the North Atlantic. The maximum near the Himalayas was about 60% stronger than the observed maximum, while the maxima in the W. Hemisphere were half as strong as observed. The transient eddy heat flux had primary maxima on the east coasts of Asia and N. America and secondary maxima in the Gulf of Alaska and eastern Europe, similar to observations. The zonally and vertically averaged total eddy heat flux at 50°N was 16.5 °C ms^{-1} in the standard run, compared with an observed value of 18.1 °C m s^{-1} (Oort, 1983). The success of this simple model, as

with early GCMs, demonstrates that many basic features of the general circulation depend primarily on large-scale topography, radiative forcing, and frictional dissipation in the lower troposphere.

4. EFFECT OF RADIATIVE FORCING

Fig. 1 shows the eddy heat flux as ΔT_e was varied in experiments with and without topography. Eddy heat flux generally increased with stronger radiative driving. For values of $\Delta T_e >$ 30°C in experiments with topography, the stationary eddy heat flux increases less rapidly with ΔT_e than the transient eddy flux. In fact, the stationary eddy transport appears to have reached a maximum for large ΔT_e.

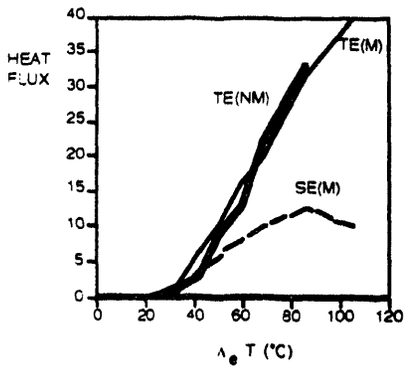

Fig. 1 Stationary (SE) and transient (TE) eddy heat flux at 50°N in °C ms^{-1} for experiments with (M) and without (NM) mountains.

Eddy momentum fluxes (not shown) increased sharply with the radiative driving for $\Delta T_e <$ 60°C. However, for $\Delta T_e >$ 60°C momentum transports increased much more slowly, with the transient eddy flux actually decreasing in the mountain experiments. Thus, the Eliassen-Palm flux became increasingly dominated by eddy heat flux as the climate was driven to a relatively inviscid, diabatically forced regime (Stone and Branscome, 1992).

The transient eddy fluxes were more zonally homogeneous for stronger radiative driving, while the zonal distribution of stationary eddy fluxes was unchanged. Conversely, the storm tracks formed by the transient eddies were more zonally confined for weaker driving.

The baroclinic eddy adjustment of the zonal mean state worked equally well in experiments with and without mountains. Beyond low values of radiative driving, static stability and meridional temperature gradient followed a nearly linear relationship as ΔT_e was varied.

Both stationary and transient eddy heat fluxes decreased as τ was increased from 2 to 40 days, with fixed ΔT_e. The ratio of fluxes was nearly constant.

5. CONCLUSIONS

The ratio of stationary to transient eddy heat flux gradually decreased in model as the radiative driving was increased. This result does not agree with the observed behavior of a sharp increase in this ratio as the Northern Hemisphere moves from summer to winter. Thus, it seems likely that seasonal changes in zonally asymmetric diabatic heating, found in continent-ocean contrasts, make a significant contribution to the seasonal variation in stationary eddy transports. Such processes are currently being examined with this simple model.

6. REFERENCES

Manabe, S., and T.B. Terpstra, 1974: The effects of mountains on the general circulation of the atmosphere as identified by numerical experiments. *J. Atmos. Sci.*, **31**, 3-42.

Oort, A., 1983: *Global Atmospheric Circulation Statistics, 1958-1973*.NOAA Prof. Pap. 14, U.S. Dept. of Commerce, Washington, DC, 180 pp.

Stewart, D.A., 1993: On the forcing of persistent anomalies in a 2-level general circulation model. *J. Atmos. Sci.*, **50**, 2710-2730.

Stone, P.H., and D. A. Miller, 1980: Empirical relations between seasonal changes in meridional temperature gradients and meridional fluxes of heat. *J. Atmos. Sci.*, **37**, 1708-1721.

Stone, P.H., and L.E. Branscome, 1992: Diabatically forced, nearly inviscid eddy regimes. *J. Atmos. Sci.*, **49**, 355-367.

DIAGNOSIS OF BALANCED AND UNBALANCED MOTIONS IN A SYNOPTIC-SCALE BAROCLINIC WAVE LIFE CYCLE

Andrew B.G. Bush, W.R. Peltier, and James C. McWilliams

University of Toronto/NCAR
Ontario, Canada/Boulder, Colorado

1. INTRODUCTION

For numerical simulations of large scale dynamics, balanced models are attractive because their governing equations preclude gravity waves and one is thereby free to use a larger time step than is possible with a model governed by the primitive equations. Recent comparative studies have proven the so-called balance equations (eg., Charney, 1955, Bolin, 1955) to be the most accurate of the intermediate models (Gent and McWilliams, 1982; McWilliams *et al.* 1986; Norton *et al.* 1986; Barth *et al.* 1990; Allen *et al.* 1990, Snyder *et al.* 1991).

In this particular study, a new set of balance equations is derived for the three-dimensional anelastic equations of motion based on expansions in Rossby and Froude number in a manner similar to the study of the shallow water equations by Spall and McWilliams (1992). Terms that comprise the usual balance equations are here formally retained in addition to terms of the same order arising from the vertical variation of the background density field. As an application of the derived set of equations, we apply them in diagnostic form to a three-dimensional primitive equation numerical simulation of a synoptic-scale baroclinic wave (Bush and Peltier, 1993). Of particular interest in this analysis is the degree to which, and the time at which, the flow becomes substantially unbalanced, and what form of imbalance is present. Two regimes of unbalanced motion may here be identified: 1) unbalanced motion that is slaved to the higher order advective terms of the large-scale balanced motion, therefore having the same time- and length-scales (ie., higher order corrections) , and 2) unbalanced motion that is on a faster time scale than the large-scale balanced motion, but is nevertheless forced by these same higher order advective terms. Forced internal gravity waves are an example of this latter motion. It will be shown in our study that both forms of imbalance arise in the frontal zones generated during the numerical simulation, but that the gravity wave generation is a numerical artifact of insufficient vertical resolution as the slope of the surface front decreases below the threshold for consistent horizontal and vertical resolution (Lindzen and Fox-Rabinovitz, 1989). The total unbalanced motion field is dominated by the slower, advective motion but the numerically generated gravity waves nevertheless reach an amplitude of roughly 0.5 times that of the slower motion.

2. THE BALANCE EQUATIONS

The anelastic primitive equations of motion for an adiabatic, ideal gas on an f-plane may be written in the form

$$\frac{D\mathbf{U}}{Dt} + 2\mathbf{\Omega}\mathbf{x}\mathbf{U} = -\frac{1}{\bar{\rho}_a}\nabla p + \left(\frac{\rho}{\bar{\rho}_a}\right)\mathbf{g} \qquad (1a,b,c)$$

$$\nabla \cdot (\bar{\rho}_a \mathbf{u}) = 0 \qquad (2)$$

$$\frac{1}{c_s^2}\frac{Dp}{Dt} - \frac{D\rho}{Dt} = 0 \qquad (3)$$

in which $\bar{\rho}_a = \bar{\rho}_a(z)$ is the adiabatic background density field about which the total density ρ is expanded. The continuity equation (2) suggests a decomposition of the solenoidal vector field $\bar{\rho}_a\mathbf{u}$ in poloidal/toroidal form, ie.,

$$\bar{\rho}_a\mathbf{u} = \nabla \times \hat{k}\Psi + \epsilon\nabla \times (\nabla \times \hat{k}\chi) \qquad (4)$$

in which the parameter ϵ is assumed to be small. The two scalars Ψ and χ are referred to here as the rotational and the divergent components of the flow, although they should perhaps more properly be called the rotational flux and divergent flux components. We decompose the density and pressure fields into three constituent parts: the adiabatic background component, the stratified background component, and the fluctuation from the background. We rewrite equations (1)-(3) in terms of the four variables Ψ, χ, ρ, and p and nondimensionalise with values appropriate for synoptic-scale motions. A multi time- and length-scale expansion is then performed as we decompose the four variables into their balanced and unbalanced (primed) components according to

$$\Psi = \Psi(x,y,z,t) + \frac{\mu}{\omega R}\Psi'(\nu x, \nu y, \nu z, \omega t)$$

$$\epsilon\chi = \epsilon\chi(\delta x, \delta y, \delta z, t) + \frac{\mu}{\nu}\chi'(\nu x, \nu y, \nu z, \omega t) \qquad (5)$$

$$\rho = \rho(x, y, z, t) + \mu\Pi\rho'(\nu x, \nu y, \nu z, \omega t)$$

$$p = p(x, y, z, t) + \mu\Pi p'(\nu x, \nu y, \nu z, \omega t)$$

where

$$\Pi = \frac{\omega RB[1, \nu^2]}{[1, R][1, B]}.$$

$R = V/fL$ is the Rossby number, $F = V/NH_s$ is the Froude number (where H_s is the scale height), and $B = R^2/F^2$ is the Burger number. The frequency ratio between the unbalanced and the balanced components is ω and the inverse length scale ratio is ν. An additional inverse length scale separation has been included between the balanced divergent flow and the balanced rotational flow, its ratio being δ. We expect δ to be $O(1)$ for a synoptic-scale baroclinic wave. Substituting the expressions in (5) into the nondimensional equations, assuming hydrostatic balance, and retaining terms up to and including $O(\epsilon)$, we derive the balance equations appropriate for the anelastic system:

Hydrostatic Balance

$$p_z + \rho = 0$$

The Vorticity Equation

$$\nabla^2\Psi_t = \frac{\epsilon}{R}\nabla^2\chi_z - \frac{1}{\bar{\rho}_a}J(\nabla^2\Psi, \Psi) -$$
$$\frac{\epsilon}{\bar{\rho}_a}\Big[\nabla(\nabla^2\Psi)\cdot\nabla\chi_z - \nabla^2\chi\nabla^2\Psi_z + \nabla^2\Psi\nabla^2\chi_z$$
$$- \nabla\Psi_z\cdot\nabla(\nabla^2\chi) - \frac{d_z\bar{\rho}_a}{\bar{\rho}_a}\Big(\nabla\Psi\cdot\nabla(\nabla^2\chi) +$$
$$\nabla^2\Psi\nabla^2\chi\Big)\Big]$$

The Divergence Equation

$$\nabla^2 p + \Big[\nabla^2\Psi + \frac{2R}{\bar{\rho}_a}J(\Psi_y, \Psi_z)\Big] = 0$$

A balanced omega equation may be formed by a suitable linear combination of the above three equations plus the balanced energy equation (not given).

The Omega Equation

$$\Big[-\frac{B}{\bar{\rho}_a}\Big[(d_z\bar{\rho}_a - \Big(\frac{M}{V}\Big)^2 gH_a d_z\bar{\rho}_a) + (d_z\bar{\rho}_s$$
$$- \Big(\frac{M}{V}\Big)^2 gH_s d_z\bar{\rho}_s)\Big]\nabla^2 + \partial_{zz}\Big]\frac{\epsilon}{R}\nabla^2\chi$$
$$= \Big[\Big(\frac{J(\nabla^2\Psi, \Psi)}{\bar{\rho}_a}\Big)_z - 2R\Big(\frac{J(\Psi_y, \Psi_z)_t}{\bar{\rho}_a}\Big)_z\Big]$$
$$- \frac{\nabla^2 J(\rho, \Psi)}{\bar{\rho}_a} + \Big(\frac{M}{V}\Big)^2 (NH_s)^2\Big[\nabla^2 p_t + \frac{\nabla^2 J(p, \Psi)}{\bar{\rho}_a}$$
$$+ \epsilon\Bigg[\frac{\nabla^2(\nabla\rho\cdot\nabla\chi_z)}{\bar{\rho}_a} + \frac{\nabla^2(\nabla^2\chi\rho_z)}{\bar{\rho}_a}$$
$$+ \Bigg(\Big(\frac{\nabla(\nabla^2\Psi)\cdot\nabla\chi_z}{\bar{\rho}_a}\Big)_z - \Big(\frac{\nabla^2\chi\nabla^2\Psi_z}{\bar{\rho}_a}\Big)_z$$
$$+ \Big(\frac{\nabla^2\chi_z\nabla^2\Psi}{\bar{\rho}_a}\Big)_z - \Big(\frac{\nabla\Psi_z\cdot\nabla(\nabla^2\chi)}{\bar{\rho}_a}\Big)_z\Bigg)$$
$$- \Big(\frac{d_z\bar{\rho}_a}{\bar{\rho}_a^2}\Big)_z\Big[\nabla\Psi\cdot\nabla(\nabla^2\chi) + \nabla^2\Psi\nabla^2\chi\Big]$$
$$- \Big(\frac{d_z\bar{\rho}_a}{\bar{\rho}_a^2}\Big)\Big[(\nabla\Psi\cdot\nabla(\nabla^2\chi))_z + (\nabla^2\Psi\nabla^2\chi)_z\Big]$$
$$+ \Big(\frac{M}{V}\Big)^2\frac{gH_s}{\bar{\rho}_a}\Big[\nabla^2(\nabla p\cdot\nabla\chi_z) + \nabla^2(\nabla^2\chi p_z)\Big]\Bigg]$$

in which $M = V/c_s$ is the Mach number. It is through this rather onerous equation that we calculate the balanced vertical mass flux $\bar{\rho}_a w$.

3. AMPLITUDE ESTIMATES

We estimate the amplitude of the balanced divergent potential, ϵ, by the leading order balance in the omega equation,

$$\epsilon = \frac{R[1, R]}{\delta^2[1, \delta^2 B]}$$

We note that ϵ is small whenever $R << 1$ or $F << 1$, $R > 1$. Two estimates for the amplitude of the unbalanced motion, one for $R << 1$ and one for $F << 1$, $R > 1$, may be estimated from terms in the omega equation and the divergence equation of higher order than those given here (ie., terms of $O(\mu)$ are balanced by those terms of $O(\epsilon R)$, $O(\epsilon^2)$). However, in the simulation to be examined, local values of R and F reach values of $O(1)$ (especially later in the simulation as frontal zones are formed), so we will not present these scaling estimates here since they are not directly relevant.

4. THE NUMERICAL SIMULATION

The simulation we wish to examine is perfomed using a three-dimensional primitive equation model under the anelastic approximation. A complete model description is available in Clark (1977) and a more detailed description of the simulation may be found in Bush and Peltier (1993). The baroclinic wave life cycle is initialized with a mixed baroclinic/barotropic mean state upon which we superimpose the structure of the fastest growing mode of linear theory calculated from a Galerkin-type stability analysis of the meanstate. The model (x, y, z) dimensions are $(3590, 8000, 18)$ kilometers and the integrations are performed with a

constant Coriolis parameter. The model domain is a channel configuration with periodic boundary conditions in the zonal direction, the zonal dimension being chosen to be equal to the wavelength of the normal mode perturbation. (x, y, z) grid sizes are respectively (52.8, 63.5, 0.6) kilometers, so for features of typical aspect ratio f/N (eg., balanced fronts) we expect to have adequate vertical resolution (see Lindzen and Fox-Rabinovitz (1989) and Persson and Warner (1991) for a discussion on consistency between vertical and horizontal resolution).

Evolution of the surface potential temperature is given in Figure 1.

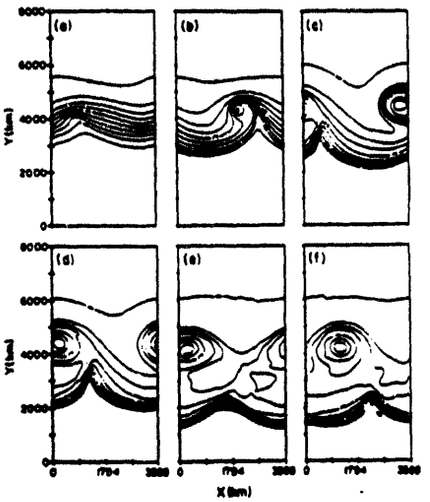

Figure 1: Evolution of the surface potential temperature. a) day 2.5, b) day 3.5, c) day 4.5, d) day 5, e) day 8.5, f) day 9.5. The maximum temperature in the core of the low is 282 K with a contour interval of 3 K.

The low occludes at roughly day 4, although intense frontal zones are evident by day 3 in the region from which the low eventually detaches.

6. THE BALANCE ANALYSIS

Poloidal/toroidal scalars are calculated from the model data according to

$$\nabla^2 \Psi = -\bar{\rho}_a \zeta$$

$$\nabla^2 \chi = -\bar{\rho}_a w$$

We then assume that the total Ψ field is balanced. The errors inherent in this assumption (which arise from the imbalance present in the normal mode perturbation) may be shown to be small, and the amplitude of the initial imbalance is an order of magnitude smaller than the unbalanced amplitude that arises later in the frontal zones. We then calculate the balanced pressure through the divergence equation (which is a simple statement of gradient wind balance) from which we find the balanced density through the hydrostatic relation. The vorticity and omega equations are then iterated upon until convergence for the variables $\partial_t \Psi$ and $\nabla^2 \chi$, the latter of which delivers the balanced vertical mass flux. Unbalanced fields are computed as the difference between the model data and the balanced fields.

Estimates of the balanced and unbalanced amplitudes may be obtained from the following expressions.

$$\epsilon = \frac{< \chi >}{< \Psi >}$$

$$\mu = \frac{< \chi' >}{< \Psi >}$$

in which the norm $< \cdot >$ of a field Ψ is defined on an (nx,ny,nz) grid by

$$< \Psi > = \left[\frac{1}{(nx \cdot ny \cdot nz)} \sum_{i=1}^{nx} \sum_{j=1}^{ny} \sum_{k=1}^{nz} \Psi^2(i,j,k) \right]^{1/2}$$

We can also estimate the length scales of the balanced rotational, the balanced divergent, and the unbalanced divergent components according to

$$\left(\frac{< \Psi >}{< \nabla^2 \Psi >} \right)^{1/2}, \left(\frac{< \chi >}{< \nabla^2 \chi >} \right)^{1/2}, \left(\frac{< \chi' >}{< \nabla^2 \chi' >} \right)^{1/2}$$

The spatial distribution of the kinetic energies of the balanced rotational, the balanced divergent and the unbalanced divergent components may be calculated respectively according to

$$KE_{br} = \bar{\rho}_a ({\Psi_x}^2 + {\Psi_y}^2)$$

$$KE_{bd} = \bar{\rho}_a ({\chi_{xz}}^2 + {\chi_{yz}}^2 + (\nabla^2 \chi)^2)$$

$$KE_{ud} = \bar{\rho}_a ({\chi'_{xz}}^2 + {\chi'_{yz}}^2 + (\nabla^2 \chi')^2)$$

In Figure 2a we display a time series of the volume-averaged kinetic energy components as calculated from the above expressions with a blow-up of the divergent components in Figure 2b. The exponential growth of the wave is evident up to day 3.5. The increase in unbalanced divergent KE lags that of the balanced divergent KE by roughly 0.4 days, and is consistent with the fact that the unbalanced motion is being driven by the terms of $O(\epsilon R, \epsilon^2)$ so that as ϵ increases, μ does also.

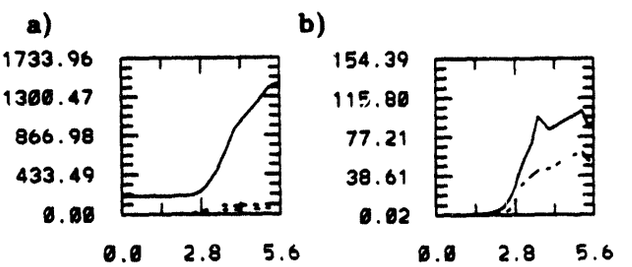

Figure 2: a) Time series of the volume-averaged balanced rotational kinetic energy (solid), the balanced divergent kinetic

energy (longdash-dash), and the unbalanced divergent kinetic energy (dashed). b) A blow-up of the balanced divergent (solid) and unbalanced divergent (dashed) components.

Estimates of the balanced (ϵ) and unbalanced (μ) divergent potentials calculated by the above expressions are given in Figure 3. The initial fluctuations in the unbalanced component are caused by an inertial oscillation that is a result of the imbalance in the normal mode perturbation. Saturation of the divergent motion corresponds to a saturation of the baroclinic conversion terms associated with this wave. The rapid increase in the balanced divergent motion drives a corresponding increase in the unbalanced divergent motion. Typical local Rossby and Froude numbers for the flow reach values above unity after day 3 in the frontal regions. Before day 3, local values may reach 0.7, so assumptions of globally small Rossby and Froude numbers are at best marginal.

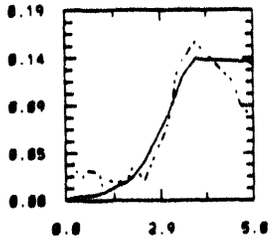

Figure 3: Amplitude estimates of the balanced divergent (solid) and the unbalanced divergent (dashed) components of the flow versus time. The initial imbalance of the normal mode perturbation is evident, as well as the subsequent inertial oscillation. Note the exponential rise in the balanced divergent flow which drives the increase in magnitude of the unbalanced flow.

The balanced and unbalanced pressure, normalized by Ψ, are displayed in Figure 4. The marked rise in the unbalanced pressure around day 3 is associated with an underestimation of the pressure in the surface low by the balanced divergence equation.

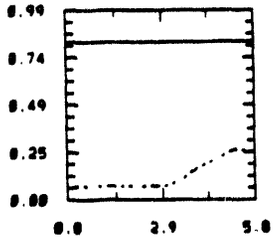

Figure 4: Time series of the volume-averaged balanced (solid) and unbalanced (dashed) pressure, normalized by Ψ. A majority of the unbalanced pressure is caused by an underestimation of the surface low by the balance equations.

Length scale estimates for the balanced rotational, the balanced divergent and the unbalanced divergent components of the flow are given in Figure 5. The balanced rotational motion has an initial length scale of approximately 2300 km, then decreases to roughly 870 km. This synoptic- to mesoscale cascade is typical of a synoptic-scale baroclinic wave that develops intense frontal zones. The balanced and unbalanced length-scales, on the other hand, are relatively constant at 700 km, a value indicative of mesoscale frontal motions.

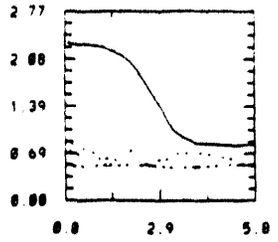

Figure 5: Length scale estimates (x 10^{-3} km) for the balanced rotational (solid), the balanced divergent (londash-dash), and the unbalanced divergent (dashed) components of the flow. Decrease in the balanced rotational component is indicative of the cascade from synoptic-scale to mesoscale motion.

A comparison between upper and lower level frontal balance is also of interest. In Figure 6 we display xy cross-sections of the unbalanced vertical mass flux in the lower and upper levels. Taking into account the variation in $\bar{\rho}_a$, we find that upper level imbalance is less by approximately 2/3 during frontogenesis.

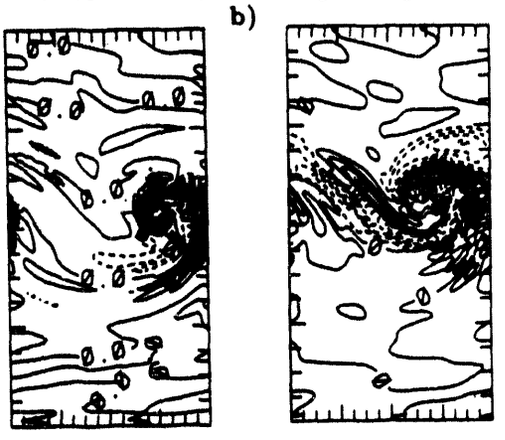

Figure 6: XY cross-sections taken at a) z=1 km and at b) z=8 km. Unbalanced motion in the upper level is approximately 2/3 times that in the lower levels. Gravity wave activity near the surface cold front is evident.

A temporal analysis of the unbalanced vertical mass flux field will separate any slow, advective imbalance (higher order corrections) from the fast gravity waves. A time sequence of isosurface plots of unbalanced vertical mass flux $\bar{\rho}_a w$ is given in Figure 7. The initial frontal imbalance is evident in Figure 7a, as the fronts begin to collapse and higher order corrections become significant. Gravity wave generation is initially seen in Figure 7b on the southern side of the surface cold front, and this wave activity becomes more pronounced near the time of occlusion (Figure 7c). Well after occlusion, gravity wave activity is still persistent over the surface cold front (Figure 7d), although higher order corrections are dominant.

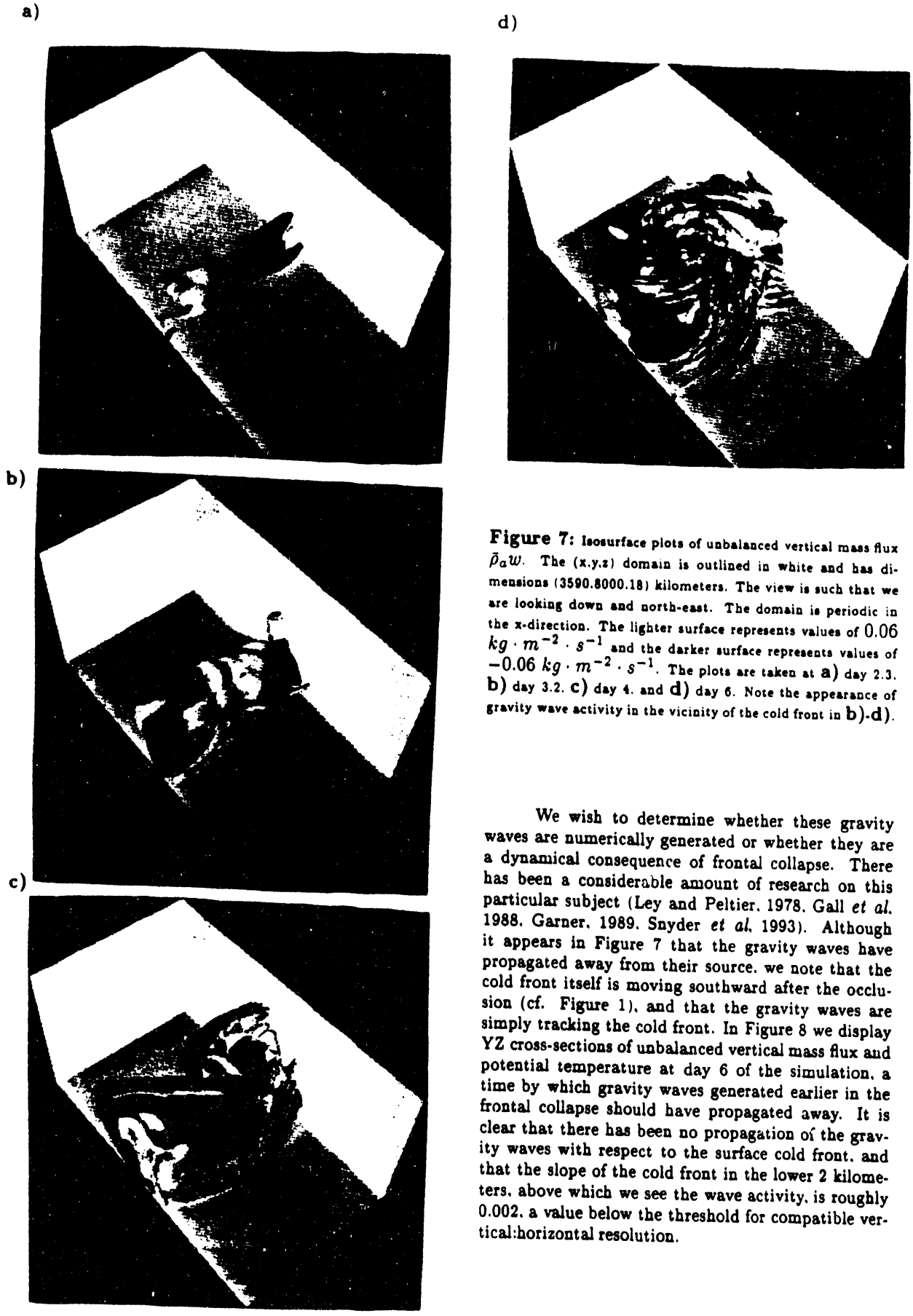

Figure 7: Isosurface plots of unbalanced vertical mass flux $\bar{\rho}_a w$. The (x,y,z) domain is outlined in white and has dimensions (3590.8000.18) kilometers. The view is such that we are looking down and north-east. The domain is periodic in the x-direction. The lighter surface represents values of $0.06\ kg \cdot m^{-2} \cdot s^{-1}$ and the darker surface represents values of $-0.06\ kg \cdot m^{-2} \cdot s^{-1}$. The plots are taken at **a)** day 2.3. **b)** day 3.2. **c)** day 4. and **d)** day 6. Note the appearance of gravity wave activity in the vicinity of the cold front in **b)**-**d)**.

We wish to determine whether these gravity waves are numerically generated or whether they are a dynamical consequence of frontal collapse. There has been a considerable amount of research on this particular subject (Ley and Peltier, 1978, Gall *et al.* 1988, Garner, 1989, Snyder *et al.* 1993). Although it appears in Figure 7 that the gravity waves have propagated away from their source, we note that the cold front itself is moving southward after the occlusion (cf. Figure 1), and that the gravity waves are simply tracking the cold front. In Figure 8 we display YZ cross-sections of unbalanced vertical mass flux and potential temperature at day 6 of the simulation, a time by which gravity waves generated earlier in the frontal collapse should have propagated away. It is clear that there has been no propagation of the gravity waves with respect to the surface cold front, and that the slope of the cold front in the lower 2 kilometers, above which we see the wave activity, is roughly 0.002, a value below the threshold for compatible vertical:horizontal resolution.

a)

b)

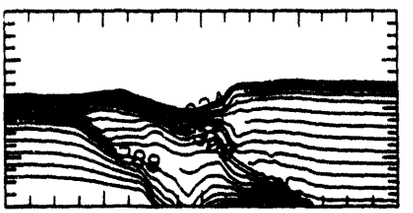

Figure 8: YZ cross-sections at x=1661 kilometers of a) unbalanced vertical mass flux and b) potential temperature at day 6. Note the gravity wave activity above the foot of the cold front: there are no signs of gravity waves having propagated away from their source region.

7. CONCLUSIONS

We have developed a set of balance equations for the anelastic equations and have tested them diagnostically on a three-dimensional, anelastic, primitive equation simulation of a synoptic-scale baroclinic wave. Results indicate that both forms of imbalance, slow higher-order corrections and fast gravity wave motions, arise in the simulation. The unbalanced motion field is dominated by the slower advective motions, although the gravity waves reach a significant amplitude. Further investigation into the origin of these gravity waves reveals that the frontal slope near the time of occlusion decreases in the lower 2 kilometers to a value beyond compatibility with the vertical and horizontal resolution employed, and we conclude that the waves are numerically generated.

8. REFERENCES

Allen, J.S., J.A. Barth, and P.A. Newberger, 1990: On Intermediate Models for Barotropic Continental Shelf and Slope Flow Fields. Part II: Comparison of Numerical Model Solutions in Doubly Periodic Domains. *J. Phys. Oceanogr.*, **20**, 1044-1076.

Barth, J., J. Allen, and P. Newberger, 1990: On intermediate models for barotropic continental shelf and slope flow fields: Part II, Comparison of numerical model solutions in doubly-periodic domains. *J. Phys. Ocean*, **20**, 1044-1076.

Bolin, B., 1955: Numerical Forecasting with the Barotropic Model. *Tellus*, **7**, 27-49.

Bush, A.B.G. and W.R. Peltier, 1993: Tropopause Folds and Synoptic-Scale Baroclinic Wave Life Cycles. *J. Atmos. Sci.*, in press.

Charney, J., 1955: The Use of Primitive Equations of Motion in Numerical Prediction. *Tellus*, **7**, 22-26.

Clark, T., 1977: A small-scale dynamic model using a terrain- following coordinate transformation. *J. Comput. Phys.*, **24**, 186-215.

Gall, R.L., R.T. Williams, and T.L. Clark, 1988: Gravity Waves Generated during Frontogenesis. *J. Atmos. Sci.*, **45**, 2204-2219.

Garner, S.T., 1989: Fully Lagrangian numerical solutions of unbalanced frontogenesis and frontal collapse. *J. Atmos. Sci.*, **46**, 717-739.

Gent, P.R. and J.C. McWilliams, 1982: Intermediate Model Solutions to the Lorenz Equations: Strange Attractors and Other Phenomena. . Atmos. Sci., **39**, 3-13.

Keyser, D., and M.J. Pecknick, 1985: Diagnosis of Ageostrophic Circulations in a Two-Dimensional Primitive Equation Model of Frontogenesis. *J. Atmos. Sci.*, **42**, 1283-1305.

Ley, B.E. and W.R. Peltier, 1978: Wave Generation and Frontal Collapse. *J. Atmos. Sci.*, **35**, 3-17.

Lindzen, R.S. and M. Fox-Rabinovitz, 1989: Consistent vertical and horizontal resolution. *Mon. Wea. Rev.*, **117**, 2575-2583.

Norton, N., J. McWilliams, and P. Gent, 1986: A numerical model of the Balance Equations in a periodic domain and an example of balanced turbulence. *J. Comp. Phys.*, **67**, 439-471.

Persson, P.O.G. and T.T. Warner, 1991: Model generation of spurious gravity waves due to inconsistency of the vertical and horizontal resolution. *Mon. Wea. Rev.*, **119**, 917-935.

Reeder, M.J. and D. Keyser, 1988: Balanced and Unbalanced upper-level frontogenesis. *J. Atmos. Sci.*, **45**, 3366-3386.

Spall, M.A. and J.C. McWilliams, 1992: Rotational and Gravitational Influences on the Degree of Balance in the Shallow-Water Equations. *Geophys. Astrophys. Fluid Dynamics*, **64**, 1-29.

Snyder, C., W.C. Skamarock, and R. Rotunno, 1991: A comparison of primitive equation and semigeostrophic simulations of baroclinic waves. *J. Atmos. Sci.*, **48**, 2179-2194.

Snyder, C., W.C. Skamarock, and R. Rotunno, 1993: Frontal dynamics near and following frontal collapse. *J. Atmos. Sci.*, in press.

Low–Frequency Variation of a Zonally Localized Jet Stream:

Observation and Theory

Ming Cai

CICS, Department of Meteorology
University of Maryland
College Park, MD 20742

Introduction: The climatological mean circulation in the extratropics of the Northern Hemisphere is characterized by two zonally localized jet streams over the east coasts of the two major continents. The zonal inhomogeneity of the climatological mean circulation is believed to be a primary factor determining the geographical locations of the maximum activity centers of the atmospheric transients, such as storm tracks over the east coasts of the two major continents and frequent blocking episodes occurring over the central regions of the two oceans (Frederiksen, 1982; Pierrehumbert, 1984; Mak and Cai, 1989; Cai and Mak, 1990). The impact of the transients on the zonally localized jet streams is studied mostly in the linear dynamics framework in terms of so-called "feedback" diagnosis (Hoskins et al. 1983; Lau and Holopainen, 1984; Cai and Mak, 1990). This study investigates nonlinear instability of a zonally localized jet stream. The emphasis is on the nonlinear adjustment of a zonally localized jet stream associated with the development of the transients via local instability. The adjustment of a zonally localized jet stream would naturally consists of two parts: one is the time-invariant part and the other is the transient part (temporal variation of the adjustment). In conjunction with the observation, the time–mean adjustment is part of the climatological mean flow and hence is "invisible". The transient part of the adjustment is evidenced by the changes of the jet streams in terms of both location and intensity. In this study, we tend to relate the transient part of the adjustment of the jet stream to the maximum activity centers of low–frequency variability. The underlying mechanisms that are responsible for the temporal variation of the adjustment will be investigated. The time-mean adjustment will be also studied to better understand the temporal variation of the adjustment.

Observational evidence: To determine the spatial structure of the temporal variation of the jet streams in the atmosphere, we have analysed the 10-year monthly-averaged ECMWF zonal wind data at 200 mb from January, 1980 to December, 1989. The anomaly zonal wind is obtained by removing the climatological mean and the annual cycle from this dataset. As found in other studies, the anomaly dataset exhibits three local maxima in the extratropics, two of them over the central regions of the oceans and the other over the upstream region of the Asia jet stream. We then performed an EOF analysis with the anomaly dataset over the region from 20° N to 50° N and from 40° E to 120° W where the Pacific jet stream lies. Plotted in Fig. 1 are the first three leading EOFs, which explain 16.8%, 10.1%, and 9.1% of the variance of the anomalous zonal wind, respectively. The first EOF primarily accounts for the east-west movement of the jet stream, with a positive phase implying an eastward shift of the jet core and a negative phase a westward shift of the jet core. The north–south movement of the jet stream is also evident in this map, but is overwhelmed by the east-west movement. The second EOF is very similar to the first EOF, representing an east-west shifting of the jet stream. The difference is the phase of the north-south movement of the jet stream. While the eastward movement of the jet core represented by the first EOF is accompanied by the southward shifting the jet stream, the second EOF indicates the eastward shifting of the jet core is accompanied with the northward movement of the jet stream. The third EOF represents an oscillation of the jet stream from a narrower jet (positive phase) to a wider jet (negative phase).

In summary, there are two principle modes associated with the temporal variation of the

Pacific jet stream. The first one represents a location change of the jet core, which primarily takes place in the form of east-west movement. The second mode represents an oscillation between a wider jet core and a narrower jet core. In the remaining part of this report, we will discuss the underlying dynamics associated with the temporal variation of the zonally localized jet stream in the context of a quasi-geostrophic two-layer channel model forced by a zonally asymmetric jet stream.

Model: The two-layer channel model used in this study is otherwise identical to the one used in the linear local instability study by Cai and Mak (1990) with only two new features: (i) all the nonlinear terms are retained; and (ii) an asymmetric Ekman layer friction parameter is used. The time scale of the Ekman layer damping at the upper level is 20 days and that for the lower level is 5 days. Additionally, we also have a scale-dependent biharmonic friction at each layer to take care of the enstrophy cascade towards small scales due to nonlinear interaction. The model resolution is 16 zonal waves by 8 meridional waves with total number of unknowns equal to 528. The time scale of the biharmonic friction is a few days for the highest wavenumber component of the model.

The model is forced by a basic flow consisting of two parts: one is a zonally symmetric baroclinic shear representing a zonally uniform north-south temperature contrast and the other is a zonally varying baroclinic/barotropic shear. The amplitude of the zonally varying baroclinic shear is identical to that of the barotropic shear so that the presence of the zonal inhomogeneity in the basic flow only appears in the upper level and the basic flow at the lower level is purely parallel flow. We solve the nonlinear problem in terms of the anomaly flow (or the departure flow from the prescribed jet stream). Because the nonlinearity in this model is only quadratic, the anomaly model is equivalent to the model for the total flow with a relaxation towards the prescribed jet stream. In this sense, the time scale of the upper level Ekman layer friction corresponds to a relaxation time scale of this model.

Results: We have numerically integrated the model starting from an unstable local model up to 2000 days with various model parameters. Here we only show the representative results obtained with one setting of the parameters. For all the maps plotted below, we will use grids (0, 64) and (0, 32) as our reference for longitudes and latitudes, respectively.

Fig. 2a is the map of the upper-level streamfunction of the prescribed jet stream. The jet core of the prescribed jet stream is at the center ($x = 32$) of the domain and the jet stream is symmetric about the jet core with a length equal to one–eighth of the channel length. Fig. 2b is the time–mean map of the adjusted jet stream obtained by adding the time mean part (the last 1500 days) of the departure flow calculated from the numerical integration to the prescribed jet stream. Clearly, due to the development of the transients arising from local baroclinic instability, the zonally localized jet stream has been modified significantly. The location of the adjusted jet core has been moved upstream ($x \approx 26$) and the strength of the jet has been reduced. The adjusted jet stream also appears to have a weak asymmetry about the jet core with stronger diffluent flow in the exit region and weaker confluent flow in the entrance. Detailed analyses in terms of energetics and feedback calculations (not shown here) reveal that the local baroclinic instability (or development of storm track) plays a less important role in giving rise to the time mean adjustment of the jet stream than the finite–amplitude instability of the jet stream with respect to itself. The role of the local instability is to introduce a finite-amplitude perturbation to the jet stream which would amplify itself by further extracting energy from the prescribed jet stream. As a result, the jet stream becomes less unstable than the unadjusted (prescribed) jet stream.

As seen from Fig. 2b, the wavy part of the time-mean flow is primarily made of the waves with an even meridional wavenumber, which is anti-symmetric about the center latitude ($y=16$) of the channel. The local unstable modes (not shown here) are all compose of the waves with an odd meridional wavenumber (symmetric about the center latitude). For easy reference, we shall refer to the anti-symmetric part of the departure flow (from the prescribed basic flow) as basic departure flow and the symmetric part of the departure flow as eddy departure flow. The time-mean part of the basic departure flow (which is equal to the difference between the two maps in Fig. 2) is a measure of the time-mean adjustment of the prescribed jet stream and the transient

part corresponds to the temporal variation of the adjustment of the prescribed jet stream. Although such definitions of basic disturbances and eddies are somewhat arbitrary, they serve the purpose of separating the temporal variation of the jet stream from the development of storm tracks. It is found that the temporal variation of the jet stream has two local maxima: one upstream (x = 20) of the new jet core and the other downstream (x = 36). This is in agreement with the observation (there two major jet streams and three local maxima of low–frequency variability). Fig. 3a shows a representative portion of the time series (from day 1200 to day 1400) of the upper-level basic departure streamfunction at x = 20 and y = 8. Panel (b) of Fig. 3 is the counterpart for the eddies at x = 32 and y = 16, where the temporal variability of the eddies reaches its maximum. The two time series indicate that whereas the nonlinear evolution of the storm track (eddy departure flow) has a time scale (a few days) comparable to the linear dynamics, the time scale of the nonlinear evolution of the jet stream can be much longer (about 60 days). Such longer time scale is a result of the nonlinear interaction of local instability and finite-amplitude instability of the jet stream (details of the analyses are not given here).

Fig. 4 shows the first two leading EOFs of the transient part of the basic departure flow. The first EOF corresponds to an east-west shifting of the jet core and the second EOF represents an oscillation of the jet stream between a wider jet and a narrow jet. Clearly, it captures the main features of the leading modes in the observed zonal wind variations shown in Fig. 1. Hence, we conclude that a large portion of the monthly variability in the zonal wind over the extratropics can be interpreted as a result of the nonlinear adjustment of the zonally localized jet streams.

References:

Cai, M. and M. Mak, 1990: On the basic dynamics of regional cyclogenesis. **J. Atmos. Sci., 47**, 1417–1442.

Frederiksen, J. S., 1982: An unified three-dimensional instability theory of onset of blocking and cyclogenesis. **J. Atmos. Sci., 39**, 969–982.

Hoskins, B. J., I. N. James, and G. H. white, 1983: The shape, propagation and mean–flow interaction of large–scale weather systems. **J. Atmos. Sci., 40**, 1595–1612.

Lau, N.–C., and E. O. Holopainen, 1984: Transient eddy forcing of the time–mean flow as identified by geopotential tendencies. **J. Atmos. Sci., 41**, 313–328.

Mak, M., and M. Cai, 1989: Local barotropic instability. **J. Atmos. Sci., 46**, 3289–3311.

Pierrehumbert, R. T., 1984: Local and global baroclinic instability of zonally varying flow. **J. Atmos. Sci., 41**, 2141–2162.

Figure Legends:

Fig. 1 The first three leading EOFs of the ECMWF anomaly zonal wind data at 200 mb. The shaded area indicates location of the zonal wind greater than 40 m/sec..

Fig. 2 The upper-level stream function in the two-layer model. (a) the imposed basic state and (b) the time mean of the total flow.

Fig. 3 Time series of the upper-level streamfunction at a particular location. (a) anti-symmetric component of ψ_1 at x = 20, y = 8. (b) symmetric component of of ψ_1 at x = 32, y = 16.

Fig. 4 The first two leading EOFs of the anti–symmetric transients of the baroclinic streamfunction.

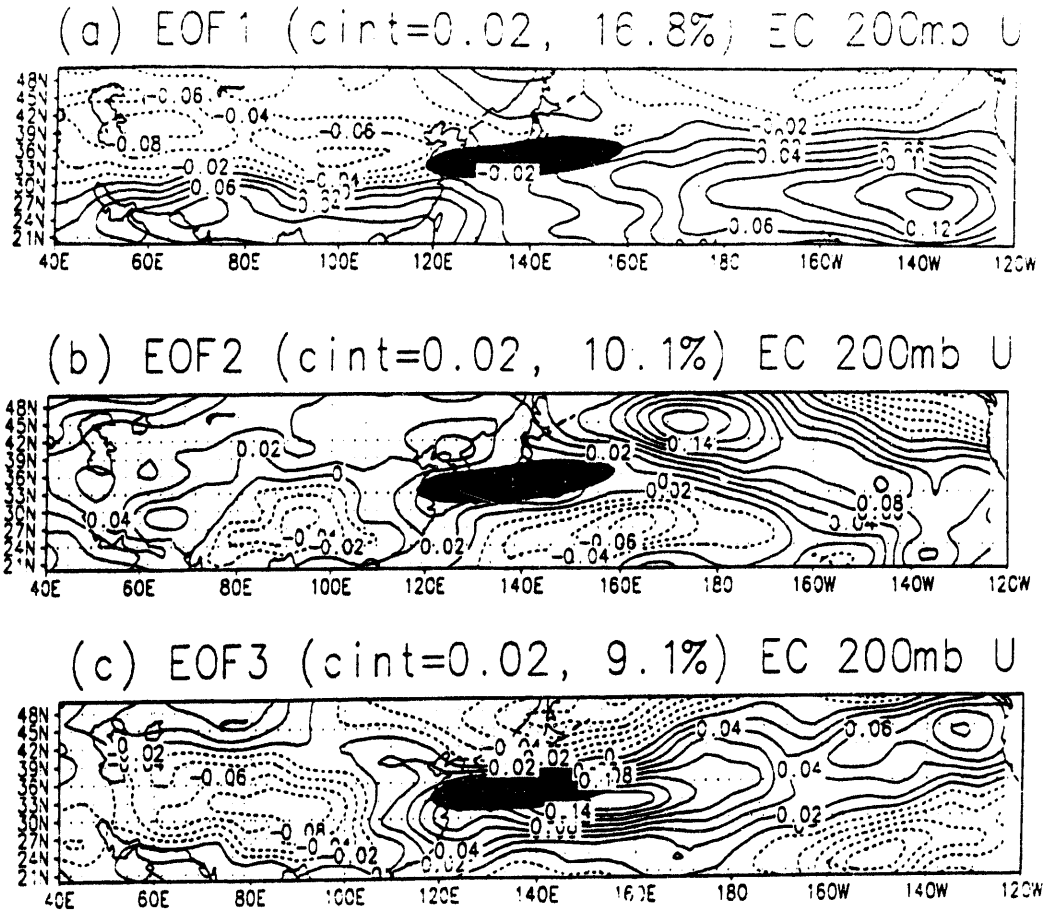
(a) EOF1 (cint=0.02, 16.8%) EC 200mb U
(b) EOF2 (cint=0.02, 10.1%) EC 200mb U
(c) EOF3 (cint=0.02, 9.1%) EC 200mb U
40E
60E
80E
100E
120E
140E
160E
180
160W
140W
120W

Fig. 1

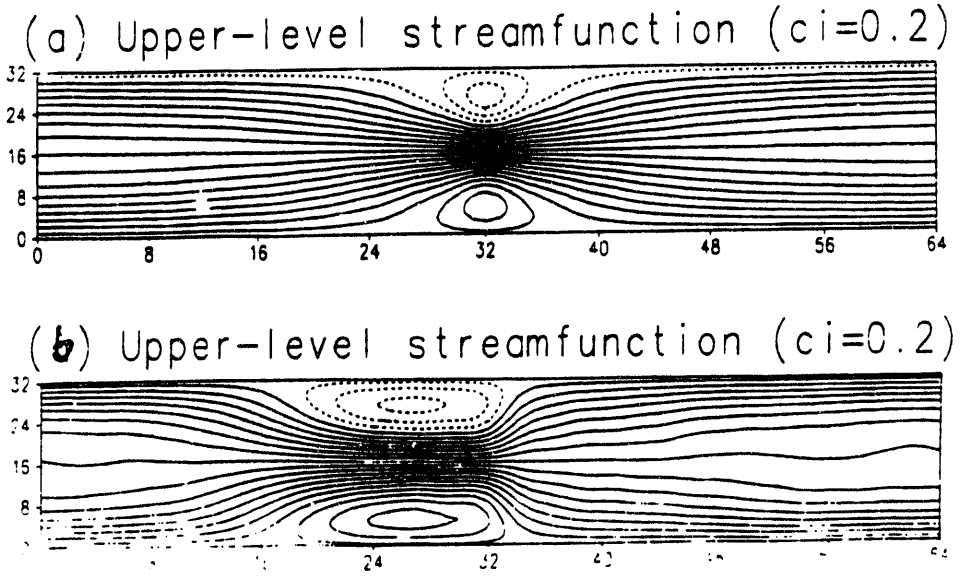
(a) Upper-level streamfunction (ci=0.2)
(b) Upper-level streamfunction (ci=0.2)
0
8
16
24
32
40
48
56
64

Fig. 2

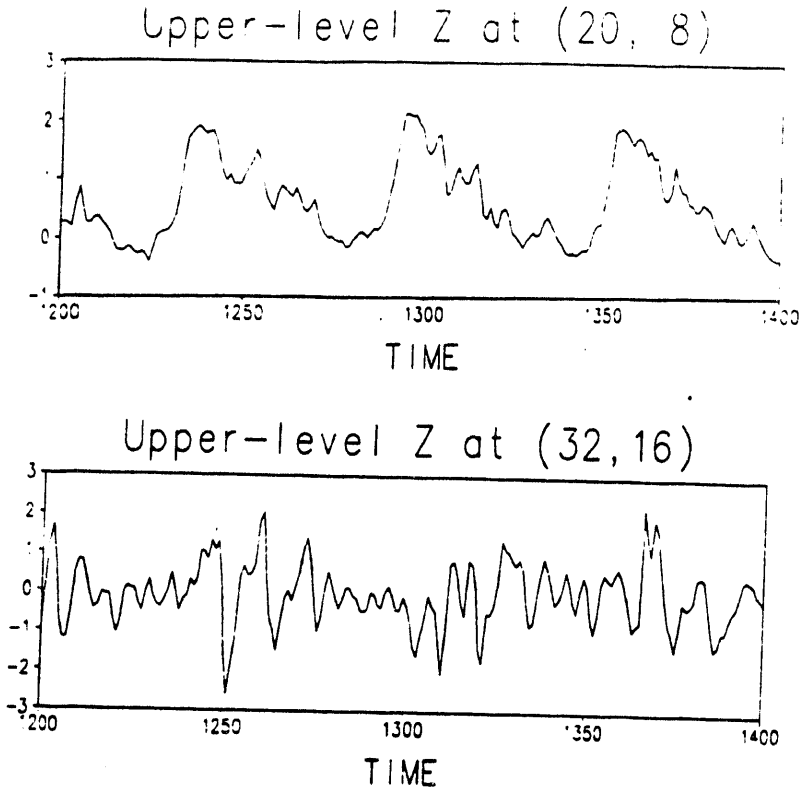
Upper-level Z at (20, 8)
3
2
0
-1
1200
1250
1300
1350
1400
TIME
Upper-level Z at (32,16)
3
2
1
0
-1
-2
-3
1200
1250
1300
1350
1400
TIME

Fig. 3

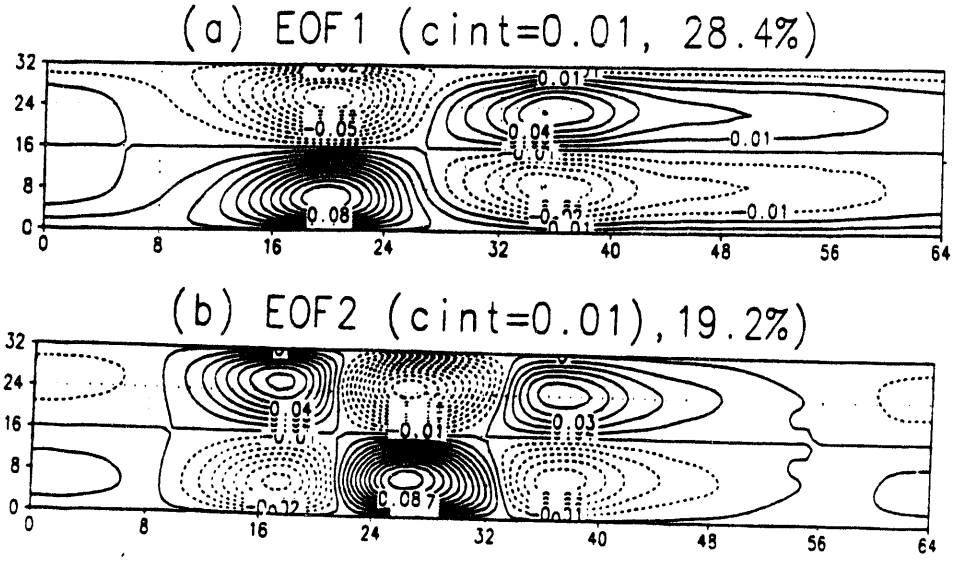
(a) EOF1 (cint=0.01, 28.4%)
32
24
16
8
0
0.01
-0.05
0.04
-0.01
0.01
0.08
-0.01
0
8
16
24
32
40
48
56
64
(b) EOF2 (cint=0.01), 19.2%)
32
24
16
8
0
0.04
-0.01
-0.01
0.03
0.087
0
8
16
24
32
40
48
56
64

Fig. 4

LOW-FREQUENCY ANOMALIES IN THE NMC MRF MODEL AND REALITY

Wilbur Y. Chen
Climate Analysis Center
NOAA/NWS/NMC
Washington, D.C. 20233

A low resolution version (Triangular 40) of the National Meteorological Center medium range forecast (MRF) model was employed to obtain simulated meteorological data for 10 continuous years. The wintertime Z500 fields were analyzed for its capability to generate persistent short-term climate anomalies. An 11-day running mean temporal filter was applied to obtain the low frequency components of its variability.

The climatology of the model data resembles well the observed, though the model's amplitudes of its stationary waves are somewhat larger. Comparison of the geographical distribution of the low-frequency variance indicates that, in addition to smaller magnitude, the model tends to misplace its variance maxima about 1500 miles farther east over the N Pacific and farther southeast over the N Atlantic.

Since the frequency distribution of the low-frequency anomalies (LFAs) are significantly skewed for both model (MDL) and observed (OBS) data, investigations were conducted separately for the positive and negative large-amplitude LFAs. Amplitude thresholds of 200m for the OBS and 150m for the MDL were applied to

extract the large-amplitude LFAs. The thresholds used were found to be suitable for isolating the most persistent anomalies in both the model and real atmosphere.

Four-way comparisons among MDL, OBS, positive, and negative LFAs were examined. For large positive LFAs, the MDL and the OBS have comparable probability of occurrence over the N Pacific and N Siberia. But, over the N Atlantic, the model displays little chance of occurrence (Fig. 1, upper panels). For large negative LFAs, the MDL's occurrence percentage is only half as much as the OBS (2% versus 4%) over both N Pacific and N Atlantic. However, over the N Siberia, the model shows twice as frequent (8% versus 4%) as the observed (Fig. 1, lower panels).

Over the northern oceans, the MDL's LFAs of both polarities are frequently about 1500 miles too far east or southeast. As a consequence, their respective associated composite circulation patterns are substantially different from the observed. For instance, over the N Pacific, the real atmospheric pattern (for LFA > 200 m in Pacific) displays a giant PNA (Pacific/North America) wavetrain, while the model yields only a short and more or less zonally oriented wave-"train" (Fig. 2). Many more subtle difference between the OBS circulation patterns associated with positive and negative LFAs can also be observed from Fig 2 (right panels).

The NMC MRF model does have the capability of generating long-lasting weather anomalies, especially over the northeastern oceans

and the adjacent western continents. Over the eastern N Pacific, while the OBS negative LFAs may persist as long as 40 days versus 20 days for the positive LFAs, the MDL LFAs display an opposite behavior, with negative LFAs persisting for a much shorter time than the positive ones (10 days versus 30 days).

The principal stormtracks as well as the 250mb mean zonal winds were also examined to supplement the investigation of the large-amplitude LFAs. Contrasted with the observed, the model's U250s display considerable eastward extension over both N Pacific and N Atlantic oceans, and their associated stormtracks show substantial equatorward displacement near the exit (Fig. 3). These model characteristics are consistent with the behavior that the model's large LFAs prefer to develop over the regions far east and southeast of those observed in the real atmosphere.

For skillful prediction on a time scale of two weeks and beyond, it is necessary for the model to simulate correctly first the location of the low-frequency anomalies. At the present time, the pronounced misplacement of the model's large LFAs presents a major challenge. Much more effort is needed in order to gain further insight into the physical processes leading to these deficiencies as well as finding the ways to improve the model's performance.

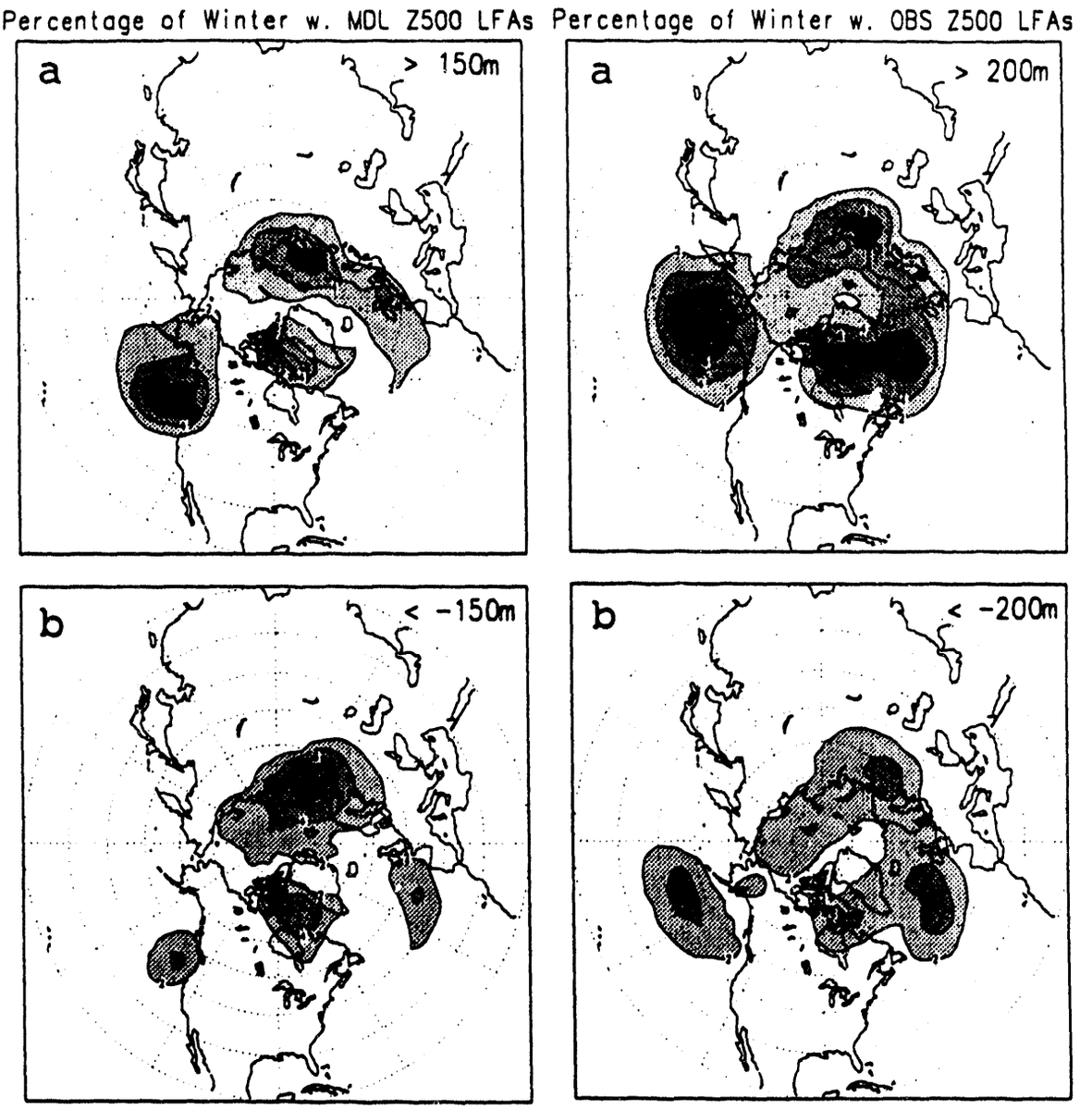

Fig. 1 For the left panels, percentage of time during 1510 wintertime days that the MDL's positive LFA exceeds 150m (a), negative LFA exceeds -150m (b). For the right panels, percentage of time during 3948 wintertime days that the observed positive LFA exceeds 200m (a), negative LFA exceeds -200m (b). The first shading/contour is 2 %, the contour interval is also 2 %.

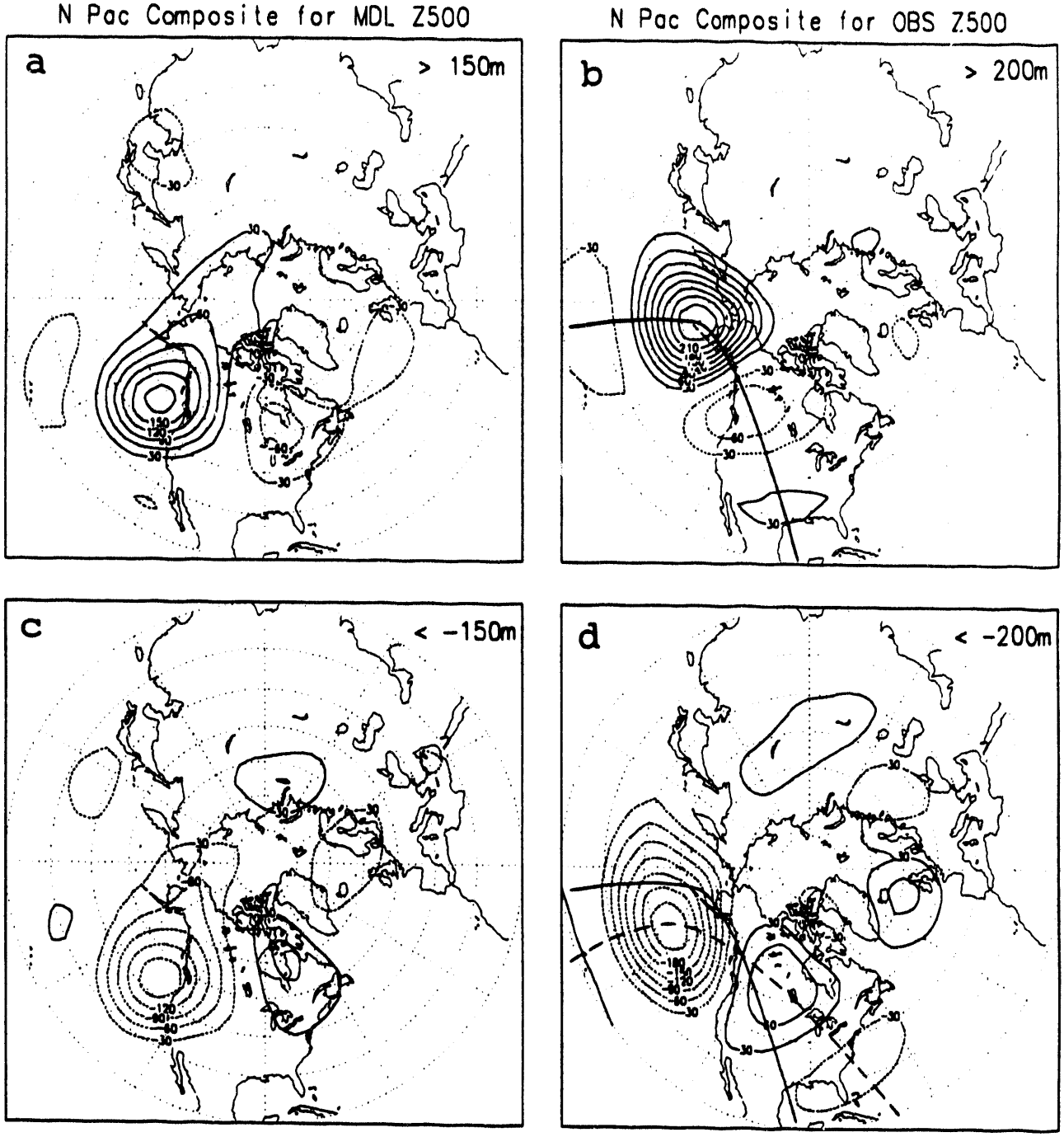

Fig. 2 Composite circulation patterns based on the LFA variance centers over the N Pacific. Left panels for MDL runs, right panels for OBS data. Upper panels for those based on the positive LFA centers and lower panels based on the negative LFA centers.

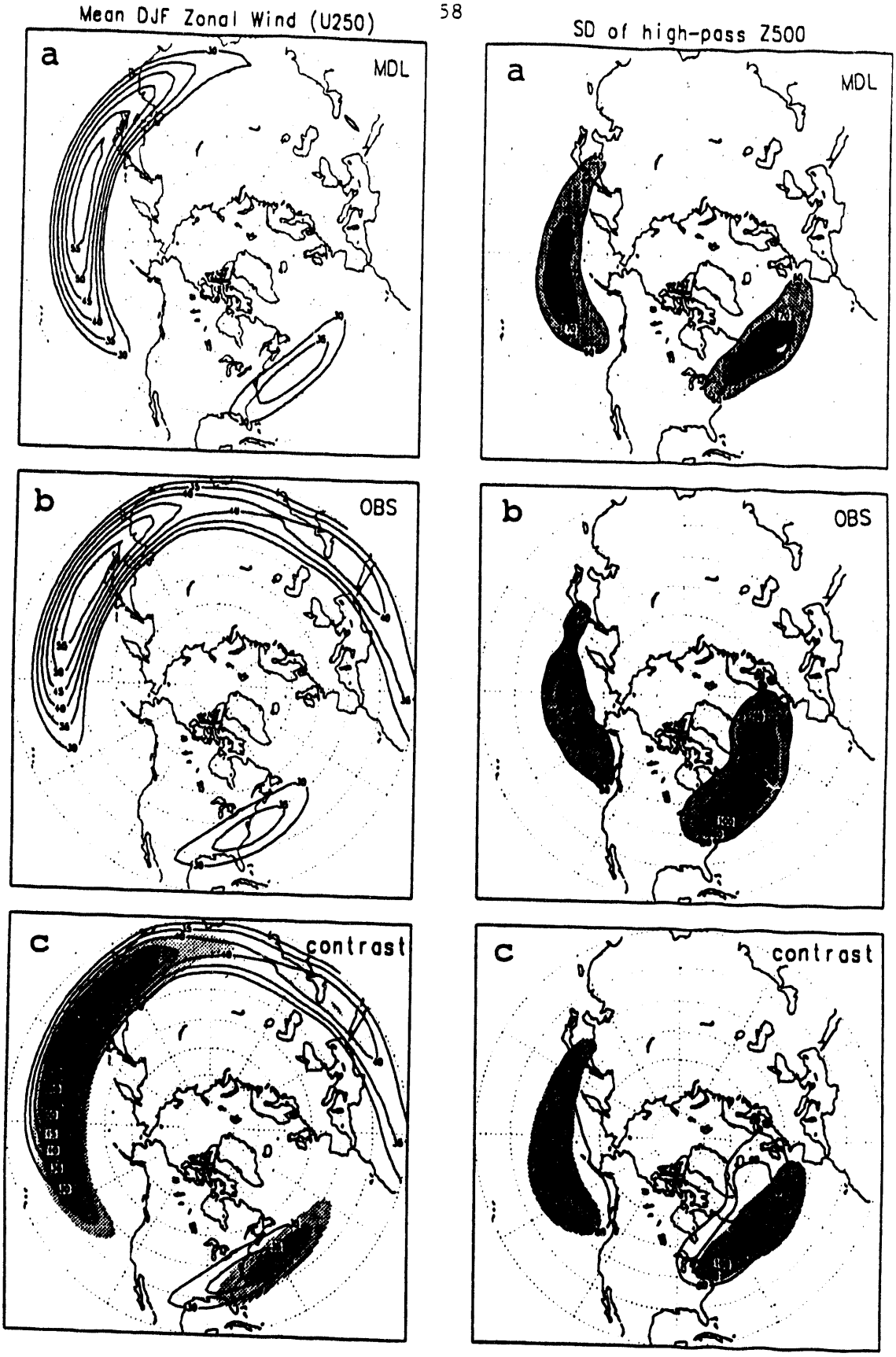

Fig. 3. The Dec-Jan-Feb mean zonal wind at 250mb level. First shading/contour begins at 30 m/s with increment of 5 m/s (left panels). For the right panels, the standard deviations of the high-pass Z500 synoptic-scale disturbances. (a) for 10-year MDL runs and (b) for 28-year NMC analyses. First shading/contour is 60m for the MDL runs and 80m for the OBS data. Interval is 10 m.

Synoptic Scale Eddies in the Northern Hemisphere Summer: A POP Analysis

John Fyfe
Canadian Climate Centre
Downsview, Ontario

1.0 Introduction

This abstract summarizes some recent comparisons between observed and simulated summertime (JJA) band pass filtered (2-10 day) eddies in the Atlantic region (Table 1). Our main diagnostic tool is the Principal Oscillation Pattern (POP) technique.

Table 1. NMC and CCC GCM Comparisons in the Atlantic Region

Subregion	Variable	NMC[a]	GCMII[b]	GCMIII[c]
Extratropics	Φ	◆	◆	
Tropics	ζ	◆	◆	◆

a. 8 summers (1984-91)
b. 8 summers, T32, 10 levels
c. 3 summers, T32, 30 levels, parameterized deep convection. GCMIII is under development.

2.0 The POP Concept

The POP analysis is a technique for obtaining the space-time characteristics of a data set objectively, and can be thought of as a normal mode analysis using an estimated system matrix (Storch et. al., 1988). The so-called "POP" is the eigenvector of the estimated system matrix which explains most of the variance in the data set. The POP's corresponding eigenvalue yields a period of oscillation, T. When complex the POP is interpreted as a propagating mode (Fig. 1). In this study all POPs are complex with real and imaginary parts nearly in quadrature, so we present real parts only.

Figure 1. Anatomy of a Propagating POP.

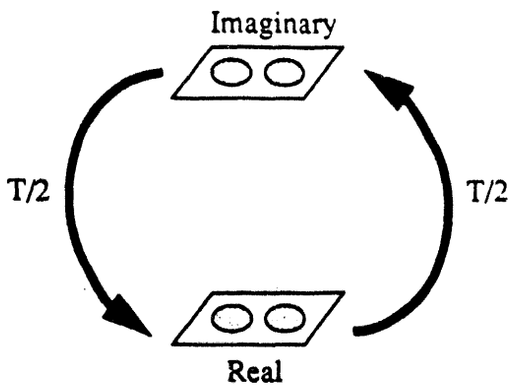

3.0 Extratropics

In Fig. 2 we see that, as in winter, the summertime extratropical Atlantic storm track maximum is downstream and poleward of the North American time-mean jet core (indicated with an arrow). Using the POP technique we will obtain the propagating pattern which explains most of this variance. We note that the POPs presented here extend through the troposphere but for brevities sake we show POPs on a single pressure level only.

Figure 2. Summertime variance of the filtered 300 mb geopotential.

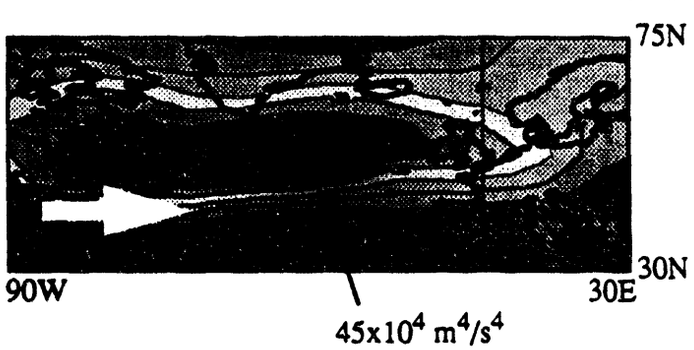

3.1 Observed

The observed POP (Fig. 3a) has $T \approx 4.1$ days and $c_x \approx 10$ m/s. The pronounced N-S meander reflects a like meander in the time-mean flow (not shown). In Fig. 3b the divergence of

Trenberth's (1986) barotropic $\vec{E}$ vector reveals westerly acceleration (+) of the time-mean flow along the storm track well into the Atlantic, and deceleration beyond (-).

Figure 3. Observed filtered 300 mb geopotential. (a) POP; (b) $\vec{E}$ and $\nabla \bullet \vec{E}$.

(a)

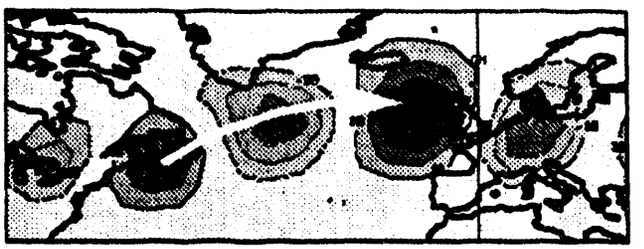

(b)

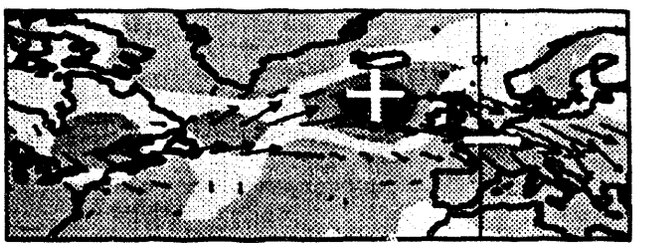

3.2 Simulated: Current and Double CO_2

The GCMII (McFarlane et. al., 1992) summertime extratropical Atlantic storm track (Fig. 4) is very well reproduced (compare with Fig. 2), giving us some confidence when moving on to our POP analysis. [For unknown reasons the simulated variance maximum is slightly higher in the atmosphere, i.e., at 200 instead of 300 mb.]

Figure 4. Simulated variance of the filtered 200 mb geopotential

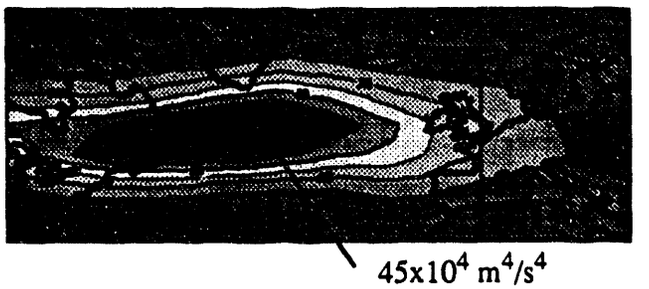

The GCMII POP has T ≈ 3.7 days and $c_x \approx 10$ m/s (Fig. 5a). The comparatively zonal track of this POP is presumably related to a simulated time-mean jet (not shown) that itself

is too zonal. $\vec{E}$ and $\nabla \bullet \vec{E}$ (not shown) are quite similar to observed. On the basis of the reasonably well simulated POP we repeat our calculation (Fig. 5b) in a $2xCO_2$ experiment (Boer et. al., 1992). The filtered variance in this experiment (not shown) is reduced by half, which is consistent with reduced time-mean baroclinicity found in midlatitudes.

Figure 5. Simulated filtered 200mb geopotential POP. (a) $1xCO_2$; (b) $2xCO_2$.

(a)

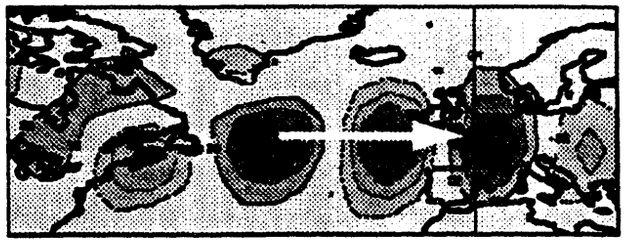

(b)

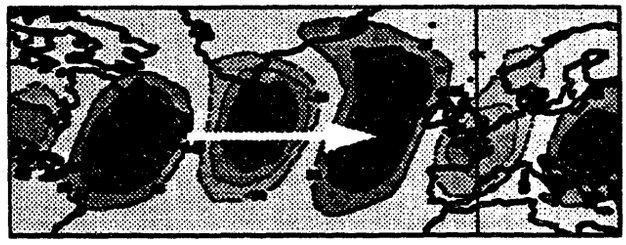

The period and phase speed of the $2xCO_2$ POP are about equal to the $1xCO_2$ POP but the structure is meridionally stretched and it has a more pronounced SW-NE tilt. There are noticeable differences in $\vec{E}$ and $\nabla \bullet \vec{E}$ (not shown) as well.

4.0 Tropics

In Fig. 6 we see that the tropical Atlantic storm track has maxima on the coast of Africa and in the Caribbean. A Hovmöller plot at 20°N (not shown) shows westward propagating waves originating over Africa and travelling into the Caribbean. These so-called "African Easterly Waves" are thought by many to originate as shear instabilities in the African Easterly Jet (indicated by the arrow).

Figure 6. Summertime variance of the filtered 700 mb vorticity.

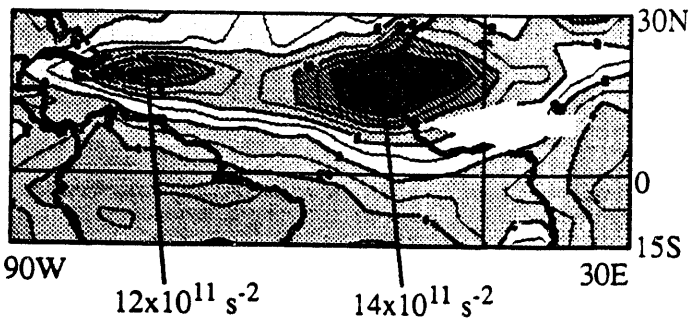

4.1 Observed

The observed POP (Fig. 7) is westward propagating with T ≈ 4.1 days. There appears to exist northern (20°N) and southern (10°N) tracks which merge over the Atlantic and then veer to the NW. Lau and Lau (1990) obtained a similar result using extended EOFs. A vertical cross-section through the lower troposphere (not shown) shows the POP is near surface over Western Africa but elevates to about 700 mb as it passes the African coast.

Figure 7. Observed filtered 850 mb vorticity POP.

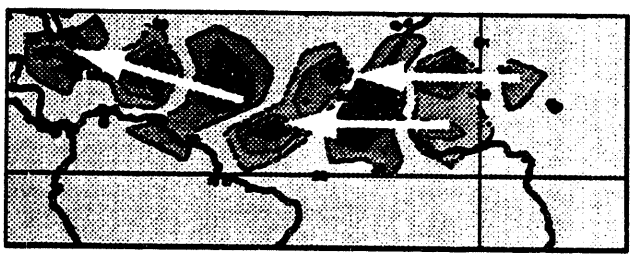

4.2 Simulated

The pattern in Fig. 8a is the 4th most dominant oscillation pattern in GCMII. The other more dominant patterns are associated with an unrealistic filtered variance maximum in Central America. That problems exist in the tropics in GCMII is well known and is part of the motivation for developing GCMIII. The pattern in Fig. 8a (T ≈ 4.4 days) appears to be physical but has obvious shortcomings, most notable of which is it's termination at the African coast.

The GCMIII POP (Fig. 8b) has T ≈ 3.7 days and a more respectable structure. This POP's vertical structure (not shown) is also quite realistic. Clearly GCMIII performs better in this regard, however it is unknown why at this time. Increased vertical resolution and parameterized deep convection are certainly playing a role in the improvement.

Figure 8. 850 mb filtered vorticity. (a) GCMII OP; (b) GCMIII POP.

(a)

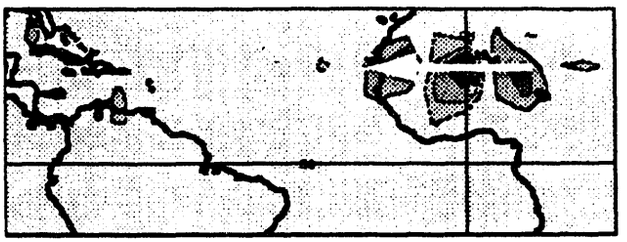

(b)

5.0 Summary

Table 2. Observation and CCC GCM Comparisons in the Atlantic Region

Subregion / Variable	GCM	Results
Extratropics Φ	II($1xCO_2$)	•Variance good •POP and E-P flux good but too zonal
	II($2xCO_2$)	•Variance reduced by 1/2 •POP y-stretched and E-P flux shifted
Tropics ζ	II	•Variance and POP poor
	III	•Variance and POP fair

References

Boer, G.J., N.A. McFarlane, and M. Lazare, 1992: Greenhouse gas-induced climate change simulated with the CCC second-generation general circulation model. J.Clim, **5**, 1045-1077.

Lau, K-H, N-C Lau, 1990: Observed structure and propagation characteristics of tropical summertime synoptic scale disturbances. J.A.S., **118**, 1888-1913.

McFarlane, N.A., G.J. Boer, J.-P. Blanchet, M. Lazare, 1992: The Canadian Climate Centre second-generation general circulation model and its equilibrium climate. J. Clim., **5**, 1013-1044.

Storch, H. v., T. Bruns, I. Fischer-Bruns, K. Hasselmann, 1988: Principal oscillation pattern analysis of the 30- to 60-day oscillation in general circulation model equatorial troposphere. Geophys. Res., 11,022-11,036.

Trenberth, K.E., 1986: An assessment of the impact of transient eddies on the zonal flow during a blocking episode using localized Eliassen-Palm flux diagnostics. J.A.S., **43**, 2070-2087.

Hydrologic and Radiative Feedbacks on Extratropical Transient Eddies: Implications of Global Warming

William J. Gutowski, Jr.,[1] and Lee E. Branscome[2]

[1]Dept. of Geological & Atmospheric Sciences, Iowa State University
Ames, Iowa, USA 50011

[2]Environmental Dynamics Research, Inc.
Palm Beach Gardens, Florida, USA 33418

I. Introduction

Atmospheric transient eddies contribute significantly to global energy and water cycles through their transports of sensible heat and water vapor. Changes in global climate induced by greenhouse enhancement will likely alter transient eddy behavior. General circulation models (GCMs) can simulate such alterations, but unraveling all the feedbacks that occur in GCMs is difficult.

Here we isolate transient eddies from the feedbacks by studying of the response of eddy life cycle simulations to changes in the initial, zonally symmetric temperature, wind and moisture distributions, using a primitive equations model. By specifying zonally symmetric initial conditions that correspond to GCM simulations of either the current or doubled-CO_2 climates, we use the life cycle simulations to evaluate the potential impact of CO_2 doubling on the water transports and energetics of extratropical transient eddies. This abstract summarizes results previously reported by Branscome and Gutowski (1992; BG) and extends them with an expanded discussion of Eliassen-Palm (EP) fluxes. We also use the model to examine how changes in atmospheric water vapor amounts might affects the temporal variability of eddy transports.

II. Model and Experiments

Our model is a global, primitive-equations, spectral model whose characteristics have been described in Gutowski et al. (1992) and references therein. We assume that atmospheric, extratropical eddies are governed by baroclinic instability of large-scale flow and that eddy life cycle simulations reveal how eddy dynamics would change under global warmings resulting from a doubling of atmospheric carbon dioxide in GCM simulations. We use the zonal-mean wintertime climates of the NCAR (Washington and Meehl 1984) and GFDL (Manabe and Wetherald 1987) GCMs using current ($1xCO_2$) and doubled ($2xCO_2$) amounts of CO_2 as initial conditions for our experiments.

We perform all experiments with zonal wavenumber 7 and two higher harmonics, 14 and 21. Meridional truncation is the equivalent of rhomboidal 30 for the retained zonal waves. Vertical structure is resolved using 10 sigma layers of equal thickness. We run our model by adding a wave perturbation to the zonal mean temperature field and then performing several 40-day integrations. Due to the short-term nature of our experiments, changes in eddy evolution are caused by changes in the zonal-mean climate only and are isolated from other feedbacks present in complete GCM simulations. Further details of the computations appear in BG.

III. Results of Life Cycle Simulations

The principal changes in the life cycle simulations when CO_2 is doubled are a weakening of maximum eddy kinetic energy (EKE) during the life cycle and a poleward shift in the hydrologic cycle produced by the eddy. Details of these changes appear in BG. We present here some additional discussion of these changes in terms of the EP flux.

Maximum EKE is smaller in the $2xCO_2$ experiments because CO_2 doubling in the GCM simulations produces a weaker mid-latitude, meridional temperature gradient and hence less available potential energy for the growing disturbance. Despite differences in EKE, during the early stage of eddy growth, the eddies in the 1xCO2 and 2xCO2 experiments have a similar structure with a maximum in EKE at 45°N. However, eddies in the $1xCO_2$ experiments spread laterally into the subtropics to a greater extent than eddies in corresponding $2xCO_2$ experiments.

Differences in lateral spreading are exemplified by EP-flux diagrams on the day of peak EKE in experiments using the NCAR climates (Fig. 1). Comparable behavior occurs using the GFDL climates. Compared to the $2xCO_2$ experiment, the $1xCO_2$ simulation has a more clearly defined and stronger zone of EP-flux convergence in the upper, subtropical troposphere. More important for meridional transports, however, is the substantially larger EP flux in the lower, subtropical troposphere, indicated by the stronger convergence/divergence pattern in the $1xCO_2$ simulation. In contrast, the lower atmosphere EP fluxes on the poleward flank of the eddy are more nearly comparable in the two simulations. The weaker intrusion of the eddy into the subtropics during the $2xCO_2$ simulation contributes to an effective poleward shift in eddy transports, since eddy transports in the subtropics become weaker. This behavior appears, for example, in the vertical-average meridional moisture flux (Fig. 2).

Also contributing to the poleward shift in Fig. 2 is the larger amount of atmospheric water vapor in the $2xCO_2$ climates. For both the NCAR and GFDL models, atmospheric water vapor increases by 50 - 100% in mid-latitudes as a consequence of CO_2 doubling, enabling the weaker eddies in the $2xCO_2$ simulation to transport as much or more water vapor in high latitudes as their

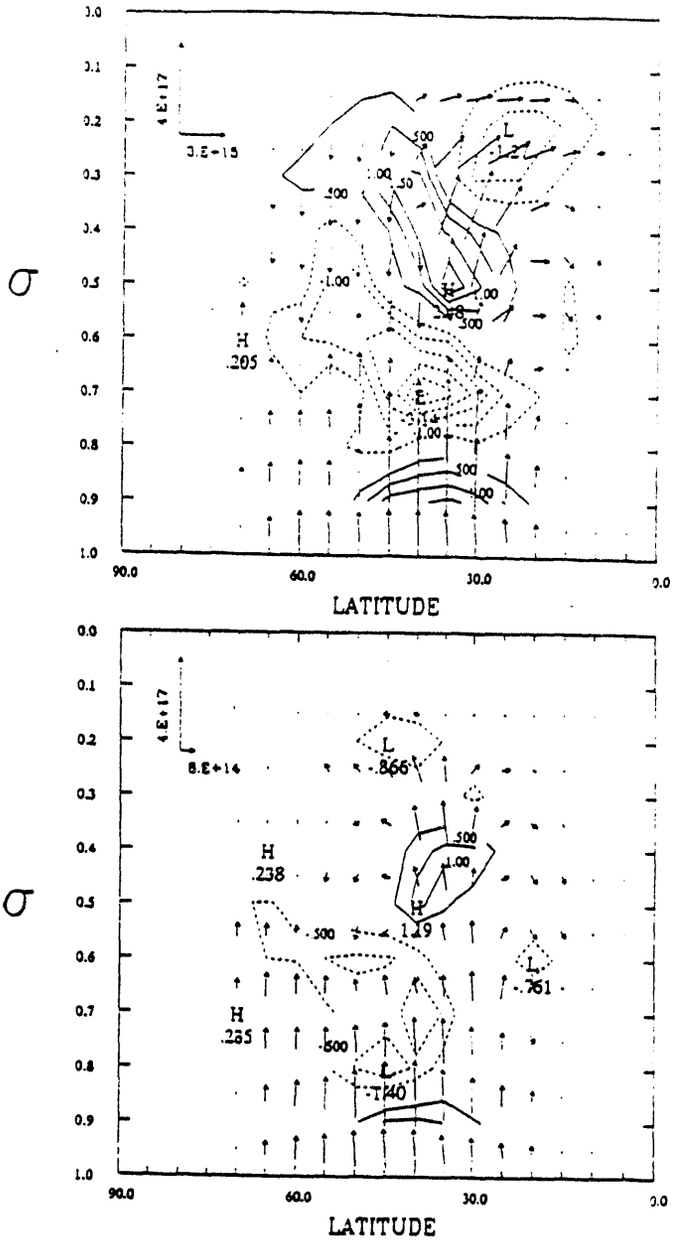

FIG. 1. Eliassen-Palm flux and its divergence on day 20 of eddy life cycle simulations using $1xCO_2$ (top) and $2xCO_2$ (bottom) zonal mean states from the NCAR simulation. Contour interval for divergence is $0.5 \cdot 10^{16} m^3$. Scale for flux components appears in upper left of each figure; units are $m^3 kPa$ for the vertical component and m^3 for the horizontal component.

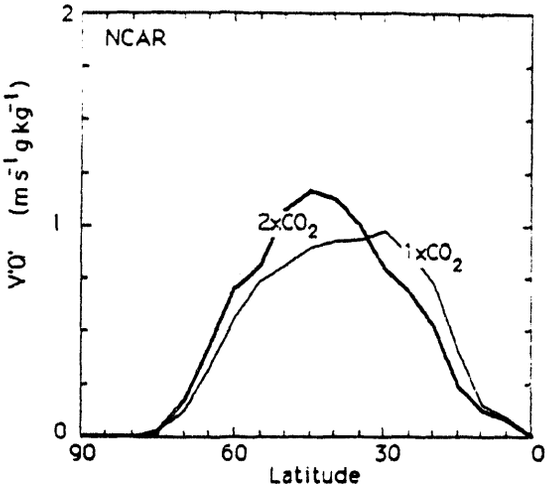

FIG. 2. Vertical and zonal average eddy flux of specific humidity from experiments using NCAR climates as initial conditions. Flux is averaged over the eddy life cycle.

$1xCO_2$ counterparts. An important hydrologic outcome of this shift is that the precipitation produced by the eddy life cycle is also redistributed, decreasing in the subtropics and increasing at higher latitudes. This behavior is consistent with and helps us understand the extratropical precipitation changes produced by the GCM CO_2-doubling simulations.

IV. Eddy Variability and Static Stability Adjustment

The increased specific humidity in mid-latitudes that accompanies simulated global warming should have a marked influence on atmospheric radiative transfer, since water vapor is the primary greenhouse gas in the Earth's atmosphere. In particular, increased atmospheric humidity could inhibit radiative cooling of the lower troposphere. In the present climate, this cooling tends to decrease the lower troposphere's static stability. Counteracting this behavior in mid-latitudes is the tendency by transient eddies to increase lower troposphere static stability (Gutowski 1985; Gutowski et al. 1989). If left unchecked, the eddies would increase the static stability severalfold, markedly reducing the baroclinic instability of the atmosphere and the available potential energy, and ultimately yielding much weaker transient eddies. Radiative cooling is thus an important counterbalance to the eddies' static stability adjustment.

We have made an initial exploration of this interaction using a simplified version of the spectral model described above so that we could easily perform simulations of extratropical eddy dynamics lasting several months. The model in this instance uses six layers in the vertical, with the lowest two having only half the thickness of the upper layers to resolve better static stability changes in the lower atmosphere. Only zonal wavenumbers 0, 7 and 14 were included, with a meridional truncation equivalent to rhomboidal 15. The model had no moisture, but used a dry convective adjustment with a critical lapse rate of 5.8 K/km. The model was forced by a fixed, zonally symmetric surface temperature distribution that matches Northern Hemisphere's observed, zonally-averaged surface temperatures. For each run, a "radiative cooling" of 1 K/day was specified for one of the model's layers, with cooling elsewhere being zero. In addition, surface drag was applied to winds in the lowest layer and scale-dependent diffusion was applied to winds and temperatures in all layers, with specified parameters the same as in Branscome et al. (1989).

Three runs of 200 days were performed: (1) cooling in the model's 400-600 mb layer (mid-troposphere cooling or MTC), (2) cooling in the 200-400 mb layer (upper troposphere cooling or UTC), and (3) no cooling in any layer (NoTC). Cooling in MTC run resembles (crudely) the cooling distribution for the observed atmosphere, whereas cooling in the UTC run may be thought of as resulting from the extreme case of an atmosphere with considerably greater moisture and cloud cover so that radiative emission to space (and hence radiative cooling of the atmosphere) effectively occurs only in the upper troposphere.

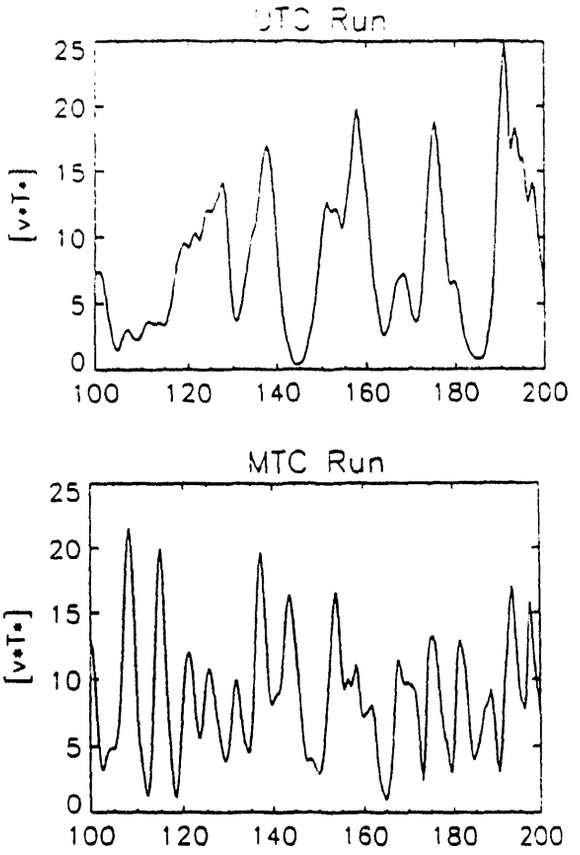

FIG. 3. Vertical average meridional heat flux for days 100-200 in the UTC and MTC runs. All data have been averaged over 37N-57N. Units: °C-m/s.

According to discussion above, the lack of atmospheric cooling in the NoTC run should severely restrict the ability of the model to counteract the increases in mid-latitude static stability by transient eddies. Over the last 100 days of this run, lower troposphere static stability is roughly twice as large as in the other two runs. As a consequence, NoTC eddy amplitudes are an order of magnitude smaller than those in the UTC and MTC runs, even though the surface temperature gradient is the same for each run.

The presence of cooling somewhere in the atmosphere evidently can have a marked effect on eddy amplitudes. The location of the cooling also appears to be important, as can be seen in Fig. 3 which shows time series the vertically averaged meridional eddy heat transport, averaged over 37N-57N, from the last 100 days of the UTC and MTC runs. The eddy fluctuations occur in concert with static stability fluctuations (not shown), with growth of the eddy heat flux tending to occur when static stability is near a minimum. Some variability of near-surface meridional temperature gradient also occurs, but to a much weaker degree. The results suggest a close relationship between N^2 and the strength of baroclinic eddies, for this model configuration.

The most notable feature of Fig. 3 is the slower evolution of eddy heat flux in the UTC run compared to the MTC run. The results suggest that the modulation of radiative emission to space by atmospheric moisture and cloud cover can exert a significant control on eddy amplitudes through static stability changes. The feedback here suggests an internal radiative control of finite amplitude atmospheric eddies that is capable of acting in concert with the solar forcing of near-surface temperature gradients. By means of this radiative cooling feedback, extratropical eddies may be able to throttle themselves through the moisture they transport and the cloud formation they induce.

IV. Summary

The global warming produced by GCMs under a doubling of atmospheric carbon dioxide has a strong impact on interactions between the hydrologic cycle and extratropical transient eddies driven by baroclinic instability. A weakening of subtropical eddy dynamics coupled with increased atmospheric water vapor yields a net poleward shift of the eddy-driven portion of the cycle. In addition, in the higher humidity climate of a warmer Earth, the results here suggest a more sluggish evolution of mid-latitude eddies, with potentially longer episodes of temperature and precipitation extremes as a consequence.

Acknowledgments: This work has been supported by National Science Foundation grants ATM-8815290, ATM-9123552, ATM-9213852 and National Aeronautics and Space Administration grants NAG8-656 and NAGW-2993.

References

Branscome, L. E., and W. J. Gutowski, 1992: The impact of doubled CO2 on the energetics and hydrologic processes of mid-latitude transient eddies. *Climate Dynamics*, 8, 29-37.

Gutowski, W. J., L. E. Branscome and D. Stewart, 1989: Life cycles of baroclinic waves: Mean flow adjustment. *J. Atmos. Sci.*, **46**, 1724-1737.

Gutowski, W. J., 1985: Baroclinic adjustment and mid-latitude temperature profiles. *J.Atmos. Sci.*, **42**, 1733-1745.

Gutowski, W. J., L. E. Branscome and D. Stewart, 1992: Life cycles of moist baroclinic eddies. *J. Atmos. Sci.*, **49**, 306-319.

Manabe, S., and R. Wetherald, 1987: Large-scale changes of soil wetness induced by an increase in atmospheric carbon dioxide. *J. Atmos. Sci.*, **44**, 1211-1235.

Washington W, and G. Meehl, 1984: Seasonal cycle experiment on the climate sensitivity due to the doubling of CO_2 with an atmospheric general circulation model coupled to a simple mixed-layer ocean model. *J. Geophys. Res.*, **89**, 9475-9503.

TRANSIENT AND STATIONARY EDDIES IN DIFFERING GCM CLIMATES

Nicholas M. J. Hall and Paul J. Valdes
Department of Meteorology,
University of Reading,
Reading RG6 2AU, U.K.

Abstract

The response of transients to changing forcing / boundary conditions can be just as striking as the response of mean fields such as surface temperature. Indeed the two are intimately linked and the extent to which the transients are either controlled by, or shape the mean flow is difficult to quantify. Diagnostics are presented from several GCM equilibrium climate simulations using the UGAMP GCM. These include representations of: the present climate; the Last Glacial Maximum and the Jurassic climate (150 M years ago). Changes in the distribution of transient eddy activity are compared with changes in low level baroclinicity to assess the direct response of the storm tracks to local conditions. Budget calculations are also presented to identify the changing roles of different components of the atmospheric circulation in transporting heat and moisture from equator to pole.

1 Introduction

The Earth's climate has seen many dramatic changes. Such changes are often discussed in terms of the mean conditions, particularly temperature and precipitation. However, changes in transient activity are also important in their own right as well as being intimately connected with the mean state. Certain geological indicators of past climate relate to variability (see for example Barron, 1989) and any projection of the future climate and its impact should also include an assessment of the change in variability.

In this contribution we describe numerical simulations of two past climates using the UGAMP (UK Universities' Global Atmospheric Modelling Program) GCM. The analysis focuses on the

response of the northern hemisphere storm tracks to changes in the time mean flow and its associated temperature structure. We restrict our attention to the winter season (December to February) when the signal is strongest. The way in which the different climates equilibrate themselves by transferring energy polewards is also analysed and the changing roles of the mean flow and transients in this process is quantified.

The following section gives an introduction to the model and the analysis procedures used. Three different simulations are then considered: present day; 21 thousand years before present (the last glacial maximum) and 150 million years before present (the Jurassic period), in sections 3 to 5 respectively. For the sake of brevity, discussion of the $2\times CO_2$ work given in the talk is omitted. This is covered in detail by Hall *et al* (1993). A short summary is given in section 6.

2 The Model and Analysis Procedures

The UGAMP GCM is based on the forecast model of the European Centre for Medium Range Weather Forecasting. It is a spectral model, using a triangular truncation at total wavenumber 42 (except for the Jurassic run which is T31) with 19 levels in the vertical, 5 of which are within 150 mb of the surface (*i.e.* in the boundary layer). The physical parameterisations are evaluated on a longitude/latitude grid of 128 x 64 points. The model includes a fairly standard set of parameterisations. The radiation scheme is that of Morcrette (1990), and includes a predictive cloud scheme based on relative humidity criteria (Slingo, 1987). A parameterisation of the effect on the large scale flow of small scale atmospheric gravity waves generated by sub-grid scale orography is also included. This is referred to as gravity wave drag (Palmer *et al.* 1986). The vertical advection uses a total variance diminishing scheme (Thuburn, 1993). This scheme improves the representation of vertical moisture transports, but has the disadvantage of being relatively dissipative. An important modification included in this version of the model is that the convection scheme is based on the work of Betts and Miller (1993) and Slingo and Blackburn (1992). The land surface parameterisation prescribes surface albedo and roughness length, and uses a three layer diffusive soil model to calculate surface temperature and moisture. There is a no-flux boundary condition at the bottom of the soil model (approximately 6m thick). The model sea surface temperatures are prescribed in all cases. A simple sea ice model identical to that in Slingo *et al* (1985) is used to calculate the surface temperature of sea ice. This is a purely thermodynamic model in which heat is stored by and diffused across a slab of ice which is two metres thick.

A useful local measure of the susceptibility of the basic state to baroclinic instability is the growth rate of the fastest growing Eady wave (see Lindzen and Farrell, 1980; Hoskins and Valdes, 1990). This is defined as $\sigma_{BI} = 0.31 f \frac{N}{} \frac{\partial \mathbf{v}}{\partial z}$ where f is the Coriolis parameter, N is the Brunt Vaisalla frequency, z is the upward vertical coordinate and $\mathbf{v}$ is the horizontal wind vector. This quantity is calculated on the 500 mb pressure surface for each climate to provide a link between the mean flow and the transients. It is compared with the transient eddy meridional temperature flux, ($\overline{v'T'}$) at 850 mb and the transient eddy kinetic energy (EKE$= \frac{1}{2}(\overline{u'^2} + \overline{v'^2})$) at 250 mb, where overbar denotes time mean and prime departures therefrom. High pass eddy correlations are obtained using a simple block filter as used by Hoskins *et al* (1989). High pass fields approximate the variations on time scales between one and six days.

The zonal mean energy budget is assessed by way of vertically integrated cross-latitude fluxes of moist static energy, ($= c_pT + \Phi + Lq$, hereafter MSE), which are given by

$$\frac{2\pi a \cos\phi}{g} \overline{\left[\int_{p_s}^{0} v\,(c_pT + \Phi + Lq)\,dp \right]} \qquad (1)$$

where a is the Earth's radius, ϕ latitude, c_p the specific heat capacity of dry air at constant pressure, T temperature, Φ geopotential, L the latent heat of condensation, q the specific humidity, p pressure and square brackets denote zonal mean. The integral is carried out on model levels and moist and dry components, and transient and time mean components are calculated separately as well as the total fluxes.

The analysis is based on 5 years of integration of the model except for the Jurassic which was run for 8 years.

3 Present Day Climate

Figure 1(a) shows the 500 mb Eady growth rate for the simulation of present day climate. The maxima in this quantity delineate the northern hemisphere storm tracks nicely, with peaks at mid-latitudes off the eastern coasts of the major land masses reflecting the land-sea temperature contrasts in these areas. Large values extend out over the oceans and back into the continents. The positions of the mid-latitude jets are also closely related to this quantity as it reflects the vertical shear in the mid-troposphere. It is also a measure of the static stability and this accounts for the long tail of large values back over the Asian continent. One might expect rapid growth and propagation of high frequency disturbances where this quantity is large.

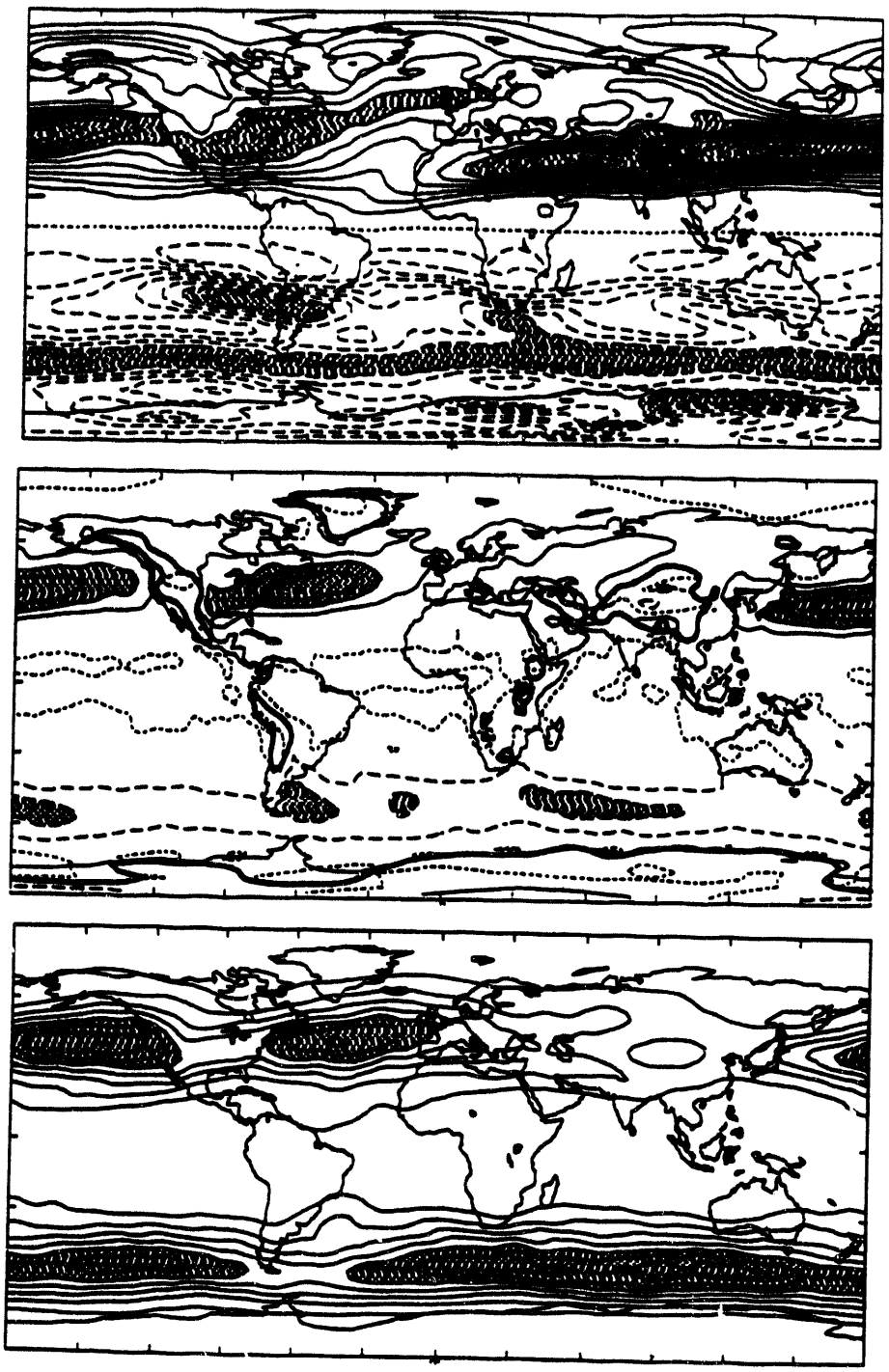

Figure 1: Present day climate. (a) Eady growth rate. Contours every 0.1 days^{-1}, values greater that 0.6 days^{-1} shaded. (b) 850 mb high pass $\overline{v'T'}$. Contours every 5 K ms^{-1}, values greater than 10 K ms^{-1} shaded. (c) 250 mb high pass EKE. Contours every 20 m^{2}s^{-2}, values greater than 100 m^{2}s^{-2} shaded

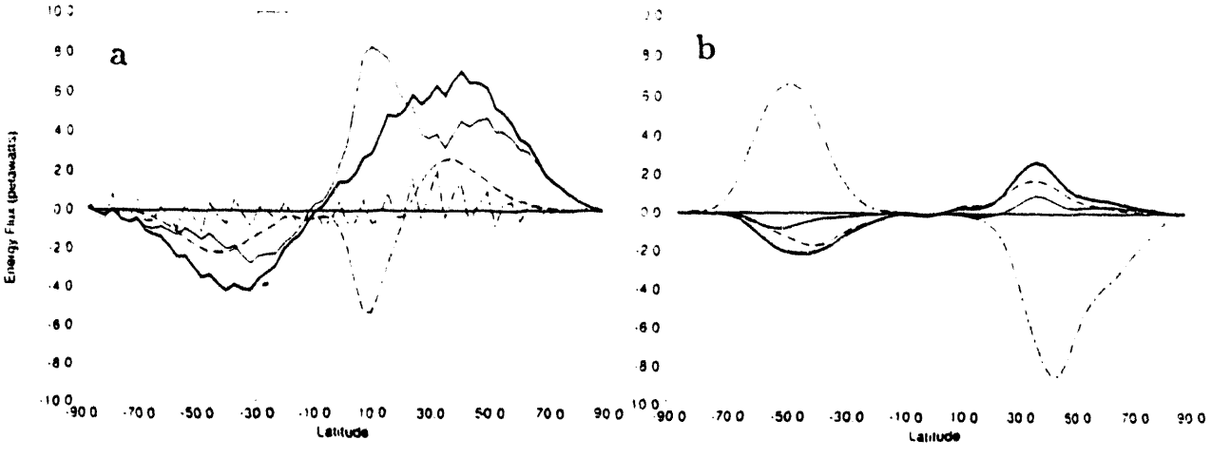

Figure 2: Present day climate. Cross latitude northward energy flux for (a) total and (b) transient component of the flow. The heavy solid line is the flux of MSE. The lighter solid line is the flux of dry static energy while the dashed line shows the flux of latent heat (Lq). The dot-dashed line shows mass flux, for which the ordinates should be re-interpreted as representing units of 10^9 Kg s^{-1}.

Figure 1(b) shows the 850 mb high pass $\overline{v'T'}$, a measure of the intensity of growing baroclinic disturbances. Maxima in this quantity are located fairly well in the positions of maximum growth rate. The maxima in high pass 250 mb EKE, shown in figure 1(c) are somewhat downstream, as may be expected (see Hoskins (1983)). The location and magnitude of these features are in excellent agreement with observational data as given in (Hoskins *et al.* 1989).

Figure 2(a) shows the cross latitudinal flux of MSE in petawatts. There is a maximum in the northern hemisphere of 7 PW, rather more than half of which is due to the flux of dry static energy ($= c_pT + \Phi$, hereafter DSE) and the rest due to moisture flux (Lq). The mass flux is also plotted for comparison as a dot-dashed line. This is simply the vertical integral of v as in equation (1) and reduces to spectral noise in the total flux. The contribution from transients is shown in figure 2(b). It is about 3 PW at 40^0N, of which about two thirds is due to moisture flux. Note that there is a significant equatorward mass flux by the transients which is compensated by a poleward flux of mass by the mean flow. The general form of these fluxes compares well with observations (see Michaud and Derome (1991)) but the total flux in the model is slightly stronger and the transient flux slightly weaker, particularly in the DSE component.

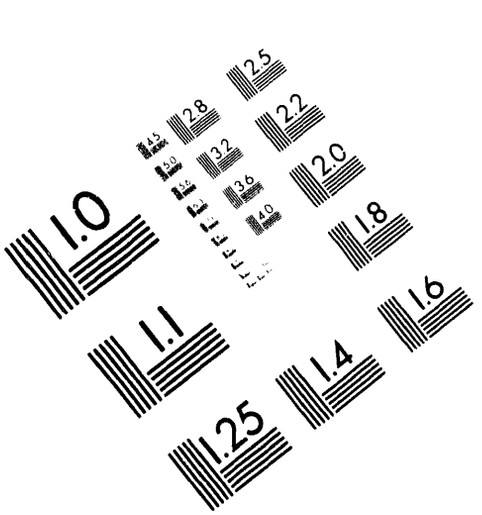

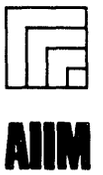

AIIM

Association for Information and Image Management
1100 Wayne Avenue, Suite 1100
Silver Spring, Maryland 20910
301/587-8202

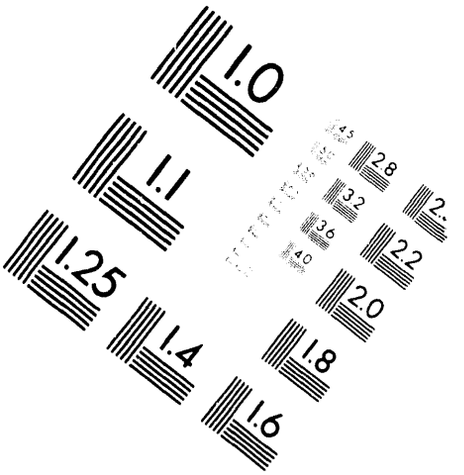

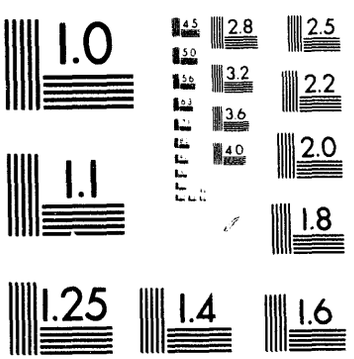

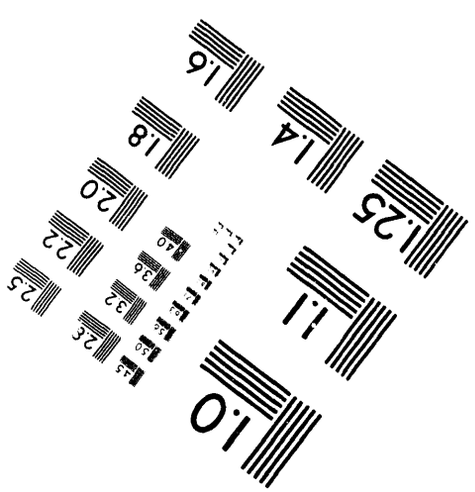

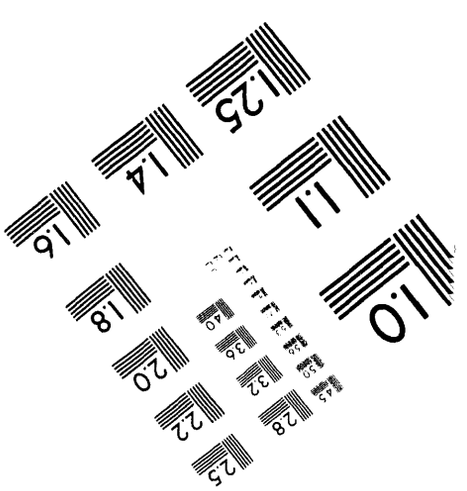

MANUFACTURED TO AIIM STANDARDS
BY APPLIED IMAGE, INC.

2 of 3

4 The Last Glacial Maximum: 21 thousand years before present

The simulation of the last glacial maximum differs from the present day simulation in three ways. Primarily the orography (Figure 3(a)) and the sea surface temperatures (figure 3(b)) have been prescribed according to the CLIMAP boundary conditions (1981), with large (up to 3 km) ice sheets over Canada and Scandinavia, and a greatly increased extent of sea ice. The CO_2 is set at 190 ppm, rather than the 354 ppm used for the present day, and the Earth's orbital parameters have been adjusted appropriate to the period. The impact on the upper level circulation is seen in figure 3(c), which shows the 250 mb stream function. Strong diffluence in the jet is seen in the East Pacific, upstream of the Laurentide ice sheet and the Atlantic jet has been split with stronger westerlies appearing over the baroclinic zone marked by the sea ice edge and a second, weaker jet core in the sub-tropics.

The greatly enhanced baroclinicity at the sea ice edge is revealed by the 500 mb Eady growth rate in figure 4(a) which is much stronger and spreads further to the east, particularly in the North Atlantic. This trend is closely followed by the 850 mb high pass $\overline{v'T'}$ (figure 4(b)): the maximum in low level heat flux in the North Atlantic is now 35.9 K ms^{-1} rather than the present day value of 22.6 K ms^{-1}. The heat flux is slightly weaker in the Pacific storm track but the maximum has been displaced to the eastern side of the ocean basin in both cases. The 250 mb high pass EKE shown in figure 4(c) is also shifted considerably eastwards and is more meridionally confined, although it is actually somewhat weaker than for the present day simulation for both storm tracks.

Figure 5(a) shows the cross-latitude energy fluxes. The most striking feature is a spike of 9 PW at 55^0N, almost entirely due to the flux of DSE by the time mean flow. This is the latitude of the baroclinic zone just north of the Atlantic sea ice edge and thence the Atlantic jet. This feature is not seen at all in the transient energy flux (figure 5(b)), which is actually weaker than in the present day simulation. This result appears to be in conflict with the impression given by figure 4(b), but it must relate to a degree of compensation between the responses of the two northern hemisphere storm tracks. Note, however, that the mass flux is still almost identical in the two cases, so one cannot ascribe the difference in transient energy flux to a change in the average strength of the disturbances. Both moist and dry components of the transient flux are reduced for the last glacial maximum, by roughly the same proportion: the reduction in the moist component is greater than the reduction in the DSE flux. This is consistent with the idea of equally vigourous systems transporting drier air in a cooler climate.

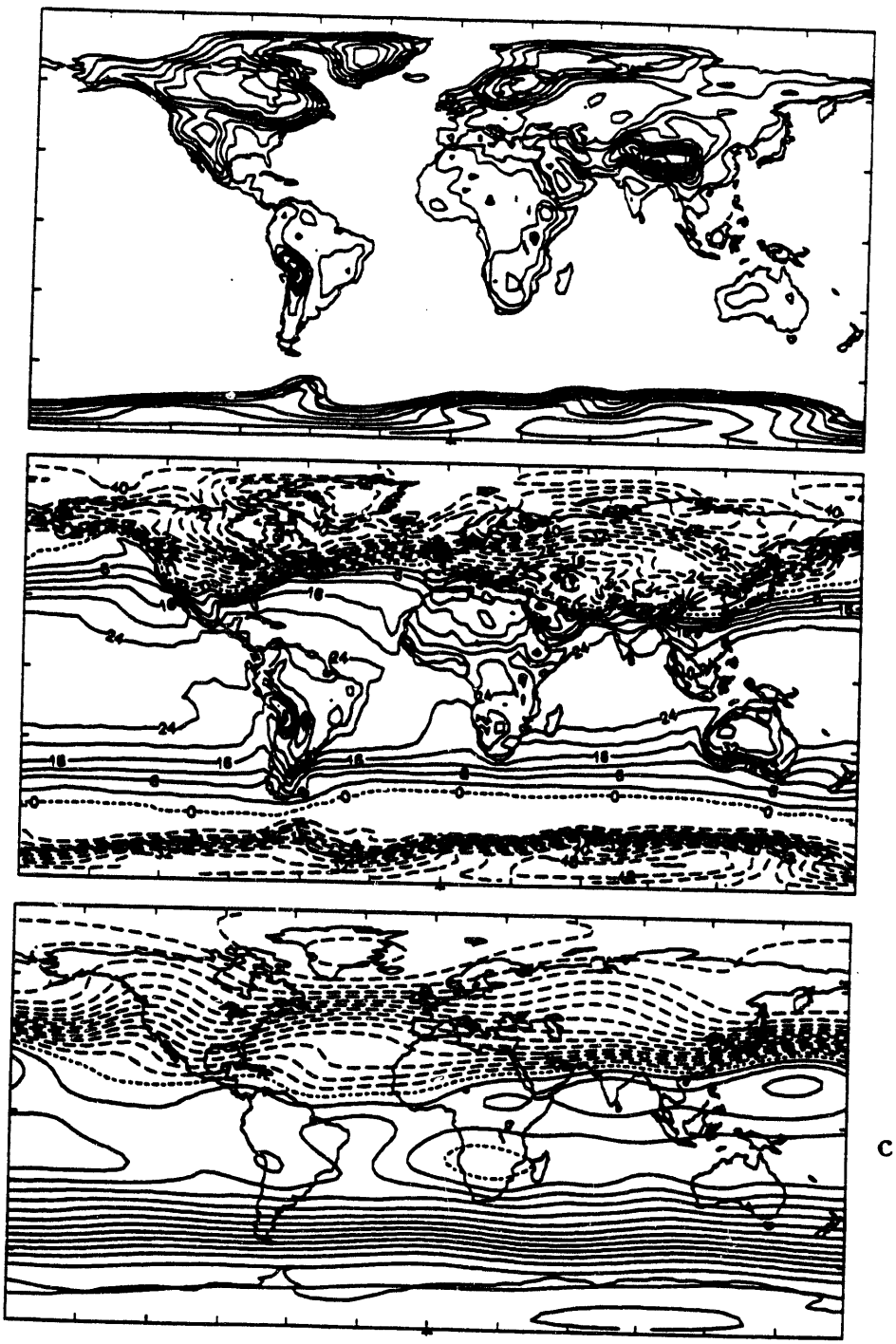

Figure 3: Last glacial maximum. (a) Orography. Contours every 500 m. (b) Surface air temperature. Contours every 4 K. (c) 250 mb stream function. Contours every 10^7 m^2s^{-1}.

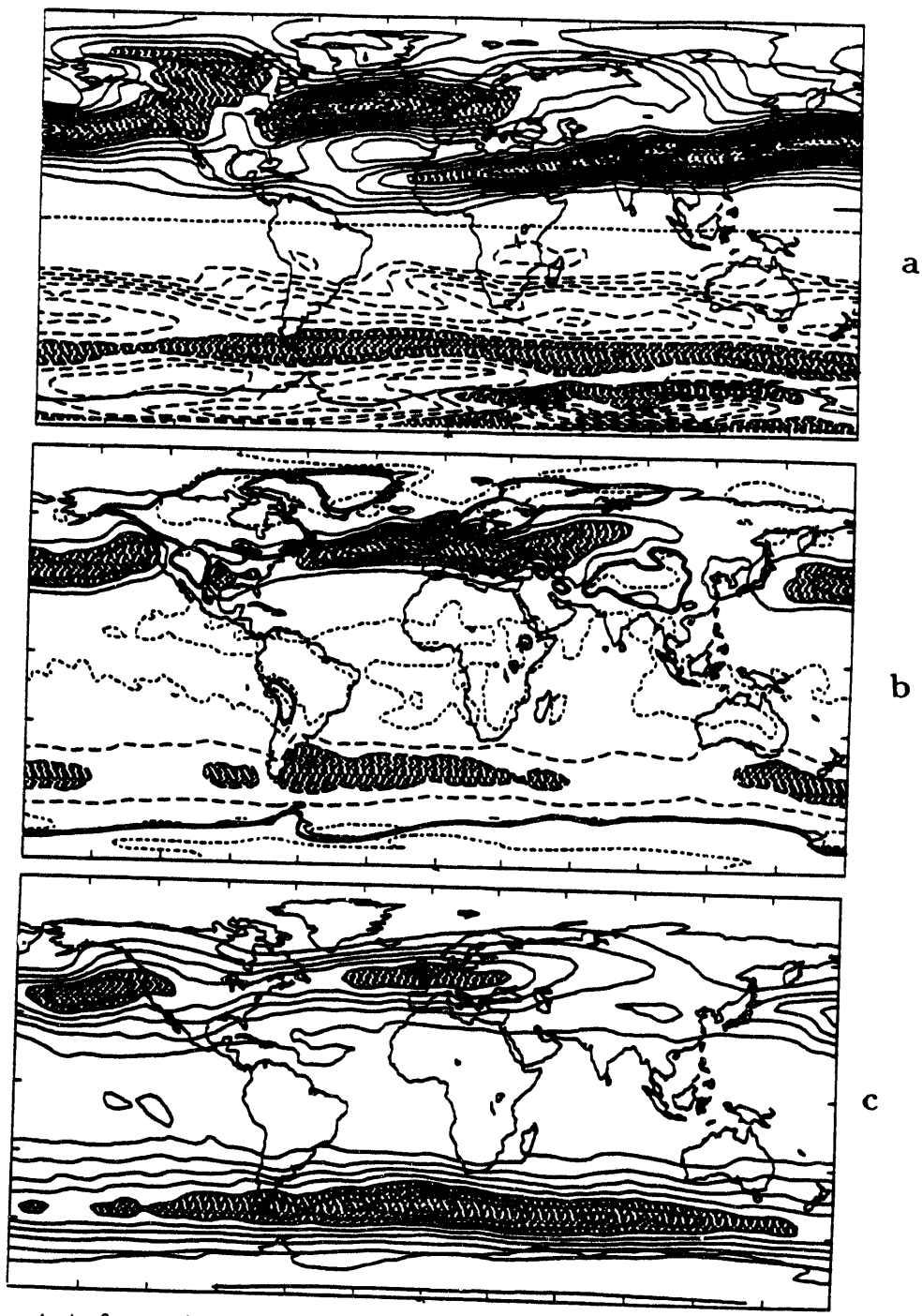

Figure 4: As figure 1 but for the last glacial maximum.

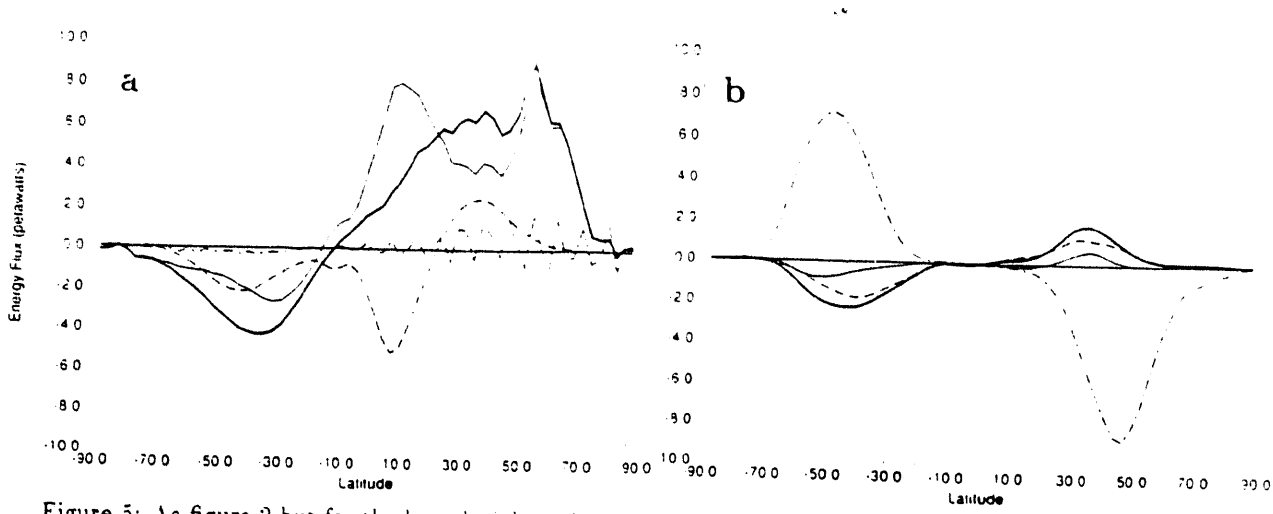

Figure 5: As figure 2 but for the last glacial maximum.

5 The Jurassic Climate: 150 million years before present

In this section we present a simulation of the climate at a time when the continents were in different positions, and the CO_2 was 1120 ppm. Figure 6(a) shows the orography, deduced from the geological data (see Valdes and Sellwood, 1992) and figure 6(b) shows the surface air temperature. The sea surface temperatures are prescribed from a simple cosine-of-latitude assumption, so all departures from zonal symmetry come from the arrangements of the continents. In the northern hemisphere winter, the northern continents cool resulting in a relatively low latitude, zonally orientated baroclinic zone, which is closely delineated by the 500 mb Eady growth rate (figure 7(a)). A second, high latitude baroclinic zone exists in the large western ocean (*Panthalassa*). The characteristic phase speeds of the baroclinic disturbances in this simulation are significantly slower than for the present day simulation. The time filter detailed in section 2 is therefore inappropriate and instead we shall simply present the total transients. The 850 mb total $\overline{v'T'}$ (figure 7(b)) shows clear relation to the pattern of the 500 mb growth rate. The strongest maximum is centred in the paleo Atlantic slightly down stream of the growth rate maximum. There is another maximum on the edge of the sub-zero region of the northernmost (*Eurasian*) continent and a broad region of larger values in the northern Panthalassa Ocean. The 250 mb total EKE (figure 7(c)) also broadly conforms to these patterns, while the magnitudes should obviously not be directly compared with the high pass results.

The most striking feature of the cross latitude energy budget (figure 8) is the massive cancellation of the dry and moist transports in a considerably enhanced meridional circulation of the

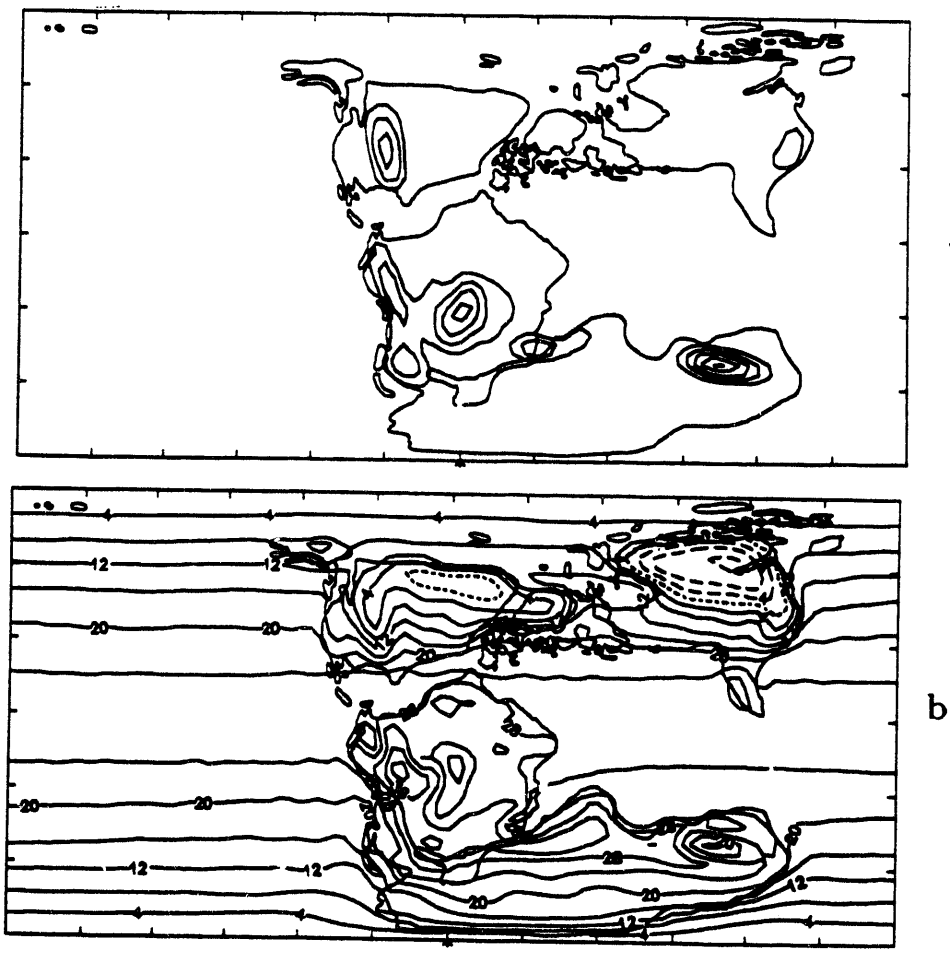

Figure 6: As figure 3 (a) and (b) but for the Jurassic.

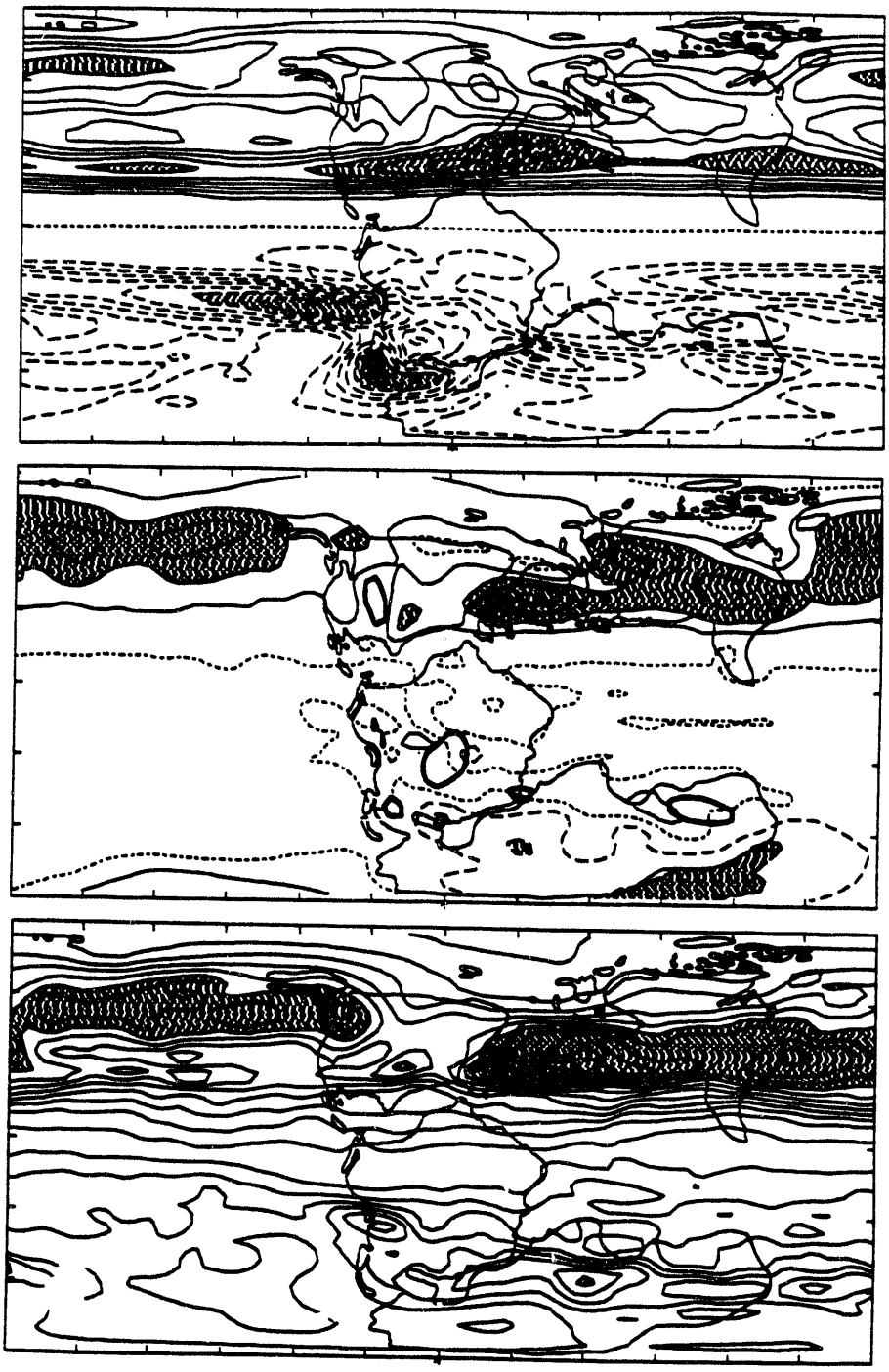

Figure 7: as figures 1 and 4 but for the Jurassic. Also note that in this case eddy correlations are total rather than high pass, and the shading for the EKE is now just for values higher than 160 m^2s^{-2}.

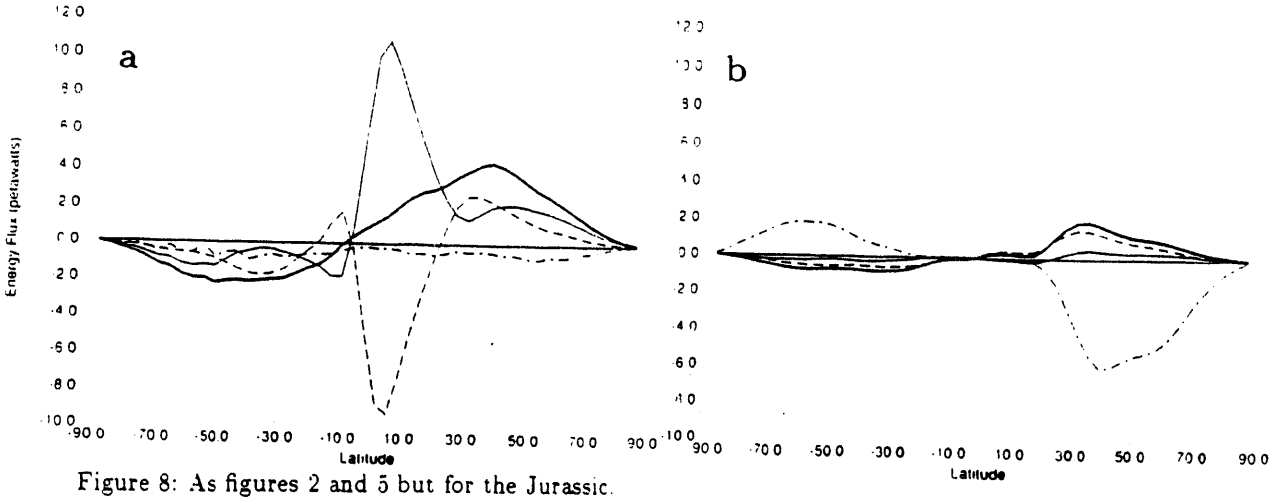

Figure 8: As figures 2 and 5 but for the Jurassic.

winter Hadley cell, which stradles the equator. The southern hemisphere continent (*Gondwanaland*) is very warm in this season, giving rise to an equatorial monsoon circulation which consists of a strong upper level outflow and two counter-rotating anticyclones either side of the equator (see Kutzbach and Gallimore, 1989). The transient energy flux obviously has contributions from distinct storm tracks at very different latitudes and thus displays a much broader signal. It is also interesting to note the increased role of water vapour in the transient flux, consistent with a warmer climate.

6 Summary

Two powerful diagnostic approaches have been used to assess the relationship between the time mean component of climate, and the equally important transient component. The extent to which these processes are really separate can never be fully ascertained simply from diagnostics, but the impression from these results is that the transient component can be reasonably well predicted if one knows the details of the mean circulation: transient activity appears to follow shifts in temperature gradient or vertical shear quite faithfully. Furthermore, the mean flow appears to be quite capable of responding to the changing energy flux requirements brought on by different boundary conditions. This appears to leave the transients 'free' to follow these adjustments of the mean flow. To quantify the role of the transients themselves in shaping this mean circulation in differing climates, past present and future, requires further modelling effort.

References

Barron, B.J., 1989: Severe storms during Earth's history. *Geol. Soc. of America Bulletin* **101**, 601-612.

Betts A.K. and M.J. Miller, 1993: The Betts Miller scheme. Chapter in *The representation of cumulus convection in numerical models of the atmosphere*. (Eds. K.A. Emmanuel and D.J. Raymond), American Meteorological Society.

Hall, N.M.J., B.J. Hoskins, P.J. Valdes and C.A. Senior, 1993: Storm tracks in a high resolution GCM with doubled CO_2. *Quart. J. Roy. Met. Soc.*, accepted

Hoskins, B.J., H.H. Hsu, I.N. James, M. Masutani, P.D. Sardeshmukh and G.H. White, 1989: *Diagnostics of the global atmospheric circulation.* WRCP report 27.

Hoskins, B.J. and P.J. Valdes, 1990: On the existence of storm tracks. *J. Atmos. Sci.* **47**, 1854-1864.

Kutzbach, J.E. and R.G. Gallimore, 1989: Pangaean climates: megamonsoons of the megacontinent. *J. Geophys. Res.* **94**, 3341-3357.

Lindzen, R.S. and B. Farrell, 1980: A simple approximate result for maximum growth rate of baroclinic instabilities. *J. Atmos. Sci.* **37**, 1648-1654.

Michaud, R. and J. Derome, 1991: On the mean meridional transport of energy in the atmosphere and oceans as derived from six years of ECMWF analyses. *Tellus* **43A**, 1-14.

Morcrette, J-J, 1990: Impact of changes to radiative transfer parameterisations plus cloud optical properties in the ECMWF model. *Mon. Wea. Rev.* **118**, 847-873.

Palmer, T.N., G.J. Shutts and R. Swinbank, 1986: Alleviation of a systematic westerly bias in general circulation and numerical weather prediction models through an orographic gravity wave parameterisation. *Quart. J. Roy. Met. Soc.* **112**, 1001-1040.

Slingo, J.M., 1987: The development and verification of a cloud prediction scheme for the ECMWF model. *Quart. J. Roy. Met. Soc.* **113**, 899-927.

Slingo, J.M. *et al.* 1992: Mean climate and transience in the tropics of the UGAMP GCM. Part 1: Sensitivity to convective paramaterisation. *Quart. J. Roy. Met. Soc.* Submitted.

Thuburn, J., 1993: Use of a flux limited scheme for vertical advection in a GCM. *Quart. J. Roy. Met. Soc.* In press.

Valdes, P.J. and B.W. Sellwood, 1992: A palaeoclimate model for the Kimmeridgian. *Palaeogeography, Palaeoclimatology, Palaeoecology* **95**, 47-72.

Transient eddies and low frequency variability in the Northern Hemisphere winter climates of two GCMs

by

Tony Hansen
Center for Atmospheric and Space Sciences
Augsburg College
Minneapolis, MN 55454

and

Alfonso Sutera
Dipartimento di Matematica e Fisica
Universita di Camerino
Camerino, Italy

1. Introduction

An aspect of the climate change problem that is also important to our understanding of the general circulation is the relative roles and interactions between baroclinic-scale transient eddies and the larger scale, lower frequency variability of the flow in midlatitudes. A question may be raised as to how a reduced (or enhanced) level of high-frequency transient eddy activity may influence the character of the large-scale flow. If the transient eddies play an important role in determining the large-scale flow patterns in the atmosphere, then we might expect a profound impact from a changed level of high frequency transient eddy activity on the large-scale flow. For example, in a recent paper, Held (1993) discusses possible influences of atmospheric dynamics in a changing climate including possible consequences to transient eddies and their subsequent feedback on the circulation.

An opportunity to address this question is presented by the intercomparison of two general circulation models, the differences in whose formulations lie primarily in their physical parameterizations. We will compare Northern Hemisphere (NH) conditions for perpetual January simulations each 1200 days long of two versions of the NCAR Community Climate Model, designated CCM0 and CCM1. Both models are run at R15 resolution with identical fixed boundary conditions. CCM1 was designed to be warmer than CCM0 in the winter hemisphere in order to overcome CCM0's systematically too cold winter polar latitudes. We focus on the dynamical implications of the warmer versus colder climates of the models and attempt, as a consequence, to provide some insight into possible sources of the well known deficiencies in the grid point height variance of CCM1. We find that a large portion of this climatic error in CCM1 appears to be connected to the generally weaker level of baroclinic instability in that model.

It is well known that CCM1 exhibits weaker 500 mb grid point height variance compared to observations or compared to CCM0, particularly in storm track regions and over the eastern midlatitude oceans. The latter are regions which could be characterized as the ends of the storm tracks over the respective midlatitude oceans, and which in observations are regions of persistent anomalies like blocking. These regions of weaker variance are 20% to 25% lower over the North Pacific and 25% to 35% lower over the Atlantic in CCM1 compared to CCM0. The question arises as to why there should be such a difference between the models, and specifically whether there is a scale dependence to the differences in the variance.

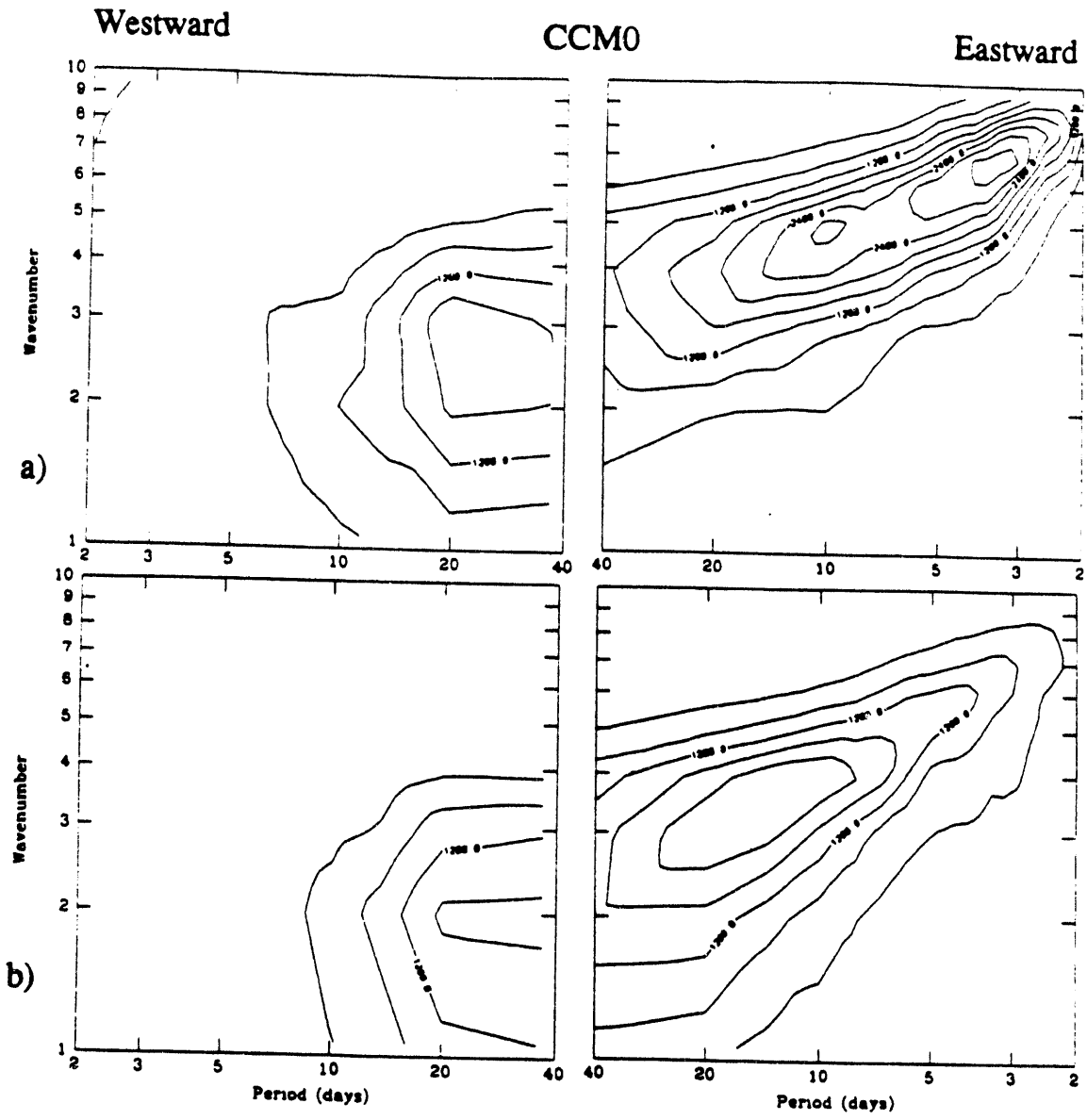

Figure 1. Power spectral density of the westward and eastward propagating variance for CCM0 perpetual January 500 mb geopotential height averaged for a) the 42°N-56°N midlatitude zone and b) the 56°N-69°N high latitude zone. Units are m^2 and the contour interval in this and subsequent spectral figures is 400 m^2.

2. Spectral Analysis

We use a spectral analysis technique developed by Hayashi (1982) to compare the spectral distribution and partitioning of the variance in the two models in order to clarify the differences in their variance climatologies. Spectra are presented for NH January conditions within 2 latitude zones, a middle latitude zone (42°N-56°N), and a high latitude zone (56°N-69°N) for perpetual January simulations of the two models. The variance spectra are presented as eastward traveling, westward traveling and standing variance.

2.1 Traveling variance

The eastward and westward traveling variance for CCM0 and CCM1 in the two chosen latitude zones are presented in Figs. 1 and 2 respectively. In middle latitudes, the intermediate-scale eastward traveling variance in CCM0 increases dramatically from subtropical

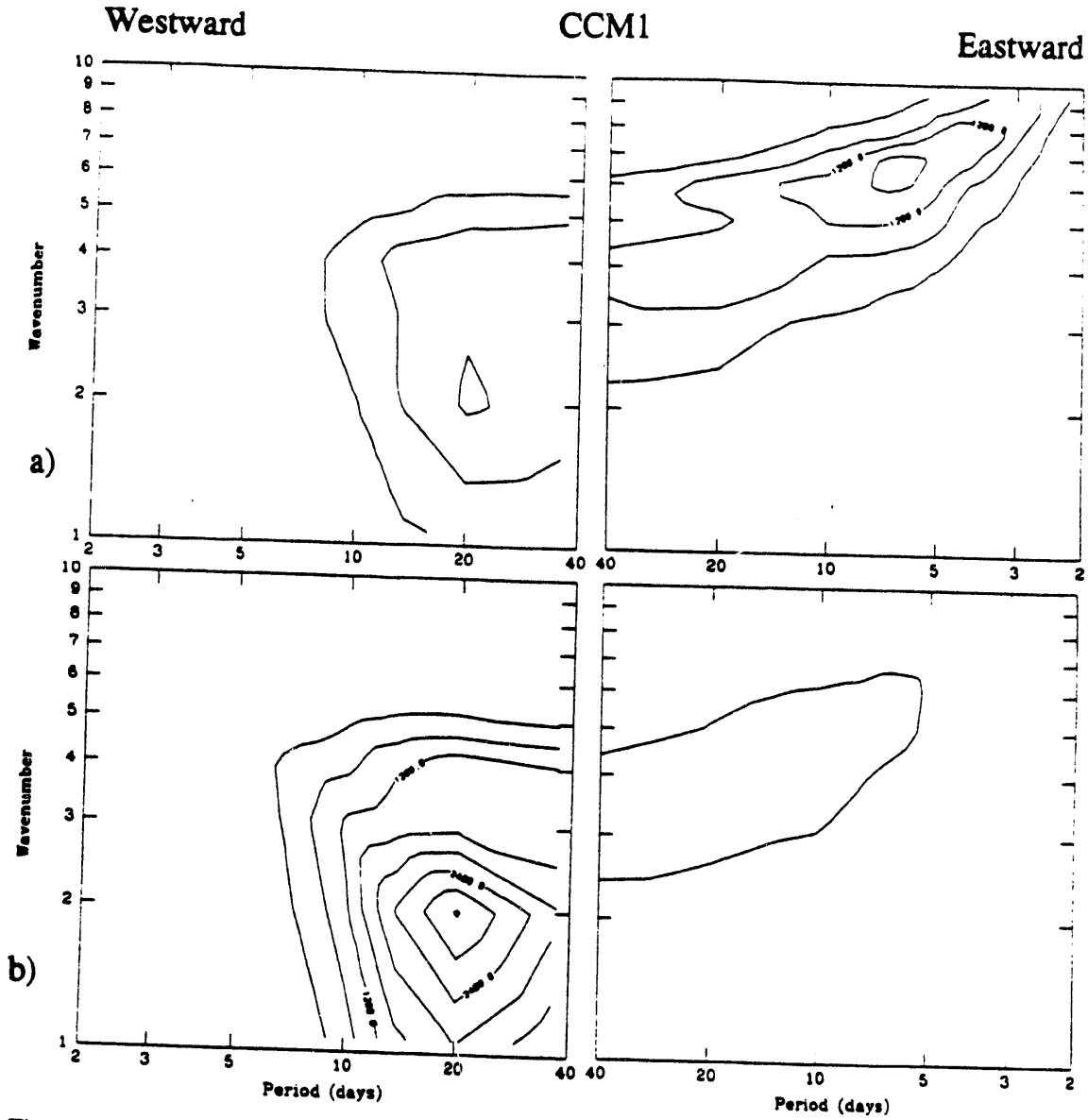

Figure 2. As in Figure 1 except the power spectral density of the westward and eastward propagating variance for CCM1 perpetual January 500 mb geopotential height averaged for a) the 42°N-56°N midlatitude zone and b) the 56°N-69°N high latitude zone.

values (not shown) and in particular, achieves peak values over a factor of 2 greater than CCM1. The deficiency in CCM1's variance compared to CCM0 is particularly striking at shorter periods. At higher latitudes this trend continues has CCM0 continues to have strong variance with the peak values moving toward lower frequencies and lower wavenumbers. On the other hand, the eastward traveling variance at high latitudes in CCM1 is negligibly small.

This same characteristic is not found in the westward traveling variance. In middle latitudes, CCM0 has greater westward traveling power than CCM1 but the contrast is smaller compared to that for the eastward variance. Conversely, CCM1 has far greater power than CCM0 at high latitudes by a factor of 2 with the largest value at wavenumber 2, 20 day period. Thus, at high latitudes, CCM1 is dominated by westward traveling variance with virtually no eastward variance.

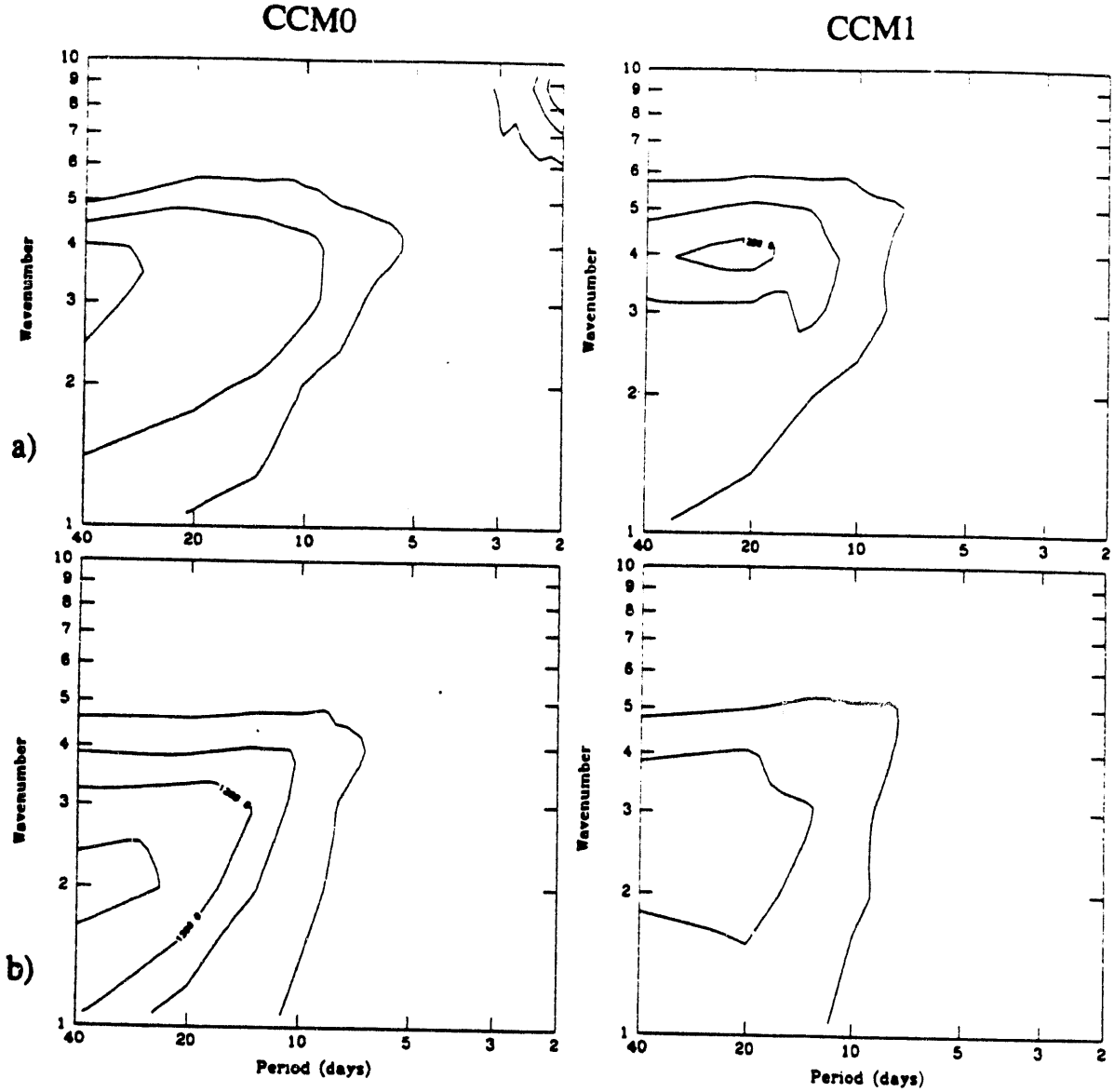

Figure 3. As in Figure 1 except the power spectral density of the standing variance for CCM0 and CCM1 perpetual January 500 mb geopotential height averaged for a) the 42°N-56°N midlatitude zone and b) the 56°N-69°N high latitude zone.

With the much weaker eastward traveling, high-frequency, baroclinic-scale variance in CCM1 compared to CCM0, it is interesting to examine the differences in the storm tracks between the two models. In fact, CCM1 has weaker and less extensive storm tracks over both NH midlatitude oceans in terms of high pass filtered grid point height variance (not shown). Further, there is a close correspondence between the differing levels of high pass filtered eddy rms height and the local 850 mb meridional temperature gradient. This suggests that weaker baroclinic instability leads to the weaker high-frequency transient eddies. The lower level of baroclinic instability in CCM1 compared to CCM0 is also reflected in the zonal mean meridional temperature gradients and in the vertical shear of the zonal mean wind.

2.2 Standing variance

For the standing component of the variance (Fig. 3), the models exhibit comparable values in the middle latitude zone. Averaged

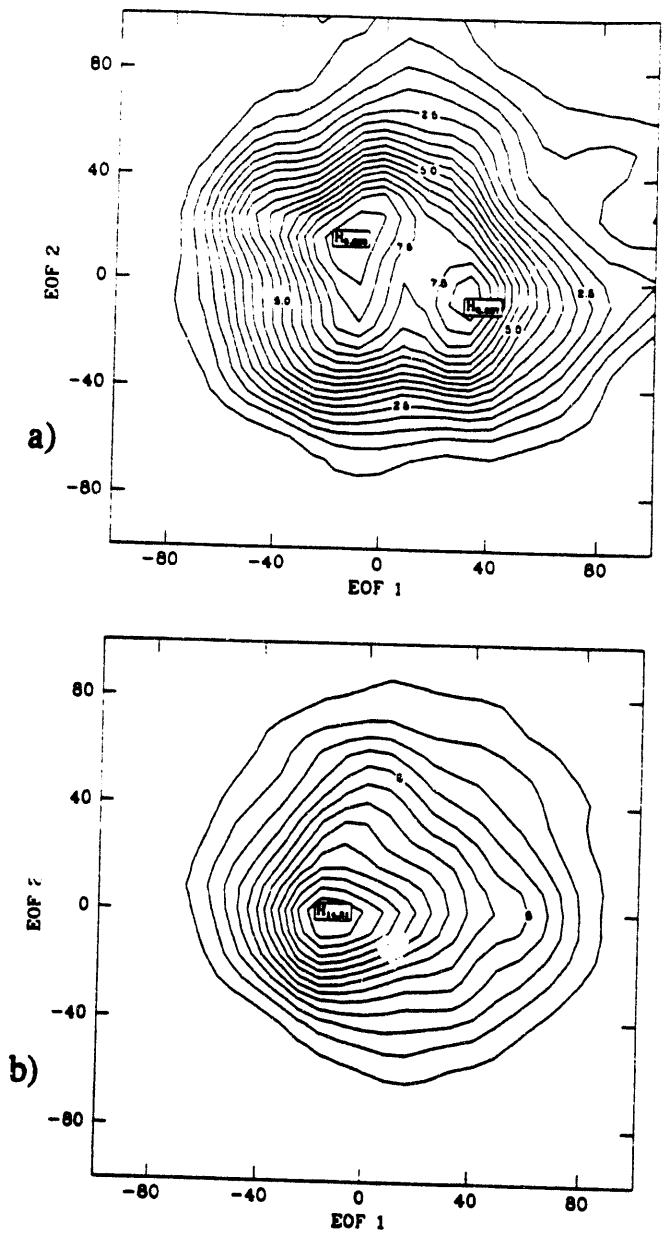

Figure 4. Probability density distribution of a) CCM0 and b) CCM1 estimated with a smoothed two dimensional histogram in the subspace of the first two EOFs of the respective models. Contour units are arbitrary. See Hansen and Sutera (1992) for computational details.

over the entire wavenumber-frequency space, CCM0 has slightly stronger standing variance in the midlatitude zone. At higher latitudes, CCM1 experiences diminished standing power, while CCM0 has a greater standing power at high compared to middle latitudes and twice as strong as CCM1. To a certain extent, the standing variance comparison of the models mimics the eastward variance results.

To further exemplify the weaker standing variance in CCM1, let us consider a simple EOF analysis of both models. In an earlier study, Hansen and Sutera (1992) showed that a bimodal structure exists in the subspace of

CCM0 defined by the leading two eigenvectors of the CCM0 500 mb eddy height covariance matrix. Since a real EOF analysis such as theirs seeks to represent the variance as a linear combination of standing modes, the structure in the phase space of the leading eigenvectors implies a strong standing fluctuation in the model with certain preferred configurations. Given the weaker standing variance at higher latitudes diagnosed in the power spectral analysis of CCM1, it is interesting to perform a similar EOF analysis with the CCM1 January dataset. As shown in Fig. 4, CCM0 exhibits a bimodal structure while CCM1 is strikingly unimodal. [The CCM1 eigenvectors are different than the CCM0 eigenvectors but the some result is obtained if the CCM1 height grids are projected onto the CCM0 eigenvectors.] The more homogeneous structure in CCM1's phase space as defined by the leading EOFs is consistent with the weaker standing variance and absence of large-scale flow regimes noted in CCM1 SH simulations by Hansen et al. (1991).

3. Summary and Discussion

The Northern Hemisphere climates from perpetual January simulations of two GCMs were compared. One model (CCM1) may be characterized, in a gross sense, as warmer than the other (CCM0).

The warmer model (CCM1) exhibits a much lower level of eastward propagating variance at periods shorter than 10 days in middle and particularly higher latitudes compared to CCM0. In grid point space, this is manifest as weaker and less extensive storm tracks defined from local measures of high frequency height variance. CCM1 also has a lower level of standing variance at middle and particularly higher latitudes than does CCM0. In this respect, the character of the standing variance is similar to the high frequency, baroclinic-scale traveling variance. A simple EOF analysis suggests that CCM1 does not exhibit the large-scale flow regimes in NH January that are found in CCM0.

Numerous studies have explored the interactions between transient eddies and standing or quasi-stationary wave activity in extratropical latitudes. Therefore, it is interesting to speculate that the relative weakness in the CCM1 standing variance might be linked to the relative weakness in the baroclinic waves, which in turn results from weaker baroclinic instability in CCM1. A sufficient level of baroclinic eddy activity may be needed to induce the flow regimes. This speculation is consistent theories which imply a strong interaction between baroclinic eddy activity and large-scale flow regimes (e.g., Reinhold et al., 1993; Pandolfo and Sutera, 1993).

The well known weak level of grid point height variance in CCM1 may now be linked to both too weak eastward traveling baroclinic-scale transient eddies and too weak standing variance. The former appears to be dynamically linked to the baroclinic instability in the model. Whether a causal connection can be established between this aspect and the dynamics of the planetary-scale flow is the subject of ongoing research.

4. References

Hansen, A. R., A. Sutera, and J. J. Tribbia, 1991: The relation of multiple flow regimes to the climatic error in general circulation models: Southern Hemisphere winter. J. Atmos. Sci., 48, 1329-1335.

Hansen, A. R., A. Sutera, 1992: Structure in the phase space of a general circulation model deduced from empirical orthogonal functions. J. Atmos. Sci., 49, 320-326.

Hayashi, Y., 1982: Space-time spectral analysis and its applications to atmospheric waves. J. Meteor. Soc. Japan, 60, 156-171.

Held, I., 1993: Large-scale dynamics and global warming. Bull. Amer. Meteor. Soc., 74, 228-241.

Pandolfo, L. and A. Sutera, 1993: In preparation.

Reinhold, B. and S. Yang, 1993: The role of transients in weather regimes and transitions. J. Atmos. Sci., 50, 1173-1180.

STOCHASTIC EXCITATION OF LOW FREQUENCY VARIABILITY IN THE MIDLATITUDE ATMOSPHERE

Petros J. Ioannou
Center for Meteorology and Physical Oceanography
Massachusetts Institute of Technology
Cambridge, MA 02139

Brian F. Farrell
Department of Earth and Planetary Sciences
Harvard University
Cambridge, MA 02138

1. INTRODUCTION

Spectral analysis of the transient geopotential variance of the midlatitude atmosphere reveals a sharp peak in the wavenumber-period spectra concentrated at large scales (zonal wave numbers $m < 6$) and low-frequencies (periods $T > 10$ days (Blackmon, 1976; Hayashi and Golder, 1977; Fraedrich and Bottger, 1978; Schafer, 1979; Hansen *et al.*, 1989)). This is surprising because conventional baroclinic instability calculations (Gall *et al.*, 1979), predict a broad maximum of the variance at synoptic scale ($8 < m < 12$) with associated period of a few days.

The structure of the dominant waves responsible for this low frequency variability is most clearly discerned through analysis of the zonal wavenumber 5 eastward propagating wave with a period of approximately 10 days which is persistently present in the southern hemisphere during summer (Salby, 1982; Schoeberl and Krueger, 1983; Randel and Stanford, 1985). Observation of these waves reveal a regular eastward phase progression with amplitude fluctuating episodically over time spans of approximately 2 days (Salby, 1982; Randel and Stanford, 1985). Energetic analysis confirms active baroclinic conversions during these periods (Randel and Stanford, 1985). Consequently, a theory accounting for these sharp peaks in the power spectrum and the wavelike eastward phase progression must also account for the rapidity of growth and the episodic nature of the amplitude time series.

Egger and Shilling (1983) proposed that the observed variance at low frequencies and large scales is the response of the atmosphere at these large scales to stochastic forcing at smaller scales. In their study they employed an equivalent barotropic model of the atmosphere with a constant zonal flow. Such a flow possesses a countable infinity of modes with an accumulation point at zero doppler shifted frequency (Kasahara, 1980). To obtain the observed response at large scales Egger and Schilling (1983) also assumed the forcing spectrum to be spatially red. The behavior of this dynamical system is determined by the fact that it is governed by a normal dynamical operator. In such a normal system the magnitude of the response of each normal mode is inversely proportional to its rate of dissipation, and the dominant spectral component is the least damped mode, when weighting by the spectral power of the forcing at each modal frequency is allowed for.

The theory of stochastic dynamics as it applies to the atmosphere has recently been developed taking into account the pivotal non-normality of the underlying dynamics (Farrell and Ioannou, 1993a, FIa). The maintained variance in this non-normal system is not determined by a balance between the energy input by stochastic forcing and the energy lost to dissipation, as is the case in familiar normal systems, but rather the primary balance is between dissipation and energy transferred from the mean flow by the perturbations with the energy input by the stochastic forcing playing a relatively minor role. This additional source of energy from the mean to the perturbation field leads to greatly increased variance over what would have been anticipated from the modal dissipation alone. It was found using these methods that background forcing at a level of 0.1 Wm^{-2} is capable of maintaining the observed transient energy of the midlatitude atmosphere and of producing the observed transient heat flux (Farrell and Ioannou, 1993b, FIb).

In this work we first review the method for calculating the maintained variance and associated fluxes and then discuss some results pertaining to the interpretation of the EOF's which arise from the stochastic dynamics of non-normal dynamical systems. Next, we will present results from the stochastic excitation of a baroclinic midlatitude jet with realistic zonal velocity and static stability. The stochastic forcing will be taken white in order to facilitate investigation of the spectral properties of the variance as determined by the non-normal dynamics.

2. STOCHASTIC DYNAMICS OF BAROCLINIC WAVES

a. Formulation of the stochastic equations and their solution

Consider stochastic excitation of perturbations on a zonal baroclinic flow. Harmonic geopotential height perturbations with zonal wavenumber k and meridional wavenumber l in a β - plane channel obey the linearized quasi-geostrophic potential vorticity equation:

$$\frac{d\phi}{dt} = \mathbf{B}\,\phi \ , \qquad (1)$$

where

$$\mathbf{B} = \frac{e^{z/2}}{\sqrt{\varepsilon}} \left[\Delta^{-1}\,(-ikU - R)\,\Delta - ik\,\Delta^{-1}\,Q_y\right] \frac{\sqrt{\varepsilon}}{e^{z/2}} \qquad (2)$$

with

$$\Delta \equiv \frac{d^2}{dz^2} - \left[\frac{\alpha^2}{\varepsilon} + S^2 - \frac{dS}{dz}\right] . \qquad (3)$$

Here U is the mean zonal wind, ε the square ratio of the Coriolis parameter to the Brunt-Vaisala frequency, α the total wavenumber, and R a linear potential vorticity damping coefficient. The mean potential vorticity gradient is given by

$$Q_y = \frac{\beta}{\varepsilon} + 2S\frac{dU}{dz} - \frac{d^2U}{dz^2} \ , \qquad (4)$$

and the stability parameter is defined as

$$S \equiv -\frac{1}{2}\left[\frac{1}{\varepsilon}\frac{d\varepsilon}{dz} - 1\right] . \qquad (5)$$

The operator Δ^{-1} is rendered unique by incorporation of the usual boundary conditions at the ground arising from the vertical velocity arising from Ekman pumping associated with a coefficient of vertical diffusion ν. The boundary condition at the top of the atmosphere is taken to be vanishing vertical velocity at 4 scaleheights. A realistic stratification and zonal wind distribution is included (see FIa for details).

Using the finite difference approximation of (1) we reduce the continuous dynamical system to a finite dynamical system.

As a perturbation measure we take the energy density

$$E^t = \phi^+ \mathbf{M}\,\phi \qquad (6)$$

in which ϕ^+ is the hermitian transpose of ϕ and the energy metric is given for a grid of width δ by:

$$\mathbf{M} = -\frac{\delta}{8}\left(\mathbf{E}\mathbf{T}^2\mathbf{E} - \alpha^2\mathbf{P}\right) , \qquad (7)$$

with $\mathbf{T}$ the discretized d/dz operator, $\mathbf{P}_{ij} \equiv \rho_i\,\delta_{ij}$, $\mathbf{E}_{ij} \equiv \sqrt{\rho_i\,\varepsilon_i}\,\delta_{ij}$, and ρ_i the mean density at the i-th grid.

We transform (1) into generalized velocity variables $u = \mathbf{M}^{\frac{1}{2}}\phi$. In these generalized velocity variables the stochastically forced perturbation potential vorticity equation takes the form:

$$\frac{du_i}{dt} = \mathbf{A}_{ij}\,u_j + \mathbf{F}_{ij}\,\xi_j \ , \qquad (8)$$

where $\mathbf{A} = \mathbf{M}^{\frac{1}{2}}\,\mathbf{B}\,\mathbf{M}^{-\frac{1}{2}}$ and ξ is the random forcing assumed to be a δ-correlated Gaussian white-noise process with zero mean, and with variance:

$$\langle \xi_i(t)\,\xi_j^*(t')\rangle = \delta_{ij}\,\delta(t-t') \ , \qquad (9)$$

where $\langle\cdot\rangle$ denotes the ensemble average. Note that the stochastic forcing excites independently and with equal unit magnitude each spatial forcing distribution as specified by the columns $f^{(j)}$ of the matrix $\mathbf{F}_{ij}$. We want to determine the evolution of the variance sustained by (8), which in physical variables is the ensemble averaged energy density $\langle E^t\rangle = \langle u_i^*(t)\,u_i(t)\rangle$, and its limit $\langle E^\infty\rangle = \lim_{t\to\infty}\langle u_i^*(t)\,u_i(t)\rangle$ when this limit exists.

Note that the operator $\mathbf{A}$ is in general non-normal i.e. $\mathbf{A}^+\mathbf{A} \neq \mathbf{A}\,\mathbf{A}^+$ ($^+$ denotes the hermitian transpose) so that the eigenvectors of $\mathbf{A}$ are not necessarily orthogonal and transient growth that is not associated with modal instability is possible. If $\mathbf{A}$ were normal, as is the case in the absence of basic state shear, transformation into normal coordinates leads to the result that the total variance is the sum of the variance arising independently in each of the normal coordinates forced independently (Wang and Uhlenbeck, 1945). Due to energy exchange with the mean, non-normal dynamical systems do not allow such a straightforward characterization, and a generalized calculus for determining the evolution of the ensemble average variance for non-normal systems has only recently been developed (Farrell and Ioannou, 1992 (FIa)).

The random response, u, is linearly dependent on ξ and consequently is also Gaussian distributed. Therefore the statististics of the response of the dynamical system are fully characterized by the first two moments. The first moment vanishes for large times if $\mathbf{A}$ is asymptotically stable. The expression for the second moment, the ensemble average energy density, can be reduced to:

$$\langle E^t\rangle = \langle u(t)_i^*\,u(t)_i\rangle = \mathrm{Trace}(\mathbf{F}^*\,\mathbf{K}^t\,\mathbf{F}) \ , \qquad (10)$$

where

$$\mathbf{K}^t \equiv \int_0^t e^{\mathbf{A}^+(t-s)}\,e^{\mathbf{A}(t-s)}\,ds \ . \qquad (11)$$

When $\mathbf{A}$ is asymptotically stable it can be shown (see to FIa) that

$$\mathbf{K}^t = \mathbf{K}^\infty - e^{\mathbf{A}^+ t}\,\mathbf{K}^\infty\,e^{\mathbf{A}t} \ , \qquad (12)$$

and that the asymptotic value can be determined by solving the Liapunov equation:

$$\mathbf{A}^+ \mathbf{K}^\infty + \mathbf{K}^\infty \mathbf{A} = -\mathbf{I} \quad . \qquad (13)$$

Note that when **A** is not asymptotically stable $\mathbf{B}^\infty$ diverges, according to the linear dynamics, but that the time development of variance can still be obtained by direct numerical integration of a time dependent version of the Liapunov equation (see Fla). Note also that with an orthogonal set of forcing functions such that $\mathbf{F}\ \mathbf{F}^+ = \mathbf{I}$, the expression for the energy density simplifies to $\langle E^t \rangle$ = Trace ($\mathbf{K}^t$) and the variance is independent of the specific forcing distribution.

It is also useful to determine the ensemble average correlation matrix of the response $C^t_{ij} = \langle u(t)_i\ u(t)_j^* \rangle$. It can be shown that the correlation matrix for unitary forcing takes the form:

$$\mathbf{C}^t = \int_0^t e^{\mathbf{A}(t-s)}\ e^{\mathbf{A}^+(t-s)}\ ds \quad , \qquad (14)$$

which satisfies

$$\mathbf{C}^t = \mathbf{C}^\infty - e^{\mathbf{A}t}\ \mathbf{C}^\infty\ e^{\mathbf{A}^+ t} \quad , \qquad (15)$$

and that the asymptotic correlation matrix is determined by solving the Liapunov equation:

$$\mathbf{A}\ \mathbf{C}^\infty + \mathbf{C}^\infty\ \mathbf{A}^+ = -\mathbf{I} \quad . \qquad (16)$$

which differs from (13) when **A** is non-normal.

b. Dynamical interpretation of the EOF's and determination of the optimal stochastic forcings

We showed in the previous section that the ensemble average energy density for a full rank unitary forcing distribution can be derived either from $\mathbf{K}^t$ or equivalently from the trace of the correlation matrix $\mathbf{C}^t$. Both $\mathbf{K}^t$ and $\mathbf{C}^t$ are by construction positive definite Hermitian forms with positive real eigenvalues associated with mutually orthogonal eigenvectors. Each eigenvalue equals the variance accounted for by the pattern of its corresponding eigenvector and the pattern that corresponds to the largest eigenvalue contributes most to the variance. The decomposition of the correlation matrix into its orthogonal components is called the EOF decomposition.

The EOF decomposition of $\mathbf{C}^\infty$ determines the structures that contribute most to the ensemble average variance of the statistically steady state. These are the primary response structures of the dynamical system. They are determined by solving the eigenvalue problem:

$$\mathbf{C}^\infty \mathbf{u}^{(i)} = \lambda^{(i)} \mathbf{u}^{(i)} \quad , \qquad (17)$$

in which the variance accounted by the structure $\mathbf{u}^{(i)}$ is given by $\lambda^{(i)}$.

The EOF's can be interpreted dynamically using the stochastic theory developed here thus providing a link between observed atmospheric statistics and dynamical theory. The leading EOF can be determined as the eigenfunction corresponding to the maximum eigenvalue of the operator:

$$\mathbf{C}^\infty \equiv \lim_{t\to\infty} \int_0^t e^{\mathbf{A}(t-s)}\ e^{\mathbf{A}^+(t-s)}\ ds \quad . \qquad (18)$$

Note that due to the non-normality of **A** the eigenfunctions of (18) do not coincide with the eigenfunctions of the dynamical operator **A**. Only for normal dynamical operators, for which **A** and $\mathbf{A}^+$ commute, do the eigenfunctions of (18) coincide with the modes of the system.

Eigeanalysis of $\mathbf{K}^\infty$, on the other hand, allows ordering of the forcing distributions according to their contribution to the variance of the statistically steady state. This follows from (10) and the observation that the eigenvalues of $\mathbf{K}^\infty$ are stationary values of the Rayleigh-Ritz quotient:

$$I[f] = \frac{f^* \mathbf{K}^\infty f}{f^* f} \quad . \qquad (19)$$

Consequently, the forcings, $f^{(i)}$, obtained from eigenanalysis of

$$\mathbf{K}^\infty \equiv \lim_{t\to\infty} \int_0^t e^{\mathbf{A}^+(t-s)}\ e^{\mathbf{A}(t-s)}\ ds \qquad (20)$$

can be ordered according to their relative contribution to the stochastically maintained variance. The optimal stochastic excitation consists of the eigenfunction corresponding to the largest eigenvalue of (20). Note once again that because of the non-normality of **A** the eigenfunctions of **A**, $\mathbf{K}^\infty$, and $\mathbf{C}^\infty$ do not coincide. In Fla examples of the differences in these structures are given.

According to the theory presented here eigenanalysis of (18) is expected to yield the observed EOF's if **A** is taken to correspond to the linearized operator of an observed atmospheric state.

c. Determination of the power spectrum of the maintained variance

Fourier transformation of (8) readily yields that

$$\langle E^\infty \rangle = \frac{1}{2\pi} \int_{-\infty}^{\infty} F(\omega)\ d\omega, \qquad (21)$$

where the frequency response

$$F(\omega) = \mathrm{Trace}(\mathbf{R}^+(\omega)\ \mathbf{R}(\omega)) \quad , \qquad (22)$$

follows from the resolvent

$$\mathbf{R}(\omega) = (i\omega\mathbf{I} - \mathbf{A})^{-1} \quad . \qquad (23)$$

Note that the energy response function $F(\omega)$ can not be simply characterized as a summation of the contributions from the poles of the resolvent as it would be if the operator were normal. To estimate the range of values attained by (23) consider the inequality (Kato, 1966):

$$\frac{1}{\mathrm{dist}(i\omega, \Lambda(\mathbf{A}))} \le \| \mathbf{R}(\omega) \| \le \frac{1}{\mathrm{dist}(i\omega, F(\mathbf{A}))} \qquad (24)$$

where the right inequality is valid for $i\omega$ not in the closure of $F(\mathbf{A})$ and the left inequality for $i\omega$ not in $\Lambda(\mathbf{A})$ where $\Lambda(\mathbf{A})$ is the spectrum set of **A**, and

dist denotes the distance function of a point from a set. We denote by $F(\mathbf{A})$ the numerical range of $\mathbf{A}$ i.e. the set of values $u^* \mathbf{A} u$ for $\|u\|=1$. It can be shown that the largest eigenvalue of $\frac{1}{2}(\mathbf{A} + \mathbf{A}^*)$ provides a bound on the instantaneous rate of growth of perturbations and that this bound coinciders with the supremum of Re ($F(\mathbf{A})$). Consequently, a non-normal operator will exhibit transient growth whenever $\mathbf{A} + \mathbf{A}^*$ has a positive eigenvalue. This can happen even if all the eigenvalues of $\mathbf{A}$ have negative real part. For a normal operator the numerical range $F(\mathbf{A})$ is the convex hull of $\Lambda(\mathbf{A})$ and consequently the inequalities in (24) become equalities signifying that the system response at a given frequency ω is characterized solely by the proximity of $i\omega$ to the spectrum of the operator $\mathbf{A}$. However, (24) indicates that for a non-normal operator the norm of the resolvent may be large even if $i\omega$ is far from the spectrum, rendering the familiar estimate of the response by the distance from the contour $i\omega$ to the poles inadequate. For further discussion of these points refer to Farrell and Ioannou (1993c) and Reddy *et al.* (1993).

d. Determination of the ensemble average heat fluxes

The ensemble average heat flux can be shown (see FIb) to be proportional to the trace of the matrix:

$$\mathbf{H}^t = \frac{k}{2} \, \mathrm{Im}\left[\mathbf{E}\,\mathbf{T}\,\mathbf{M}^{-1/2}\,\mathbf{C}^t\,\mathbf{M}^{-1/2}\,\mathbf{E}^+\right] , \quad (25)$$

where $\mathbf{C}^t$ is the correlation matrix given in (14).

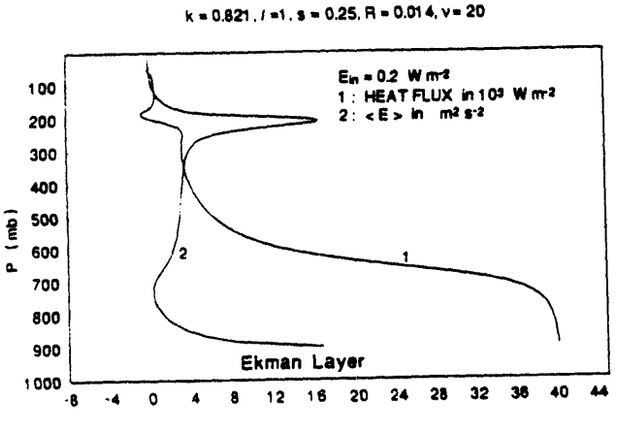

Fig. 1: The distribution with height of the ensemble average energy and heat flux for global zonal wavenumber 5 waves (k=0.821 and l=1). The dissipation parameters are chosen to be ν=10 $m^2 s^{-1}$ and R=0.014. The stochastic forcing is 0.2 Wm^{-2}.

It is worth noting that the correlation matrix of the generalized velocities determines the heat flux and, in particular, the diagonal elements of $\mathbf{H}^t$ give the height distribution of the heat flux. An example of the distribution of the ensemble average heat flux is shown in Fig. 1.

e. On the assumption of asymptotic stability of the dynamical operator

In the formulation we have presented it is not necessary that a statistically steady state exists. However, it is reasonable to assume that the mean state of the atmosphere as it is maintained against dissipation by the mean forcing (including both external and internally generated Reynolds stresses) is asymptotically stable i.e. all the eigenvalues of $\mathbf{A}$ have negative real parts. Under this assumption the asymptotic values of the ensemble average energy and heat flux exist and can be readily evaluated from the Liapunov equations presented in the previous section.

This fundamental underlying assumption should be contrasted with the alternative view that the mean atmospheric state is unstable and coherent unstable waves dominate the variance. In the theory presented here the dynamics are assumed stable and the energetics and fluxes are controlled by the non-normality of the dynamical operator. From this perspective the atmospheric variance results from stochastic amplification of the background stochastic forcing rather than from equilibration of unstable modes.

The appropriate choice of dissipation parameters for representative eddy scales in the atmosphere and for a typical jet with a maximum velocity of 45 ms^{-1} are coefficients of vertical diffusion ν>5 $m^2 s^{-1}$ and coefficients of linear potential damping R<0.01, corresponding to e-folding times smaller than 11 days. These render the operator $\mathbf{A}$ asymptotically stable. The most crucial parameter for asymptotic stability of the dynamical operator turns out to be the linear potential vorticity damping, R, which models the disruption of motion due to nonlinear scattering and should be viewed as an eddy viscosity (Salmon, 1980; Vallis, 1985). To obtain an upper bound on the eddy viscosity note that the observed decorrelation time for atmospheric motions is 7 days (Leith , 1973), implying R=0.016. For a lower bound note that the radiative relaxation time is approximately 20 days. In most of the calculations we take an e-folding time between 7 days and 11 days.

3. THE SPECTRUM OF THE RESPONSE TO STOCHASTIC FORCING

We consider a baroclinic atmosphere and large scale waves with meridional wavenumber $l=1$ (for the dimensional equivalent see FIa). Note that the meridional confinement implied by $l=1$ is consistent with the atmospheric state given by Salby (1982) (using the correspondence between the separable and non-separable problem established by Ioannou and Lindzen (1986)).

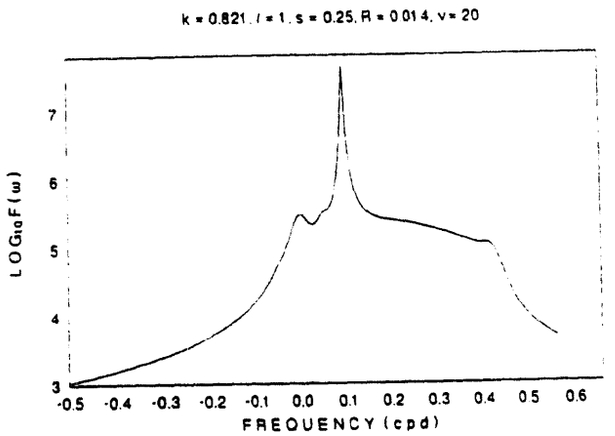

Fig. 2: The frequency response (in cycles per day) of the maintained variance for zonal wavenumber 5 (k=0.821), $l=1$. The vertical diffusion coefficient has been chosen to be $v=20$ m^{2}s^{-1}, and the e-folding time for the linear damping to be 8 days (R=0.014).

The distribution of the maintained variance for zonal wavenumber 5 as a function of frequency is shown in Fig. 2. This graph shows that the pronounced response with an approximate 10 day period observed by Salby (1982) is consistent with stochastically forced baroclinic dynamics. Although noise in the atmosphere is certainly red, the color of the noise is not required to obtain the observed pronounced response.

The full spectrum of the response as a function of period and zonal wavenumber is shown in Fig. 3. Comparison with observations (i.e. Hansen et al., 1989) reveals that the derived spectra are in remarkable agreement with observations.

Dimensional values of ensemble average energy and associated heat flux as a function of zonal wavenumber are shown in Fig. 4 for stochastic forcing of 1 Wm^{-2} (for the dimensional forms of these quantities refer to FIb). The maximum response is concentrated between zonal wavenumbers 5 and 6 (note also the reduction of the variance and the fluxes as dissipation increases). The fact that the atmosphere often exhibits enhanced variance at these scales suggests further that the atmosphere is stochastically maintained in a state of near neutrality

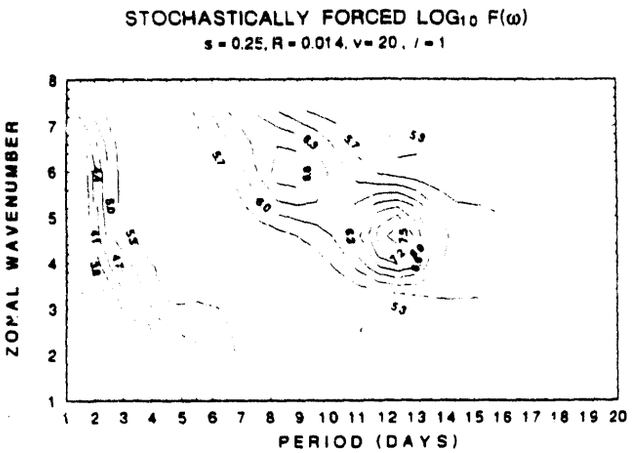

Fig. 3: The variance as a function of period (in days) and zonal wavenumber for $l=1$. The vertical diffusion coefficient has been chosen to be $v=20$ m^{2}s^{-1}, and the e-folding time for the linear damping to be 8 days (R=0.014).

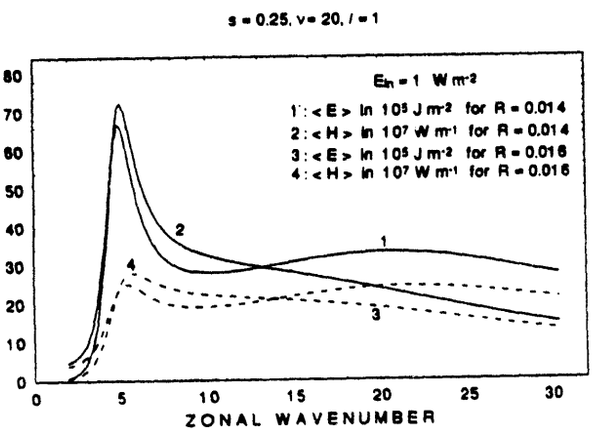

Fig. 4: The ensemble average energy and heat flux as a function of zonal wavenumber for $l=1$. The vertical diffusion coefficient has been chosen to be $v=20$ m^{2}s^{-1}, and the e-folding time for the linear damping to be 8 days (R=0.014); the dotted curves are for linear damping of 7 days (R=0.016).

4. CONCLUSIONS

We have shown that stochastic excitation of a stable baroclinic model of the atmosphere results in a spectrum of variance remarkably close to that observed. The dominance of zonal wavenumber 5 in observed spectra suggests that the atmosphere is equilibrated to a state of near neutrality in which a balance has been achieved between the stochastically determined mean flow tendencies and the large scale thermal forcing.

One implication of this work for GCM's is that the models must be sufficiently resolved so as to include the small scale waves required to stochastically force the large scales. In such a circumstance the stochastically maintained mean state of the GCM can be expected to be subcritical.

Acknowledgement

Petros J. Ioannou was supported by NSF ATM-92-16189. Brian F. Farrell was supported by DOE through the Northeast Regional Center of NIGEC, and by NSF ATM-92-16813.

References

Egger, J. and H-D. Schilling, 1983: On the theory of the long-term variability of the atmosphere. *J. Atmos. Sci.*, **40** , 1073-1085.

(FIa) Farrell B. F. and P. J. Ioannou, 1993a: Stochastic dynamics of baroclinic waves. *J. Atmos. Sci.*, in print.

(FIb) Farrell B. F. and P. J. Ioannou, 1993b: A sensible heat flux theory for transient baroclinic waves. *J. Atmos. Sci.*, submitted.

Farrell B. F. and P. J. Ioannou, 1993c: Variance maintained by stochastic forcing of a non-normal dynamical system arising in fluid shear flow. *Phys. Rev. Lett.*, submitted.

Fraedrich, K. and H. Bottger, 1978: A wavenumber-frequency analysis of the 500 mb geopotential at 50° N. *J. Atmos. Sci.*, **35** , 745-750.

Hansen A. R., A. Sutera and D. E. Venne, 1989: An examination of midlatitude power spectra: evidence for standing variance and the signature of El Nino. *Tellus* , **41 A**, 371-384.

Ioannou, P. J. and R. S. Lindzen, 1986: Baroclinic instability in the presence of barotropic jets. *J. Atmos. Sci.*, **43** , 2999-3014.

Kasahara, A., 1980: Effect of zonal flows on the free oscillations of a barotropic atmosphere. *J. Atmos. Sci.*, **37** , 917-929.

Kato, S, 1976: *Perturbation Theory for Linear Operators* , Springer-Verlag, New York.

Leith, C. E., 1973: The standard error of time-average estimates of climatic means. *J. Appl. Met.*, **12**, 1066-1069.

Randel, W. J. and J. L. Stanford, 1985: An observational study of medium-scale wave dynamics in the southern hemisphere summer. Part I: wave structure and energetics. *J. Atmos. Sci.*, **42** , 1172-1188.

Reddy S. C., P. Schmid, and D. Henningson, 1993: Pseudospectra of the Orr-Sommerfeld operator. *SIAM J. Appl. Math.* , **53**, 15.

Salmon, R. S., 1980: Baroclinic instability and geostrophic turbulence.*Geophys. and Astrophys. Fluid Dyn.*, **15**, 167-211.

Salby, M. L., 1982: A ubiquitous wavenumber-5 anomaly in the southern hemisphere during FGGE. *Mon. Wea. Rev.*, **110**, 1712-1720.

Schafer, J., 1979: A space-time analysis of tropospheric planetary waves in the Northern Hemisphere geopotential heights. *J. Atmos. Sci.*, **36** , 1117-1123.

Schoeberl, M. R., and A. J. Krueger, 1983: Medium scale disturbances in total ozone during southern hemisphere summer. *Bul. Am. Meteor. Soc.*, **64**, 1358-1365.

Vallis, G. K., 1988: Numerical studies of eddy transport properties in eddy-resolving and parametrized models. *Q. J. R. Met. Soc.*, **114**, 183-204.

Wang, M. C., and G. E. Uhlenbeck, 1945: On the Theory of the Brownian Motion II, *Rev. Modern Phys.*, **17**, 323-342.

Northern hemispheric response to large volcanic eruptions in relation to El Niño - winter case studies

Ingo Kirchner
Max-Planck-Institut Hamburg, FR Germany
Paper presented at the 17th Stanstead Seminar June 13-18, 1993
Lennoxville, Quebec, Canada.

1. Introduction

A large part of the global climate variability is attributed to variations of the Indian Monsoon and of El Niño/Southern Oscillation (e.g. PHILANDER, 1990). Facing the recent violent volcanic eruption of Mount Pinatubo in June 1991, and searching for the climate signal of the increased greenhouse effect, the climate impact of volcanic aerosols becomes more and more interesting.

The explosivity and chemical properties of volcanic ejections play an important role for the variability of climate in time scales between one month and some seasons. However, not only the eruption height is of importance, but also the total mass of aerosol-building-gases passing the tropopause. The stratospheric aerosol has residence times of a few years and thus stratospheric volcanic aerosol may influence the global climate for years. All parameters commonly used to measure the strength of eruptions have their specific deficiencies. Especially they do not give an objective measure of the SO_2 content of the ejecta, the most important parameter for the potential climate effectiveness of an eruption.

The volcanic aerosol perturbation leads to a combination of short- and longwave radiation effects due to scattering of shortwave and absorption of longwave radiation at the volcanic aerosol in the stratosphere. This forces regional and seasonal changes of the meridional temperature gradient in the stratosphere. The wintertime stratospheric circulation strengthens during periods with high aerosol concentration in the tropical stratosphere.

The stratospheric circulation has a strong annual cycle. Stratospheric meridional tracer transport between tropics and extratropics mainly takes place during the rearrangement of the seasonal circulation types. This modulates the volcanic aerosol distribution as a function of the latitude of the volcano and the eruption date.

During El Niño episodes the strong ocean-atmosphere-interaction suppresses the upwelling of cold and nutrient water in the eastern Pacific. The Walker circulation cell shifts zonally, obtaining an ascending branch over the central Pacific region. The strong latent heat release in the ascending Walker cell branch intensifies the meridional poleward energy transport of heat and momentum. The cyclone activities in middle and higher latitudes are modulated via an strengthened Hadley circulation. The strong Aleutian Low during El Niño winters certainly plays an important role for the change of the tropospheric circulation pattern, but it may weaken the wintertime stratospheric polar vortex (LABITZKE/LOON, 1989).

Thus the strength of the stratospheric vortex can be differently influenced by both factors (volcanic aerosol and El Niño). Linear theory of atmospheric mean flow/wave interaction suggests that a strong polar vortex

reflects the vertically propagating energy of tropospheric planetary waves back to the troposphere and thus alters the standing wave pattern in the troposphere (GELLER/ALBERT, 1980).

Since potential volcanic and El Niño effects often coincided during the last century (GRAF, 1986) (e.g. El Chichon in April 1992 and strong El Niño 1982/83), and the observational basis is only small for such rare events like violent volcanic eruptions, it is difficult to select the different effects of volcanos and El Niño in climate variability, and to delimit these changes from those of other climate forcing factors like e.g. greenhouse warming. A combination of observations and model studies may help overcoming these problems.

2. Data processing and experimental design

Not all important features of volcanic activity are measured over a time range long enough to apply statistical techniques. Information on the eruption height (Volcanic Explosivity Index > 3), the total aerosol loading (Dust Veil Index >= 200), the geographical position and season of the eruption were therefore used to generate a table of volcanic events with high climate perturbation potential. Only in few cases information about the sulphur content are available. It is suggested that only in the first winter after a volcanic eruption in tropical regions and in the second winter after a volcanic eruption in latitudes poleward of 40° north or south a volcanic signal may be detectable.

The volcanic potential impact estimations and the El Niño statistics since 1854, were used to separate all years between 1854 and 1989 into four different classes. Following this classification, 62 periods without El Niño or volcanic perturbation in northern winter were selected. In 26 winter seasons El Niño exist, 23 periods with high stratospheric aerosol loading potential occur and 25 periods with a combination of El Niño and volcanic forcing were observed.

This volcano/El Niño classification was used as the basis for a superposed epoch analysis of the global data set of the surface air temperature (JONES et al., 1986). At many grid points data exist only for the last few years. This might (e.g. in case of any trends in the time-series) affect the results, and therefore it was used grid points with less than 20 % of missing values.

The volcano/El Niño superposed epoch analyse was compared with a polar vortex superposed epoch analyse. The selection into strong and weak vortex winter months is based on radiosonde observations of the 50 hPa layer (LABITZKE, 1992) since 1957, as analysed in the EOF (Empirical Orthogonal Function) space (PERLWITZ, 1992; GRAF et al., 1993a).

In addition four perpetual January experiments corresponding to the four different volcano/El Niño classes were performed with the T21 version of the ECHAM2 (ROECKNER et al., 1987; CUBASCH ed., 1991). Since the internal radiation scheme of the ECHAM2 climate model uses a climatologically prescribed aerosol distribution, an external 2D-radiation-aerosol transport model (SCHULT, 1991) was used to calculate the aerosol effects explicitly. The computed heating rates in the lower stratosphere and the shortwave radiation effect at the top of the atmosphere for January were inserted into the climate model (GRAF et al. 1993b).

All experiments were integrated over 60 Januaries. The reference experiment (CTRL) runs with climato-

logically prescribed sea surface temperature and without additional aerosol effects. In the volcano case experiment (PERM3) the boundary conditions are the same as in the control case. External heating rate anomalies were added in the upper six model levels and the shortwave radiation reduction effect was simulated with the reduction of the solar radiation at the top of the model atmosphere according to the external 2D-calculations. For the El Niño experiment (SST2) the sea surface temperature anomalies in the area between 25°N and 25°S, as observed in January 1983, were added to the climatological mean sea surface temperature. In the fourth experiment (PERM6) the El Niño experiment boundary conditions were combined with the heating rates and the shortwave radiation reduction corresponding to the volcano experiment.

The applied statistical methods to analyse the GCM experiment data are a combination of the local t-test statistics and signal detection methods based on EOFs (HASSELMANN, 1991; SANTER et al., 1993). The average signal $\bar{P}_e$ was calculated as an overlay of a small set of EOF-patterns weighted with the mean amplitude of the corresponding principal components.

The simulated response was compared with observed winter mean geopotential height anomalies of the 500 hPa layer following NMC (National Meteorological Centre of the U.S. Weather Service) analysis, transformed to a 5 * 5° grid in Hamburg. In order to compare the simulated temperature response the Microwave Sounding Unit (MSU) data set (SPENCER/CHRISTY, 1991) was used. It was suggest that this data set is better comparable with the simulated temperature response in the lower troposphere than are the near surface temperature anomaly data because (1) mainly large scale dynamic processes being responsible for the anomaly patterns in the lower troposphere and (2) the strong local influences of the climatologically prescribed sea surface temperature in higher regions overlaying the patterns.

3. Results

The volcano/El Niño superposed epoch analyse shows similar anomaly patterns of the near surface temperature, especially concerning the warming over Eurasia and North America and the cooling in the Greenland region, than an independent analysis (ROBOCK/MAO, 1992) of the same data set but for the 12 strongest eruptions and with an regressive elimination of the El Niño effect. The area covered by data is very small because those areas with very strong amplitudes are considered.

The difference between the surface air temperature anomaly patterns of winter months with a strong and with a weak vortex clearly indicates the association between the strength of the polar vortex and volcanically forced anomalies. Positive wintertime temperature anomalies over northern Eurasia are a feature of winters with strong stratospheric vortex and also of winters with high stratospheric aerosol perturbation potential.

The principal component analyse of the simulated response shows that the volcanic signal is less strong than the El Niño signal in the troposphere. The opposite holds for the stratospheric response.

In the stratosphere the simulated temperature response of the volcanically forced perturbation is about ten times the amplitude of the El Niño experiment (SST2). It becomes evident that volcanic forcing leads to the expected warming of the tropical stratosphere, while it cools the stratosphere in northpolar latitudes. This cooling

is larger than the aerosol heating and compensates the positive longwave radiation effect near the pol. In contrast to the volcanic response the warm SST of the El Niño case leads to a zonally symmetric cooling of the tropical stratosphere and to the formation of a wave number one pattern in higher latitudes with a warming over the northern Pacific and cooling over the North Atlantic. This is in accordance with observations (LABITZKE/LOON, 1989).

A strong maximum of the volcanic response of the 50hPa zonal wind is observed over the North Atlantic, and a secondary maximum is over the Bering Strait. In the El Niño case the strongest signal in the zonal wind field of the 50hPa layer occurs over the Pacific. It consists of negative anomalies in the Tropics, positive ones in the Subtropics, and a weak polar vortex in high northern lautudes. In the combined experiment (PERM6) the positive anomalies are shifted somewhat to the south as compared to the volcano experiment (PERM3).

The stratospheric signal, which is strong in the volcano case, becomes weaker in the troposphere in comparison to the El Niño response in the zonal wind field. In the 200hPa level the volcano signal in the zonal wind field is restricted to the North Atlantic. In the El Niño case in the tropical upper troposphere easterly anomalies dominate over the Pacific and westerlies are found from the Atlantic crossing Africa to the Indian Ocean. Westerly anomalies occur in the Pacific subtropics. In the combined experiment the El Niño response dominates the zonal wind field.

The simulated volcano signal of the geopotential field of the middle troposphere behaves similar like the zonal wind field in the 200hPa level. Zonally symmetric positive values in the Tropics are characteristic for the signal in the geopotential field of the 500hPa layer for the El Niño case, as are a strong negative anomaly over the North Pacific and positive values over North America. For the combined forcing the El Niño signal remains dominant in the Tropics and in middle and high latitudes over the Pacific region. But, from the Atlantic to northern Eurasia the volcano signal is clearly modified. The trough over Greenland is weaker in PERM6 than in PERM3, and the positive anomaly visible in the volcano experiment over the North Atlantic is also smaller. The Greenland trough is in the middle of a large scale positive geopotential anomaly reaching from the west coast of North America to central Siberia in mid and high latitudes.

The simulated negative anomaly over Greenland was also found in all observations with volcanic perturbed stratosphere (isolated and combined with El Niño), and the negative anomaly in the Aleutian region occurs in all El Niño cases, simulated and observed.

The comparison of the 850hPa level temperature signal with the observations shows reasonable similarity in the volcano case as well as in the mixed case. Because of lacking data for the winter 1957/58 I can not compare the patterns for the single El Niño case with MSU data. In the volcano case during winter, the temperature over the North Atlantic and northern Eurasia is warmer than normal and more cold air is advected from the polar regions towards Greenland.

The volcanic response in the near surface temperature field can be traced with warming over Scandinavia and in the central part of North America. North Asia and the westcoast of North America are warmer and the East

Coast of North America is colder than normal. This feature was also observed by other authors (SPIRINA, 1973; GRAF, 1986; LOUGH/FRITTS, 1987; SEAR et al., 1987; GROISMANN, 1992) after strong volcanic eruptions and this is just the temperature pattern which was observed during the winters 1991/92 and 1992/93 after the Pinatubo eruption.

The shortwave radiation effect in the volcano case is detectable only in lower latitudes, like over Southern Asia and North Africa. A large area of negative temperature anomalies in central Asia is prominent in the mixed case of observations and simulations.

The positive temperature anomalies over Southeast Asia as well as the warming over the North American westcoast are found in the model and in the observations for El Niño winters. The same holds for the cooling over the Southeastern USA. A clear difference between observations and experiments is found over Europe. The observed negative temperature anomalies are not in agreement with the modelled El Niño response.

4. Summary

(i) El Niño and strong tropical volcanic eruptions lead to regional different anomalies during winter. In the lower troposphere the dynamically enforced part of the volcano signal is weaker than in the stratosphere and the effect of the reduction of shortwave solar radiation becomes increasingly visible over the continental Subtropics. The cooling effect over Greenland and the strong warming over northern Eurasia are the result of advection of cold and warm air masses respectively. In contrast to this pattern, in the El Niño case strong temperature anomalies are formed in high latitudes only over the northwestern part of North America.

(ii) The volcanic aerosol heating in the stratosphere is only one factor to force a natural mode of the polar vortex. The tropospheric response of the volcano perturbation is larger in the Atlantic region than elsewhere.

(iii) The effect of local cooling due to the reduction of shortwave radiation over large land areas (like Asia) in subtropical regions, and also the advective warming over Eurasia and the advective cooling over Greenland was well simulated as compared with observations during episodes with high stratospheric volcanic aerosol loading.

(iv) The El Niño signal amplitude is large in the Pacific region. It is not restricted to the Tropics. The well known anomalies in the Tropics, the warming over North America in middle and high latitudes are simulated as observed.

(v) The observed cold El Niño winters over Europe are less intense in the simulations. I suggest that this is due to the model's lacking ability to weaken the stratospheric vortex. Therefore the planetary wave patterns over the Atlantic and Europe remain unchanged.

5. Literature

Cubasch (ed.), 1991. First joint climate modelling planning workshop 24th - 25th June 1991. Deutsches Klimarechenzentrum.

Geller, M.A. and J.C. Alpert, 1980. Planetary wave coupling between the troposphere and the middle atmosphere as a possible sun-weather mechanism. J. Atmos. Sci., 37, 1197-1215.

Graf, H.F., 1986. Cooling of the northern hemisphere - a potential trigger of El Niño/Southern Oscillation events (in German). Naturwissenschaften, 73, 258-263.

Graf, H.F., J. Perlwitz and I. Kirchner, 1993a. Northern hemisphere tropospheric midlatitude circulation after violent volcanic eruptions. Geophys. Res. Letts., (submitted).

Graf, H.F., I. Kirchner, A. Robock and I. Schult, 1993b. Pinatubo eruption winter climate effects: Model versus observations. Climate Dynam., (submitted).

Groisman, P.Y., 1992. Possible regional climate consequences of the Pinatubo eruption: An empirical approach. Geophys. Res. Letts., 19, 1603-1606.

Hasselmann, K., 1992. Optimal fingerprints for the detection of time dependent climate change. MPI Report, 88, 41pp.

Jones, P.D. et al.1986. A global grid point surface air temperature data set: 1851-1984.CDIC Numeric Data Collection, NDP-020, update 1992.

Labitzke, K. and H. van Loon, 1989. The Southern Oscillation. Part IX: The influence of volcanic eruptions on the Southern Oscillation in the stratosphere. J. of Climate 2, No. 10,1224-1226.

Labitzke, K., 1992. Stratospheric temperature data based on radiosonde measurements, (pers. comm.).

Lough, J.M. and H.C. Fritts, 1987. An assessment of the possible effects of volcanic eruptions on north american climate using tree-ring data, 1602 to 1900 a.d.. Climate Change, 10, 219-239.

Perlwitz, J., 1992. Analyses of the statistical coherence between the tropospherical and stratospherical circulation of the northern hemisphere during winter using multivariate statistical methods (in German). Diplomarbeit, Humboldt Univ. Berlin, 48pp.

Philander, S.G., 1990. El Niño, La Niña, and the Southern Oscillation. International Geophys.Series, 46, Academic press, R.Dmowska and J.R.Holton (ed.), 291 pp.

Robock, A. and J. Mao, 1992. Winter warming from large volcanic eruptions. Geophys. Res. Letts., 19, 2405-2408.

Roeckner, E., et al. 1989. The Hamburg version of the ECMWF model (ECHAM). In Research activities in atmospheric and oceanic modelling. CAS/JSC Working Group on Numerical Experimentation, G.J. Boer (ed.). Report, 13, WMO/TD, 332. 7.1 - 7.4.

Santer, B.D. et al., 1993. Signal-to-noise analysis of time-dependent greenhouse warming experiments. Part 1: Pattern analysis. Climate Dynam., (submitted).

Schult, I., 1991. Formation and transport of aerosol particles in the stratosphere and their importance for the radiation budget (in German). Examensarbeit, 11, MPI, 142pp.

Sear, C.B, P.M. Kelly, P.D. Jones and C.M. Goodess, 1987. Global surface-temperature response to major volcanic eruptions. Nature, 330, 365-367.

Spencer, R.W. and J.R. Christy, 1991. Global temperature update to 31 October 1991. NASA Headquarters, Washigton, (pers. comm.).

Spirina, L.P., 1973. On the seasonal changes of the surface air temperature field of the northern hemisphere after volcanic eruptions (in Russian), Trans. of the Main Geophysical Observatory, 299, 3-7.

Temperature 850 hPa Anomalies (Kelvin)

(areas with significance level higher than 98% are shaded)

Perpetual January Experiments *MM-03-60 ECHAM2 T21*

Perm3 (volcano experiment)

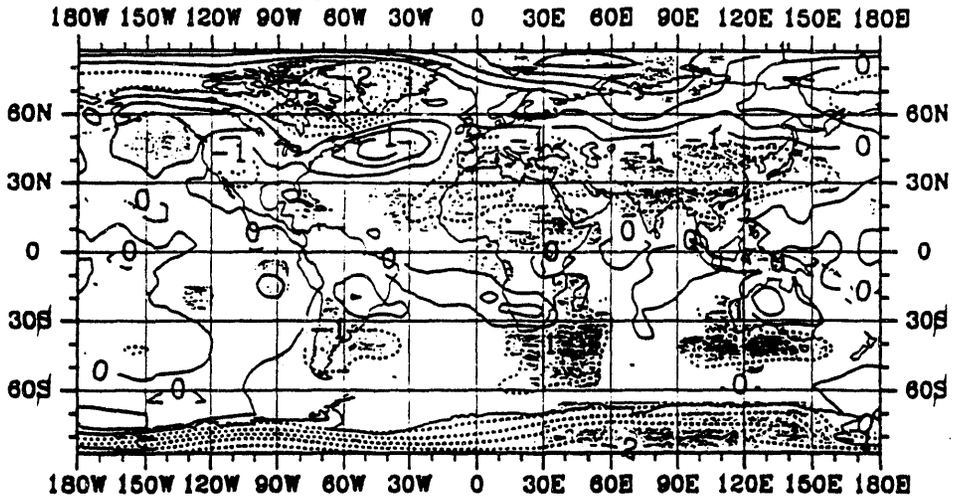

Perm6 (volcanco/El Niño experiment)

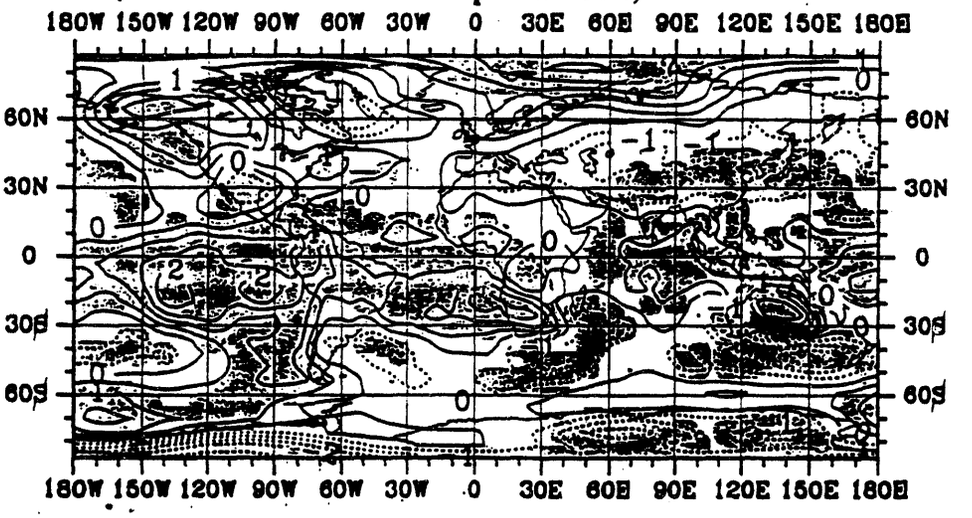

Sst2 (El Niño experiment)

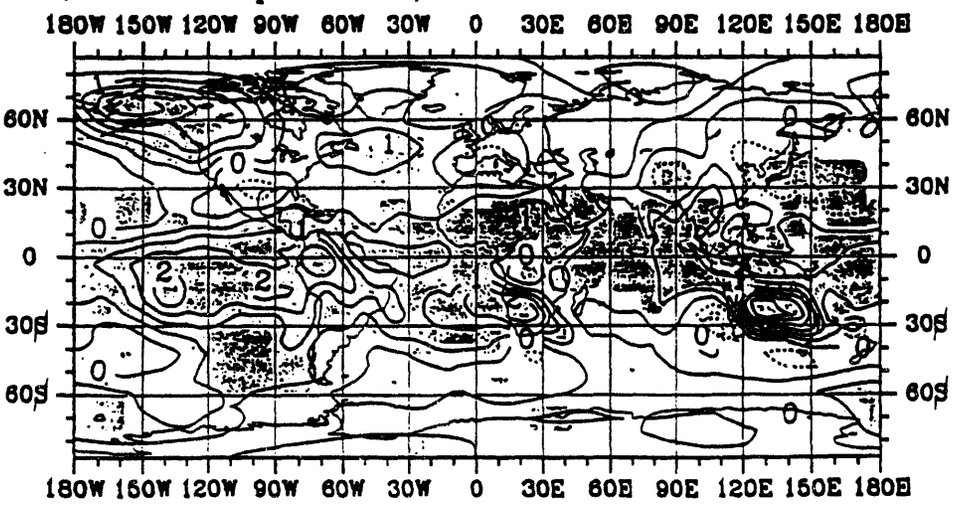

Zonal Wind 200 hPa Anomalies (m/s)

(areas with significance level higher than 98% are shaded)

Perpetual January Experiments *MM-03-60 ECHAM2 T21*

Perm3 (volcano experiment)

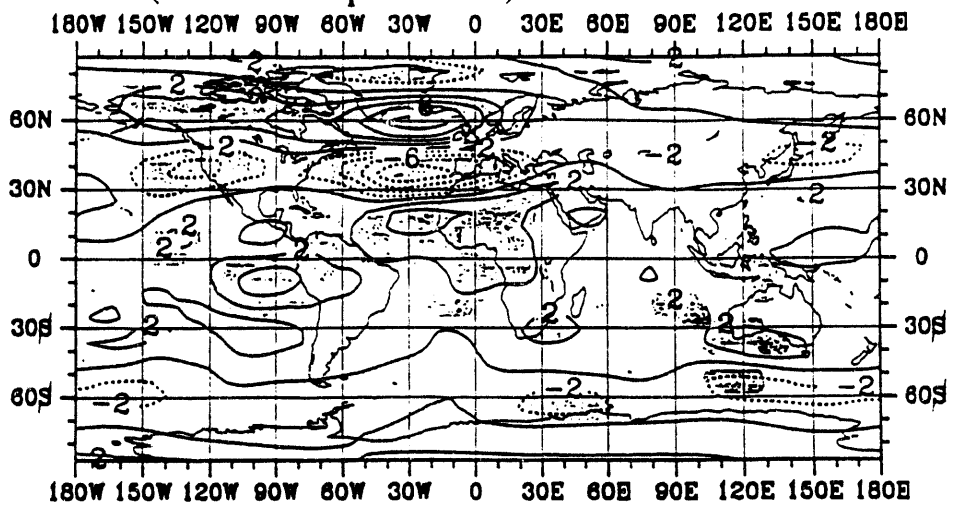

Perm6 (volcanco/El Niño experiment)

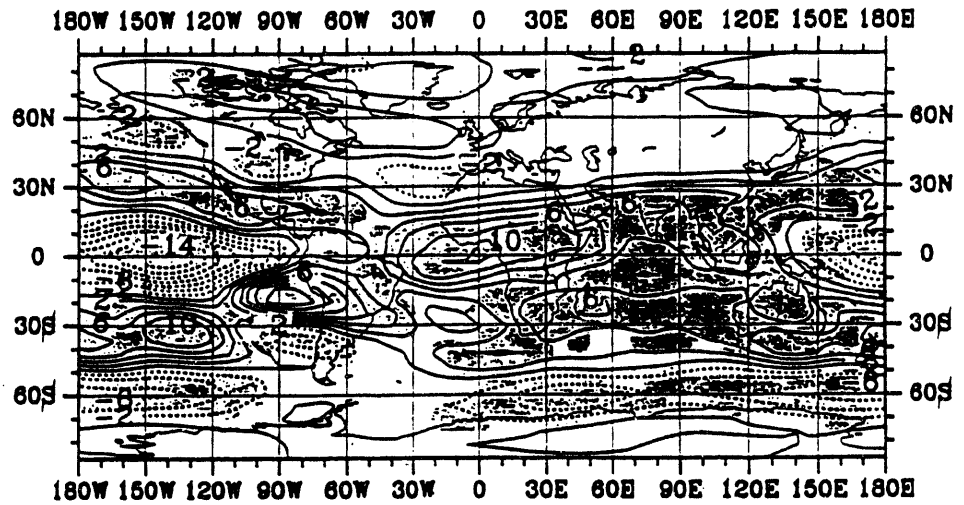

Sst2 (El Niño experiment)

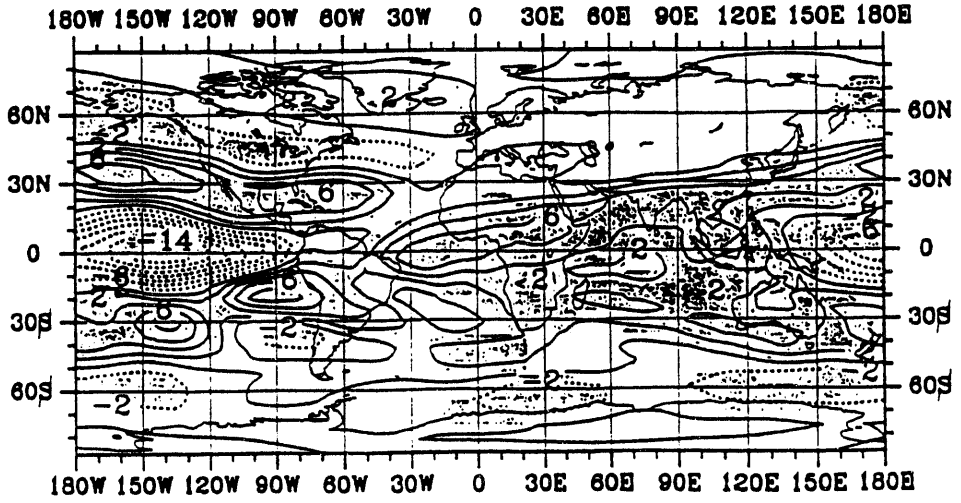

POTENTIAL VORTICITY DYNAMICS IN THE CANADIAN CLIMATE CENTRE GCM

John N. Koshyk and Norman McFarlane
Canadian Climate Centre, Downsview, Ontario

Abstract

The global distribution of Ertel potential vorticity (PV), simulated by the Canadian Climate Centre general circulation model (CCC GCM) is examined. An expression for PV in terms of an arbitrary vertical coordinate is formulated. This expression is used to calculate temporally averaged PV from the model temperature and wind fields. It is shown that a good approximation to the temporally averaged PV can be obtained from temporally averaged temperature and wind fields.

An equation governing the time evolution of PV in the model vertical coordinate system is also derived. This equation is written in flux form and the associated flux is examined in a lower stratospheric region of enhanced gravity-wave drag, above the Tibetan plateau. In this region, the southward transport of PV effected by gravity-wave drag is balanced to a large degree by the advection of PV northward.

Finally, results from a recent experimental version of the CCC GCM, with an uppermost level at 1 mb, are used to examine PV dynamics associated with a spontaneous model stratospheric sudden warming. The warming is preceded by 2 successive large amplitude wavenumber 1 disturbances in the lower stratosphere. The second of these leads to splitting of the mid-stratospheric vortex into a double vortex pattern, as is clearly evident on maps of the 850K PV field during the warming period.

1. Potential Vorticity in the "s" Coordinate

The equations required to derive a Lagrangian conservation law for PV in terms of an arbitrary vertical coordinate, $s = s(x,y,z,t)$ are the momentum, mass continuity and thermo-

dynamic equations, written respectively as follows:

$$\frac{d\mathbf{v}}{dt} + 2\Omega \times \mathbf{v} + \nabla\Phi + \frac{1}{\rho}\nabla p - \mathbf{F} = 0 \tag{1a}$$

$$\frac{d}{dt}\left[\frac{\partial p}{\partial s}\right] + \left[\frac{\partial p}{\partial s}\right] \nabla\cdot\mathbf{V} = 0 \tag{1b}$$

$$\frac{d\theta}{dt} - H = 0 \ . \tag{1c}$$

These are similar to (2.1), (2.2) and (2.4) in Laprise and Girard (1990) and were derived previously by Kasahara (1974). In (1), $\mathbf{v} = (u, v, 0)$ is the horizontal velocity, $\Omega = (0, 0, \omega \sin\phi)$ where ω is the angular frequency of the earths rotation, $\mathbf{V} = (u, v, \dot{s})$ is a generalized three-dimensional velocity vector and other symbols have their usual meanings. The vector $\mathbf{F} = (F_\lambda, F_\phi, 0)$ and the scalar H represent sources and sinks of momentum and heat respectively. The operators appearing in (1) are defined as follows:

$$\frac{d}{dt} = \frac{\partial}{\partial t} + \mathbf{V}\cdot\nabla; \qquad \nabla = \left(\frac{1}{a\cos\phi}\frac{\partial}{\partial\lambda}, \frac{1}{a}\frac{\partial}{\partial\phi}, \frac{\partial}{\partial s}\right)$$

where a is the mean radius of the earth. Using these definitions the vertical component of the momentum equations yields the hydrostatic relation, Laprise and Girard (2.5).

It can be shown that the expression for the evolution of PV in the (x, y, s) coordinate space and for arbitrary momentum and thermal forcing is

$$\frac{dq_s}{dt} = -g\left[\frac{\partial s}{\partial p}\right]\left(\nabla\times\mathbf{F}\cdot\nabla\theta + \zeta_a\cdot\nabla H\right) \tag{2}$$

where

$$q_s = -g\left[\frac{\partial s}{\partial p}\right]\zeta_a\cdot\nabla\theta \tag{3}$$

is the Ertel PV in the s coordinate. Note that substituting s = z, p or θ into (3) and invoking the hydrostatic equation yields the familiar expressions for q in a hydrostatic atmosphere.

The hybrid pressure coordinate used in the CCC GCM, η, can be defined in terms of pressure through

$$p(\eta) = p_o \eta + (p_s - p_o)\left[\frac{\eta - \eta_T}{1 - \eta_T}\right]^r \tag{4}$$

where r = 2 for the results shown in section 2 and 1.5 for those of section 3, p_o is a typical value of the surface pressure, $p_s(x,y,t) = p(x, y, \eta = 1, t)$ is the surface pressure distribution, and η_T is the value of η at the top of the model atmosphere. Using this coordinate, the Lagrangian evolution equation (2) can be written in flux form with the aid of the mass continuity equation, (1b). Setting

$$\mathbf{J}_\eta = -\frac{q_\eta}{g}\mathbf{V}\left[\frac{\partial p}{\partial \eta}\right] - \mathbf{F} \times \nabla_\eta \theta - \zeta_{a\eta} H \tag{5}$$

the flux form of (2) is

$$\frac{\partial}{\partial t}\left[-\frac{q_\eta}{g}\frac{\partial p}{\partial \eta}\right] = -\nabla_\eta \cdot \mathbf{J}_\eta \ . \tag{6}$$

This is analogous to equation 3.9 with 3.4 of Haynes and McIntyre (1990).

In figure 1a) the temporally averaged PV for a single model January is shown at η = .160 (≈ 160 mb) in PVU (1 PVU = 10^{-6} K m^2 s^{-1} kg^{-1}). The result is obtained from a model with resolution corresponding to T32 in the horizontal, 10 vertical levels and a rigid lid at 5 mb. The temporally averaged PV can be written as a sum of two terms as follows:

$$\bar{q}_\eta = -g\,\overline{\frac{\partial \eta}{\partial p}\,\zeta_{a\eta}\cdot\nabla_\eta\theta} = -g\,\overline{\frac{\partial \eta}{\partial p}}\;\overline{\zeta_{a\eta}}\cdot\overline{\nabla_\eta\theta} + \Delta q_\eta \tag{7}$$

where

$$\Delta q_\eta = -g\,\overline{\frac{\partial \eta}{\partial p}}\;\overline{\zeta_{a\eta}'\cdot\nabla_\eta\theta'} - g\,\overline{\zeta_{a\eta}}\cdot\overline{\frac{\partial \eta'}{\partial p}\nabla_\eta\theta'} \tag{8}$$

$$- g\,\overline{\nabla_\eta\theta}\cdot\overline{\frac{\partial \eta'}{\partial p}\,\zeta_{a\eta}'} - g\,\overline{\frac{\partial \eta'}{\partial p}\,\zeta_{a\eta}'\cdot\nabla_\eta\theta'}.$$

In (8), the overbar denotes the time average over a one month period and primes denote deviations of sampled (twice daily) values from this mean. In pressure coordinates the quantity Δq_η takes the simple form

$$\Delta q_p = -g\,\overline{\zeta_{ap}' \cdot \nabla_p \theta'} \tag{9}$$

which is a quantity discussed in some detail by Keyser and Rotunno (1990) who consider its contribution to the mean PV field in the vicinity of mesoscale tropopause folds. The term Δq_η is displayed in figure 1b) and has maximum values that are at most 5% of the values typifying figure 1a). This suggests that time averaged PV structure is dominated by the time averaged vorticity and potential temperature rather than by transient eddy correlations between these fields.

2. Parameterized Gravity Wave Drag Effects

Parameterized sub-grid scale processes may play an important role in the larger scale PV transport in the lower stratosphere. In figure 2, the effect of parameterized gravity-wave drag on the local PV distribution over the Tibetan plateau at $\eta = .160$ is illustrated, using the results from a short (10 day) model run. In the figure, the a) horizontal divergence of the first term on the right hand side of (5) $(\nabla_H \cdot (\frac{q_\eta}{g} \mathbf{V} \left[\frac{\partial p}{\partial \eta} \right]))$ is compared to b) the horizontal divergence of the second term on the right hand side of this equation $(\nabla_H \cdot (\mathbf{F} \times \nabla_\eta \theta))$. In the latter term, the main contribution to the momentum sink, **F**, is gravity-wave drag.

From the figure it is clear that the net effect of the wave drag in figure 2b) is a southward transport of PV (note that the operand on the left hand side of (6) is proportional to $-q_\eta$). This transport is to some degree balanced by the advection of PV by the large scale wind field depicted in a). To the extent that the parameterized wave drag used in the model provides a reasonable representation of this phenomenon in the atmosphere, our result is consistent with the conclusions of Haynes and McIntyre (1987 and 1990) who suggested that the effects of advection and mechanical forcing should indeed be comparable in magnitude, in regions where wave drag dominates the momentum sink.

3. PV Dynamics During a Model Stratospheric Sudden Warming

In this section, model results are examined from a 6 year simulation with a recent experimental version of the CCC GCM, with an uppermost level at 1 mb. As in the previous section, the horizontal resolution corresponds to T32. However, this version has 30 levels in the vertical. During the third January of this particular simulation, a major stratospheric warming occurred. According to generally accepted criteria (e.g. Andrews et al., 1987, p. 259), a warming is considered major if at 10 mb or below, the zonal mean temperature at the pole is greater than that at 60N *and* the zonally averaged zonal wind at 60N is easterly.

The reversal in wind direction from its normal wintertime westerly orientation affects the stratospheric distribution of PV in a rather spectacular manner during a major warming. The evolution of model PV through the warming period is illustrated on the 850K surface in figure 3. The distribution in a), corresponding to Dec. 28, year 2 of the simulation, is characterized by a strong positive PV maximum situated directly over the pole. This is associated with strong circumpolar westerlies and a cold pole. As the simulation proceeds however, the PV anomaly is forced off of the pole as midlatitude air with relatively lower values of PV enters higher latitude regions. Eventually, by Jan. 18 of year 3, a weak double vortex pattern has evolved, accompanied by a much warmer pole, and easterly winds at 10 mb, poleward of 60N.

The rather realistic replication of a mid-winter stratospheric warming by the model suggests several possible directions for future research. One of these, which is broadly in line with the approach to model PV dynamics suggested by the first two parts of this note, involves calculating the PV budget for the warming period by examining the time evolution of the terms on the right hand side of the PV evolution equation (5). This might yield a somewhat different perspective on the warming process itself, by clarifying the roles played by advective, frictional and diabatic effects at different stages of the warming period.

References

Andrews, D.G., J.R. Holton, and C.B. Leovy, 1987: Middle Atmosphere Dynamics.

Academic Press, 489 pp.

Haynes, P.H., and M.E. McIntyre, 1987: On the evolution of vorticity and potential vorticity in the presence of diabatic heating and frictional or other forces. *J. Atmos. Sci.*, **44,** 828-841.

Haynes, P.H., and M.E. McIntyre, 1990: On the conservation and impermeability theorems for potential vorticity. *J. Atmos. Sci.*, **47,** 2021-2031.

Kasahara, A., 1974: Various vertical coordinate systems used for numerical weather prediction. *Mon. Wea. Rev.*, **102,** 509-522.

Keyser, D., and R. Rotunno, 1990: On the formation of potential-vorticity anomalies in upper-level jet-front systems. *Mon. Wea. Rev.*, **118,** 1914-1921.

Laprise, R., and C. Girard, 1990: A spectral general circulation model using a piecewise-constant finite-element representation on a hybrid vertical coordinate system. *J. Climate*, **3,** 32-52.

McIntyre, M.E. and T.N. Palmer, 1984: The 'Surf-zone' in the stratosphere. *J. Atmos. Terr. Phys.*, **46,** 825-850.

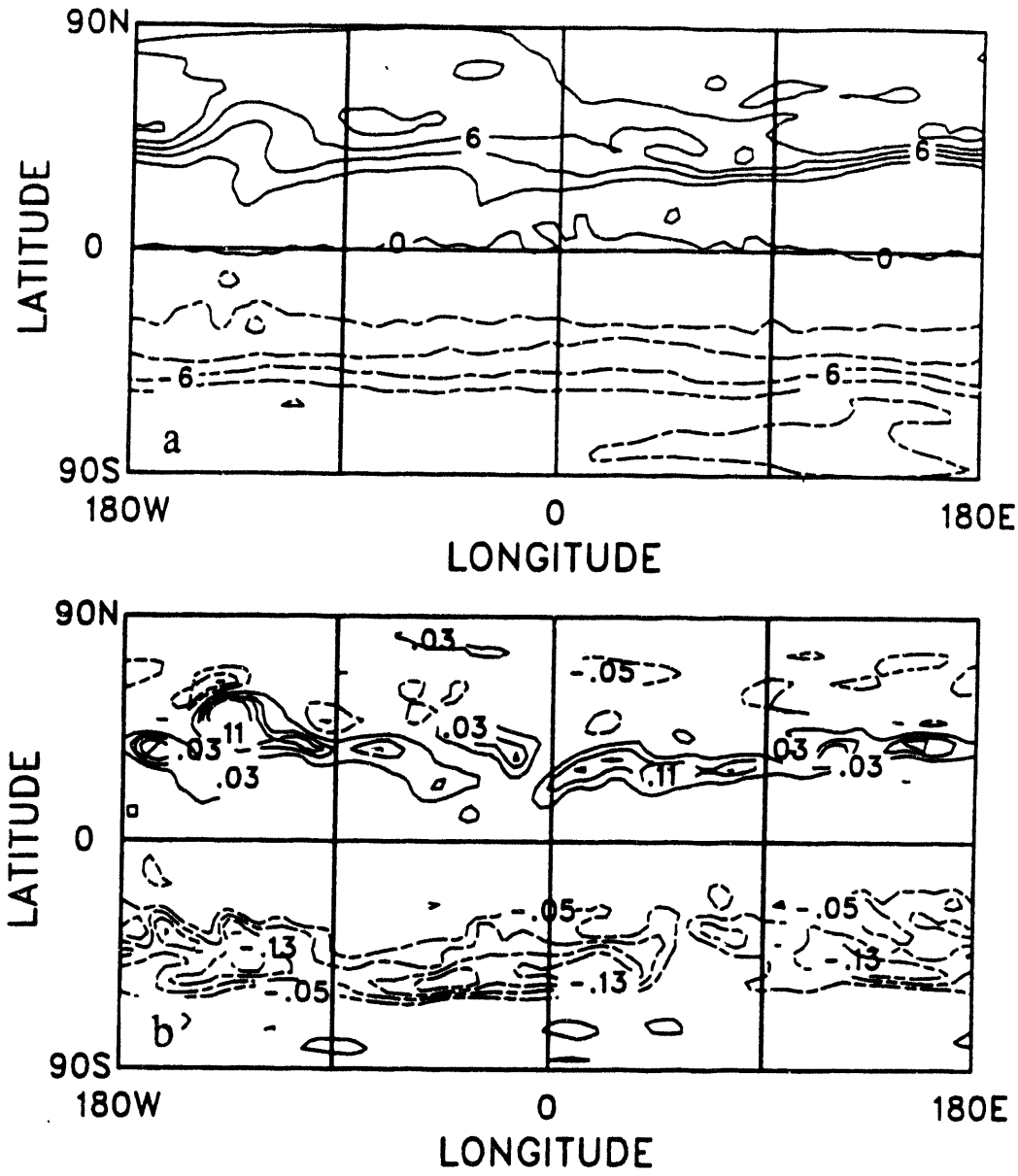

Figure 1: a) Temporallly averaged potential vorticity at η = .160 (p ≈ 160 mb) for a single model January, denoted $\overline{q_\eta}$ in the text and defined in (7). Contour interval = 2 PVU,

b) Transient eddy contribution to the field displayed in a). This field is denoted Δq_η in the text and defined in (8). Contour interval = .04 PVU. The zero contour has been suppressed.

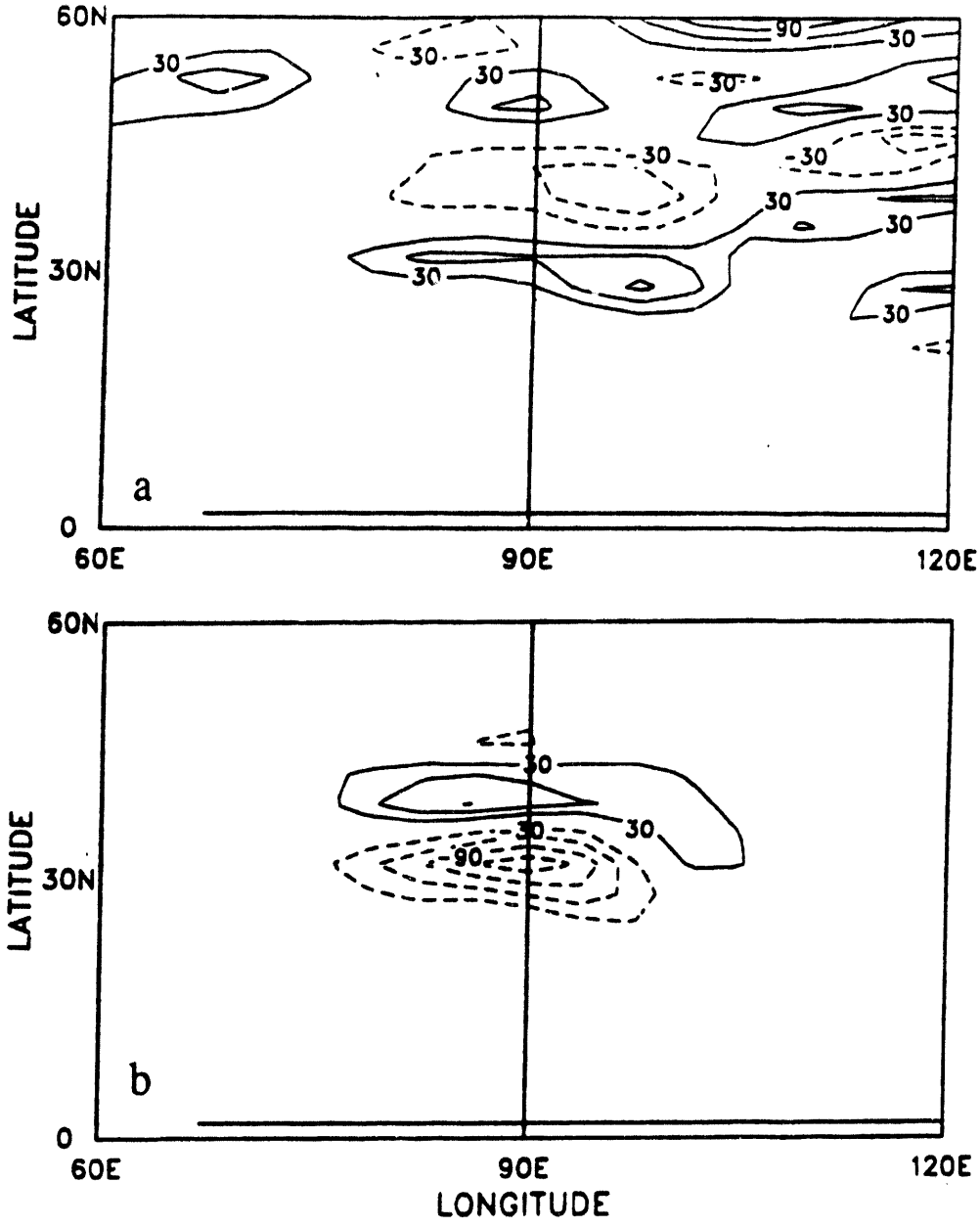

Figure 2: a) Horizontal divergence of the advective part of the PV flux, $\nabla_H \cdot (\frac{q_\eta}{g} V \left[\frac{\partial p}{\partial \eta}\right])$ $(K\,hr^{-1}\,day^{-1})$ at $\eta = .160$,

b) Horizontal divergence of the mechanical part of the PV flux, $\nabla_H \cdot (F \times \nabla_\eta \theta)$ $(K\,hr^{-1}\,day^{-1})$ at $\eta = .160$.

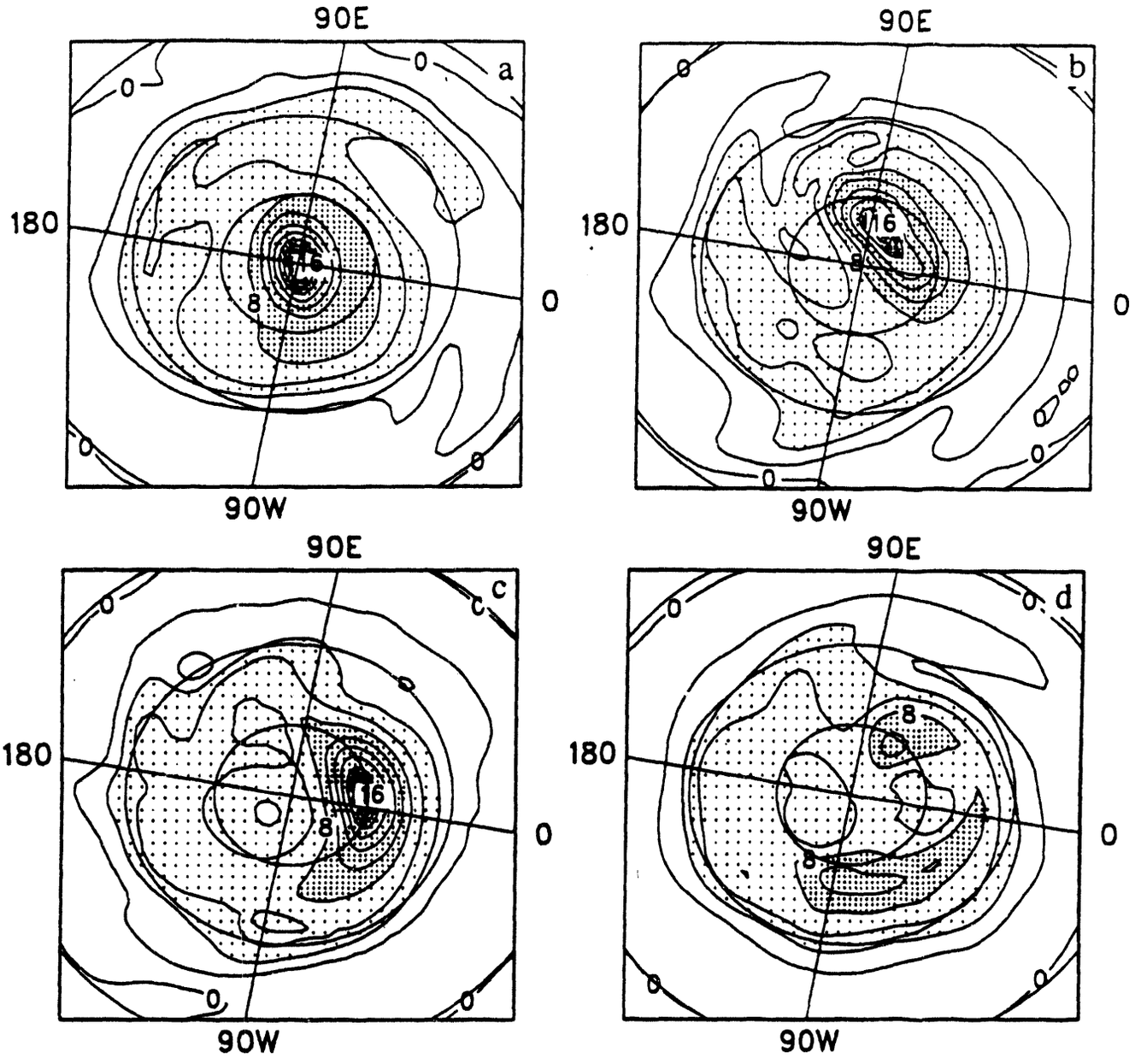

Figure 3: 850K distribution of model PV (10^{-4} K m^{-1} s^{-1}) on a) December 28, b) January 6, c) January 10 and d) January 18. The units and scaling for the fields are as in McIntyre and Palmer (1984, Appendix A).

Atlantic Interdecadal Ocean-Atmosphere Interaction

Yochanan Kushnir
Lamont-Doherty Earth Observatory of Columbia University
Palisades, NY 10964, USA

We study the climatic scale fluctuation of North Atlantic sea surface temperature (SST), and related atmospheric variability. Time series of North Atlantic SST, based on marine observations, display an almost century long swing from cold condition before 1925 to warm conditions between 1930 and the early 1960s, and back to cold conditions after 1965 or so. This fluctuation is evident with minimal processing as can be seen in Fig. 1.

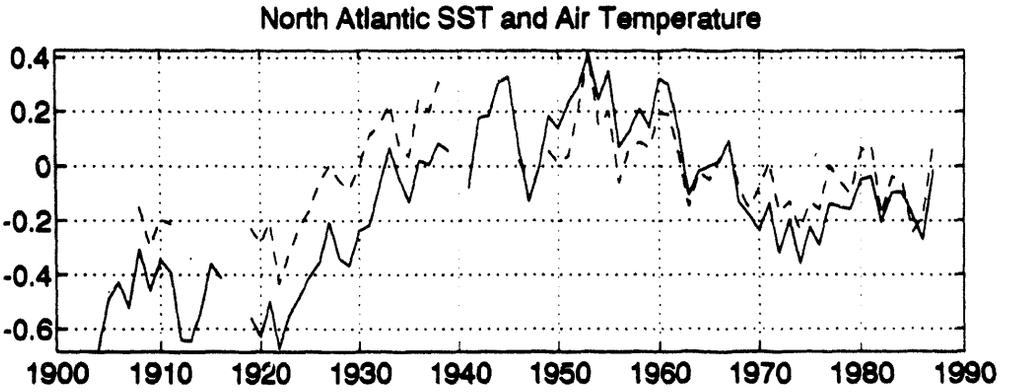

Figure 1: Time series of annual mean SST (solid) and air temperature (dashed) anomalies averaged over the North Atlantic Ocean between 30°N and 70°N. Anomalies are calculated from COADS (Comprehensive Ocean Atmosphere Data Set, Woodruff et al. 1987).with respect to the 1950-1979 climatology.

Earlier interest in the initial stages of this interdecadal temperature swing dates back to a seminal paper by Bjerknes (1964). Bjerknes showed that the gradual SST warming at the beginning of the century was associated with a sea level pressure (SLP) change corresponding to an intensification of the meridional pressure gradient across the basin. This implies that the interdecadal SST warming coincided with a strengthening of the overlying westerly winds. Such surface wind circulation will act to attenuate the underlying SST anomaly. Based on his observations, Bjerknes argued that Atlantic interdecadal ocean-atmosphere interaction entails a basin-wide interplay between ocean

and atmosphere. In contrast, he demonstrated that the ocean-atmosphere relationship associated with interannual variability displays cold SST anomalies underlying stronger than normal pressure gradients and vice versa. This pattern suggests the local thermodynamic forcing of the oceanic mixed layer by the overlying atmosphere.

Interannual ocean-atmosphere interaction was intensively studied in the past three decades (Namias, 1959; Palmer and Sun, 1985; Wallace, Smith et al., 1990; Cayan, 1992 a,b), confirming the observations and hypothesis put forward by Bjerknes (1964) regarding its nature. Recent concern with climate change sparked renewed interest in interdecadal variability. Seeking to reexamine the Atlantic interdecadal swing in SST, we compared the pattern of recent cooling with the early-century warming. Two 15-year intervals were defined corresponding to the early-century cold and warm interval seen in Fig. 1. Similar intervals were defined for the more recent period. By taking the average of the annual (January through December) SST field over each 15-year interval, and subtracting the cold-year averages from the corresponding warm-year ones, we established the patterns of up-swing and down-swing in North Atlantic SST (Fig. 2). The two patterns display a considerable degree of similarity. Both exhibit basin-wide influence with centers of action in the Greenland and Iceland Seas, in the Labrador Sea, and in the center of the midlatitude Atlantic. These areas are known to be associated with oceanic deep and intermediate water formation (e.g., Tchernia, 1980). The interdecadal SST pattern displays only minor changes when seasonal (winter or summer) data are used instead of the annual mean. The similarity between the pattern of early-century warming and the recent cooling suggests that they are both governed by the same dynamical mechanism.

The pattern of interdecadal change in SLP and surface wind conditions was determined by the same averaging procedure. Here noticeable changes occur between the winter and summer composites. Fig. 3 presents the winter composite (December through April). Both early-century and late-century composites display a large negative pressure anomaly and a cyclonic wind circulation in the middle northern basin. As noted by Bjerknes (1964), the midlatitude portion of the ocean exhibits a significant westerly wind anomaly (strengthening in the prevailing winds) over a positive SST anomaly. There exists evidence (not shown) that the atmospheric circulation in Fig. 3 is confined to the low troposphere, consistent with a shallow warming of air temperatures downstream of the midlatitude SST anomaly. A more complete description of this analysis and its results is given in Kushnir (1992).

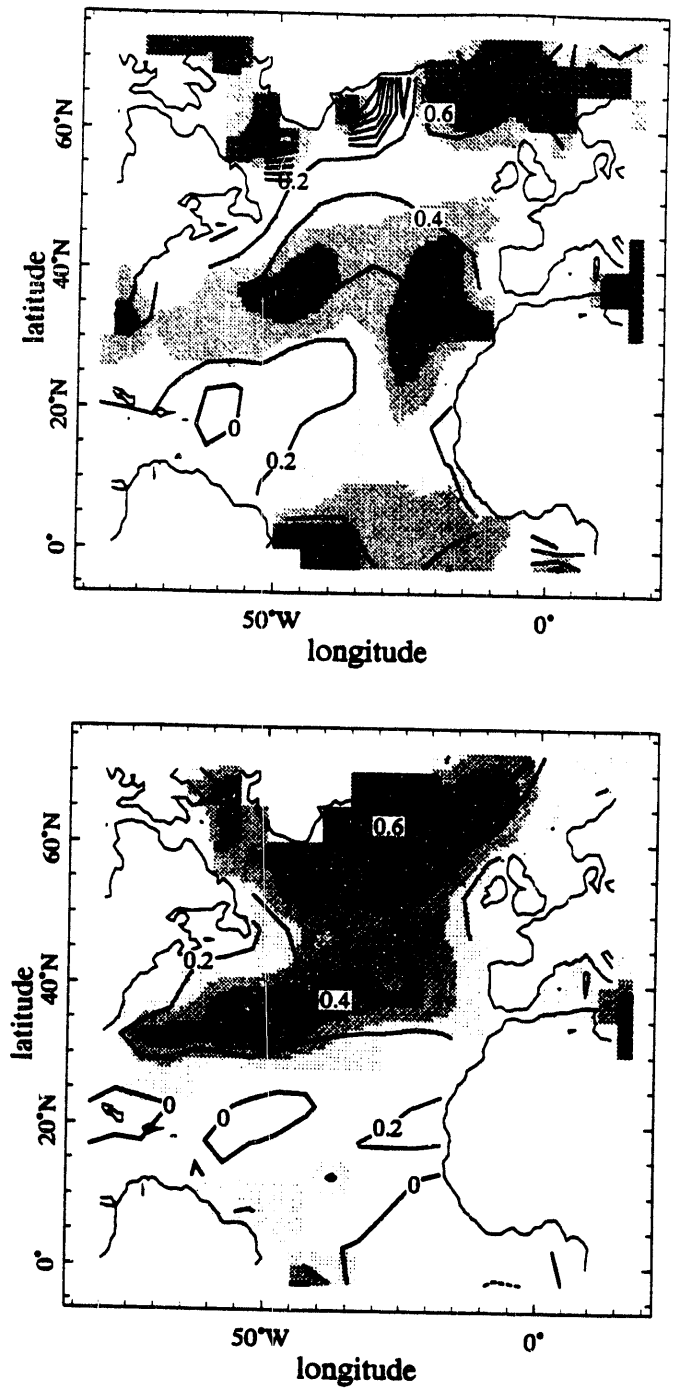

Figure 2: Upper panel: The difference between annual mean SST averaged from 1925 to 1939 (warm years), and annual mean SST averaged from 1900-1914 (cold years). Bottom panel: As above but for the average from 1950 to 1964 (warm years) minus the average from 1970 to 1984 (cold years). Contour interval is 0.2 °C, negative contours are dashed. The distribution of the corresponding t-variable is denoted in three levels of gray: Light for 2-2.5, medium for 2.5-3, and dark for 3-3.5. Data are from UK Meteorological Office archives as described in Bottomley et al. (1990).

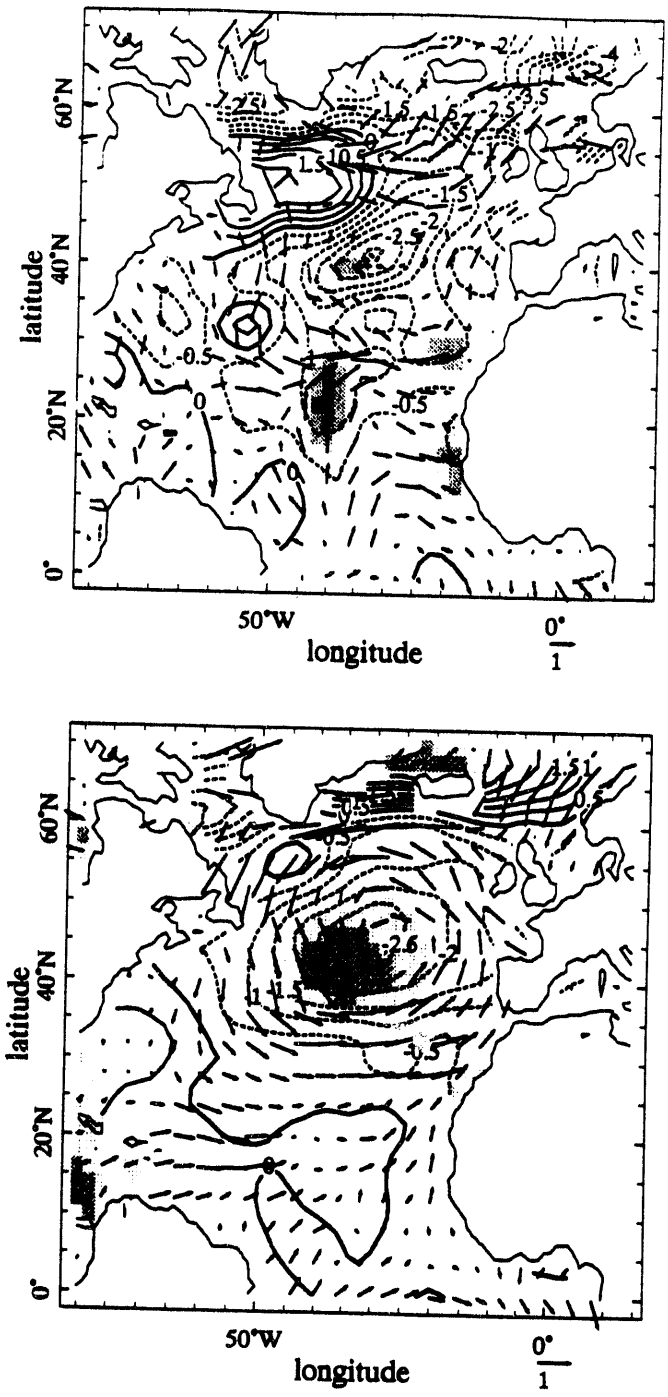

Figure 3: Upper panel: The difference between wintertime (December-April) mean sea level pressure and winds, averaged from 1925 to 1939 (warm years), and those averaged from 1900-1914 (cold years). Bottom panel: As above but for the average from 1950 to 1964 (warm years) minus the average from 1970 to 1984 (cold years). Contour interval is 0.5 mb, negative contours are dashed. The distribution of a t-variable corresponding to pressure is denoted in three levels of gray: Light for 2-2.5, medium for 2.5-3, and dark for 3-3.5. Data are from COADS.

Based on the composite patterns of Atlantic interdecadal variability, we hypothesize that the SST anomaly resulted from dynamical changes in the ocean circulation. That such anomalies may be created by internal ocean dynamics was recently shown by Delworth et al. (1993). The atmospheric pattern is more likely the quasi-stationary response to the SST change. Theoretical studies have long suggested that in the midlatitudes, a warm SST anomaly would induce a shallow atmospheric warming downstream, associated with a formation of low-level cyclone. Thermodynamic balance would be achieved in the low-troposphere by the zonal advection of the perturbation air temperature, and the anomalous meridional advection behind the low level trough (Hoskins and Karoly, 1981; Held, 1983). This was confirmed by dynamical models (Hoskins and Karoly, 1981; Hendon and Hartmann, 1982), and idealized general circulation models (GCMs, Ting, 1991). Recently, several new coarse resolution GCM experiments were conducted at the NOAA Geophysical Fluid Dynamics Laboratory (GFDL). The analysis of these experiments lends further support to our hypothesis regarding Atlantic interdecadal variability. Much remains to be understood regarding the ability of GCMs to simulate midlatitude ocean-atmosphere interaction. The models we have used display a rather weak atmospheric response mainly in the lower tropospheric thermal field. This response is stronger in idealized GCMs than in models that incorporate a full representation of the earth's orography. However, the model results display several elements in common with observations. In particular the models confirm the vertical structure of the response, and the horizontal phase relationship between the response and the SST anomalies.

References

Bjerknes, J., 1964: Atlantic air-sea interaction. *Advances in Geophysics*, H. E. Landsberg and J. V. Mieghem, ed., 1-82.

Bottomley, M., C. K. Folland, J. Hsiung, N. R.E. and D. E. Parker, 1990: *Global Ocean Surface Temperature Atlas.*, Meteorological Office Bracknell UK and Dept. of Earth, Atmospheric and Planetary Sciences, Massachusetts Institute of Technology, 20 pp. and 313 plates.

Cayan, D. R., 1992a: Latent and sensible heat flux anomalies over the northern oceans: The connection to monthly atmospheric circulation. *J. Climate*, **5**, 354-369.

_____, 1992b: Latent and sensible heat flux anomalies over the northern oceans: Driving the sea surface temperature. *J. Geophys. Oceanogr.*, **22**, 859-881.

Delworth, T., S. Manabe and R. J. Stouffer, 1993: Interdecadal variations of the thermohaline circulation in a coupled ocean-atmosphere model. *J. Climate*, in press.

Held, I. M., 1983: Stationary and quasi-stationary eddies in the extratropical atmosphere: Theory. *Large Scale Dynamical Processes in the Atmosphere*, R. P. Pearce and B. J. Hoskins, ed., 127-168.

Hendon, H. H. and D. L. Hartmann, 1982: Stationary waves on a sphere: Sensitivity to thermal feedback. *J. Atmos. Sci.*, **39**, 1906-1920.

Hoskins, B. J. and D. Karoly, 1981: The steady linear response of a spherical atmosphere to thermal and orographic forcing. *J. Atmos. Sci.*, **38**, 1179-1196.

Namias, J., 1959: Recent seasonal interaction between North Pacific Waters and the overlying atmospheric circulation. *J. Geophys. Res.*, **64**, 631-646.

Kushnir, Y., 1993: Interdecadal variations in North Atlantic sea surface temperature and associated atmospheric conditions. *J. Climate*, in press.

Palmer, T. N. and Z. Sun, 1985: A modeling and observational study of the relationship between sea surface temperature in the north west Atlantic and the atmospheric general circulation. *Q. J. Roy. Meteorol. Soc.*, **111**, 947-975.

Tchernia, P., 1980: *Descriptive Regional Oceanography*, Pergamon Press, 253 pp. 19 plates.

Ting, M., 1991: The stationary wave response to a midlatitude SST anomaly in an idealized GCM. *J. Atmos. Sci.*, **48**, 1249-1275.

Wallace, J. M., C. Smith and Q.-R. Jiang, 1990: Spatial patterns of atmosphere/ocean interaction in the northern winter. *J. Climate*, **3**, 990-998.

Woodruff, S. D., R. J. Slutz, R. L. Jenne and P. M. Steurer, 1987: A comprehensive ocean-atmosphere data set. *Bull. Am. Meteorol. Soc.*, **68**, 521-527.

CLIMATOLOGICAL FEATURES OF BLOCKING ANTICYCLONES

Anthony R. Lupo Phillip J. Smith Robert J. Oglesby

Department of Earth and Atmospheric Sciences
Purdue University
West Lafayette, IN 47907

1. INTRODUCTION

Several climatological studies have been previously performed using large observational data sets (i.e., 10 years or longer) in order to determine the predominant characteristics of blocking anticyclones, including favored development regions, duration, preferred seasonal occurrence, and frequency of occurrence (e.g., Rex, 1950; Triedl et al. 1981; and Lejenas and Oklund, 1983). These studies have shown that blocking anticyclones occur most frequently from October to April over the eastern Atlantic and Pacific oceans downstream from both the North American and Asian continental regions and the storm track regions to the east of these continents. Some studies have also revealed the presence of a third region of block formation in western Russia near 40^{o} E (Triedl, et al. 1981; and Dole and Gordon, 1983) which is associated with another storm track region over the Mediterranean and western Asia.

The objective of this study was to construct a three-year observational climatology from ECMWF analyses that not only examined standard blocking anticyclone characteristics, such as those above, but also was unique in several ways. First, it examined a broader range of characteristics as a function of region and season, including size and intensity. Second, an investigation of upstream cyclones that precede block formation was performed. Third, following the suggestion of Tsou and Smith (1990), a study of the occurrence of jet maxima between the upstream cyclones and the blocks is included. Fourth, the observational climatology was compared with a five-year winter climatology derived from the National Center for Atmospheric Research (NCAR) Community Climate Model, Version 1 (CCM1) simulation, and referred to as the control run. Fifth, a second five-year climatolgy was derived from a CCM1 simulation with double the control-run CO_2 concentration and compared to the control simulation to determine how increased CO_2 concentrations may affect the climatological characteristics of blocking anticyclones.

2. DATA AND METHODOLOGY

The ECMWF analyses are global in domain with a 2.5° latitude by 2.5° longitude resolution and consist of uninitialized gridded fields of both surface and free atmosphere variables twice daily from July 1, 1985 through June 30, 1988. A thorough description of the data set, which was provided for use by NCAR, can be found in Trenberth (1992). The variables used in the observational study were 500 mb geopotential height, 300 mb horizontal wind components, and sea-level pressure. The CCM1 is a global pseudo-spectral general circulation model (GCM) and has a horizontal resolution equivalent to 4.5° latitude by 7.5° longitude with 12 layers in the vertical (Blackmon, 1986; Williamson et al. 1987). It is important to note that both model simulations were run with the same initial conditions except for CO_2 concentration. Equivalent five-year periods of once daily model 500 mb geopotential heights were chosen from each case. For a thorough description of the initial conditions and strategies used in the model simulation, experimentation, and the data selection refer to Oglesby and Saltzman (1992).

The formulation of an appropriate blocking definition is an intriguing problem since no commonly agreed upon definition of blocking exists and almost all contain some subjectivity. The most well-known definition was provided by Rex (1950). In this investigation a combination of the Rex definition and the objective criterion of Lejenas and Oklund (1983) were the primary means used to define blocking events. The criterion of Lejenas and Oklund (LO), which is based on the zonal index of Namias and Clapp (1951) diagnoses blocking in regions where the difference between the 500 mb geopotential heights at 40° N and 60° N is small. This choice of latitudes is based on the findings of Triedl et al (1981). In the CCM1 simulations, it was necessary to use 42.5° N and 60.0° N as the latitude limits for this calculation. The size of each blocking event was determined as the distance across the anticyclone between inflection points, while the intensity was a normalized form of the maximum 500 mb height in the anticyclone averaged over the lifetime of the event. The upstream cyclones and associated jet maxima were located observationally by using the sea-level pressure and 300 mb horizontal wind components, respectively. The intensity of cyclogenesis was determined as the 12-h central pressure change in Bergerons (Sanders and Gyakum, 1980). The Northern Hemisphere was divided into three domains in which all blocking events were placed based on where the event initiated. The Atlantic, Pacific and Continental domains extended from 80° W to 40° E longitude, 140° E to 100° W, and 40° E to 140° E (Eurasian continent) and 100° W to 80° W (North American

continent), respectively. Winter, spring, summer, and fall were defined as the three month periods beginning with January, April, July, and September, respectively.

3. RESULTS AND DISCUSSION

a. The observational climatology

A total of 63 blocking anticyclone cases were found in the three-year period and they were concentrated in three preferred regions of development (Fig. 1a). Two of these were located over the oceanic regions and the third was located over the Eurasian continental region. The Atlantic and Continental regions of preferred block formation (near 10^{o} W and 40^{o} E, respectively) correspond well with the results of Triedl, et al (1981). The broad maximum representing the Pacific formation region is similar to the composite results of past studies (Rex, 1950, White and Clark, 1975, and Triedl, et al. 1981). Generally, the maximum frequency of occurrence and longest lifetimes for blocking events were in the winter months (Fig. 2). Atlantic blocking events were stronger, more numerous, and persisted longer than their Pacific or Continental counterparts, and fall and winter events tended to be stronger than their summer and winter counterparts. The average size tended to be larger in the winter than in the summer over the Atlantic and Continental domains, while the sizes of Pacific events displayed no regular seasonal trend. An analysis of cyclone activity reveals that every blocking event was preceded by an upstream cyclone and the occurrence of a jet maximum between the cyclone and the blocking anticyclone, as suggested by Tsou and Smith (1990). Cyclones that preceded oceanic (winter) blocking events developed more vigorously than their continental (summer) counterparts, and consequently a positive correlation between the intensity of cyclogenesis and block intensity was found.

b. Comparison of the model control to the observational climatology for the winter season

Comparing the regions of preferred formation (Fig. 1b,c), the model performed well by capturing the broad maximum that defines the Pacific formation region between the dateline and 130^{o} W. In the Atlantic the model captured the sharp maximum at 20^{o} W, but there was a tendency for CCM1 blocking events to occur to the west of this maximum. This result was probably due to the corresponding placement of the North American east coast storm track one grid point south and west of the observed storm track. Finally, the model results failed to show the western Russian maximum found in the observed results. The probable reason for this failure is that the model did not adequately resolve the storm track in the Mediterranean-western Asia region found in the observations.

Other model blocking characteristics in this study that compared favorably to observations were the frequency of occurrence and horizontal size. The frequency of occurrence over the Atlantic and Pacific regions compared well with observations, while the model did not capture the occurrence of continental blocking events. The horizontal size of CCM1 blocking events compared very favorably to observed, but at the same time model blocks were generally shorter-lived and less intense than observed. The shorter duration of CCM1 blocks was found in all domains. Much of the overall difference in intensity was directly attributable to Atlantic events, as events in the other two domains compared favorably to observed.

c. Comparison of the control simulation to the double CO_2 simulation winter climatologies.

In general, the double CO_2 simulation (DCS) placed blocking anticyclones further north than the control simulation (CS). This is consistent with the results of Oglesby and Saltzman (1992), who show that the mean flow is slightly weaker and displaced slightly northward in the DCS. The preferred region of block formation over the Pacific in the DCS was similar to the CS and the observed (OBS) results, and the western Russian land maximum found in the OBS appeared in the DCS (Fig. 1d). A more dramatic westward shift in the DCS compared to the CS in the broad Atlantic formation region was noted. Also, there were DCS events that formed over the North American continent, a feature that was conspicuously absent from the CS and OBS. In comparing the frequency of blocking events, the DCS compared favorably with the CS for the total occurrences and occurrences in each domain. Individual DCS blocking events were smaller than the CS events, perhaps reflecting the northward displacement of DCS blocking anticyclones by almost 5^{o} latitude. In the DCS, the average intensities of CCM1 blocks were regionally homogeneous and, in general, were less intense than the CS and OBS events. When examining the duration of blocking events in the DCS, the average event lasted longer than those in the CS with most of the increase accounted for by increases in the persistence of Pacific and continental domain blocking events. Therefore, an increase in CO_2 in our atmosphere may mean that blocking events will be smaller and weaker, but persist longer.

4. SUMMARY AND CONCLUSIONS

A three-year observational and two five-year model climatologies using ECMWF analyses and CCM1 output for present day and double CO_2 concentration simulations were compiled and analyzed using the same methods in each case. The observational climatology, while temporally shorter than other published works, exhibited similar

characteristics to the earlier results of Lejenas and Oklund (1983). Results also showed that the scenario suggested by Tsou and Smith (1990) described the relationship of block formation to the upstream cyclogenesis in all 63 observed events. The CCM1 simulated winter blocks compared favorably to observed blocks in several ways. Simulated block locations were similar to those observed in the Pacific region and were within a model grid point south and west in the Atlantic. Also, the intensity, with the exception of the Atlantic domain, the frequency of occurrence, and size of simulated blocking events matched those of the observed events. Finally, model results suggest that in an increased CO_2 world blocking anticyclones may be smaller, weaker, and located farther north, but will be more persistent, than their current counterparts.

5. REFERENCES

Blackmon, M.L., 1986: Building, testing, and using a GCM. Mathematical and Physical Sciences, 190C, 1-67.

Dole, R. M., and N. D. Gordon, 1983: Persistent anomalies of the extra-tropical Northern Hemisphere wintertime circulation: Geographical distribution and regional persistence characteristics. Mon. Wea. Rev., 111, 1567-1586.

Lejenas, and H. Oklund, 1983: Characteristics of Northern Hemisphere blocking as determined from a long time series of observational data. Tellus, 35A, 350-362.

Namias, J., and P.F. Clapp, 1951: Observational studies of general circulation patterns. Compendium of Meteorology, American Meteorological Society.

Oglesby, R.J., and B. Saltzman, 1992: Equilibrium climate statistics of a general circulation model as a function of atmospheric carbon dioxide. Part I: Geographical distributions of primary variables. J. Climate, 5, 66-92.

Rex, D. F., 1950: Blocking action in the middle troposphere and it's affect on regional climate II. The climatology of blocking actions. Tellus, 2, 275-301.

Sanders, F., and J.R. Gyakum, 1980: Synoptic-dynamic climatology of the "bomb". Mon. Wea. Rev., 108, 2421-2430.

Trenberth, K. E., 1992: Global analyses from ECMWF and atlas 1000 to 10 mb circulation statistics. NCAR Tech. Note, NCAR/TN-373+STR June 1992, National Center for Atmospheric Research, Boulder, CO, 80303,191pp.

Triedl, R. A., E. C. Birch, and P. Sajecki, 1981: Blocking action in the Northern Hemisphere: A climatological study. Atmosphere-Ocean, 19, 1-23.

Tsou, C. -H. and P.J. Smith, 1990: The role of synoptic/planetary-scale interactions during the development of a blocking anticyclone. Tellus, 42A, 174-193.

Williamson, D.L., J.T. Kiehl, V. Ramanathan, R.E. Dickenson, and J.J. Hack, 1987: Description of the NCAR Community Climate Model. NCAR Tech. Note NCAR/TN-302+STR, Boulder, CO 80303, 199 pp.

White, W.B., and N.E. Clark, 1975: On the development of blocking ridge activity over the central North Pacific. J. Atmos. Sci., 32, 489-502.

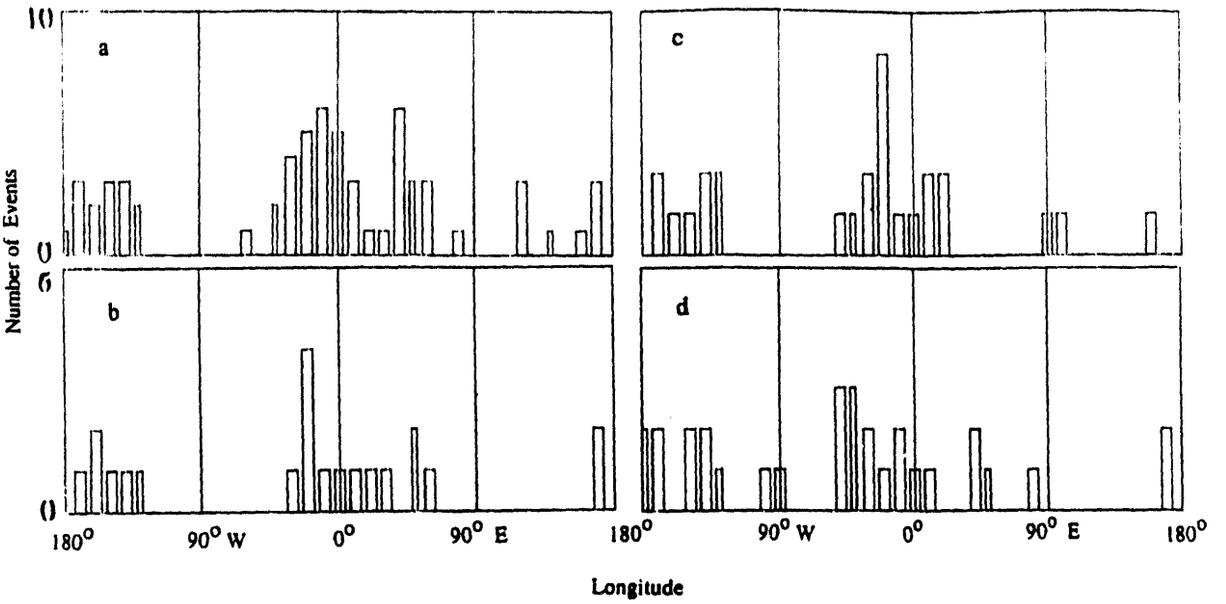

Figure 1. Number of blocking events vs. longitude for a) all observed events, b) observed winter events, c) the control winter events, and d) the double CO_2 winter events.

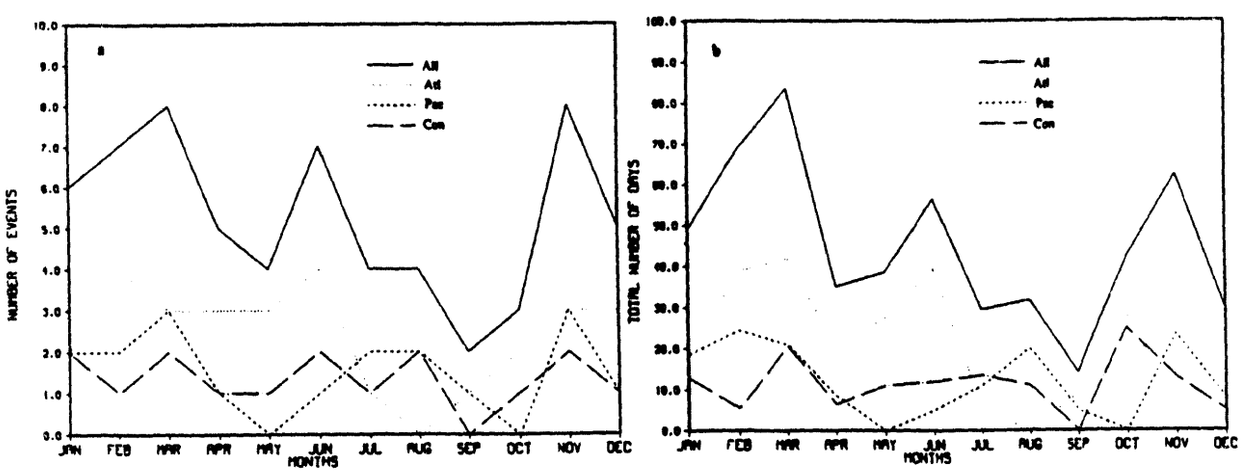

Figure 2. Monthly a) number of events and b) total number of days for observed blocks.

POTENTIAL VORTICITY DYNAMICS FOR GLOBAL SCALE CIRCULATIONS

Chungu Lu and Wayne Schubert
Department of Atmospheric Science
Colorado State University
Fort Collins, CO 80523

1. INTRODUCTION

One of the most notable advances in extratropical dynamics this decade has been the understanding of large-scale atmospheric and oceanic processes by using potential vorticity dynamics (Hoskins *et al.*, 1985; Rhines, 1986; Haynes and McIntyre, 1987; 1990), the so called "IPV thinking". This analysis method has also been successfully extended to some tropical atmospheric circulation systems such as hurricanes and the Hadley circulation (Schubert and Alworth, 1987; Schubert *et al.*, 1991). The fundamental idea behind such a dynamic system rests with the fact that PV is a tracer-like quantity since it is conserved (in the absence of friction and diabatic heating) following a fluid particle and carries both significant dynamic and thermodynamic information regarding fluid motion. Thus, the prediction and inversion of PV form the most succinct dynamic view of atmospheric and oceanic motions. Furthermore, PV dynamics provides access to many insightful dynamic analyses such as: propagation of Rossby waves, barotropic and baroclinic instabilities for shear flows, and wave-mean flow interactions. All these features make IPV analysis a very attractive tool for studying geophysical fluid systems.

The success of PV dynamics in both midlatitude and tropics suggests a unified theory that preserves the succinct PV view for a global-scale circulation. To try to extend such extratropical PV dynamics systems as the quasi-geostrophic and semigeostrophic theories to a global scale is not a trivial task. Apart from the feasibility to include an equatorial flow as the part of balanced system, two aspects related to the earth's geometry still need to be considered: (1) the full variation of the Coriolis parameter; and (2) the curvature effect. Using Hamilton's principle, Salmon (1985) and Shutts (1989) derived a variable-f semigeostrophic theory and a planetary semigeostrophic theory, respectively. Magnusdottir and Schubert (1990, 1991) proposed a β-plane and a hemispheric semigeostrophic theory. However, these theories take only the variation in the Coriolis parameter into consideration, but add no curvature vorticity to the total PV analysis.

In this study, we present an effort to extend a classical extratropical PV dynamical model to a global scale.

2. THE GOVERNING EQUATIONS AND THE CONSERVATION PRINCIPLES

a. The governing equations with the zonal and geostrophic momentum approximation

Using the combined geostrophic-gradient momentum approximation, which generalizes the geostrophic momentum (GM) approximation of the Eliassen type by properly including the curvature effect, we can write the set of governing equations expressed in the spherical and entropy coordinate system (λ, ϕ, s) in the form:

$$\frac{Du_g}{Dt} - \left(2\Omega\sin\phi + \frac{u_g\tan\phi}{a}\right)v + \frac{\partial M}{a\cos\phi\partial\lambda} = 0, \quad (2.1)$$

$$\frac{Dv_g}{Dt} + \left(2\Omega\sin\phi + \frac{u_g\tan\phi}{a}\right)\frac{u}{\gamma} + \frac{\partial M}{\gamma a\partial\phi} = 0, \quad (2.2)$$

$$\frac{\partial M}{\partial s} = T, \quad (2.3)$$

$$\frac{D\sigma}{Dt} + \sigma\left(\frac{\partial u}{a\cos\phi\partial\lambda} + \frac{\partial(v\cos\phi)}{a\cos\phi\partial\phi} + \frac{\partial\dot{s}}{\partial s}\right) = 0, \quad (2.4)$$

where

$$\frac{D}{Dt} = \frac{\partial}{\partial t} + u\frac{\partial}{a\cos\phi\partial\lambda} + v\frac{\partial}{a\partial\phi} + \dot{s}\frac{\partial}{\partial s}, \quad (2.5)$$

is the total derivative, and (u, v) the total zonal and meridional components of the velocity, while u_g the gradiently balanced zonal wind defined as

$$\left(2\Omega\sin\phi + \frac{u_g\tan\phi}{a}\right)u_g + \frac{\partial M}{a\partial\phi} = 0, \quad (2.6)$$

and v_g the geostrophically balanced meridional wind, i.e.,

$$fv_g = \frac{\partial M}{a\cos\Phi\partial\lambda}, \quad (2.7)$$

where $f = 2\Omega\sin\Phi$ is the Coriolis parameter. Note that Φ, different from ϕ, is the potential latitude which will be defined later. Although the occurrence of two kinds of latitudes in the same dynamical system seems somewhat awkward, it is of benefit when coordinate transformations are introduced in the next section. The Coriolis parameter therefore, under such a definition, is evaluated at the transformed latitude, the potential latitude, rather than the physical latitude. The curvature parameter γ in (2.2) is defined as

$$\gamma = \left(\frac{\cos\phi}{\cos\Phi}\right)\frac{2\Omega\sin\phi + u_g\tan\phi/a}{f}, \quad (2.8)$$

i.e., it measures the ratio of the combined planetary vorticity and relative curvature vorticity to the planetary vorticity itself. In accordance with this, we see that when the curvature vorticity is small compared with the planetary vorticity, Φ approximately equals ϕ [cf. (3.1)], and $\gamma \approx 1$. Then the whole system reduces to the semigeostrophic equations. If we further replace (u_g, v_g) by their full counterparts (u, v), (2.1)–(2.5) revert to the primitive equations. Together with the equation of the state (Note that the thermodynamic equation is implicit in the coordinate system), (2.1)–(2.7) form a closed system, i.e., there are seven equations for the seven unknowns u, v, u_g, v_g, M, T and σ (the formula that defines the potential latitude will be given in the next section).

b. The conservation principles

(1) The angular momentum principle:

$$\frac{Dm_g}{Dt} + \frac{\partial M}{\partial \lambda} = 0, \tag{2.9}$$

where $m_g = a\cos\phi(u_g + \Omega a\cos\phi)$ is the approximated absolute angular momentum. For a zonally symmetric flow, the second term in this equation disappears, resulting in conservation of absolute angular momentum following the motion of a fluid particle.

(2) The total energy equation:

$$\frac{\partial}{\partial t}(\sigma(K_g + c_p T)) + \frac{\partial}{a\cos\phi\partial\lambda}(\sigma u(K_g + M)) + \frac{\partial}{a\cos\phi\partial\phi}$$

$$(\sigma v(K_g + M)\cos\phi) + \frac{\partial}{\partial s}\left(\sigma\dot{s}(K_g + M) - gz\frac{\partial p}{\partial t}\right) = \sigma Q, \tag{2.10}$$

where $K_g = \frac{1}{2}(u_g^2 + v_g^2)$ is the combined geostrophic-gradient kinetic energy.

(3) The three dimensional vorticity equation:

$$\frac{D\zeta}{Dt} + \zeta\left(\frac{\partial u}{a\cos\phi\partial\lambda} + \frac{\partial(v\cos\phi)}{a\cos\phi\partial\phi}\right) - \left(\xi\frac{\partial\dot{s}}{\partial\lambda} + \eta\frac{\partial\dot{s}}{\partial\sin\phi}\right) = 0, \tag{2.11}$$

where

$$(\xi, \eta, \zeta) = f\left(\frac{\partial(\Lambda, \sin\Phi)}{\partial(\sin\phi, s)}, \frac{\partial(\Lambda, \sin\Phi)}{\partial(s, \lambda)}, \frac{\partial(\Lambda, \sin\Phi)}{\partial(\lambda, \sin\phi)}\right) \tag{2.12}$$

is the vorticity vector associated with the geostrophic and gradient winds.

(4) The potential vorticity equation:

$$\sigma\frac{DP}{Dt} = \left(\xi\frac{\partial}{\partial\lambda} + \eta\frac{\partial}{\partial\sin\phi} + \zeta\frac{\partial}{\partial s}\right)\dot{s}, \tag{2.13}$$

where $P = \zeta_r$ is potential vorticity.

3. THE CLOSED PV DYNAMIC SYSTEM

Following the formalism of semigeostrophic theory (Hoskins, 1975), we now seek a set of new coordinates which allows us to reformulate the problem. Our goal is to transform (2.1) and (2.2) to their canonical forms, and to combine or replace these transformed equations so that they can ultimately form not only a closed but also a concise system. In accordance with the angular momentum principle, let us define a potential latitude as Φ to satisfy

$$\Omega a^2\cos^2\Phi = a\cos\phi(u_g + \Omega a\cos\phi). \tag{3.1}$$

From this definition we see that the potential latitude Φ is the latitude to which an air parcel must be moved (conserving its absolute angular momentum) in order for its relative angular momentum to vanish. It can also be written in the form

$$\sin\Phi = \sin\phi - \frac{u_g\cos\phi}{\Omega a(\sin\Phi + \sin\phi)}. \tag{3.2}$$

When ϕ is approximated by Φ in the second term on the right-hand-side of (3.2), this potential latitude formula reduces to the spherical geostrophic coordinate that has been used by Magnusdottir and Schubert (1991) in deriving the hemispherical semigeostrophic theory.

We next need to consider the other horizontal coordinate. Since we assumed that the meridional momentum is in geostrophic balance, it is natural to introduce the geostrophic longitude correspondingly, that is, the longitude fluid particles would have if they moved with their geostrophic velocity at every instant. Mathematically, this coordinate can be written as

$$\Lambda = \lambda + \frac{v_g}{2\Omega a\sin\Phi\cos\Phi}. \tag{3.3}$$

We also define $S = s$ and $T = t$ as the new vertical and time coordinates, noting that $\partial/\partial s$ and $\partial/\partial t$ imply fixed r, ϕ while $\partial/\partial S$ and $\partial/\partial T$ imply fixed R, Φ. With these newly defined coordinates, we can now proceed to transform our balanced system (2.1)–(2.5) from (λ, ϕ, s, t) space to (Λ, Φ, S, T) space.

In transformed space, the total derivative (2.5) can be written as

$$\frac{D}{Dt} = \frac{\partial}{\partial T} + U\frac{\partial}{a\cos\Phi\partial\Lambda} + V\frac{\partial}{a\partial\Phi} + \dot{S}\frac{\partial}{\partial S}, \tag{3.4}$$

where

$$(U, V, \dot{S}) = \left(a\cos\Phi\frac{D\Lambda}{Dt}, a\frac{D\Phi}{Dt}, \frac{DS}{Dt}\right), \tag{3.5}$$

is the vector velocity in the transformed space.

The two horizontal momentum equations (2.1) and (2.2) can be transformed to their canonical forms

$$2\Omega\sin\Phi a\frac{D\Phi}{Dt} = \frac{\partial M^*}{a\cos\Phi\partial\Lambda}, \tag{3.6}$$

$$-2\Omega\sin\Phi a\cos\Phi\frac{D\Lambda}{Dt} = \frac{\partial M^*}{a\partial\Phi}. \tag{3.7}$$

It is interesting to note that the horizontal advective winds in the Lagrangian time derivative (3.4) are related to the Bernoulli function $M^* = M + \frac{1}{2}(u_g^2 + v_g^2)$ in such

a way that they are formally in geostrophic balance. Therefore, the major advantage of the transformation from (λ, ϕ, s, t) space to $(\Lambda, \Phi, S, \mathcal{T})$ space is that the two momentum equations are reduced to their canonical forms and substitutions of these equations into (3.4) result in the absence of ageostrophic and agradient advections. In addition, for adiabatic flow the vertical advection does not appear in (3.4), so that the total advective operator becomes quasi-horizontal in such a coordinate space.

With these relations, we can rewrite the potential vorticity equation in terms of potential pseudodensity ($P\sigma^* = 2\Omega \sin\Phi$), which gives a flux form:

$$\frac{\partial \sigma^*}{\partial \mathcal{T}} + \frac{\partial (U\sigma^*)}{a\cos\Phi \partial\Lambda} + \frac{\partial (V\sigma^* \cos\Phi)}{a\cos\Phi \partial\Phi} + \frac{\partial (\dot{S}\sigma^*)}{\partial S} = 0, \quad (3.8)$$

By the definition of σ^*, we can derive the invertibility principle:

$$\frac{\partial(\lambda, \sin\phi, p)}{\partial(\Lambda, \sin\Phi, S)} + \sigma^* = 0, \quad (3.9)$$

where it can be shown that λ, $\sin\phi$, p can all be expressed in terms of M^*. Thus, (3.9) presents a nonlinear eliptic equation for the single variable M^*. Eqs. (3.8) and (3.9) form a closed dynamic system, which preserves the unified view of PV dynamics (Hoskins *et al.*, 1985).

4. ROSSBY-HAURWITZ WAVES

We have derived a general PV dynamical system which we claim to have solutions for both the Hadley symmetric overturning and the Rossby wave motions. While we can prove that the zonally symmetric balanced theory is a special case of the present theory in the next section, here we solve (3.8) and (3.9) for their linear solutions. The resulting Rossby-Haurwitz wave solutions are then compared with those from the primitive equations by Longuet-Higgins (1968).

We begin by assuming adiabatic motion $\dot{s}$=0, and a basic state of rest with Boussinesq density profiles both in physical and pseudo-physical spaces. This basic state is summarized below:

$$\left\{ \begin{array}{c} \bar{\rho} = \rho_0 = const. \\ \bar{\sigma}^* = \sigma_0 = \frac{\rho_M - \rho_T}{S_T - S_B} = const. \\ \bar{u}_g = 0, \quad \bar{v}_g = 0 \end{array} \right\} \quad (4.1)$$

where the bar quantities denotes the quantities at basic state, ρ is the density in physical space.

With this basic state, we can linearize the potential pseudodensity equation in the form:

$$\frac{\partial}{\partial \mathcal{T}} \left(\frac{\sigma^{*\prime}}{\sigma_0} \right) - \frac{1}{2\Omega a \sin^2\Phi} \frac{\partial M^{*\prime}}{a\partial\Lambda} = 0, \quad (4.2)$$

and the invertibility principle in the form:

$$\frac{\sigma^{*\prime}}{\sigma_0} = \frac{\partial}{\cos\Phi \partial\Phi} \left[-\frac{\cos\Phi}{(2\Omega a \sin\Phi)^2} \frac{\partial M^{*\prime}}{\partial\Phi} \right] - \frac{\rho_0 R}{\kappa \sigma_0} \frac{\partial^2 M^{*\prime}}{\partial S^2}$$

$$+ \frac{\partial}{\partial\Lambda} \left[\frac{1}{(2\Omega a \sin\Phi \cos\Phi)^2} \frac{\partial M^{*\prime}}{\partial\Lambda} \right]. \quad (4.3)$$

We now combine the predictive equation (4.2) and the diagnostic equation (4.3) together to yield

$$\frac{\partial}{\partial \mathcal{T}} \left[\frac{\partial^2 M^{*\prime}}{\cos^2\Phi \partial\Lambda^2} + \frac{\sin^2\Phi}{\cos\Phi} \frac{\partial}{\partial\Phi} \left(\frac{\cos\Phi}{\sin^2\Phi} \frac{\partial M^{*\prime}}{\partial\Phi} \right) + \frac{4\Omega^2 a^2 \sin^2\Phi}{\Gamma_0 \sigma_0} \frac{\partial^2 M^{*\prime}}{\partial S^2} \right] + 2\Omega \frac{\partial M^{*\prime}}{\partial\Lambda} = 0, \quad (4.4)$$

where we have denoted $\Gamma_0 = \kappa/(R\rho_0) = 1/(c_p\rho_0)$.

We assume that the vertical structure of the motion is separable from the horizontal structure so that the allowable solution of (4.4) takes the form

$$M^{*\prime}(\Lambda, \Phi, S, \mathcal{T}) = \mathcal{M}(\Phi) \cos\left[\frac{\alpha_m (S_T - S)}{S_T - S_B} \right] e^{i(s\Lambda + \sigma\mathcal{T})}, \quad (4.5)$$

where α_m is the separation constant which will be discussed as we proceed, S_T and S_B are the values of entropy at top and bottom of model domain, s is the zonal wavenumber, and σ is the frequency.

The substitution of the wave solution (4.5) leads to the meridional structure equation

$$\mathcal{L}(\mathcal{M}) = \epsilon_m \mathcal{M}, \quad (4.6)$$

where $\mathcal{L}$ denotes the linear operator

$$\mathcal{L} = \frac{d}{\cos\Phi d\Phi} \left(\frac{\cos\Phi}{\sin^2\Phi} \frac{d}{d\Phi} \right) + \frac{1}{\sin^2\Phi} \left(\frac{s}{\omega} - \frac{s^2}{\cos^2\Phi} \right), \quad (4.7)$$

and $\omega = \sigma/2\Omega$ is the normalized frequency.

In (4.6), the constant ϵ_m denotes Lamb's parameter, which is

$$\epsilon_m = \frac{4\Omega^2 a^2}{c_m^2} \quad (4.8)$$

where $c_m = c/\alpha_m$ is the phase speed of gravity waves for different internal modes, and $c^2 = \Gamma_0 \sigma_0 (S_T - S_B)^2$. The separation constant α_m can be obtained from the linearized lower boundary condition, which is

$$\alpha_m \tan\alpha_m = \frac{S_T - S_B}{c_p}. \quad (4.9)$$

The solutions of this transcendental equation give the values of α_m and c_m, and hence Lamb's parameter ϵ_m.

In Longuet-Higgins (1968), the eigensolutions calculated from the Laplace tidal equations are presented in terms of constant Lamb's parameters with decreasing powers of ten. In accordance with the values we used for calculating ϵ_m, we may approximately regard his solutions for $\epsilon_0 = 10$ as the external mode, and those for $\epsilon_1 = 1000$ as the first internal mode, etc. For convenience of comparison of our results with the Laplace tidal equation results of Longuet-Higgins (1968), let us solve the meridional structure equation (4.6) for $\epsilon_m = 1, 10, 100, 1000$, and take the consistent normalization factors for eigenfunctions. Equation (4.6) is first

rewritten in the form of a standard eigenvalue problem, then discretized in the meridional direction on a uniform grid with a resolution of 1° of latitude. The problem is solved in a hemispheric domain (from equator to north pole). Since the gradient and geostrophic wind relations are not valid at equator, we require both u_g and v_g to vanish at the equatorial boundary. The results after solving the eigenvalue problem are shown in Table 1, along with the corresponding modes listed from the primitive equation solution of Longuet-Higgins (1968).

The balanced mass and wind fields are presented in Fig. 1 for zonal wavenumber 1 and 2, as functions of latitude. The different curves are for different Lamb's parameters. In comparison with the eigenfunctions computed from the Laplace tidal equations (the primitive equations) for waves of the second class by Longuet-Higgins (1968, Fig. 10 and 13), we can see that our new balanced model produces consistent pressure and zonal wind fields. The only difference between the two models is in the meridional wind field equatorward of 20°.

5. ZONALLY SYMMETRIC DYNAMICS

In this section we demonstrate that the zonally symmetric balanced theory proposed by Hack *et al.* (1989) and Schubert *et al.* (1991) is a two dimensional special case of our new balanced theory developed in this paper. This result suggests that the theory presented here is consistent with zonally symmetric balanced theory so that part of the solutions of this system depicts the Hadley symmetric circulation.

We begin by considering the zonal symmetry condition in our generalized three dimensional model, i.e., letting all terms involving $\partial/\partial\lambda$ (or $\partial/\partial\Lambda$ in the transformed space) be zero, except for the term $\partial\Lambda/\partial\lambda$ being unity. In doing so, from (2.6), (2.7) and (2.2), we deduce that

$$u = u_g, \quad u_a = 0, \tag{5.1}$$

$$v = v_a, \quad v_g = 0, \tag{5.2}$$

which indicate that the meridional wind becomes purely ageostrophic, while the zonal wind is purely gradient. This is precisely the view used in zonally symmetric balanced theory. With the use of (5.1) and (5.2) the set of governing equations (2.1)–(2.5) reduce to

$$\frac{Du}{Dt} - \left(2\Omega\sin\phi + \frac{u\tan\phi}{a}\right)v = 0, \tag{5.3}$$

$$\left(2\Omega\sin\phi + \frac{u\tan\phi}{a}\right)u + \frac{\partial M}{a\partial\phi} = 0, \tag{5.4}$$

$$\frac{\partial M}{\partial s} = T, \tag{5.5}$$

$$\frac{D\sigma}{Dt} + \sigma\left(\frac{\partial(v\cos\phi)}{a\cos\phi\partial\phi} + \frac{\partial\dot{s}}{\partial s}\right) = 0, \tag{5.6}$$

where the total derivative now becomes

$$\frac{D}{Dt} = \frac{\partial}{\partial t} + v\frac{\partial}{a\partial\phi} + \dot{s}\frac{\partial}{\partial s}. \tag{5.7}$$

By comparing with (2.1)–(2.5) in Schubert *et al.* (1991), one will see that these are the s-coordinate versions of the two-dimensional, zonally symmetric balanced equations on the sphere.

In transformed space, after we impose the zonally-symmetry condition $\partial/\partial\Lambda = 0$ in the PV system of (3.8)–(3.9), the fundamental predictive equation for potential pseudodensity (3.8) reduces to a very simple form:

$$\frac{\partial\sigma^*}{\partial T} + \frac{\partial(\dot{s}\sigma^*)}{\partial S} = 0, \tag{5.8}$$

and the invertibility principle (3.9) for an idealized zonally-symmetric flow simply reduces to:

$$\frac{\partial(\sin\phi, p)}{\partial(\sin\Phi, S)} + \sigma^* = 0. \tag{5.9}$$

6. THE GENERALIZED WAVE-ACTIVITY RELATION AND THE COMBINED BAROTROPIC AND BAROCLINIC INSTABILITY

We now consider a steady, zonally symmetric basic state with a vertically and horizontally sheared flow so that

$$u_g = u_g(\Phi, S), \quad v_g = 0. \tag{6.1}$$

It is straightforward to linearize (3.8) about this basic state to obtain

$$\frac{\mathcal{D}\sigma^{*\prime}}{\mathcal{D}t} + fv_g'\frac{\partial}{a\partial\Phi}\left(\frac{\bar{\sigma}^*}{f}\right) = 0, \tag{6.2}$$

where $\mathcal{D}/\mathcal{D}t = \partial/\partial T + \bar{U}\partial/a\cos\Phi\partial\Lambda$, $fv_g' = \partial M^{*\prime}/(a\cos\Phi\partial\Lambda)$ and $f = 2\Omega\sin\Phi$. $\bar{U}$ is the transformed basic state zonal wind.

Let us now define a particle displacement associated with the meridional geostrophic velocity as

$$v_g' = \frac{\mathcal{D}\eta'}{\mathcal{D}t}. \tag{6.3}$$

Substituting this definition into (6.3) and integrating the resultant equation over time and longitude, we have

$$\sigma^{*\prime} + \eta' f\frac{\partial}{a\partial\Phi}\left(\frac{\bar{\sigma}^*}{f}\right) = 0. \tag{6.4}$$

Multiplying this equation by v_g' and then taking the zonal average, we obtain

$$\frac{\partial}{\partial T}\left[\tfrac{1}{2}\overline{\eta'^2}f\frac{\partial}{a\partial\Phi}\left(\frac{\bar{\sigma}^*}{f}\right)\right] + \overline{v_g'\sigma^{*\prime}} = 0. \tag{6.5}$$

After some manipulations, the linearized invertibility principle can be written

$$f\cos\Phi\overline{v_g'\sigma^{*\prime}} = \nabla\cdot\mathbf{F}, \tag{6.6}$$

where $\nabla = (\partial/a\partial\Phi,\ \partial/\partial S)$ is the two dimensional del operator, and $\mathbf{F}$ is the combined geostrophic-gradient E-P flux in the meridional plane, taking the form

$$\mathbf{F} = \left(\frac{\partial \overline{(u_g \cos\phi)}}{\partial S} \overline{v'_g p'} - \frac{\partial \bar{p}}{\partial S} \overline{v'_g (u_g \cos\phi)'},\right.$$

$$\left. \frac{\partial \bar{p}}{a\partial\Phi} \overline{v'_g (u_g \cos\phi)'} - [f\cos\Phi + \frac{\partial \overline{(u_g \cos\phi)}}{a\partial\Phi}] \overline{v'_g p'} \right). \tag{6.7}$$

On substituting (6.6) into the linearized potential pseudodensity equation (6.5), we obtain the generalized wave-activity relation for the PV dynamic system on the sphere:

$$\frac{\partial}{\partial \mathcal{T}} \left[\tfrac{1}{2} \overline{\eta'^2} f^2 \cos\Phi \frac{\partial}{a\partial\Phi} \left(\frac{\vartheta^*}{f} \right) \right] + \nabla \cdot \mathbf{F} = 0. \tag{6.8}$$

Eqs. (6.6) and (6.8) may provide key understanding of the wave-mean flow interaction problem.

With proper boundary conditions, we can now integrate (6.8) over the meridional-height plane, which yields

$$\frac{\partial}{\partial \mathcal{T}} \iint \tfrac{1}{2} \overline{\eta'^2} f^2 \cos^2\Phi \frac{\partial}{a\partial\Phi} \left(\frac{\vartheta^*}{f} \right) a d\Phi dS = 0. \tag{6.9}$$

This leads to the stability argument as follows: since the integral in (6.9) must be constant in time, in order for disturbances to grow in time, i.e., for $\overline{\eta'^2}$ to grow in time, the radial gradient of the basic state potential pseudodensity, $\partial\vartheta^*/a\partial\Phi$, must have both signs. Such a dynamical statement can be considered as a generalization of the Charney-Stern theorem for combined barotropic and baroclinic instability.

7. CONCLUDING REMARKS

In this paper, we have presented a mathematic model which generalizes the zonally symmetric balanced theory proposed by Hack *et al.* (1989) and Schubert *et al.* (1991) to include the Rossby-Haurwitz waves superimposed on the Hadley symmetric circulation. This generalized dynamic system can also be regarded as an extension of the variable-f (Salmon, 1985), the planetary (Shutts, 1989) and the hemispheric (Magnusdottir and Schubert, 1991) semigeostrophic theories by including curvature vorticity induced by the earth's spherical geometry in the total PV inversion. The significance of these generalizations lies in the fact that this new balanced system may provide a succinct PV view for a global-scale circulation with complete or nearly complete physics in the PV inversion procedure. In this respect, the effort of the current work may be in line with or complement the idea in Hoskins (1991) about a PV-θ diagnostics of the general circulation.

From the linear calculation conducted in section 4, we find that the Rossby-Haurwitz waves predicted by the present PV model are generally consistent with those by the primitive equation model. However, the difference in the meridional wind fields within 20° equatorward does suggest that the balanced conditions used in the current PV model are not general enough to treat the cross-equatorial flows. An investigation of this problem has recently been made by Raymond (1993).

REFERENCES

Hack, J. J., W. H. Schubert, D. E. Stevens, and H.-C. Kuo, 1989: Response of the Hadley circulation to convective forcing in the ITCZ. *J. Atmos. Sci.*, **46**, 2957–2973.

Haynes, P. H., and M. E. McIntyre, 1987: On the evolution of vorticity and potential vorticity in the presence od diabatic heating and frictional or other forces. *J. Atmos. Sci.*, **44**, 828–841.

Haynes, P. H., and M. E. McIntyre, 1990: On the conservation and impermeability theorems for potential vorticity. *J. Atmos. Sci.*, **47**, 2021–2031.

Hoskins, B. J., 1975: The geostrophic momentum approximation and the semi-geostrophic equations. *J. Atmos. Sci.*, **32**, 233–242.

Hoskins, B. J., M. E. McIntyre and A. W. Robertson, 1985: On the use and significance of isentropic potential vorticity maps. *Quart. J. Roy. Meteor. Soc.*, **111**, 877–946.

Hoskins, B. J., 1991: Towards a PV-θ view of the general circulation. *Tellus*, **43AB**, 27–35.

Longuet-Higgins, M. S., 1968: The eigenfunctions of Laplace's tidal equations over a sphere. *Phil. Trans. Roy. Soc. London*, **A262**, 511-607.

Magnusdottir, G., and W. H. Schubert, 1991: Semigeostrophic theory on the hemisphere. *J. Atmos. Sci.*, **48**, 1449–1456.

Raymond, D. J., 1993: Balanced models on an equatorial beta plane. Submitted to *Quart. J. Roy. Meteor. Soc.*.

Rhines, P. B., 1986: Vorticity dynamics of the oceanic general circulation. *Ann. Rev. Fluid. Mech.* **18**, 433–497.

Salmon, R., 1985: New equations for nearly geostrophic flow. *J. Fluid Mech.*, **153**, 461–477.

Schubert, W. H., and B. T. Alworth, 1987: Evolution of potential vorticity in tropical cyclones. *Quart. J. Roy. Meteor. Soc.*, **113**, 147–162.

Schubert, W. H., D. E. Stevens, P. E. Ciesielski and H.-C. Kuo, 1991: The evolution of potential vorticity in the Hadley circulation. *J. Atmos. Sci.*, **48**, 1493–1509.

Shutts, G. J., 1989: Planetary semi-geostrophic equations derived from Hamilton's principle. *J. Fluid Mech.*, **208**, 545–573.

Table 1: The eigenfrequencies of Rossby-Haurwitz waves computed from the PV model on the sphere are compared with those from Laplace's tidal equations (Longuet-Higgins, 1968).

	ϵ_m = .01(external mode)		ϵ_m = 10^{-4} (1st internal mode	
	PV	PE	PV	PE
		$s = 1$		
$n - s = 2$	0.057802	0.058026	0.006379	0.006397
$n - s = 4$	0.028473	0.028377	0.003690	0.003628
		$s = 2$		
$n - s = 2$	0.082076	0.082513	0.012533	0.012542
$n - s = 4$	0.042925	0.042775	0.007286	0.007166
		$s = 3$		
$n - s = 2$	0.089976	0.089365	0.018179	0.018215
$n - s = 4$	0.049915	0.049728	0.010700	0.010520
		$s = 4$		
$n - s = 2$	0.088430	0.088704	0.023169	0.023246
$n - s = 4$	0.052870	0.052658	0.013862	0.013649
		$s = 5$		
$n - s = 2$	0.084948	0.085126	0.027408	0.027532
$n - s = 4$	0.053619	0.053390	0.016719	0.016472

Fig. 1 Balanced mass and wind fields as functions of latitude for zonal wavenumber 1 and 2.

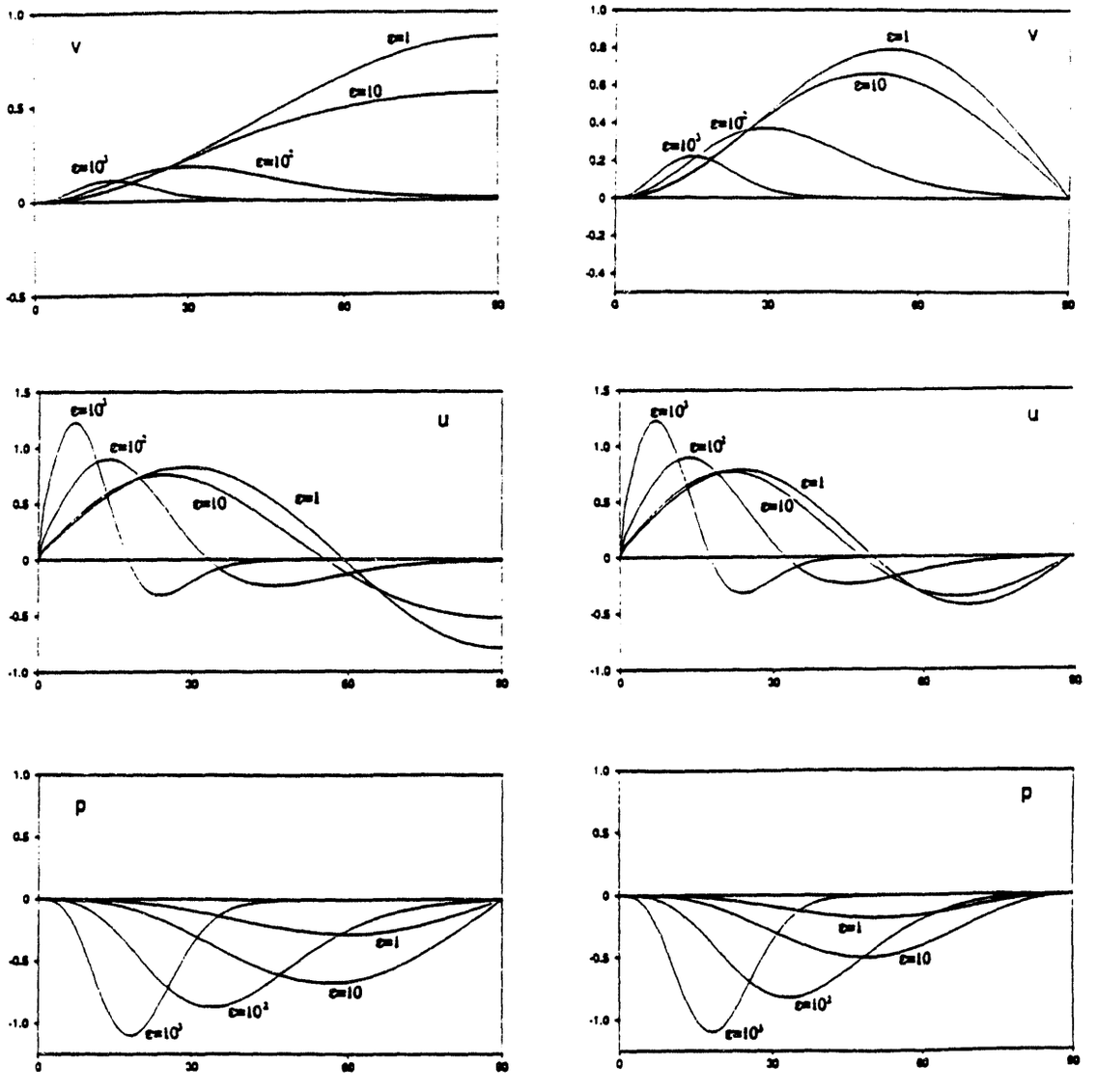

WAVE–MEAN FLOW INTERACTION AND THE BAROCLINIC ADJUSTMENT HYPOTHESIS[1]

Murray D. MacKay and G.W. Kent Moore
Department of Physics, University of Toronto,
Toronto, Ontario, Canada.

1 INTRODUCTION

It has been hypothesized that baroclinic waves interact with the zonally averaged flow in such a way as to eliminate the baroclinicity of the zone and thus the source of instability. In the context of quasigeostrophic theory this amounts to the elimination the pseudopotential vorticity gradient $\overline{Q_y}$ via adjustments in the vertical shear (Lindzen and Farrell, 1980), the static stability (Gutowski, 1985a), or both (Gutowski *et.al.* 1989). Strictly speaking baroclinic neutralization can occur simply by eliminating the temperature gradient at the ground. Gutowski (1985b), however, shows that the *minimal* (*ie.* with respect to changes in the zonal available potential energy) adjustment required to stabilize the flow is that where $\overline{Q_y}$ vanishes at the surface and in a finite layer above the surface. This is the baroclinic adjustment hypothesis.

In this paper, the mechanism of baroclinic adjustment as formulated by Gutowski *et.al.*, (1989), and Lindzen and Farrell (1980) is examined in the context of wave-mean interaction theory. The linearized quasigeostrophic potential vorticity equation is solved in a β-channel for a purely baroclinic basic state. The mean atmospheric response to the heat flux convergence of the fastest growing normal mode is then determined by solving the Eulerian-mean

[1]Part of this research was presented at the Ninth Conference on Atmospheric and Oceanic Waves and Stability, San Antonio,TX., May 10-14,1993.

equations of wave-mean interaction theory. Conventional wave-mean interaction theory considers only eddy horizontal heat flux, the vertical heat flux being formally order Rossby number smaller according to a Q.G. scaling analysis. In this study the mean atmospheric response to baroclinic eddies is evaluated both with and without vertical heat flux forcing. In the context of baroclinic adjustment, this amounts to considering adjustments in both N^2 and U_z, and U_z alone, respectively.

Once the Eulerian-mean equations are solved for tendencies in the mean flow variables, these tendencies are integrated in time to estimate the net atmospheric adjustment due to the growing wave. This assumes that the wave grows as a normal mode (*ie.* exponentially) until it saturates. Thus the wave is allowed to alter the basic state but the new basic state is not allowed to influence the instability itself. The net adjusted atmosphere determined by this method is compared with the predictions of the baroclinic adjustment hypothesis.

It was found that a finite layer in the troposphere is in fact stabilized in accordance with the baroclinic adjustment hypothesis, when both shear and static stability adjustments are considered. The atmosphere in the vicinity of the tropopause, however, is actually destabilized. A stability analysis of the adjusted atmosphere reveals an internal mode of baroclinic instability centred near the tropopause with a different vertical structure and length scale than the primary wave. Further analysis indicates that this mode is due to the vertical heat flux convergence of the primary wave in this vicinity, and thus would be filtered out by conventional Q.G. wave-mean interaction theory.

2 BAROCLINIC INSTABILITY THEORY

The linearized Q.G. potential vorticity equation is solved in a β - channel that is 6600 km wide, 20 km deep and unbounded zonally. Our basic state is characterized by linear vertical wind shear, no meridional wind shear, and a hyperbolic tangent static stability profile representing a smooth transition from troposphere to stratosphere. That is:

$$U_0(z) = \lambda(z - d)$$

$$N_0^2(z) = \left(\frac{N_1^2 + N_2^2}{2}\right) + \left(\frac{N_2^2 - N_1^2}{2}\right) tanh[r(z-d)]$$

where d is the height of the tropopause and r is a parameter representing the steepness of the transition from troposphere to stratosphere. N_1^2 and N_2^2 are the asymptotic static stabilities in the troposphere and stratosphere respectively. The parameter values used in this paper are $d = 8km$, $N_1^2 = 1 \times 10^{-4}s^{-1}$, $N_2^2 = 6 \times 10^{-4}s^{-1}$, $r = 7.5 \times 10^{-4}m^{-1}$, and $\lambda = 3.0 \times 10^{-3}s^{-1}$.

3 THE EULERIAN-MEAN RESPONSE

The feedback of a baroclinic wave on the basic state is determined by solving the Eulerian-mean equations of wave-mean interaction theory (eg. Andrews *et.al.*, 1987). In dimensionless form they are:

$$\begin{aligned} \frac{\partial \overline{u}}{\partial t} + \frac{\partial \overline{w}}{\partial z} &= -\frac{\partial}{\partial y}(\overline{u'v'}) = 0 \\ \frac{\partial \overline{u}}{\partial z} &= \frac{\partial \overline{\theta}}{\partial y} \\ \frac{\partial \overline{\theta}}{\partial t} + N^2 \frac{\partial \overline{\psi}}{\partial y} &= \mathcal{H} \end{aligned} \tag{1}$$

where ψ is the ageostrophic meridional stream function, and $\frac{\partial \overline{u}}{\partial t}$, $\frac{\partial \overline{\theta}}{\partial t}$ are tendencies in the zonally averaged zonal wind and potential temperature. The right hand side of the first equation in (1) vanishes in this study since momentum fluxes are zero in the purely baroclinic channel model. The third equation contains the forcing for the entire system. $\mathcal{H}$ is the heat flux convergence of the fastest growing normal mode. In conventional Q.G. theory, it is simply the horizontal heat flux convergence. In this study, however, the effects of including the vertical heat flux convergence, formally a second order term, are explored. This provides an extension to standard Q.G. theory. Specifically, we take:

$$\begin{aligned} \mathcal{H} &= \frac{\partial}{\partial y}(\overline{v'\theta'}) && \textit{conventional Q.G.} \\ \mathcal{H} &= \frac{\partial}{\partial y}(\overline{v'\theta'}) + Ro\frac{\partial}{\partial z}(\overline{w'\theta'}) && \textit{extended Q.G.} \end{aligned}$$

Equations (1) are reduced to a single elliptic equation for the stream function ψ, which is solved numerically using finite differences, given the eddy forcing $\mathcal{H}$. Tendencies in the

zonally averaged zonal wind and potential temperature are then solved from (1), given ψ. The tendency in the static stability ($\frac{\partial}{\partial t}N^2 = \frac{\partial}{\partial t}\frac{\partial \bar{\theta}}{\partial z}$) is determined by taking the vertical derivative of the third equation of (1), yielding:

$$\frac{\partial}{\partial t}N^2 + \frac{\partial}{\partial z}(N^2\frac{\partial \psi}{\partial y}) = \frac{\partial \mathcal{H}}{\partial z} \tag{2}$$

To simplify the calculation the second term in (2) is linearized by assuming:

$$N^2(z)\frac{\partial \psi}{\partial y} \approx N_0{}^2(z)\frac{\partial \psi}{\partial y}$$

where $N_0{}^2(z)$ is the static stability of the basic state.

We have found that inclusion of eddy vertical heat flux forcing has a dramatic effect on the mean atmospheric response. The two most important effects are a global increase in static stability in the troposphere, and its reduction near the tropopause. This has a profound impact on the stability characteristics of the flow.

4 THE NET ATMOSPHERIC ADJUSTMENT

We have solved the Q.G. potential vorticity equation to estimate the vertical structure of baroclinic eddy heat fluxes. These fluxes interact with the basic state producing a weak meridional circulation, as well as tendencies in the zonally averaged zonal wind and potential temperature. The net adjustment of the atmosphere can be estimated by integrating the tendencies in time for some prescibed period. For simplicity, the eddy is assumed to grow exponentially with time until the troposphere stabilizes, at which point growth ceases. This we have termed the linear growth phase of the wave. The purpose of this paper is to compare the modification of the basic state due to wave-mean interaction during the linear growth phase of the wave, with the predictions of the baroclinic adjustment hypothesis.

The atmospheric adjustment process is illustrated in figure 1 for the case including the effects of the eddy vertical heat flux. The initial P.V. gradient is shown (solid line) as well as net adjusted values after 2, 3, 4, and 4.3 days of baroclinic growth (dashed lines) for a vertical cross section taken through the centre of the channel. The zonal wind speed

and static stability (not shown) are adjusted, in the lower troposphere, in accordance with baroclinic adjustment theory: both are adjusting so as to reduce the baroclinicity of the zone. This manifests itself in the P.V. gradient, which has been reduced to near zero in the lower 6 km of the atmosphere.

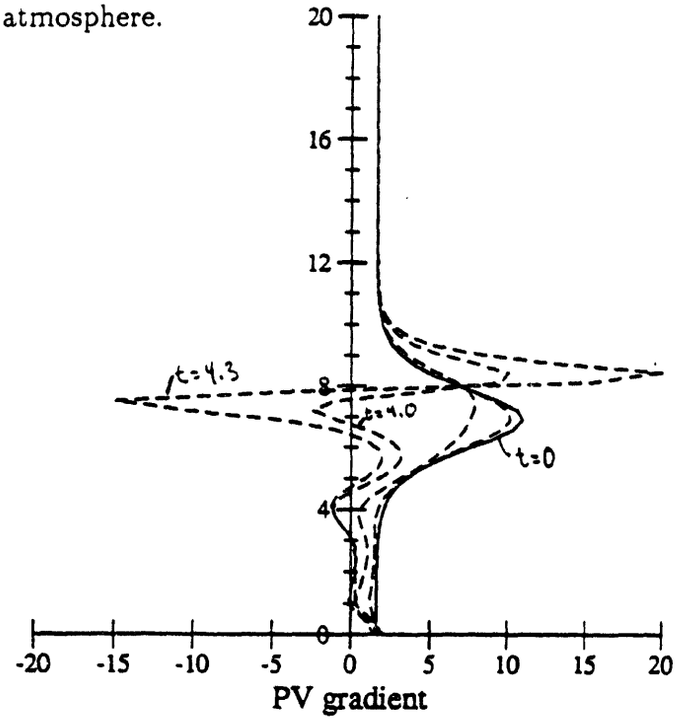

Fig. 1 Initial (solid) and adjusted (dashed) P.V. gradients after 2, 3, 4, and 4.3 days of baroclinic growth. Units are $10^{-11}\,m^{-1}s^{-1}$.

It would seem that the baroclinic wave has stabilized the lower troposphere in accordance with baroclinic adjustment. However, the atmosphere in the vicinity of the tropopause actually appears to be destabilized. A minimum of static stability exists at 8 km due to the convergence of vertical heat flux, and this generates a strong P.V. gradient "dipole" in this region. The Charney-Stern theorem suggests the possibility of an internal mode of baroclinic instability associated with this region. A 1-d linear stability analysis of the adjusted basic state for days 0,2,3,4, and 4.3 in the centre of the channel (figure 2) indicates that the original Charney-Eady mode diminishes with time and is ultimately eliminated, while a new mode with a shorter length scale has appeared. Examination of the vertical structure of the eigenfunctions and heat fluxes shows that this is in fact an interior baroclinic mode centred near the tropopause with no amplitude at the surface. For the conventional Q.G.

case without vertical heat flux forcing the troposphere never fully stabilizes in the center of the channel. Also, without vertical heat flux convergence near the tropopause there is no destabilization of an upper level mode.

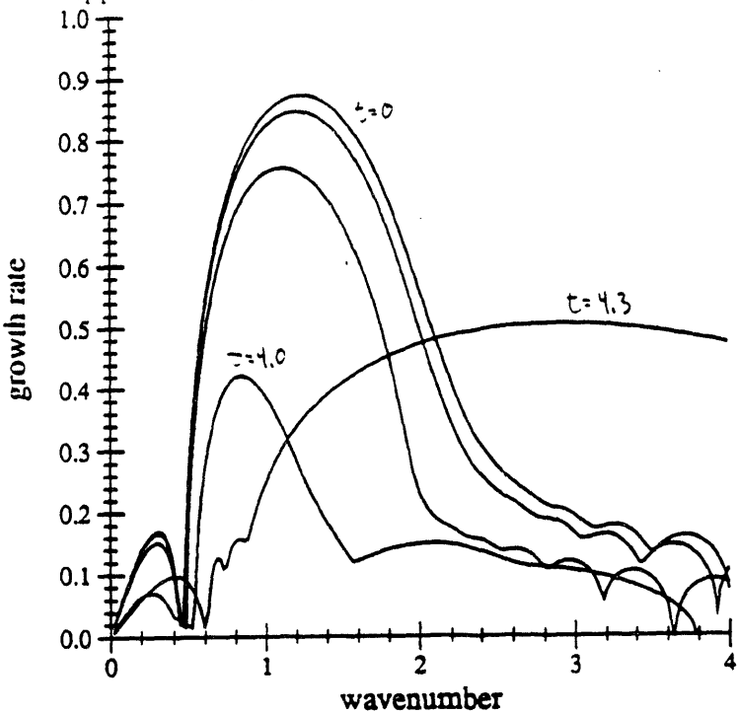

Fig. 2 Dimensionless growth rate spectra from linear stability analyses on the basic states in figure 1.

5 CONCLUSIONS

In this study, we have attempted to assess the relevance of the baroclinic adjustment hypothesis in the context of a simple integrated wave - mean interaction theory. We have found that if both shear and static stability adjustments are considered, the lower troposphere does indeed stabilize after a finite length of time using our method, at least in the centre of the channel. We have thus deemed the adjustment hypothesis of Gutowski *et.al.*, (1989) more appropriate than that of Lindzen and Farrell (1980) who considered only shear adjustments. However, for sufficiently small background shear (and thus small Rossby number), eddy vertical heat flux forcing is relatively unimportant and the atmosphere can approach baroclinic neutrality by virtue of horizontal heat fluxes alone. We have found the

time taken to reach a baroclinically neutral atmosphere decreases linearly with Rossby number, and the maximum vorticity attained increases linearly with Rossby number. This point we loosely define as the linear saturation of the wave.

It turns out that the linear saturation amplitude of the wave is comparable with that suggested by the two closure approximations of Gutowski *et.al.*, (1989), though its relation to the actual (*ie.* nonlinear) saturation amplitude is far from clear at this time. One might expect that at the point of linear saturation, the wave can no longer grow as a normal mode and nonlinear effects are probably significant. In this sense the linear saturation of the wave provides an upper bound for the length of time we might expect linear normal mode theory to be relevant.

A surprising result of this paper is the destabilization of the atmosphere near the tropopause, an effect that is not predicted by any baroclinic adjustment theory. We have shown that this destabilization is a result of eddy vertical heat flux convergence in the upper troposphere. Even though this heat flux is formally a second order term, we have shown that it is essential for the stabilization, via baroclinic adjustment, of the lower troposphere - except for small ambient shears. These results appear to be relatively insensitive to the nature of the transition from the troposphere to stratosphere. Changing the depth of the transition region (the parameter r) or the ratio of the asymptotic static stabilities ($\frac{n2}{n1}$) changes the details of the adjustment but not the basic conclusion of lower tropospheric stabilization and upper tropospheric destabilization.

That such an upper tropospheric destabilization has not been observed in fully nonlinear P.E. models may be due to their in general limited vertical resolution. In order to resolve well the shallow P.V. gradient dipole structure we find in our model, we require about 600 m resolution near the tropopause. Many P.E. models cannot achieve this resolution.

However, there may be physical processes as well that inhibit this effect. Momentum fluxes, formally zero in the baroclinic channel model, may be important in the real atmosphere with respect to baroclinic adjustment. Background meridional shear might also

suppress secondary baroclinic development via the barotropic governor mechanism (James, 1987).

6 REFERENCES

Andrews, D.C., J.R.Holton, and C.B. Leovy, 1987: Middle Atmosphere Dynamics, Academic Press Inc. 489 pp.

Gutowski, W.J.Jr., 1985a: A Simple Model for the Interaction Between Vertical Eddy Heat Fluxes and Static Stability, *J. Atm. Sci.*, **42**, 346-358.

Gutowski, W.J.Jr., 1985b: Baroclinic Adjustment and Mid-latitude Temperature profiles, *J. Atm. Sci.*, **42**, 346-358.

Gutowski, W.J.Jr., L.E. Branscome, and D.A. Stewart, 1989: Mean Flow Adjustment During Life Cycles of Baroclinic Waves, *J. Atm. Sci.*, **46**, 1724-1737.

James, I.N., 1987: Suppression of Baroclinic Instability in Horizontally Sheared Flows, *J. Atm. Sci.*, **44**, 3710-3720.

Lindzen, S. and B. Farrell, 1980: The Role of Polar Regions in Global Climate, and a New Parameterization of Global Heat Transport, *J. Atm. Sci.*, **108**, 2064-2079.

On the Intra-seasonal Variability within the Extratropics in a General Circulation Model and Observational Data

Wilhelm May
and
Lennart Bengtsson
Max-Planck-Institute for Meteorology
Bundesstr. 55
20146 Hamburg, Germany

1. Introduction

There are various phenomena on different spatial and temporal scales contributing to the intra-seasonal variability within the extratropics. One may notice higher-frequency baroclinic disturbances affecting the day-to-day variability of the atmosphere. But one finds also low-frequency fluctuations on a typical time scale of a few weeks. Blocking anticyclones are probably the most prominent example of such features. These fluctuations on different scales, however, are influencing each other, in particular the temporal evolution and spatial distribution. There has been observational work on various phenomena contributing to the intra-seasonal variability for a long time. In the last decade or so, however, with the increasing importance of General Circulation Models there have been some studies dealing with the intra-seasonal variability as simulated by these models.

2. Data

In our study we compare the observed atmospheric intra-seasonal variability within the extratropics with the variability simulated by an atmospheric **G**eneral **C**irculation **M**odel (GCM) developed at the Max-Planck-Institute in Hamburg. The model refered to as **ECHAM3** is a spectral model with triangular truncation and 42 zonal wavenumbers (T42). It has 19 vertical levels in a hybrid σ-p-coordinate system. The physical parameterization includes radiation, vertical diffusion, gravity wave drag, cumulus convection, stratiform clouds and soil processes. A detailed description of the model and its climatology is given in Roeckner et al. (1992).

We investigate results from three simulations performed with ECHAM3. In one case the boundary forcing is given by climatological **S**ea **S**urface **T**emperatures (SST), in the two other

cases by observed SST for the period September '79 through December '91. In the latter two experiments different atmospheric initial conditions were prescribed. The data are available for a period of approximately 13 years at 12 hour intervals.

As observational data we use initialized analyses from the European Centre for Medium Range Weather Forecasts (ECMWF) for the period September '79 through December '91. The data are given daily and are reduced to T42 triangular truncation for our purposes.

As we want to investigate the intra-seasonal variability we first remove the time mean and the seasonal cycle from the data. The latter one is given by the annual mean and the first 4 harmonics.

3. Wavenumber-Frequency-Analysis

In order to distinguish the phenomena influencing the atmospheric variability by different spatial and temporal scales we apply a one-sided space-time spectral analysis to the 500 hPa geopotential height field for individual seasons. Seasons are slightly overlapping segments of 96 days starting at March 1, June 1, September 1 and December 1 respectively. Following Pratt (1976) we get the total (T), the propagating (PR) and the stationary (SR) variance spectrum for a given zonal wavenumber k and frequency ω as follows

$$T(k,\omega) = \frac{1}{2}[P_\omega(C_k) + P_\omega(S_k)]$$

$$PR(k,\omega) = |Q_\omega(C_k, S_k)|$$

$$SR(k,\omega) = \sqrt{K_\omega^2(C_k, S_k) + \frac{1}{4}[P_\omega(C_k) - P_\omega(S_k)]^2}$$

where P_ω are the power, Q_ω the quadrature and K_ω the cospectrum of the cosine- ($C(k)$) and the sine-coefficient ($S(k)$) of the zonal Fourier harmonics. Here the stationary variance spectrum is meant to describe the temporal variability of the amplitude of the stationary waves. Before the spectral analysis the residual seasonal mean and the trend were removed from the data. The estimates presented here are averages for the 13-year period and the zonal channel between 30° and 70° northern or southern latitude respectively. The presentation is double-logarithmic with the period on the abscissa and the zonal wavenumber ranging from 1 to 10 on the ordinate. The spectral estimates are multiplied by wavenumber and frequency.

Figure 1 shows the total as well as the propagating and stationary variance spectrum derived from the ECMWF analyses for the Northern Hemisphere in winter. In the total spectrum (a) we find a fair amount of variability for all periods and wavenumbers. Whereas the spectral peak for wavenumber 3, 4 and 5 at periods between 6 and 16 days is due to both, the propagating (b) and stationary (c) part of the spectrum, the peak for wavenumber 6 and 7 is due to propagating fluctuations only. In the propagating spectrum we can identify three distinct spectral peaks. There is one for the ultra-long waves (1 and 2) with periods between 10 and 30 days. Waves with the zonal wavenumber 4 and 5 are most active on time scales between 6 and 10 days, the shorter ones (6 and 7) between 3 and 6 days. In the stationary spectrum, however, only the ultra-long waves (1 to 4) on time scales beyond 10 days give major contributions to the variance.

The results derived from the simulation by ECHAM3 for the Northern Hemisphere in winter are given in Figure 2. Here we present the estimates from one of the experiments with observed SST. Though the simulation shows also the three distinct spectral peaks in the propagating variance spectrum (b), it represents the major difference between the observation and the simulation. Whereas the ultra-long propagating waves are much stronger in the observation, the shorter waves reveal more activity in the simulation with maxima at somewhat shorter wavelength.

On the Southern Hemisphere (not shown) we find only one spectral peak in the total variance spectrum for wavenumbers 3, 4 and 5 with periods between 6 and 12 days for both the observation and simulation. In the simulation, however, the waves are about 50% stronger than in the ECMWF analyses. This contrast is caused by the different character of the propagating waves as simulated on the Southern Hemisphere. The reason to this is not yet very well understood. The stationary spectra as derived from the ECMWF analyses and the simulations by ECHAM3 are in good agreement .

4. Spectral Filtering

Following Blackmon (1976) we apply spectral filters to the data in order to investigate the spatial structure of the intra-seasonal variability on different time scales. Here we discuss the contributions of the transient fluctuations retaining for time scales between 2.5 and 6 days and between 10 and 90 days of the 500 hPa geopotential height rms.

Figure 3a displays the band-pass filtered rms for the ECMWF analyses for the Northern Hemisphere in winter. There are two maxima corresponding to the position of the storm

tracks in the north Atlantic and the Pacific. In the simulation (Figure 3b) we find these two maxima too. Whereas its magnitude in the Pacific is about the same as in the observation, the maximum in the Atlantic is about 10 m weaker. The maximum in the Pacific as simulated is extending further southeastward into North America.

For the low-frequency fluctuations (Figure 3b) the ECMWF analyses reveal also two maxima, one at the Aleutian Islands and one south of Iceland. The latter one is extending eastward over Scandinavia. In the simulation (Figure 4b) the Pacific maximum has the same location and magnitude as in the observation. In the Atlantic, however, the maximum is significantly weaker, but extending further eastward over northern Russia and into the Kara Sea.

On the Southern Hemisphere (not shown) the observations indicate a crescent shaped maximum of the band-pass filtered rms in the Indian Ocean at about 50° southern latitude. In the simulation we find this maximum too. However, it has a more zonally symmetric character and is located at higher latitudes. For the low-frequency fluctuations the ECMWF analyses show a maximum in the entire Pacific region. It is located downstream, but clearly separated from the region of the Southern Hemisphere storm tracks. In the simulation there is a distinct maximum located southeast of South America, which is about 20% stronger than in the observations.

5. Persistent Anomalies

Within the intra-seasonal time scale we find persistent anomalies with a typical life time between one and several weeks. Following Blackmon (1986) we investigate the distribution of positive persistent anomalies in the 500 hPa geopotential height field on the Northern Hemisphere, which we consider as an objective index for Blocking. We choose different thresholds for each season derived from the estimates of the intra-seasonal variability on time scales beyond 5 days. Table 1 gives these values for the observations and the various simulations, which are an area average over the Northern Hemisphere mid-latitudes. In winter, for example, we assume a threshold of approximately 100 m and a lifetime of 9 days and longer, the lifetime being the same for all seasons.

Figure 5a shows the relative occurrence of positive persistent anomalies for the entire 13-year period of investigation derived from the ECMWF analyses. We identify three centers of blocking action in the Pacific, the Atlantic and northern Russia. In the simulation (Figure 5b) there are also three centers, but their shape is different. In the Pacific the center is extending further towards the pole, and over North America there are significantly less persis-

'ent anomalies. In the Atlantic the maximum is located further east and passing over to the center in Russia. These differences do not appear in the individual seasons to the same extent.

6. Summary

Our results show a good correspondence between the intra-seasonal variability as observed and as simulated by ECHAM3 on the Northern Hemisphere. The stormtracks and the low-frequency variability, however, are somewhat underestimated in the Atlantic region.

On the Southern Hemisphere the correspondence is not as good. Thus are the transient fluctuations much stronger in the simulation, and there is a tendency to zonal symmetry in the simulation. In general in the simulation the circulation is shifted to higher latitudes indicating a deficiency in the simulation of the meridional circulation. However, when interpreting these results one should bear in mind that the analyses for the Southern Hemisphere may have systematic errors as well.

Here we present only results derived from one of the simulations performed with ECHAM3 with observed SST. The results derived from the two other experiments are similar on time scales shorter than 10 days. The variance due to low-frequency fluctuations, however, is significantly weaker in the Pacific region than in the ECMWF analysis and the two experiments with observed SST as well.

7. References

Blackmon, M. L., 1976: A climatological spectral study of the 500 mb geopotential height of the Northern Hemisphere. *J. Atmos. Sci.*, **33**, 1607-1623.

Blackmon, M. L., S. L. Mullen, and G. T. Bates, 1986: The climatology of blocking events in a perpetual January simulation of a spectral general circulation model. *J. Atmos. Sci.*, **43**, 1379-1405.

Pratt, R. W., 1976: The interpretation of space-time spectral quantities. *J. Atmos. Sci.*, **33**, 1060-1066.

Roeckner, E., K. Arpe, L. Bengtsson, S. Brinkop, L. Dümenil, M. Esch, E. Kirk, F. Lunkeit, M. Ponater, B. Rockel, R. Sausen, U. Schlese, S. Schubert, and M. Windelband, 1992: Simulation of the present-day climate with the ECHAM model: impact of model physics and resolution. *MPI Report*, **93**, 172 pp.

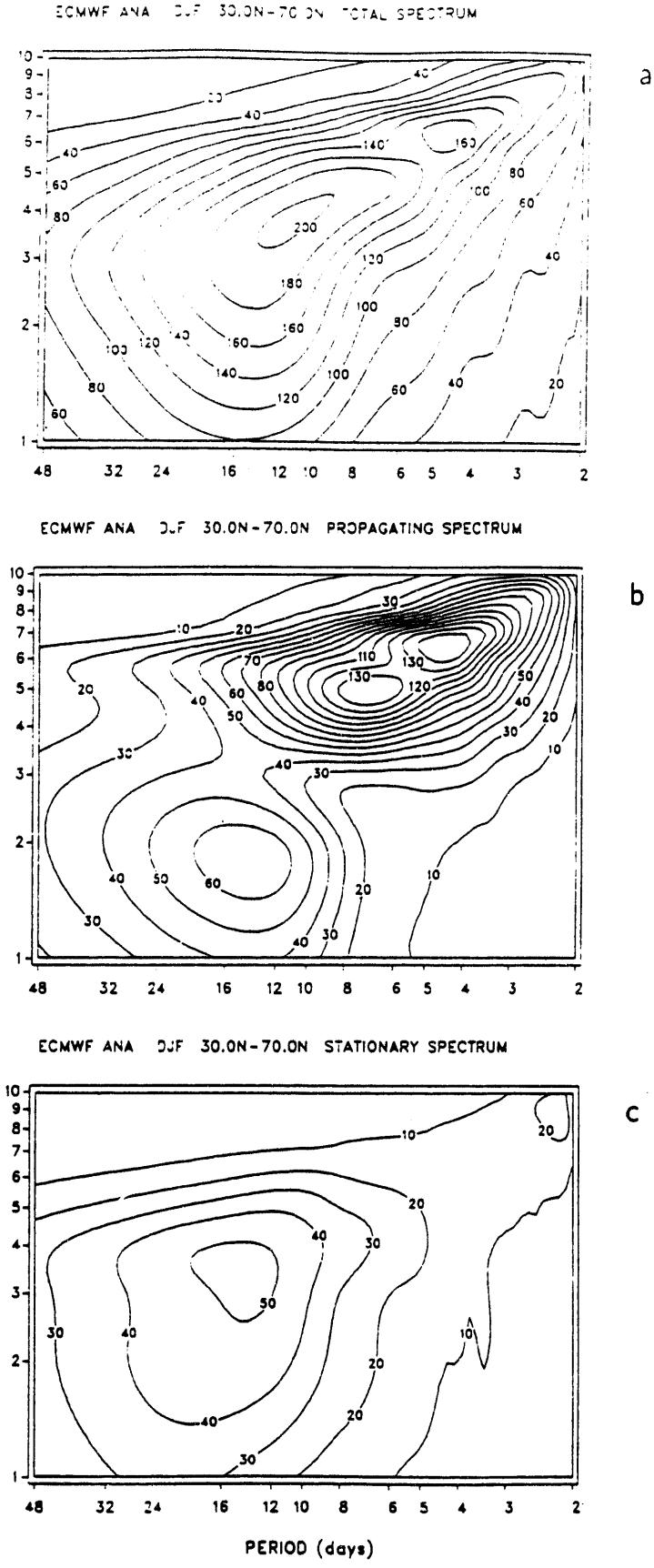

Fig. 1. Power spectrum of the 500 hPa geopotential height in 30°N-70°N for Winter derived from the ECMWF analyses for the total (a), the propagating (b) and the stationary (c) variance. Units are 100 m^2, the contour interval is 20 for the total and propagating, 10 for the stationary spectrum.

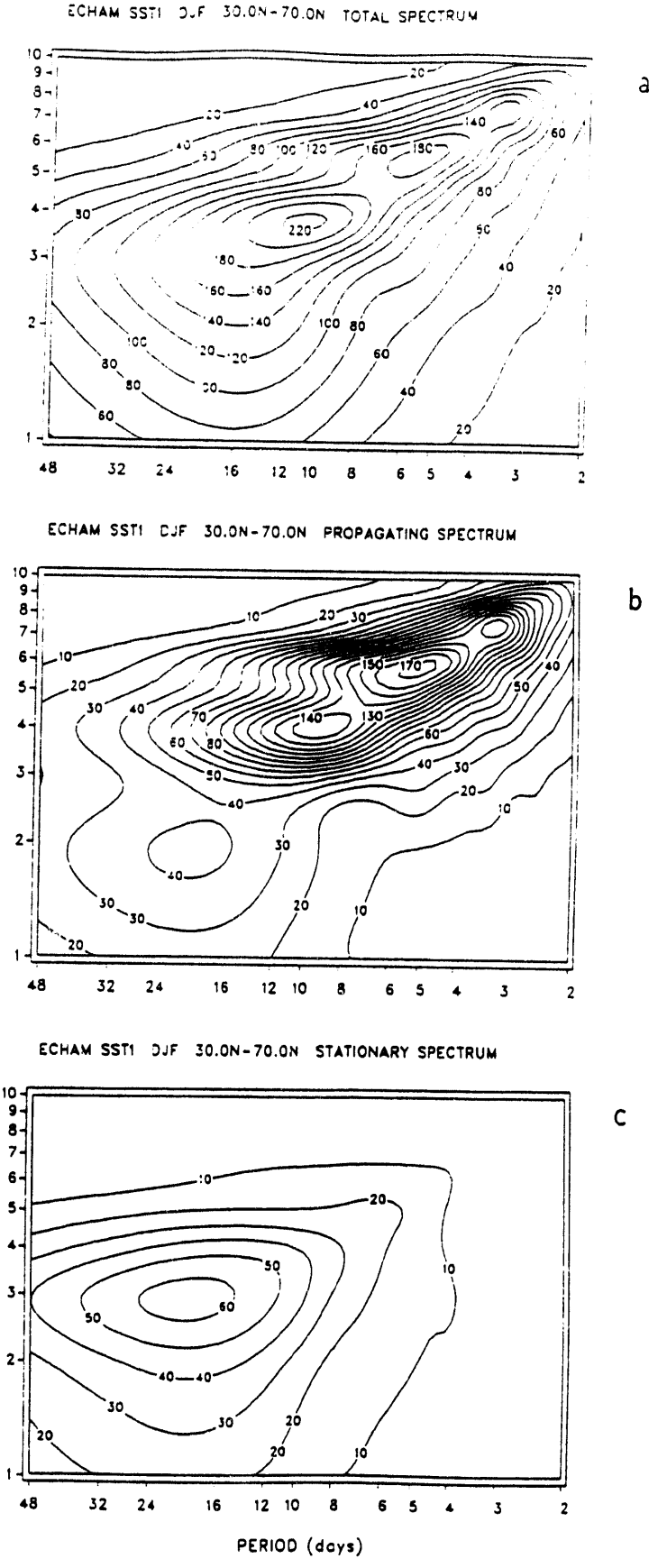

Fig. 2. As Fig. 1. but for a simulation performed with ECHAM3 with observed SST.

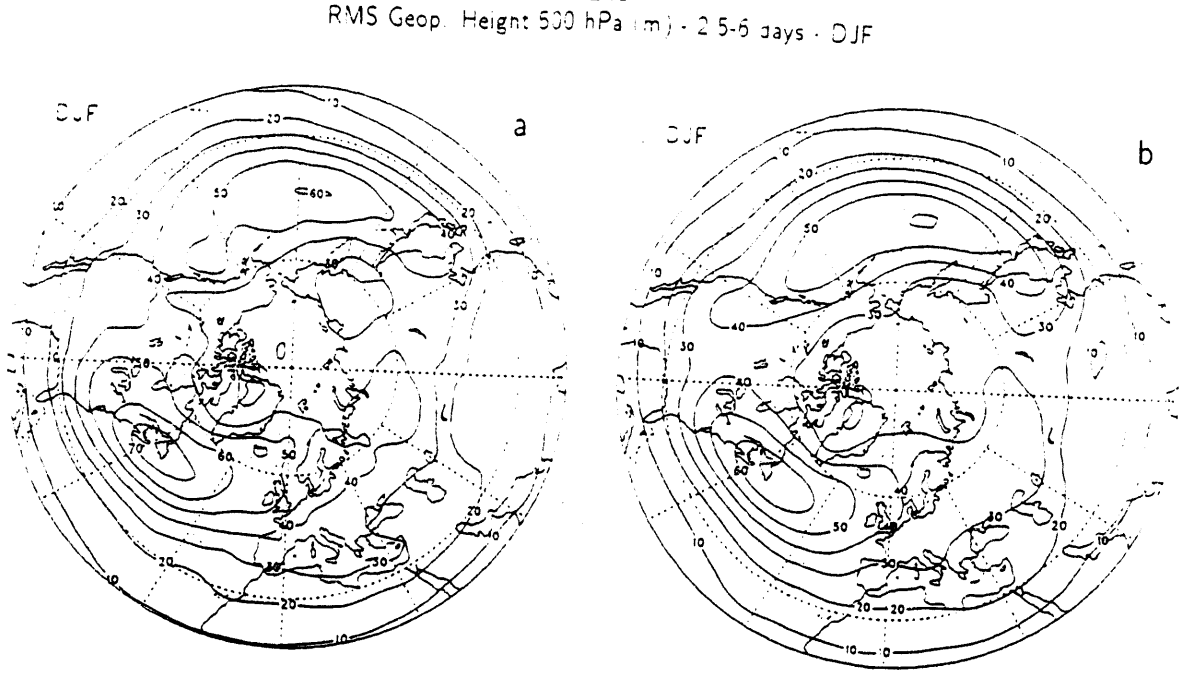

Fig. 3. RMS of the 500 hPa geopotential height retaining for time scales between 2.5 and 6 days on the Northern Hemisphere for Winter derived from the ECMWF analyses (a) and a simulation performed with ECHAM3 (b) with observed SST. Units are m, the contour interval is 10 m.

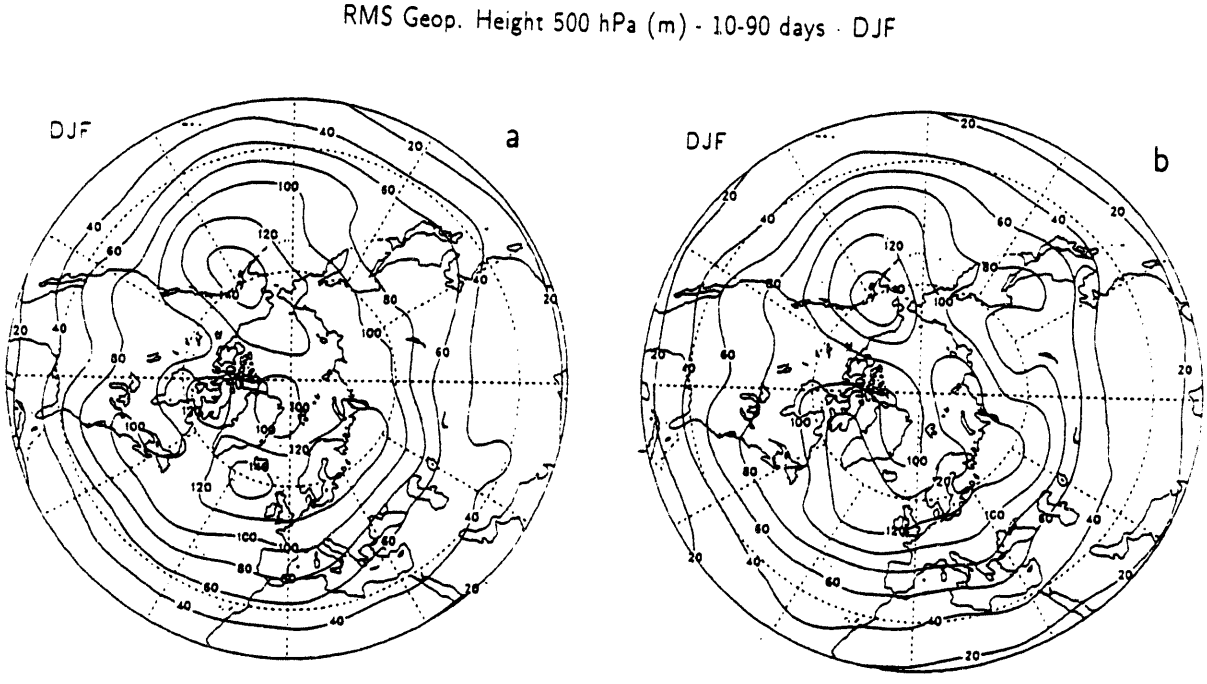

Fig. 4. As Fig. 3 but retaining for time scales between 10 and 90 days. The contour interval is 20 m.

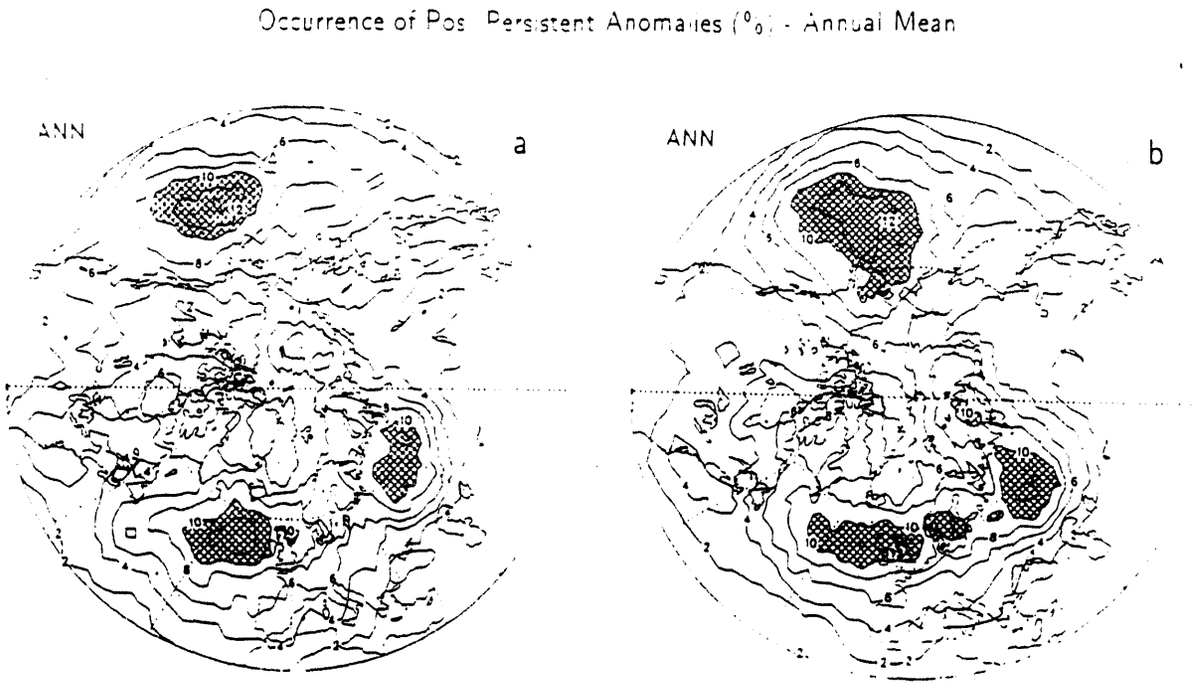

Fig. 5. Relative occurrence of positive persistent anomalies in the 500 hPa geopotential height field derived from the ECMWF analyses (a) and a simulation performed with ECHAM3 (b) with observed SST. Units are %, the contour interval is 4%. Values higher than 10% are indicated by shading.

	ECMWF	MOD CLIM	MOD SST1	MOD SST2
Spring	86.11	79.04	80.50	80.51
Summer	67.13	59.62	62.01	62.65
Autumn	80.55	73.21	74.27	73.55
Winter	100.84	88.86	93.96	91.33

Table 1. RMS of the 500 hPa geopotential height retaining for time scales between 5 and 90 days on the Northern Hemisphere mid-latitudes derived from the ECMWF analyses and simulations performed with ECHAM3 with cliamtalogical (CLIM) and observed SST (SST1 and SST2). Different atmospheric initial conditions were prescribed for SST1 and SST2. Units are m.

Fluctuations in the large-scale atmospheric circulation and ocean conditions associated with the dominant modes of wintertime precipitation variability for the contiguous United States

Todd P. Mitchell[1]
Universities Space Research Association
NASA/Goddard Space Flight Center
Greenbelt, MD 20771

Warren Blier
Department of Atmospheric Sciences
University of California, Los Angeles
Los Angeles, CA 90024

The historical Climatic Division record of monthly- and seasonal-mean wintertime precipitation totals are analyzed to document the dominant patterns of precipitation variability for the contiguous United States. The analysis technique employed is the Rotated Principal Component analysis. Time series for the leading patterns are related to global sea-surface temperatures (SSTs), and to gridded surface and upper-air analyses for the Northern Hemisphere.

The leading pattern of wintertime seasonal-mean precipitation variability is centered in northeast California and explains over half of the precipitation variance for northern California, southern Oregon, southern Idaho, and northern Nevada. Fluctuations in this pattern explain 17.9 % of the area-averaged precipitation variance for the contiguous United States for the period 1931 to 1988. Correlation analysis between the time series of this pattern and global SSTs indicate that fluctuations in this mode are only modestly related to the changes in the extratropical and tropical conditions in the Pacific Ocean associated with the El Niño/Southern Oscillation phenomenon.

Significant correlations between fluctuations in the leading mode of monthly-mean precipitation variability and atmospheric conditions are also documented. Anomalously wet months are found to be associated with a multiplicity of flow configurations; however, the typical atmospheric conditions associated with extreme wet months, as constructed from linear regression statistics, bear little resemblance to those associated with individual significant precipitation events.

The results of these analyses are in preparation for submission to the *Journal of Climate*.

---

[1] Present Affiliation: Joint Institute for the Study of the Atmosphere and Ocean, University of Washington, Seattle, WA 98195

On the Differences Between Early and Middle Winter Atmospheric Responses to Sea Surface Temperature Anomalies in the Northwest Atlantic

Shiling Peng, L.A. Mysak, H. Ritchie*, J. Derome and B. Dugas*

Centre for Climate and Global Change Research and
Department of Atmospheric and Oceanic Science, McGill University,
Montreal, PQ., H3A 2K6; Tel: 514-398-7448; Fax: 514-398-6115

*Recherche en Prevision Numerique (RPN),
Atmospheric Environment Service, Dorval, Quebec, H3P 1J3

Using an atmospheric global spectral model at RPN with T42 horizontal resolution, we have shown that the winter atmosphere in the mid-latitudes is capable of reacting to the SST anomalies prescribed in the northwest Atlantic (see Fig. 1) with two different responses. The nature of the response is determined by the climatological conditions of the winter system. Experiments are conducted using either the perpetual November or January conditions, with or without the SST anomalies prescribed. Six 50-day integrations, with positive (or negative) SST anomalies prescribed, initialized from independent November analyses and similarly, four runs initialized from January analyses, have been examined in comparison with their control runs.

We found that the warm SST anomalies in the early (middle) winter, namely November (January), result in a significant anomalous ridge (trough) downstream over the Atlantic with a nearly equivalent barotropic structure (see Figs. 2 and 3). The presence of the SST anomalies also causes a northward (southward) shift of the Atlantic storm tracks in the November (January) case. A diagnostic analysis of the anomalous heat advection in the simulations reveals that, in the January case, the

surface heating is offset primarily by the strong horizontal cold advection in the lower troposphere; in the November case, the vertical heat advection is vitally important. Hence, the positive air temperature anomalies exhibit a deep vertical penetration in the November case but not in the January case.

The simulated atmospheric responses to the warm SST anomalies in both the November and January cases are observed to be in qualitative agreement with the results from an observational data analysis using 50-year (1930-1979) records. The atmospheric responses to the cold SST anomalies in the simulations are found not to be statistically significant.

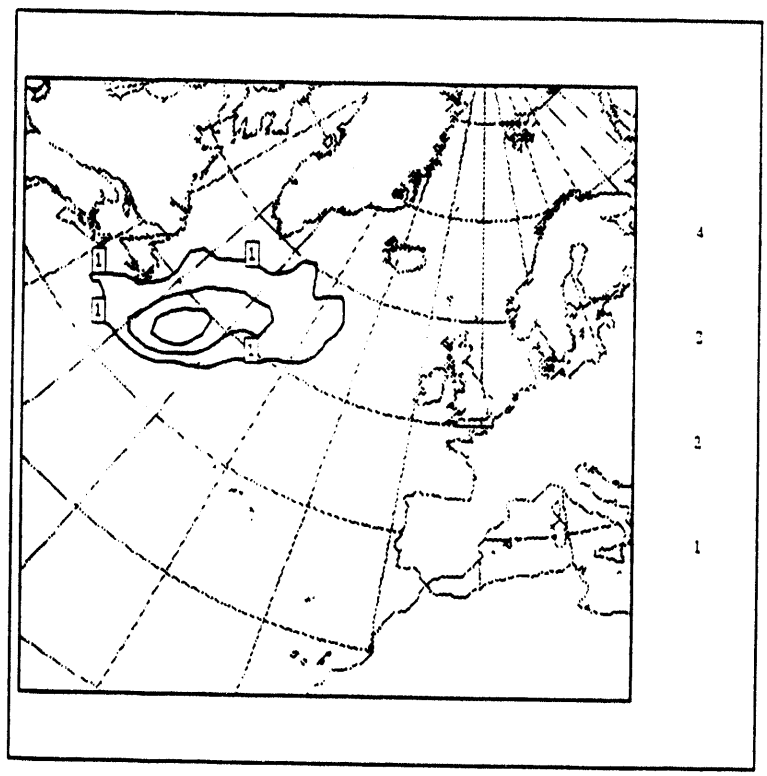

Fig. 1 The SST anomaly used in the experiments. The contour interval is 1.0 (° C).

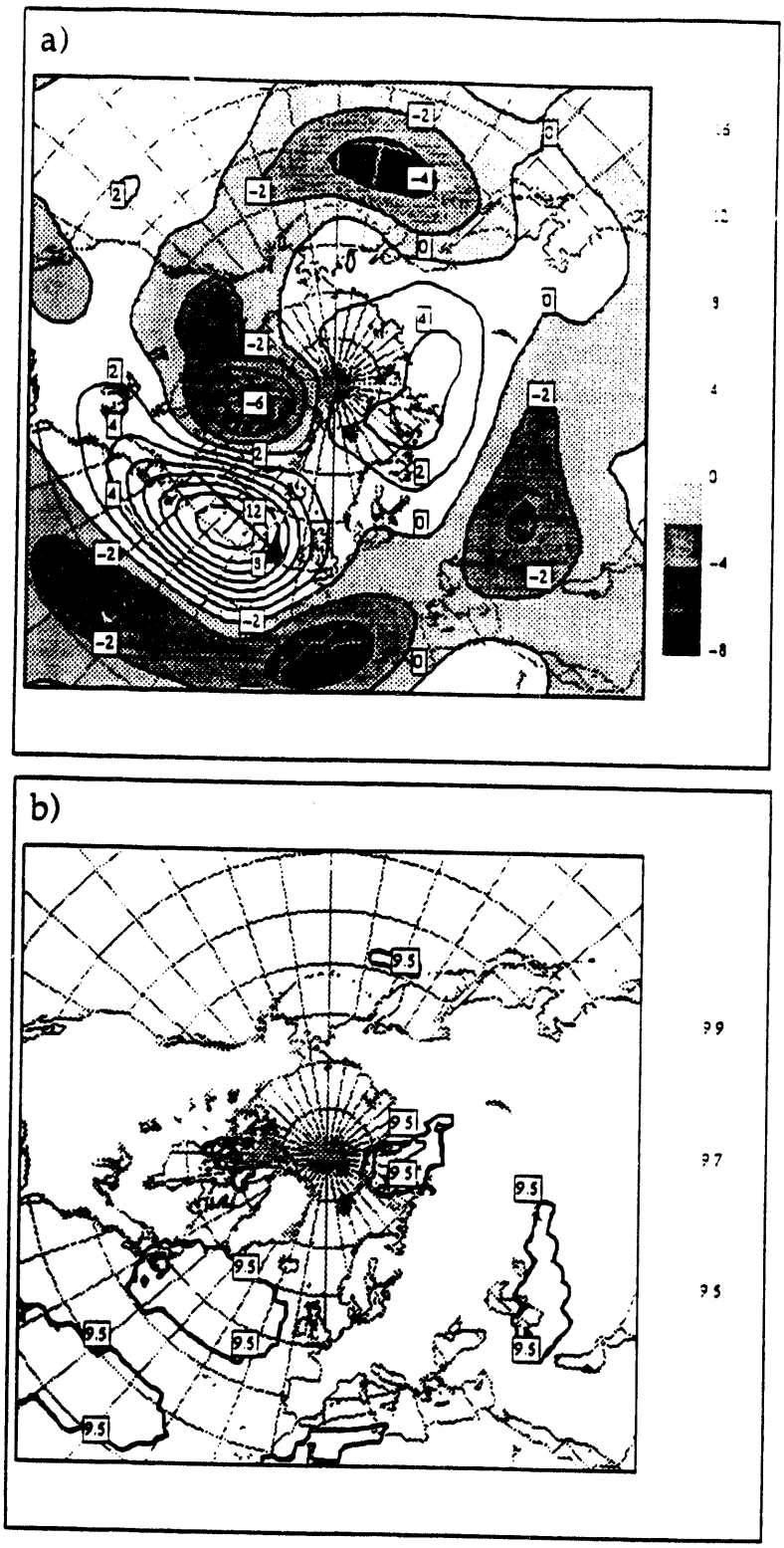

Fig. 2 a) Geopotential height response at 500 mb in the difference field of warm minus control runs, averaged over six November cases. Results are based on the last 30-days of each 50-day simulation. Negative anomalies are shaded. The contour interval is 2 decameter.
b) Significance level of the difference field in a) estimated by a student t-test. Areas with significance over the 5% level are contoured.

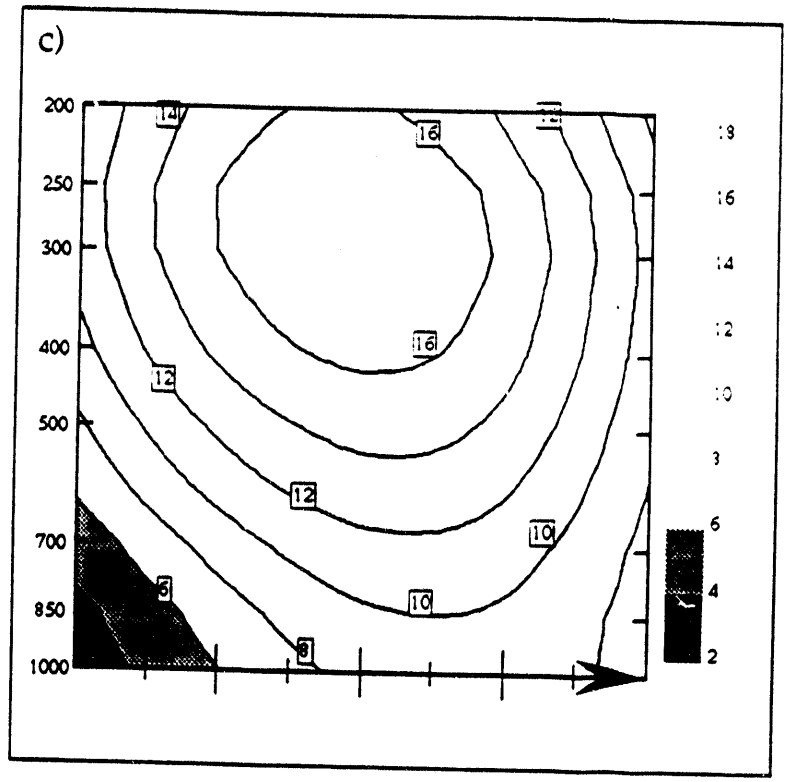

Fig. 2 c) Geopotential height response in the November vertical cross section along the central positions of the anomalous meridional wind at 500 mb over the North Atlantic as marked in a). Anomalies less than 6 decameters are shaded.

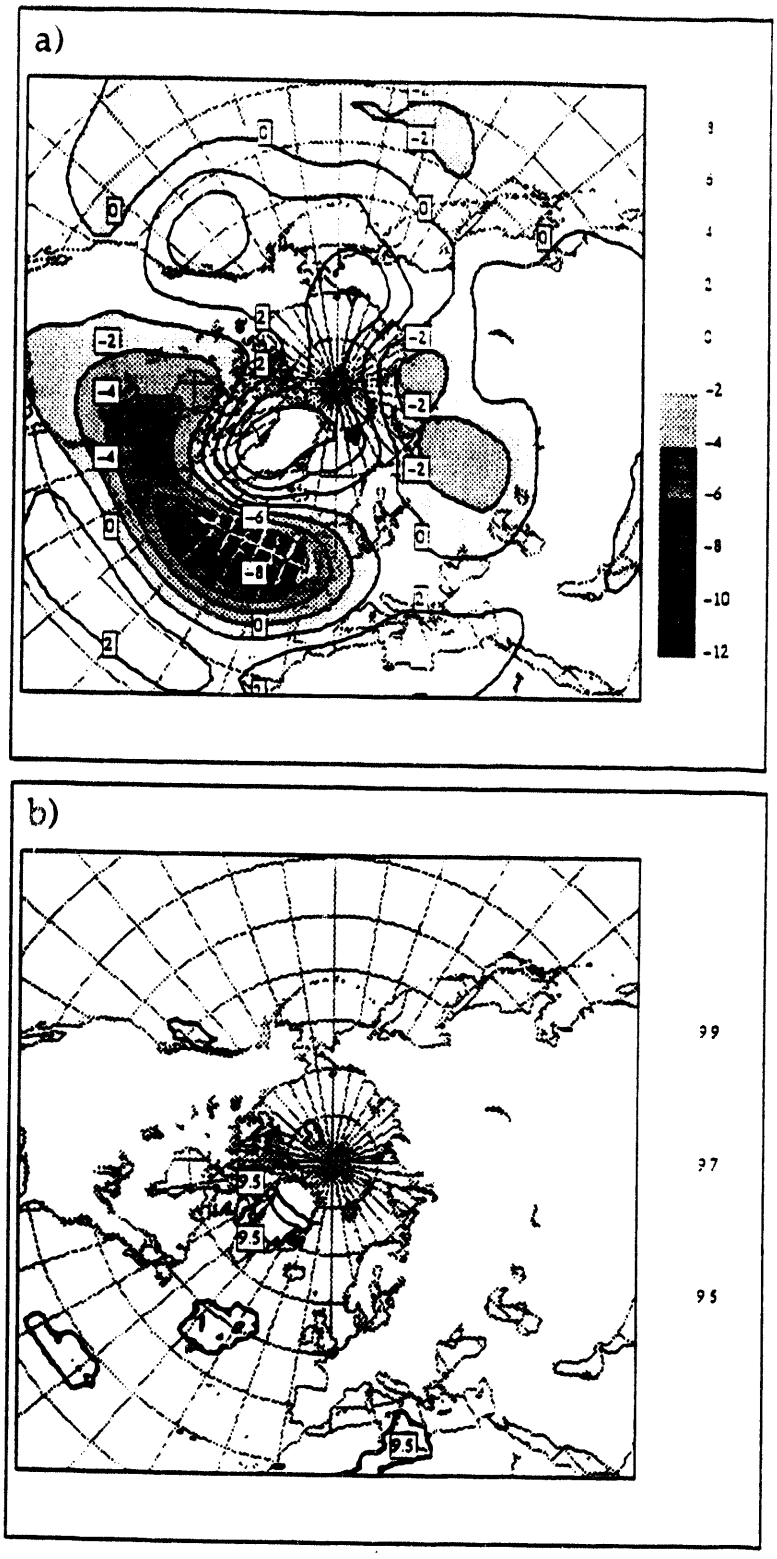

Fig. 3 a) Same as Fig. 2a but for the January cases.
b) Same as Fig. 2b but for a).

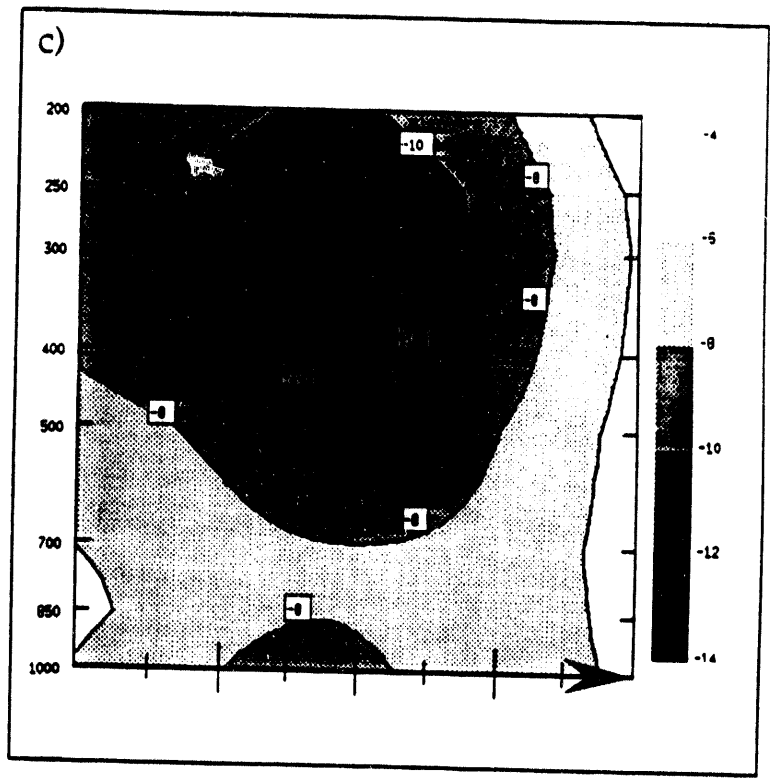

Fig. 3 c) Same as Fig. 2c but along the January vertical cross section marked in a). Anomalies less than -6 decameters are shaded.

Transient Eddy Feedback and Low-frequency Variability

Walter A. Robinson
University of Illinois at Urbana-Champaign

Introduction

Superposed on any externally driven secular climatic change are fluctuations that arise from the internal nonlinear dynamics of the climate system. These internally generated variations may involve interactions between the atmosphere and the ocean, as in the case of El Niño, or they may arise from the dynamics of the atmosphere alone. Here we discuss the dynamics of interactions between transient eddies and lower-frequency motions in the atmosphere.

The interactions between more transient and more persistent motions can be divided into two types. Nonlinear interactions among the transient motions can act as an essentially random source of low-frequency motion. The idea that the low-frequencies respond in a linear way to stochastic forcing from higher frequencies has been applied to the generation of planetary waves (Egger and Schilling, 1984) and to the forcing of changes in global angular momentum (Robinson, 1993). In addition to stochastic coupling, there are systematic interactions, denoted feedbacks, through which the persistent motions modulate their own forcing by the transient eddies. This paper discusses the dynamics of these feedbacks.

First, the mechanism coupling low-frequency (10-day low-pass) and synoptic eddies is reviewed, and a possible explanation for a discrepancy between observations and several models is suggested. Secondly, the coupling between slow variations in the zonal flow and transient eddies is discussed. Here it turns out that low-frequency eddies play an important role, and the organization of their forcing of the zonal flow by the zonal flow appears to be very different from that of the synoptic eddies.

Synoptic eddy feedbacks on low-frequency eddies

Numerous modeling studies have shown that low-frequency eddies, resembling trains of quasi-stationary Rossby waves, appear in the absence of anomalous boundary forcing and under conditions in which their generation by instabilities of the time averaged flow is unlikely. Thus, nonlinear interactions with synoptic scales are probably an important source of low-frequency eddies. This is confirmed in a two-level model by calculating the enstrophy budget for low-frequency eddies (Robinson 1991). Nonlinear interactions among synoptic (10-day high pass filtered) eddies are a source of low-frequency enstrophy that is subsequently lost to dissipation and

interactions with the time averaged flow. That these synoptic-low frequency interactions involve a feedback is confirmed by experiments in which the low frequency eddies in the model are generated by an external forcing. The high-frequency forcing of the low-frequency eddies may be defined as the low-pass filtered convergence of the vorticity flux by the high frequencies. In the imposed forcing experiments this high-frequency forcing takes on the same relationship to the low-frequency eddies as is found in the unforced model where the low-frequency eddies arise spontaneously.

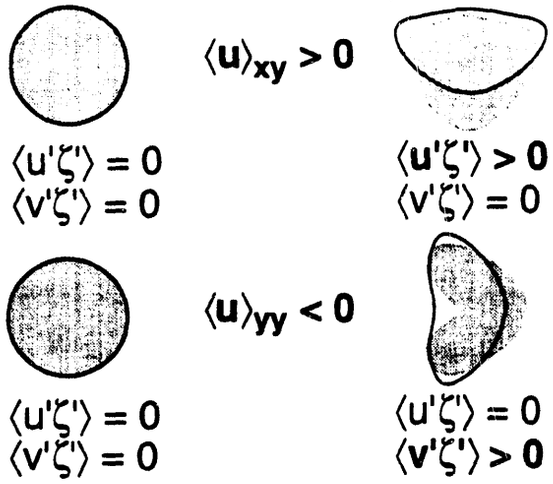

Fig 1. Schematic of mechanism for synoptic-low frequency interaction. Shading represents a patch of vorticity, and the solid curves are contours of the induced streamfunction.

In considering possible mechanisms for this feedback, there are a few salient facts:

1) The high-frequency forcing has components in phase with and in quadrature with (to the west of) the low-frequency eddies.

2) The quadrature component of the high-frequency forcing is stronger for shorter wavelength low-frequency eddies, so that high-frequency forcing of very long (zonal wavenumbers 1 and 2) low-frequency waves is predominantly in phase with the wave, while forcing of shorter waves is predominantly in upstream quadrature.

3) The quadrature component of the high-frequency forcing is produced by east-west vorticity fluxes, while the in phase component results from north-south fluxes.

Qin and Robinson (1992) suggested a theory, consistent with these facts, for the synoptic-low frequency interaction. Consider a patch of vorticity associated with a synoptic scale disturbance. The shape of this patch is distorted as it is advected by the low-frequency flow (fig 1). The winds induced by the distorted patch will cause a net flux of the patch's vorticity. The top

right drawing in the figure shows the distortion obtained as the patch is advected towards the ridge of a long wave, with the greatest distortion achieved at the ridge. The distorted eddy has an eastward vorticity flux (an eddy in the trough would have a westward flux) leading to a vorticity flux convergence upstream of the largescale trough, and so giving rise to upstream quadrature feedback. In the lower panels the patch is distorted by the winds found in the core of a zonal jet. The northward vorticity flux so induced reinforces the jet. This is simply Victor Starr's "negative viscosity".

These ideas, tested in a linear barotropic model, agree very well with the results from the two-level model. Their agreement with observations, however, is less satisfactory. Cai and van den Dool (1991) found stronger in phase feedback and weaker upstream feedback in observations, though the feedback did shift upstream for shorter low-frequency waves. A similar discrepancy shows up in Ting and Hoerling's (1993) comparison of observations and GCM results for the midlatitude response to the 1986/87 El Niño. The transient eddy vorticity fluxes are more important in the observations than in the model. The synoptic eddy contribution is more nearly in phase with the streamfunction in the observations, but is shifted upstream from the stationary eddy in the model.

A possible explanation for these results comes from recent work by Held and Phillips (1993). They find that the meridional eddy momentum flux in models is very sensitive to meridional resolution. Thus, models with relatively coarse meridional resolution (R15 for the two-level model, T31 for the CCM used by Ting and Hoerling) may be underestimating that component of the vorticity flux that contributes the in-phase feedback. Several tests of this idea are planned: repeating the two-level model experiments and Qin and Robinson's barotropic calculations at higher meridional resolutions, and comparing the synoptic-low frequency feedback between R15 and R30 versions of the GFDL GCM.

Transient eddy feedbacks on the zonal flow

Several numerical models display vacillations in the zonal flow as an important mode of low-frequency variability (GFDL GCM, Feldstein 1993; seven-level idealized model, Yu and Hartmann 1993; two-level model, Robinson 1992). Such variations in the "zonal index" are supported by transient eddy momentum fluxes in the models and in observations from the Southern Hemisphere (Karoly, 1990). Yu and Hartmann show that the positive eddy feedback on the zonal index is consistent with the difference between momentum fluxes integrated over

baroclinic lifecycles that begin with high and low index zonal flows. Several questions remain, however, regarding the transient eddy feedback on the zonal index. For example, in the two-level model, the spectrum of index variations (fig 2) deviates significantly from a red-noise spectrum, with an apparent deficit of variance at periods around 50 days. This suggests that the eddy feedback is more complex than simply a positive feedback opposing dissipation.

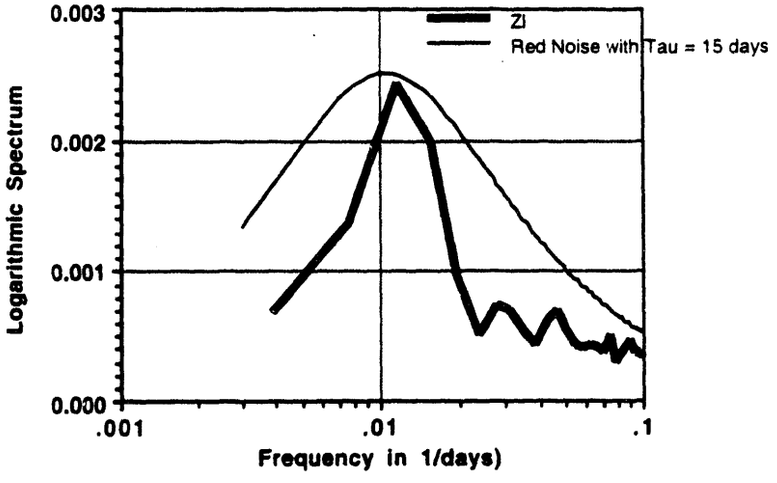

Fig 2. Spectrum of zonal index variations in a two-level model

To explore the dynamics of the feedback, the technique of using an externally imposed forcing with a simple structure in space and time is again employed. The barotropic component of the zonal wind in the two-level model is driven periodically with the forcing whose meridional structure is displayed in fig 3. A coarse grain exploration of the parameter space of forcing period and amplitude has been carried out. Because of the strong internal variability in the model, each case requires at least 20 periods to obtain reliable results. Figure 4 shows an example of the results with a period of 60 days. The amplitudes and temporal phases of the synoptic eddy (wavenumbers 6-15) and longwave (wavenumbers 1-5) feedbacks on the zonal flow are shown in fig 5. Synoptic eddy and longwave feedbacks have similar strengths, and their influences on the zonal wind are somewhat stronger than that of the model's linear drag (1/10 days). Their phases, however, are very different. At 50 °N the synoptic eddy feedback lags the zonal wind slightly, perhaps consistent with the timescale of a baroclinic lifecycle. The longwave feedback lags the

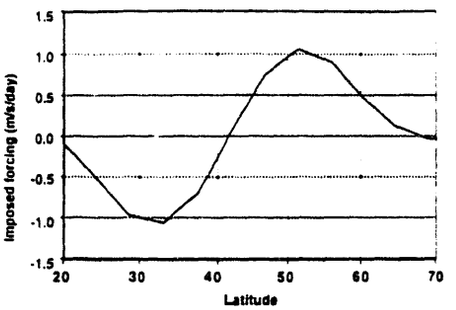

Fig 3. Periodic forcing imposed on the zonal flow.

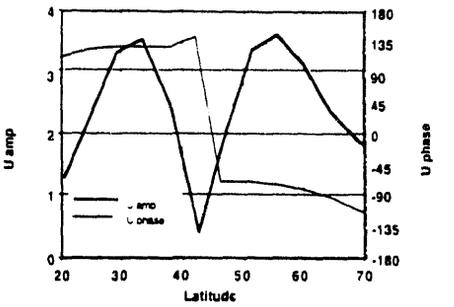

Fig 4. Zonal wind response to forcing with a period of 60 days.

zonal wind by more than a quarter period. This means that the longwave feedback opposes the imposed forcing, and it significantly reduces the zonal wind response. Also, the longwave feedback opposes the zonal wind tendency. This leads to a reddening of the spectral response of the zonal wind (fig 6), and may explain the spectrum in fig 2.

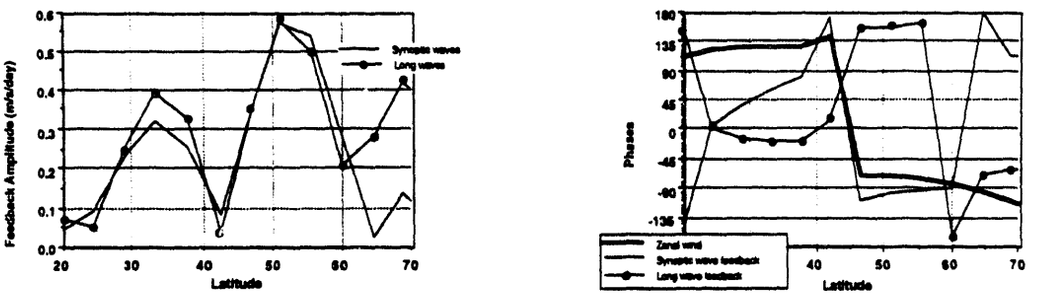

Fig 5. Amplitudes and phases of synoptic and long wave feedbacks.

Assuming that the synoptic eddy feedback can be understood as the negative eddy viscosity that occurs during the barotropic decay phase of baroclinic lifecycles, the question remains as to the mechanism for the longwave feedback. One possibility is that it is a consequence of wave-mean flow interactions induced by the time dependence of the zonal flow. Zonal jets are regions of strong meridional gradients in the potential vorticity, and Rossby wave activity tends to be concentrated in such regions. As the jet weakens or moves away, this wave activity is released, causing an EP flux divergence in the region of the weakening jet that will oppose the weakening. This idea can easily be tested in a linear barotropic model, and such tests will be carried out in the next few months.

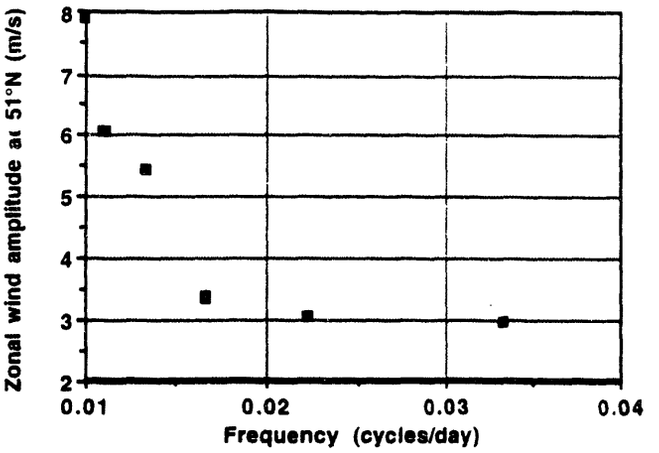

Fig 6. Frequency dependence of the zonal wind response to periodic forcing.

Acknowledgments

This work is supported by the Climate Dynamics and Large-scale Dynamic Meteorology Programs of the National Science Foundation, grants ATM-9222578 and 9024832.

References

Cai, M., and H. M. van den Dool, 1991: Low-frequency waves and traveling storm tracks. Part I: Barotropic component. *J. Atmos. Sci.*, **48,** 1420-1436.

Egger, J., and H.-D. Schilling, 1984: Stochastic forcing of planetary scale flow. *J. Atmos. Sci.*, **41,** 779-788.

Feldstein, S. B., 1993: Interannual variability in atmospheric angular momentum in a GCM with climatological SST's. submitted to *J. Climate.*

Held, I. M., and P. J. Phillips, 1993: Sensitivity of the eddy momentum flux to meridional resolution in atmospheric GCM's. *J. Climate,* **6,** 499-507.

Karoly, D. J., 1990: The role of transient eddies in low-frequency zonal variations in the Southern Hemisphere. *Tellus,* **42A,** 41-50.

Qin, J., and W. A. Robinson, 1992: Barotropic dynamics of interactions between synoptic and low-frequency eddies. *J. Atmos. Sci.*, **49,** 71-78.

Robinson, W. A., 1991: The dynamics of low-frequency variability in a simple model of the global atmosphere. *J. Atmos. Sci.*, **48,** 429-441.

---, 1992: The dynamics of the zonal index in a simple model of the atmosphere. *Tellus,* **43A,** 295-305.

---, 1993: The generation of ultralow-frequency variations in a simple global model. *J. Atmos. Sci.*, **50,** 137-143.

Ting, M., and M. P. Hoerling, 1993: Dynamics of stationary wave anomalies during the 1986/87 El Niño. submitted to *Climate Dynamics*

Yu, J.-Y., and D. L. Hartmann, 1993: Zonal flow vacillation and eddy forcing in a simple GCM of the atmosphere. *J. Atmos. Sci.*, (in press).

The importance of resolution on the response of mid-latitude transients to enhanced CO_2

C A Senior

The Hadley Centre For Climate Prediction and Research

The impact of global warming on the activity of the mid-latitude transients is not well understood. Work with simple models suggests that there will be two competing effects on transient activity. Firstly there will be a reduction in the baroclinicity due to a smaller pole-equator temperature gradient and secondly there will be increased moisture availability in a warmer atmosphere.

A comparison of the mid-latitude transients from two versions of the Hadley Centre for Climate Prediction and Research GCM run at different resolutions is presented and the importance of resolution on the simulation of the high and low frequency variability is discussed. At higher resolution, one of the largest responses of the model to a doubling of atmospheric CO_2 is an enhancement of the westerly flow in the North Atlantic (Hall et al 1993), but this is much reduced at lower resolution. Consistency is sort between changes in the time mean flow and the transient behaviour.

The model

The model is a version of the Hadley Centre for Climate Prediction and Research GCM as described by Senior and Mitchell (1993). The two horizontal resolutions described here are 2.5° x 3.75° Latitude/Longitude (Km250) and 5.0° x 7.5° Latitude/Longitude (Km500). The models were run for between fifteen and twenty years to reach equilibrium and the results shown are DJF averages over the final 10 years of the integrations. For Km500 the transient fields are only available for the last three years of the integration.

Model Climates and Systematic Error

(a) Mean Flow

The Low resolution model seriously underestimates the depth of the Southern Hemisphere circumpolar trough and the height of the subtropical highs. The simulation in the Northern Hemisphere is substantially better. The Aleutian low extends rather too far into the North American continent and the Icelandic low extends too far east with errors of up to -8 mb over Britain. The simulation at Km250 is much more realistic in the Southern Hemisphere, but represents little improvement in the Northern Hemisphere. The error over Britain is slightly larger, with a zonalization of the atlantic flow This has been noticed in other studies of increasing resolution even in models, such as this one, that include a representation of gravity wave drag (eq Dyson 1985, Boer and Lazare 1988). It is worth noting that the improvement with resolution in JJA is obvious in both hemispheres.

(b) Variability

Band Pass and Low pass filters were applied to the variance of the 500 mb height field (Blackmon 1976) to isolate variability on timescales between 2 and 6 days and greater than 6 days respectively. The resulting fields shows the regions of maximum high frequency variability or 'storm tracks' and regions of low frequency variability.

Km500 simulates the positions of the three major storm-tracks, in the North Atlantic, the North Pacific and the Southern Ocean (not shown) reasonably well but substantially underestimates the amount of variability in each region (Figure 1 a,d). In the Northern Hemisphere the model tends to shorten the storm tracks with the largest errors occuring at the eastern end of the ocean basin. In the Pacific the maximum variability is situated too far west. Km250 has generally more high-frequency variability than Km500, but still less than the analysed values (Figure 1 b, c). The error in the eastern North Atlantic is reduced by 50% (Figure 1 e). Neither model captures the northward tilt of the observed North Atlantic storm track (Figure 1 c). so that the model storms continue into continental Europe. In the Pacific storm track, the high resolution model performs better in the centre and to the west but is somewhat worse in the east.

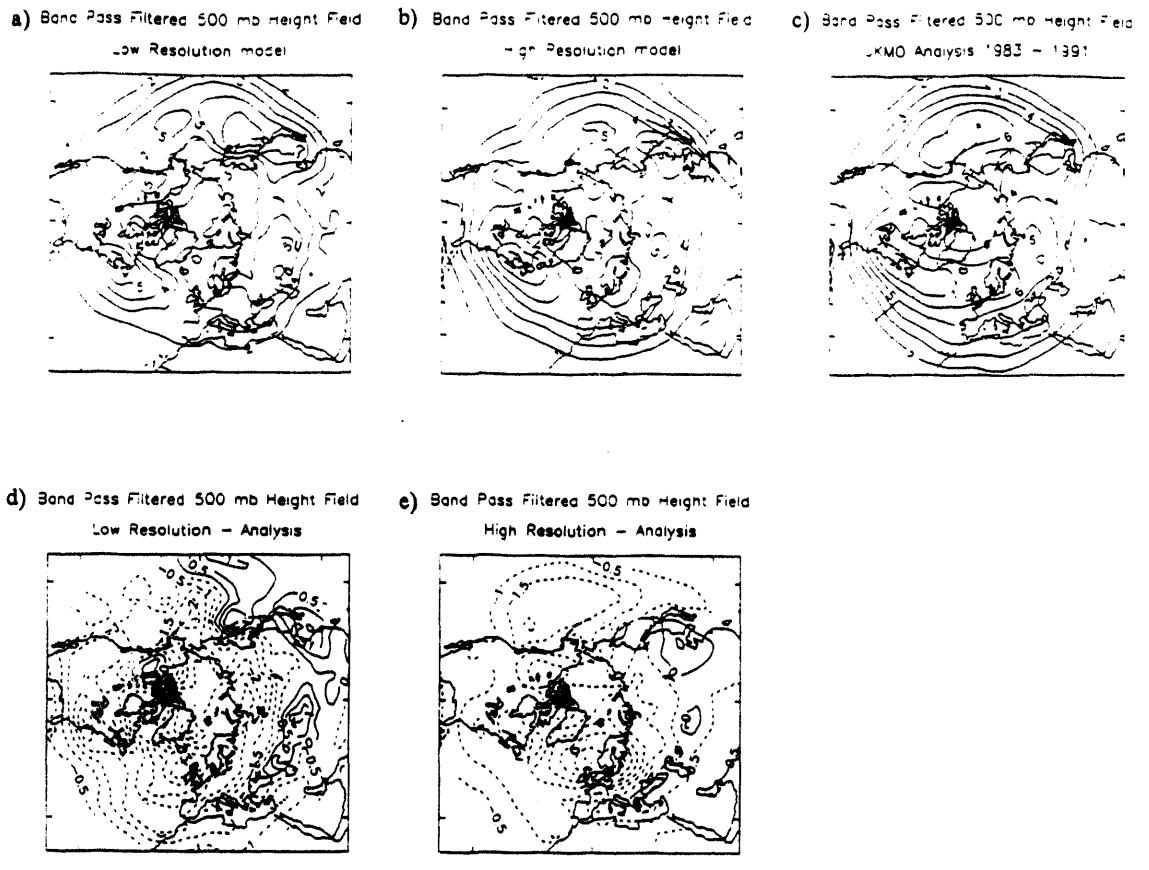

Figure 1: Band pass filtered variance of 500mb height. a) Low resolution b) High resolution c) UKMO analysis 1983-1991 d) Low Resolution - Analysis e) High Resolution - Analysis

The eastern end of the storm track is also a region of maximum observed low frequency variability. The simulation of the low frequency variability in Km500 is poor, with the maxima in both ocean basins being situated too far north, giving large errors to the south At higher resolution the Atlantic low frequency variability is improved in the west but is still deficient further east over Britain. This is consistent with the short Atlantic storm track. The observed maximum over central Siberia is well reproduced. The Pacific storm track is positioned further south than in Km500 as in the analysis, but there is a minimum in the magnitiude of the variability in the central pacific where the analysis has a maximum.

The Response to increased CO2

Mean Changes

One of the largest responses of the High resolution model is the enhanced westerly flow in the North Atlantic and to a lesser extent in the north Pacific. There are increases of 4-6 mb in Mean sea level pressure across the Atlantic at about 45° North, with similar reductions at 65°N. The northward shift of the jet can also be seen in the zonal mean wind. In Km500 the response in the North Atlantic is somewhat similar but of a smaller magnitude and in the Pacific the changes are very small. The zonally averaged wind does not show a northward shift.

In both models there is a general increase in the pole to equator temperature gradient at upper levels due to the enhanced warming of the upper tropical troposphere when compared to that at higher latitudes (Figure 2). In the lower troposphere there is a general reduction in the meridional pole-equator temperature gradient because the high latitudes warm more than lower latitudes due to the sea-ice albedo feedback mechanism (eg Ingram et al 1989). However, superimposed on this in Km250 there is an enhanced warming over northern continents which is advected eastwards over the ocean. The picture in the western north Atlantic is further complicated by the strong local minimum in the warming to the south of Greenland. The result is an increase in the baroclinicity to the north and east and a reduction to the south. In Km500, the change in the lower tropospheric meridional temperature gradient is qualitatively similar with a high latitude amplification of the warming (which is larger than in KM250) and a smaller warming in the tropics. The eastward advection of the continental warming over the western ocean basins is much reduced in Km500 especially in the Pacific, but the local minimum in the warming off the tip of greenland is still evident.

In the Atlantic, in Km250, there is a reduction in the sensible heating off the eastern US coast where the land/sea temperature contrast has reduced. Both models show an increase in specific humidity which gives rise to increased latent heat release at the storm track exit regions. This is in the western Atlantic in Km250 but further east in Km500 as the storm track in the control did not extend as far west. In the Pacific storm track there are also reductions in sensible heating in the west where the heating of the continent has advected over the ocean, again this is larger in Km250. The change in latent heating is quite different in the two models with a clear northward shift in Km250

and an eastward shift in Km500. These changes are consistent with the changes in the storm tracks outlined below.

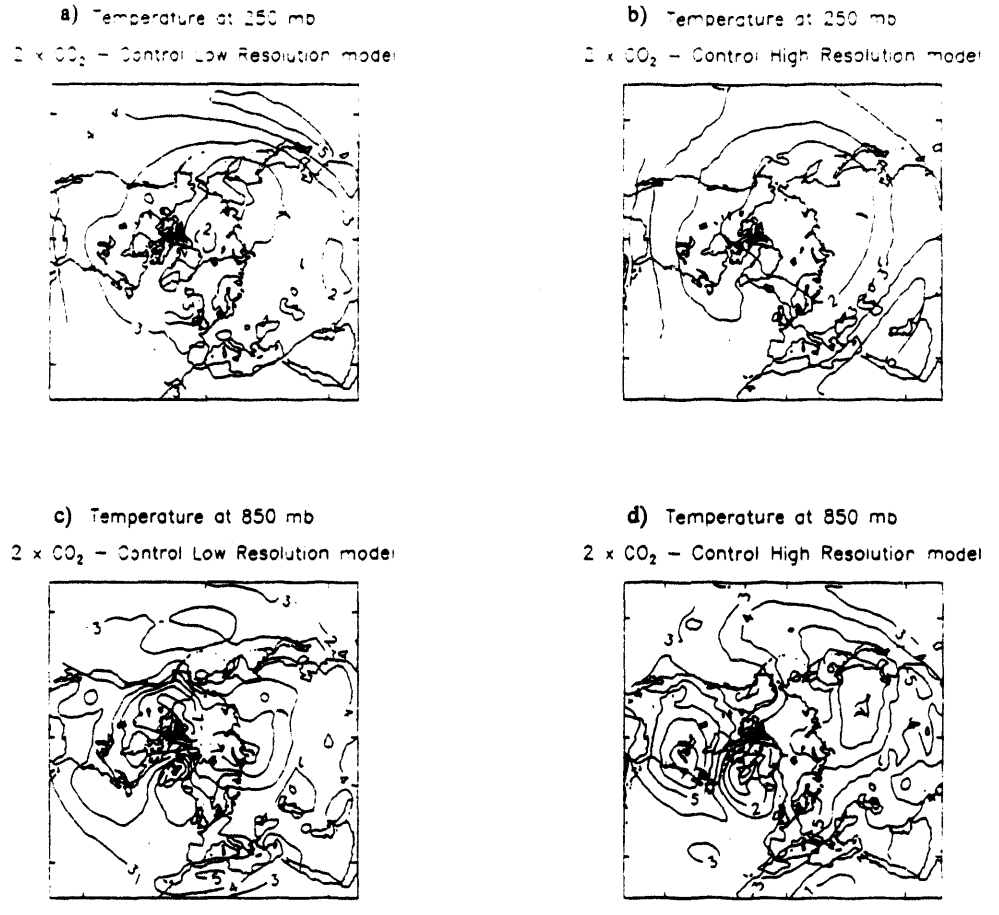

Figure 2: 2 x CO2 - Control Temperature. a) Low resolution at 250mb b) High resolution at 250mb c) Low resolution at 850mb d) High resolution at 850mb

Changes in Variability

Km250 simulates a poleward and downstream intensification of both Northern Hemisphere storm tracks and this is most marked in the Atlantic, with large changes over north west Europe as well (Figure 3).

Km500 shows a similar intensification and downstream shift of the Atlantic storm track, but of a reduced magnitude and there is little evidence of a northward movement. Both models show an error in the orientation of the western end of the Atlantic storm track in the control simulations, with

the lows tracking too far westwards into europe rather than northwards as in the observations. This is most pronounced in Km500 and the lack of a northward shift in the enhanced CO_2 run may be related to the large systematic error. In the Pacific the maximum variability moves from the west side to the central pacific and reduces in intensity . Once again this is in the sense to correct the error in the control simulation. There is no evidence of a poleward movement in the storm track.

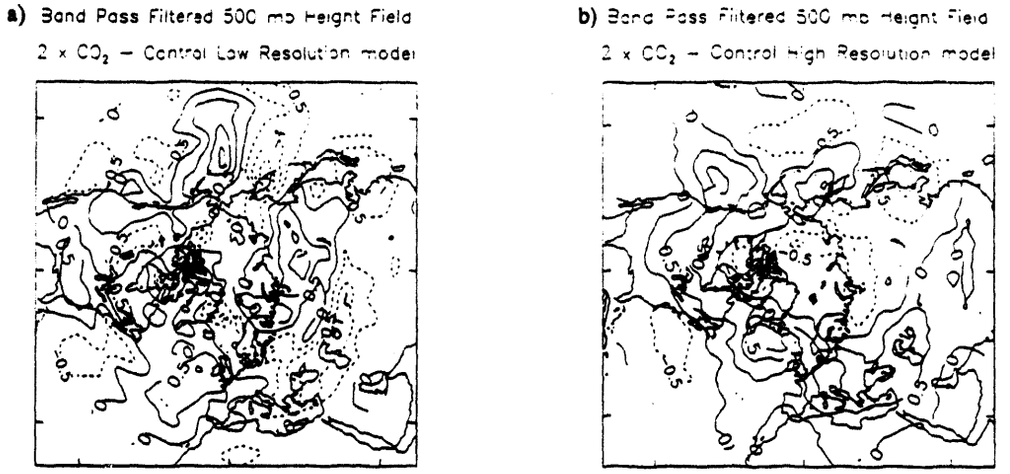

Figure 3: 2 x CO2 - Control Band pass filtered variance of 500mb height. a) Low resolution b)High resolution

In Km250 there is a poleward and eastward extension of the low frequency variability as seen for the band pass filtered results, in both the North Atlantic and Pacific. In KM500, there is an overall reduction in the low frequency variabilty to the north where the maximum variability was in the control integration and increases to the south. This again corrects a bias in the control.

Conclusions

The low resolution model achieves a surprisingly good simulation of the mean Northern Hemisphere flow which seems to be explained by a fortuitous cancellation of errors as the model does not simulate either the high or low frequency variability with any accuracy. The simulation of the mean Northern Hemisphere flow shows little improvement at higher resolution and is degraded in some regions, notibly the North Atlantic and western Europe, where there is a relatively large

systematic error. The higher resolution model has an improved simulation of the high frequency variability in the Atlantic and Pacific storm tracks but does not simulate well the observed low frequency variability. The omission of the maximum in low frequency variability situated at the eastern end of the storm track tends to produce overly zonal flow in the North Atlantic and Western Europe. Both models simulate a downstream shift and intensification of the North Atlantic storm track with enhanced CO_2 and consistent changes in the time mean flow, however the signal is much greater at higher resolution Caution must be used in interpreting these results due to the large systematic errors in both models in this region.

References

Blackmon, M.L., 1976: A Climatological Spectral study of the 500mb Geopotential height of the Northern Hemisphere. J. Atmos. Sci. **33**, 1607-1623

Boer, G.J. and M. Lazare, 1988: Some results concerning the eefects of Horizontal resolution and Gravity wave drag. J. Climate **8**, 789-806

Dyson, J., 1985: The effect of resolution and diffusion on the simulated Climate. Research activites in Atmospheric and Oceanic Modelling, Report No. **8** WMO Geneva.

Hall, N. M. J., B. J. Hoskins, P. J. Valdes and C. A. Senior, 1993. Storm Tracks in a High resolution GCM with Doubled CO2. Accepted for publication in Q.J.R.M.S

Ingram, W. J. , C.A. Wilson and J.F.B. Mitchell, 1989: Modelling Climate Change: An assessment of sea-ice and surface albedo feedbacks. J. Geophys. Res. **94** 8609-8622

Senior, C.A. and Mitchell, J. F. B., 1993: CO2 and Climate: The impact of Cloud parameterization. J. Climate. **6** 393-418

Scaling of saturation amplitudes in baroclinic instability

Theodore G. Shepherd

Department of Physics, University of Toronto, Toronto M5S 1A7 Canada

1. Introduction

By using finite-amplitude conservation laws for pseudomomentum and pseudoenergy, rigorous upper bounds have been derived on the saturation amplitudes in baroclinic instability for layered and continuously-stratified quasi-geostrophic models. Bounds have been obtained for both the eddy energy and the eddy potential enstrophy. The bounds apply to conservative (inviscid, unforced) flow, as well as to forced-dissipative flow when the dissipation is proportional to the potential vorticity.

This approach provides an efficient way of extracting an analytical estimate of the dynamical scalings of the saturation amplitudes in terms of crucial non-dimensional parameters. A possible use is in constructing eddy parameterization schemes for zonally-averaged climate models. The scaling dependences are summarized, and compared with those derived from weakly-nonlinear theory and from baroclinic-adjustment estimates.

2. Pseudoenergy, pseudomomentum, and nonlinear stability

The method employed here uses finite-amplitude conservation laws for disturbances to given basic flows. Note that in general, this assumes unforced, inviscid dynamics. It is well known (McIntyre & Shepherd 1987) that when the basic flow is *steady*, then the *pseudoenergy* $\mathcal{A}(t)$ is conserved; and when the basic flow is *zonal*, then the *pseudomomentum* $\mathcal{M}(t)$ is conserved. The pseudoenergy and pseudomomentum have the following important properties: (i) they are conserved by the full, nonlinear dynamics; (ii) they are quadratic to leading order in disturbance amplitude; and (iii) they may be constructed systematically. These properties all follow directly from the underlying Hamiltonian structure of geophysical fluid dynamics (see McIntyre & Shepherd 1987; Shepherd 1990).

Familiar examples of such "pseudo"-invariants include available potential energy (Shepherd 1993*a*), Eliassen-Palm wave activity (Killworth & McIntyre 1985), and wave action (Andrews & McIntyre 1978; Shepherd 1990). The associated conservation laws may be written in local or global form. It may be helpful to recall the expressions in the barotropic

case where $P = \nabla^2\Phi + f + \beta y$ is the potential vorticity, and Φ is the streamfunction. We introduce a basic state (Ψ, Q) and consider finite-amplitude disturbances (ψ, q) to it:

$$\Phi = \Psi + \psi, \qquad P = Q + q. \tag{1}$$

The pseudoenergy relative to this basic state is given by (McIntyre & Shepherd 1987)

$$\mathcal{A} = \int \left\{ \frac{1}{2}\overline{|\nabla\psi|^2} + \overline{\int_0^q [\Psi(Q+\tilde{q}) - \Psi(Q)]\, d\tilde{q}} \right\} dy \approx \int \frac{1}{2}\left\{ \overline{|\nabla\psi|^2} + \frac{d\Psi}{dQ}\,\overline{q^2} \right\} dy, \tag{2}$$

the second expression being a small-amplitude approximation. In the above, the functional relation $\Psi = \Psi(Q)$, which exists for any steady basic state, has been used. The overbar denotes an average in x. It is clear from (2) that if $d\Psi/dQ > 0$ then $\mathcal{A} > 0$, even at finite amplitude. The pseudomomentum is given by (Killworth & McIntyre 1985)

$$\mathcal{M} = -\int \left\{ \overline{\int_0^q [\mathcal{Y}(Q+\tilde{q}) - \mathcal{Y}(Q)]\, d\tilde{q}} \right\} dy \approx -\int \frac{1}{2}\frac{\overline{q^2}}{Q'(y)}\, dy, \tag{3}$$

the second expression again being the small-amplitude approximation. In the above, $\mathcal{Y}(Q)$ denotes the inverse of the function $Q(y)$: that is, $y = \mathcal{Y}(Q(y))$. It is clear from (3) that if $Q'(y) \neq 0$ for all y then $d\mathcal{Y}/dQ \neq 0$ and so $\mathcal{M} \neq 0$, even at finite amplitude.

When $\mathcal{A}$ or $\mathcal{M}$ are sign-definite for arbitrary disturbances, then one can establish nonlinear stability of the basic state. Many well-known linear stability theorems can be understood in this way, and can be shown thereby to extend to finite amplitude. Examples of such nonlinear theorems based on pseudoenergy are: static stability (Holliday & McIntyre 1981; Shepherd 1993*a*); Rayleigh's centrifugal stability theorem (Shepherd 1991); symmetric baroclinic stability (Cho, Shepherd & Vladimirov 1993); the Arnol'd (1966) theorems; and the Fjørtoft-Pedlosky theorem (Holm *et al.* 1985; McIntyre & Shepherd 1987). Examples of nonlinear stability theorems based on pseudomomentum are: the Rayleigh-Kuo theorem (McIntyre & Shepherd 1987); and the Charney-Stern theorem (Shepherd 1988, 1989). The invariants may also be combined for steady, zonal basic flows.

3. Saturation bounds on instabilities

How does the above discussion relate to our original question concerning saturation amplitudes of baroclinic instabilities? The first clue is that these stability theorems all apply to disturbances of *finite* (not necessarily small) amplitude. Hence they constrain dynamical evolution in the vicinity of stable states. Therefore, given some state of the system, consider it as a disturbance to a stable state, and then use the stability theorems to constrain the evolution. For best effect, try all possible stable states!

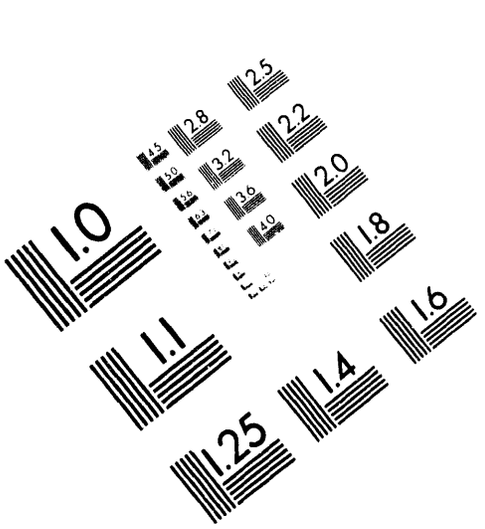

Association for Information and Image Management

1100 Wayne Avenue, Suite 1100
Silver Spring, Maryland 20910

301/587-8202

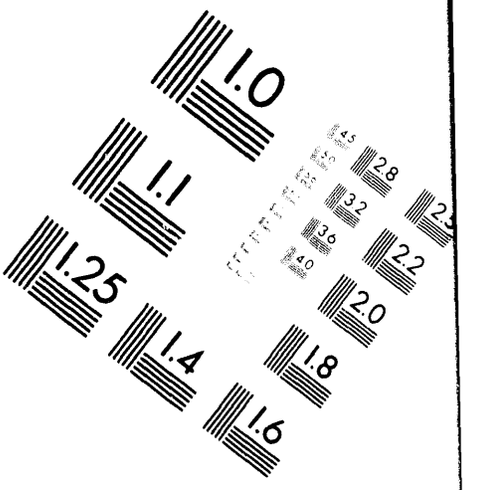

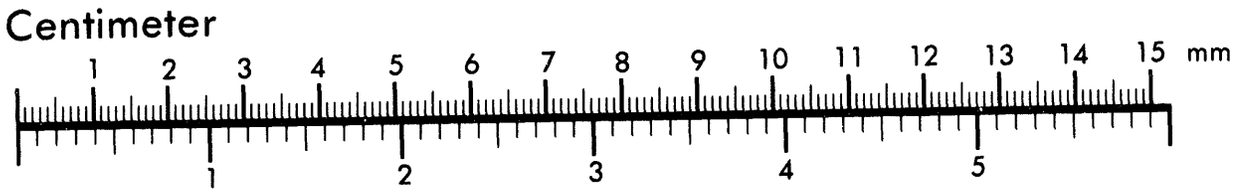

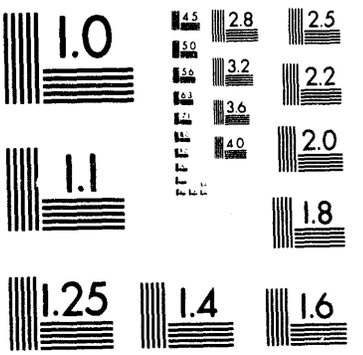

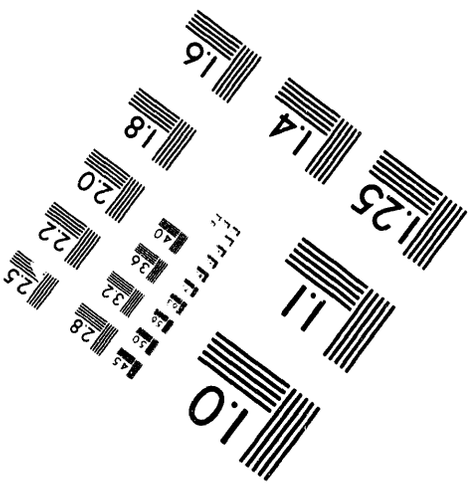

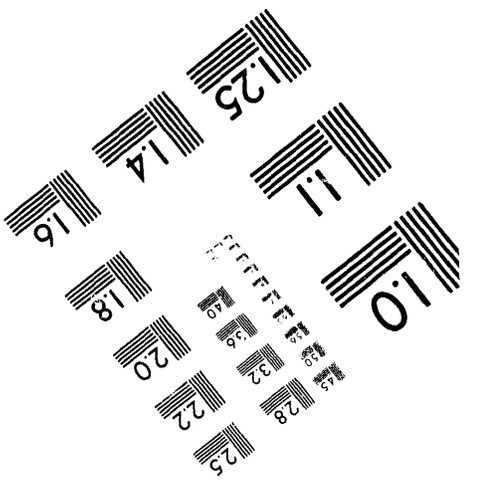

3 of 3

To illustrate the method, let's see how this works for the barotropic case. Suppose the initial condition is

$$\Phi(t=0) \equiv \Phi_0 = \overline{\Phi}_0 + \Phi_0', \qquad P(t=0) \equiv P_0 = \overline{P}_0 + P', \tag{4}$$

the overbars denoting the zonal average and the primes the departures therefrom. We choose (Ψ, Q) to be a stable, steady, zonal flow, in which case $\Phi' = \psi'$ and $P' = q'$, the disturbance (ψ, q) being defined by (1). If $d\Psi/dQ > 0$, then we have the following bound on the eddy energy:

$$\begin{aligned}\mathcal{E}'(t) &\equiv \int \tfrac{1}{2}\overline{|\nabla\Phi'|^2}\,dy = \int \tfrac{1}{2}\overline{|\nabla\psi'|^2}\,dy \le \int \tfrac{1}{2}\overline{|\nabla\psi|^2}\,dy \\ &\le \int \left\{\tfrac{1}{2}\overline{|\nabla\psi|^2} + \overline{\int_0^q \left[\Psi(Q+\tilde{q}) - \Psi(Q)\right] d\tilde{q}}\right\} dy = \mathcal{A}(t) = \mathcal{A}(0).\end{aligned} \tag{5}$$

Now, $\mathcal{A}(0) = \mathcal{A}[\Phi_0, P_0; \Psi, Q]$ is a functional of the initial flow and the basic flow; so for given (Φ_0, P_0), one may vary (Ψ, Q) over all possible stable basic flows to get the best bound on the eddy energy $\mathcal{E}'(t)$. On the other hand, if $dQ/dy \neq 0$ then we have the following bound on the eddy enstrophy:

$$\begin{aligned}\mathcal{Z}'(t) &\equiv \int \tfrac{1}{2}\overline{(P')^2}\,dy = \int \tfrac{1}{2}\overline{(q')^2}\,dy \le \int \tfrac{1}{2}\overline{q^2}\,dy \\ &\le |Q_y|_{\max} \left| \int \left\{ \overline{\int_0^q \left[\mathcal{Y}(Q+\tilde{q}) - \mathcal{Y}(Q)\right] d\tilde{q}} \right\} dy \right| \\ &= |Q_y|_{\max} \left|\mathcal{M}(t)\right| = |Q_y|_{\max} \left|\mathcal{M}(0)\right|.\end{aligned} \tag{6}$$

As above, the upper bound $|Q_y|_{\max}\left|\mathcal{M}(0)\right|$ is a functional of the initial flow and the basic flow; so one may vary Q over all possible stable basic flows to get the best bound on the eddy enstrophy. If the domain is bounded, this also gives a bound on the eddy energy: e.g. in a channel of width L, one has the Poincaré inequality $\mathcal{E}'(t) \le (L/\pi)^2 \mathcal{Z}'(t)$.

These upper bounds are *rigorous*. But the question is: are they good estimates of *equilibrated* eddy amplitudes?

4. Application to Phillips model: bound on eddy energy

Consider the two-layer model, with potential vorticity

$$P_i = \nabla^2\Phi_i + (-1)^i F(\Phi_1 - \Phi_2) + f + \beta y \qquad [i = 1, 2], \tag{7}$$

where the domain is taken to be a periodic zonal channel $0 \leq y \leq 1$. We assume the initial condition to consist of the Phillips basic flow

$$U_1 = -\frac{d\overline{\Phi}_1^{(0)}}{dy} = \frac{\beta}{F}(1+\epsilon) + u_0, \qquad U_2 = -\frac{d\overline{\Phi}_2^{(0)}}{dy} = u_0, \tag{8}$$

plus (for simplicity) an infinitesimal initial eddy perturbation, so that $\Phi_0 \approx \overline{\Phi}_0$. The flow (8) is unstable for $\epsilon > 0$. The eddy energy is

$$\mathcal{E}' = \int_0^1 \frac{1}{2}\Big\{\overline{|\nabla\Phi_1'|^2} + \overline{|\nabla\Phi_2'|^2} + F\overline{(\Phi_1' - \Phi_2')^2}\Big\}\, dy. \tag{9}$$

Application of the method outlined in Section 3, using (5), gives (Shepherd 1993*b*)

$$\mathcal{E}'(t) \leq \frac{\beta^2\epsilon}{6F}\Big(1 + \frac{12\epsilon}{F}\Big) \qquad \text{[valid for } \epsilon \leq \mathcal{O}(1)\text{]}. \tag{10}$$

Note that the total energy in the system is

$$\mathcal{E} = \frac{\beta^2}{24F}\Big(1 + \frac{6}{F}\Big)(1+\epsilon)^2, \tag{11}$$

which, for small supercriticality $\epsilon \ll 1$, is *much* larger than $\mathcal{E}'$. Hence the bound (10) is providing a significant constraint on the dynamics. In the regime $\epsilon \ll 1$, the bound (10) suggests

$$\mathcal{E}'_{\max} \approx \frac{\beta^2\epsilon}{6F}. \tag{12}$$

How does this compare with other approaches? Weakly-nonlinear theory, applied to single-wave equilibration in the non-resonant case, gives (Pedlosky 1970)

$$\mathcal{E}'_{\max} \approx \frac{\beta^2\epsilon}{\pi^2 F}. \tag{13}$$

Weakly-nonlinear theory, applied to single-wave equilibration in the resonant case, gives (Warn & Gauthier 1989)

$$\mathcal{E}'_{\max} \approx \frac{\beta^2\epsilon}{8F}, \qquad \mathcal{E}'_{\text{equil}} \approx \frac{\beta^2\epsilon}{12F}. \tag{14}$$

On the other hand, an estimate appealing to the notion of baroclinic adjustment (Stone 1978; see Shepherd 1993*b*) suggests

$$\mathcal{E}'_{\text{est}} \approx \frac{\beta^2\epsilon}{12F}\Big(1 + \frac{6}{F}\Big). \tag{15}$$

The remarkable thing is that *all* these quantities scale like $\beta^2\epsilon/F$, except for a weak dependence on F in (15), with multiplicative constants as follows:

$0.167 = 1/6$ (rigorous bound)
$0.125 = 1/8$ (weakly-nonlinear, resonant case: maximum)
$0.125 = 1/8$ (baroclinic adjustment, for $F = 12$: channel width of 30° latitude)
$0.101 = 1/\pi^2$ (weakly-nonlinear, non-resonant case: maximum)
$0.083 = 1/12$ (weakly-nonlinear, resonant case: equilibrated)

Therefore the rigorous upper bound (10) captures the essential dynamical scalings of baroclinic saturation, and is quantitatively quite accurate too. In terms of dimensional variables,

$$\frac{\beta^2\epsilon}{F} \quad \longrightarrow \quad \frac{\beta_0^2 N^2 D^3 L^3 \epsilon}{f_0^2}. \tag{16}$$

Presumably *all* these quantities are over-estimates in the "wide-jet" limit $L \to \infty$, since in that case one expects the eddy energy to increase only like L, not L^3 (Haidvogel & Held 1980). The physical understanding of this is that the most unstable wave, which all the estimates (12)–(15) must contain, breaks down well before reaching its maximum amplitude (Panetta & Held 1989).

5. Application to Charney model: bound on eddy potential enstrophy

Consider continuously-stratified flow, with potential vorticity

$$P = \nabla^2\Phi + \Phi_{zz} - h^{-1}\Phi_z + f + \beta y, \tag{17}$$

where the domain is taken to be a periodic zonal channel $0 \le y \le 1$, with $0 \le z < \infty$. We assume the initial condition to consist of the Charney basic flow $U(z) = \xi z$, which is unstable for all $\xi > 0$, plus (as above) an infinitesimal initial eddy perturbation. The eddy potential enstrophy is

$$\mathcal{Z}' = \int_0^\infty \int_0^1 \frac{1}{2} e^{-z/h} \overline{(P')^2}\, dy dz. \tag{18}$$

Application of the method outlined in Section 3, using (6), gives (Shepherd 1989)

$$\mathcal{Z}'(t) \le \begin{cases} \dfrac{\beta}{6} & \text{for } \beta h \ge 1, \\ \dfrac{(\beta h + 1)^2}{24h} & \text{for } \beta h \le 1, \end{cases} \tag{19}$$

where $\beta h = \beta_0 N^2 H / f_0^2 \xi$. Recall (Held 1978) that $\beta h \gg 1$ implies $D \approx H/\beta h \ll H$ (shallow limit), while $\beta h \ll 1$ implies $D \approx H$ (deep limit), where D is the vertical scale of the unstable baroclinic wave.

The baroclinic adjustment estimate (Lindzen & Farrell 1980; see Shepherd 1989) is $\mathcal{Z}'_{\rm est} \approx (\beta h + 1)/24h$. So in the "shallow" limit $\beta h \gg 1$, we have

$$\mathcal{Z}'_{\rm max} \approx \frac{\beta}{6} \quad \text{(rigorous bound)}, \qquad \mathcal{Z}'_{\rm est} \approx \frac{\beta}{24} \quad \text{(baroclinic adjustment)}. \tag{20}$$

Both estimates scale the same way. The total potential enstrophy is $\mathcal{Z} = (\beta h + 1)^2/24h$, which is *much* larger than $\mathcal{Z}'$ in this regime. In the "deep" limit $\beta h \ll 1$, we have

$$\mathcal{Z}'_{\rm max} \approx \frac{1}{24h} \quad \text{(rigorous bound)}, \qquad \mathcal{Z}'_{\rm est} \approx \frac{1}{24h} \quad \text{(baroclinic adjustment)}, \tag{21}$$

both of which are equal to the total potential enstrophy $\mathcal{Z}$. Note that in the atmosphere, $\beta h = \mathcal{O}(1)$.

It turns out (P.H. Stone, personal communication) that the rigorous bound (19) is consistent with energy equipartition arguments. To see this, note that in dimensional variables, (19) takes the asymptotic limits

$$\mathcal{Z}' \le \begin{cases} \dfrac{\rho_0 \beta_0 f_0^2 L^3 \xi}{6N^2} & \text{for } \beta_0 \gg 1, \\ \dfrac{\rho_0 f_0^4 L^3 \xi^2}{24 H N^4} & \text{for } \beta_0 \ll 1. \end{cases} \tag{22}$$

Now estimate

$$\mathcal{Z}' \approx \frac{1}{2} \rho_0 L D \langle P'^2 \rangle, \qquad P' \approx \frac{u'}{L_R} \equiv \frac{f_0}{ND} u', \tag{23}$$

where the angle brackets denote some local average in the baroclinic zone. This gives an estimate of the eddy kinetic energy:

$$\langle u'^2 \rangle \approx \frac{N^2 D^2}{f_0^2} \langle P'^2 \rangle \approx \frac{2N^2 D}{f_0^2 \rho_0 L} \mathcal{Z}', \tag{24}$$

which when combined with (22) leads to the bound

$$\langle u'^2 \rangle \le \begin{cases} \dfrac{\beta_0 L^2 D \xi}{3} = \dfrac{f_0^2 L^2 \xi^2}{3N^2} & \text{for } \beta_0 \gg 1, \\ \dfrac{f_0^2 L^2 D \xi^2}{12 H N^2} = \dfrac{f_0^2 L^2 \xi^2}{12 N^2} & \text{for } \beta_0 \ll 1. \end{cases} \tag{25}$$

Note that in both limits, the bounds scale the same way; i.e. there is no dependence on β_0! To compare with the zonal APE, take

$$T^* \approx L\frac{\partial\overline{T}}{\partial y} \approx \frac{LT_0 f_0 \xi}{g} \quad \text{(thermal wind relation)}, \tag{26}$$

which leads to a local estimate of ZAPE (dimensionally consistent with $\langle u'^2 \rangle$ above)

$$\frac{g^2}{T_0^2 N^2}\langle T^{*2}\rangle \approx \frac{f_0^2 L^2 \xi^2}{N^2}. \tag{27}$$

This is the same factor that arose in (25) with respect to EKE! So (25) and (27) suggest

$$\frac{\text{EKE}}{\text{ZAPE}} \leq \begin{cases} \dfrac{2}{3} & \text{for } \beta_0 \gg 1, \\ \dfrac{1}{6} & \text{for } \beta_0 \ll 1. \end{cases} \tag{28}$$

Thus the rigorous bound (19) is consistent with the notion of energy equipartition: namely, EKE/ZAPE = $\mathcal{O}(1)$. (The relative size of EAPE compared with EKE depends on the ratio L_R/L.)

It is interesting to contrast this with the analysis for the Phillips model presented in Section 4. There, (10) implies that EKE $\to$ 0 in the limit $\epsilon \to 0$, despite the fact that there is plenty of APE remaining in the zonal flow!

6. Discussion

It is important to note that the bounds described above can be extended to general horizontal jet profiles, to finite initial eddy amplitudes, and to forced-dissipative flows under PV relaxation. For other kinds of forcing, things are not yet clear. Of course in fully-developed (equilibrated) baroclinic instability, eddy amplitudes must strike a balance between baroclinic growth and dissipation via a potential-enstrophy cascade. There also remains the question of how to fit all this into a transient-eddy parameterization scheme. Some thoughts along these lines are presented in Shepherd (1989, §8).

REFERENCES

Andrews, D.G. & McIntyre, M.E. 1978 On wave-action and its relatives. *J.Fluid Mech.* **89**, 647–664. (*Corrigenda* **95**, 796.)

Arnol'd, V.I., 1966 On an a priori estimate in the theory of hydrodynamical stability. *Izv. Vyssh. Uchebn. Zaved. Matematika* **54**, no.5, 3–5. [English transl.: *Amer. Math. Soc. Transl., Series 2* **79**, 267–269 (1969).]

Cho, H.-R., Shepherd, T.G. & Vladimirov, V.A. 1993 Application of the direct Liapunov method to the problem of symmetric stability in the atmosphere. *J.Atmos.Sci.* **50**, 822–836.

Haidvogel, D.B. & Held, I.M. 1980 Homogeneous quasi-geostrophic turbulence driven by a uniform temperature gradient. *J.Atmos.Sci.* **37**, 2644–2660.

Held, I.M. 1978 The vertical scale of an unstable baroclinic wave and its importance for eddy heat flux parameterizations. *J.Atmos.Sci.* **35**, 572–576.

Holliday, D. & McIntyre, M.E. 1981 On potential energy density in an incompressible, stratified fluid. *J.Fluid Mech.* **107**, 221–225.

Holm, D.D., Marsden, J.E., Ratiu, T. & Weinstein, A. 1985 Nonlinear stability of fluid and plasma equilibria. *Phys.Reports* **123**, 1–116.

Killworth, P.D. & McIntyre, M.E. 1985 Do Rossby-wave critical layers absorb, reflect, or over-reflect? *J.Fluid Mech.* **161**, 449–492.

Lindzen, R.S. & Farrell, B. 1980 The role of polar regions in global climate, and a new parameterization of global heat transport. *Mon.Wea.Rev.* **108**, 2064–2079.

McIntyre, M.E. & Shepherd, T.G. 1987 An exact local conservation theorem for finite-amplitude disturbances to non-parallel shear flows, with remarks on Hamiltonian structure and on Arnol'd's stability theorems. *J.Fluid Mech.* **181**, 527–565.

Panetta, R.L. & Held, I.M. 1989 Baroclinic eddy fluxes in a one-dimensional model of quasi-geostrophic turbulence. *J.Atmos.Sci.* **45**, 3354–3365.

Pedlosky, J. 1970 Finite-amplitude baroclinic waves. *J.Atmos.Sci.* **27**, 15–30.

Shepherd, T.G. 1988 Nonlinear saturation of baroclinic instability. Part I: The two-layer model. *J.Atmos.Sci.* **45**, 2014–2025.

Shepherd, T.G. 1989 Nonlinear saturation of baroclinic instability. Part II: Continuously-stratified fluid. *J.Atmos.Sci.* **46**, 888–907.

Shepherd, T.G. 1990 Symmetries, conservation laws, and Hamiltonian structure in geophysical fluid dynamics. *Adv.Geophys.* **32**, 287–338.

Shepherd, T.G. 1991 Nonlinear stability and the saturation of instabilities to axisymmetric vortices. *Eur.J.Mech.B/Fluids* **10**, N° 2–Suppl., 93–98.

Shepherd, T.G. 1993*a* A unified theory of available potential energy. *Atmos.-Ocean* **31**, 1–26.

Shepherd, T.G. 1993*b* Nonlinear saturation of baroclinic instability. Part III: Bounds on the energy. *J.Atmos.Sci.* **50**, 2697–2709.

Stone, P.H. 1978 Baroclinic adjustment. *J.Atmos.Sci.* **35**, 561–571.

Warn, T. & Gauthier, P. 1989 Potential vorticity mixing by marginally unstable baroclinic disturbances. *Tellus* **41A**, 115–131.

INTRASEASONAL OSCILLATIONS AND THEIR PREDICTABILITY IN A HEMISPHERIC BAROTROPIC MODEL WITH SEASONAL FORCING

Christopher Strong, Fei-fei Jin* and Michael Ghil

Climate Dynamics Center, Department of Atmospheric Sciences
and Institute of Geophysics and Planetary Physics, University of California, Los Angeles, CA 90024-1565

* Present affiliation: Dept. of Meteorology, University of Hawaii at Manoa, Honolulu, Hawaii 96822

1. Introduction and motivation

Intraseasonal oscillations with a period of 40-50 days were discovered in zonal winds over the tropical Pacific by Madden and Julian (1971, 1972). Since that time, considerable modeling and observational literature on intraseasonal tropical variability has emerged. Anderson and Rosen (1983) and Benedict and Haney (1988), among others, have established links between such fluctuations and those in global atmospheric angular momentum (AAM).

In addition to tropical variability on the 40-50 day timescale, extratropical oscillations of such periods have attracted increasing attention. The extratropical component of global variance in AAM is about an order of magnitude less than that observed in the tropics (Gutzler and Madden, 1993); it seems to be related, however, to fluctuations of planetary-scale waves on this time scale (Ghil and Mo, 1991a, b), that are of interest to extended-range prediction over North America.

Weickmann (1983) and Lau and Phillips (1986) have shown extratropical responses to tropical convective variability on the 40-50 timescale, especially in the Northern Hemisphere winter. Ghil (1987) suggested that the observed 40-50 day variability over the Northern Hemisphere midlatitudes may have its source in a Hopf bifurcation of westerly flow over topography. This idea has been pursued in a hierarchy of increasing realism, from the barotropic models of Jin and Ghil (1990) and Strong *et al.* (1993), through the UCLA General Circulation Model (Marcus, 1990), to observations (Dickey *et al.*, 1991; Ghil and Mo, 1991a; Kimoto *et al.*, 1991). Marcus (1990) and Strong *et al.* (1993) in simulations with no topography and no Madden-Julian oscillation, found no extratropical 40--50-day variability. The relationship of the extratropical oscillations to those of the tropics on this time scale is still not clear. Dickey *et al.* (1991) and Strong *et al.* (1993) provided evidence that the two oscillations may be essentially independent, as suggested by Ghil (1987), but noted that the two oscillations may occasionally interact.

More understanding of extratropical 40-50-day oscillations is needed. To summarize what is currently known: the patterns are hemispheric, of standing wavenumber-two, with an average period of 40 days (Dickey *et al.*, 1991; Marcus, 1990; Ghil and Mo, 1991a; Keppenne and Ghil, 1993; Strong *et al.*, 1993); the largest oscillations in mountain torque occur over the Rockies, Himalayas, Greenland, and the Andes, in that order (Marcus, 1990); the signal is generally most active in and around the winter season, and quiescent at other times of the boreal year (Knutson and Weickmann, 1987; Ghil and Mo, 1991a; Gutzler and Madden, 1993; Strong *et al.*, 1993).

This study sheds further light on the last aspect, the seasonal dependence of intraseasonal variability:

Floquet theory (Hartman, 1982) is used to study the stability of the large-scale, midlatitude atmospheric system's periodic basic state. This method provides not only information about the growth rate of unstable modes -- similar to the linear stability analysis of a steady basic state -- but also the annual modulation of the eigenvector field. Finally, we assess the seasonal dependence of predictive skill for this idealized signal, using low-order maximum entropy methods (MEM: Keppenne and Ghil, 1992, and references therein).

2. Review of time-dependent results

2.1. *The model*

The atmospheric model used in this study is one of equivalent-barotropic flow forced by a zonally-symmetric stress and dissipated by surface friction:

$$\frac{\partial}{\partial t}\left(\Delta - \Gamma^2\right)\psi + J\left[\psi, \Delta\psi + 2\mu(1+\gamma h)\right] = -\alpha\Delta\left(\rho\psi^* - \psi\right) - \nu\Delta^k\psi. \qquad (1)$$

Here, ψ is the streamfunction, h is the topographic height and γ is a topographic height parameter. A relaxation forcing ψ^* is introduced into the right-hand side with a characteristic time scale α^{-1}. The forcing streamfunction ψ^* can be considered as a zonal flow driven directly by differential heating in an idealized purely zonal circulation. Γ is the external Rossby radius. A very small viscous term, $\nu\Delta^k\psi$, whose scale selectivity depends on k, is also included; Δ is the horizontal Laplacian, and J the Jacobian operator. The horizontal coordinates in the spherical model are the longitude λ and the sine of latitude $\mu = \sin\theta$. The non-dimensional number ρ, analogous to a Rossby number in the real atmosphere, measures the intensity of the forcing. In our model, this number parameterizes the zonal thermal forcing, due to the variation with latitude of net radiative heating, and the zonally-averaged effects of baroclinic eddies. The spectral transform method on the sphere is used in the discretization of Eq. (1), with triangular-21 (T21) resolution. The model is hemispheric, with symmetry about the equator assumed.

2.2. *Seasonal Forcing*

Real NH topography is used, along with a zonal forcing given by the periodically-shifting jet at 250 mb obtained from the European Center for Medium-Range Weather Forecast's 1980-1986 climatology. This forcing jet peaks around 35°N in winter and around 50°N in summer, with the annual cycle being approximated by

$$\rho\psi^* = \rho_1\left[\left(1+\cos\frac{2\pi t}{365}\right)/2\right]\psi_w^* + \rho_2\left[\left(1-\cos\frac{2\pi t}{365}\right)/2\right]\psi_s^*. \qquad (2)$$

Here, ψ_w^* denotes the winter jet, forced at intensity ρ_1, while ψ_s^* denotes the summer jet, forced at intensity ρ_2; t denotes the day of the year.

2.3 *Intraseasonal oscillations in the model*

Band-pass-filtered AAM from a 100-year model run (cf. Strong *et al.*, 1993) indicates significant amplification of intraseasonal activity for the late fall, winter, and early spring, and attenuation of the activity in the summer. Lowest values of filtered AAM indicate blocked phases, while highest values correspond to zonal phases in atmospheric streamfunction patterns (cf. Legras and Ghil, 1985; Strong *et al.*, 1993).

3. Stability analysis of periodically-forced solutions

3.1. Elementary Floquet Theory

Following Hartman (1982), we consider the linear system of ordinary differential equations

$$y' = P(t)y, \tag{3}$$

where the coefficient matrix P has period p,

$$P(t) = P(t+p), \tag{4}$$

and the prime denotes differentiation with respect to time. For our model, $P(t)$ represents the spectral form of the linear operator L arising from the linearization of (1) with respect to the periodically-forced basic state. At T21 truncation, $P(t)$ is a matrix of dimension 231×231.

The system (3) has a fundamental set of solutions (a set of n linearly independent functions of which all other solutions are linear combinations) $Y(t)$, where $Y(0) = I$. Any fundamental matrix $Y(t)$ of (3) can be represented as

$$Y(t) = Z(t)e^{Rt}, \tag{5}$$

where $Z(t) = Z(t+p)$, R is a constant matrix, and $Z(t)$, R are $N \times N$ matrices. Eq. (3) does not uniquely determine R or its eigenvalues, since $Z(t)$ can always be replaced by $Z(t)e^{-2\pi it}$ and R by $R + 2\pi iI$. The eigenvalues of e^R, however, *are* uniquely determined by (3).

Equation (3) can be integrated forward in time by well-known methods, so that

$$Y(t+p) = Y(t)C. \tag{6}$$

Eq. (6) shows that fundamental solutions of (3) at the end of the period are related to those at the beginning by the constant nonsingular matrix C,

$$C = e^{Rp}. \tag{7}$$

The eigenvalues of C are uniquely determined and are the *characteristic roots*, σ_j, (j = 1,2, ... N) of the system (3). The eigenvalues λ_j of the matrix R are determined by the relation

$$\lambda_j = \frac{1}{p}\left(\ln \sigma_j + m2\pi i\right); \tag{8}$$

they are called the *Floquet exponents* of the system (3). Note that λ_j is defined only up to an additive multiple m of $2\pi i/p$. It can be fixed by requiring $-\pi < \mathrm{Im}(\lambda_j) \le \pi$, where the principal value of the logarithm is taken.

Stability properties of the solution to system (3) are diagnosed as follows:

- $y(t)$ is unstable if $\mathrm{Re}(\lambda_j) > 0$ because $y(t)$ grows exponentially with t.
- $y(t)$ is stable if $\mathrm{Re}(\lambda_j) \le 0$.

The model's periodic basic state is obtained by averaging the seasonal cycle of the solution to (1, 2) over 50 years of integration. The resulting unstable Floquet exponents for C of the model's linearization about this basic state appear in Figure 1. It shows three unstable modes -- two oscillatory and one purely exponential -- while the large number of stable modes is not shown. We will focus on the most unstable mode, with an e-folding time of 27 days.

3.2. Floquet eigenvectors

For an eigenvector y_o of R belonging to an eigenvalue λ, $e^{Rt}y_o = y_o e^{\lambda t}$, so that the solution $y = Y(t)y_o$ of (3) is of the form $z_1 e^{\lambda t}$ where the vector $z_1(t) = Z(t)y_o$ has period p.

Here, $z_1(t)$ is a solution to the initial value problem

$$\frac{dz_j}{dt} + \lambda_j z_j(t) = P(t)z_j(t). \qquad (9)$$

The resulting eigenvector corresponding to the most unstable mode exhibits intraseasonal oscillations, modulated by the season (Fig. 2). Figure 2a illustrates AAM and Fig. 2b the most unstable eigenvector in two Hovmöller diagrams; the key features are:

- The eigenvector's AAM shows higher variability in and around the winter season;
- The oscillation patterns are most robust for the late fall-winter-early spring, exhibiting a standing pattern around the Rocky Mountains and the Himalayas;
- The period of these oscillations is about 40 days.

The structure of the eigenvector solution for this standing mode agrees favorably with streamfunction anomaly patterns and most unstable eigenvectors for time-dependent and steady-state solutions, respectively (Strong *et al.*, 1993).

Predictive skill for this illustrative intraseasonal signal was assessed by way of an MEM-based autoregressive model (cf. Keppenne and Ghil, 1992). Figures 3a and 3b show statistically-significant streamfunction-anomaly forecasts out to 45 days, at the expense of forecasting the remaining variability of the model. The intraseasonal signal is modulated by, and predictive skill varies with, the season: greatest forecast success occurs in the winter, when the signal's amplitude envelope is steady and robust; less successful forecasts obtain in the spring and fall (Fig. 3c), when the envelope is decaying or growing, respectively (not shown). Forecast success is also limited in the summer months (Fig. 3c), when such variability is quiescent or dominated by other, higher-frequency oscillations in the model.

4. CONCLUSIONS

- Time-dependent solutions with seasonal forcing are still chaotic in structure:
  1. Intraseasonal activity is stronger in the winter season;
  2. The spatial patterns are standing and their average period is 40 days.
- The Floquet method is a useful tool in studying the periodically-forced basic state of a dynamical system. In our case, the method:
  1. Confirms the enhancement of intraseasonal activity around the winter seasons;
  2. Provides a way of tracking the growth and attenuation of the intraseasonal activity by way of the annual eigenvector structure.
- Predictive skill out to 40 days obtains for this ideal intraseasonal signal in the winter months, but is less successful at other times of the year.

REFERENCES

Anderson, J. R. and R. D. Rosen, 1983: The latitude-height structure of the 40-50 day variations in atmospheric angular momentum. *J. Atmos. Sci.*, **40**, 1584-1591.

Benedict, W. L., and R. L. Haney, 1988: Contribution of tropical winds to subseasonal fluctuations in atmospheric angular momentum and length of day. *J. Geophys. Res.*, **93**, 15973-15978.

Dickey, J. O., M. Ghil, and S. L. Marcus, 1991: Extratropical aspects of the 40-50 day oscillation in length-of-day and atmospheric angular momentum. *J. Geophys. Res.*, **96**, No. D12, 22643-22658.

Eubanks, T. M., J. A. Steppe, J. O. Dickey and P. S. Callahan, 1985: A spectral analysis of the Earth's rotation budget. *J. Geophys. Res.*, **90**, 5385-5404.

Ghil, M., 1987: Dynamics, statistics, and predictability of planetary flow regimes. *Irreversible Phenomena and Dynamical Systems Analysis in the Geosciences*, C. Nicolis and G. Nicolis, Eds., D. Reidel, 241-283.

Ghil, M., and K. Mo, 1991a: Intraseasonal oscillations in the global atmosphere. Part I: Northern Hemisphere and tropics. *J. Atmos. Sci.*, **48**, 752-779.

Ghil, M., and K. Mo, 1991b: Intraseasonal oscillations in the global atmosphere. Part II: Southern Hemisphere. *J. Atmos. Sci.*, **48**, 780-790.

Gutzler, D. S., and R. A. Madden, 1993: Seasonal variations of the 40-50 day oscillation in atmospheric momentum. *J. Atmos. Sci.*, **50**, 850-860.

Hartman, P., 1982: *Ordinary Differential Equations*, Birkhaüser, Boston, pp. 60-62.

Jin, F.-f., and M. Ghil, 1990: Intraseasonal oscillations in the extratropics: Hopf bifurcations and topographic instabilities. *J. Atmos. Sci.*, **47**, 3007-3022.

Keppenne, C. L. and M. Ghil, 1992: Adaptive filtering and prediction of the Southern Oscillation Index. *J. Geophys. Res.*, **97**, 20449-20454.

Keppenne, C. L., and M. Ghil, 1993: Intraseasonal oscillations in the Northern Hemisphere: barotropic and baroclinic effects in a two-layer model. *J. Atmos. Sci.*, submitted.

Kimoto, M., M. Ghil, and K.-C. Mo: Spatial structure of the 40-day oscillation in the Northern Hemisphere extratropics, in *Proc. Eighth Conference on Atmospheric and Oceanic Waves and Stability*, Amer. Met. Soc., Boston, MA, pp. 115-116.

Knutson, T. R., and K. M. Weickmann, 1987: 30-60 day atmospheric oscillations: composite life cycles of convection and circulation anomalies. *Monthly Weather Review*, **115**, 1407-1436.

Lau, K. -M. and T. J. Phillips, 1986: Coherent fluctuations of extratropical geopotential height and tropical convection in intraseasonal time scales. *J. Atmos. Sci.*, **43**, 1164-1181.

Legras, B., and M. Ghil, 1985: Persistent anomalies, blocking and variations in atmospheric predictability. *J. Atmos. Sci.*, **42**, 433-471.

Madden, R. A. and P. R. Julian, 1971: Detection of a 40-50 day oscillation in the zonal wind of the tropical Pacific. *J. Atmos. Sci.*, **28**, 702-708.

Madden, R. A. and P. R. Julian, 1972: Description of global-scale circulation cells in the tropics with a 40-50 day period. *J. Atmos. Sci.*, **29**, 1109-1123.

Marcus S. L., 1990: *Intraseasonal Oscillations in the Earth-Atmosphere System*, Ph.D. Thesis, University of California, Los Angeles, CA, 184 pp. [Available from Steve Marcus, Jet Propulsion Laboratory, California Institute of Technology, 4800 Oak Grove Dr., Pasadena, CA 91109.]

Strong, C. M., F.-f. Jin and M. Ghil, 1993: Intraseasonal variability in a barotropic model with seasonal forcing. *J. Atmos. Sci.*, in press.

Weickmann, K. M., 1983: Intraseasonal circulation and outgoing longwave radiation modes during the Northern Hemisphere winter. *Mon. Wea. Rev.*, 111, 1838-1858.

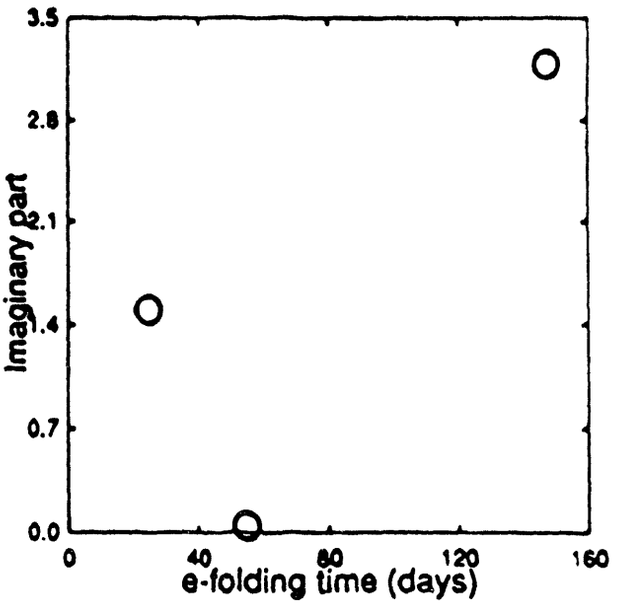

Fig. 1. Unstable Floquet exponents of the model's seasonal cycle; *x*-axis represents *e*-folding time in days and *y*-axis the imaginary part of the Floquet exponent in radians.

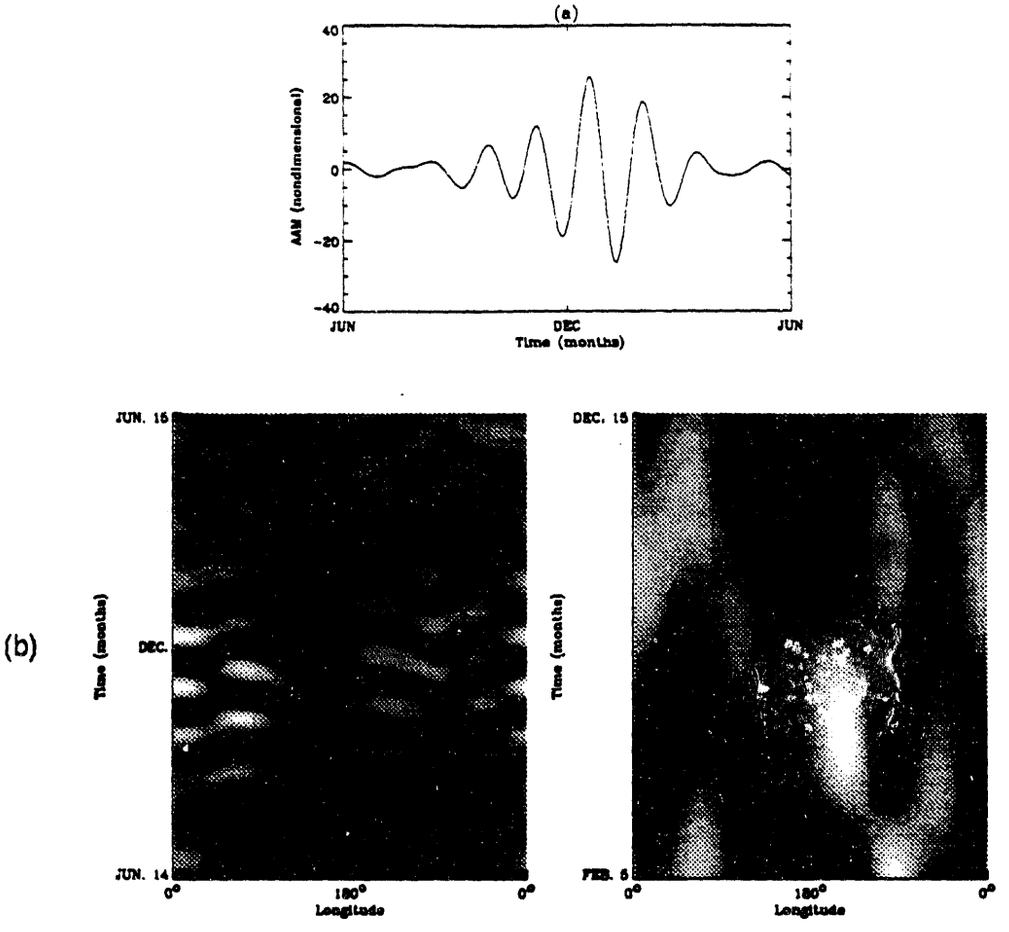

Fig. 2. (a) Annual eigenvector AAM (nondimensional) for June 15 - June 14. (b) Annual eigenvector structure for the most unstable Floquet exponent, in two Hovmöller diagrams, taken at 40° N. Left panel: eigenvector structure with 3-day time step for June 15 - June 14; time is on the *y*-axis and longitude on the *x*-axis. Right panel: same as left panel, but for Dec. 15 - Feb. 5 only.

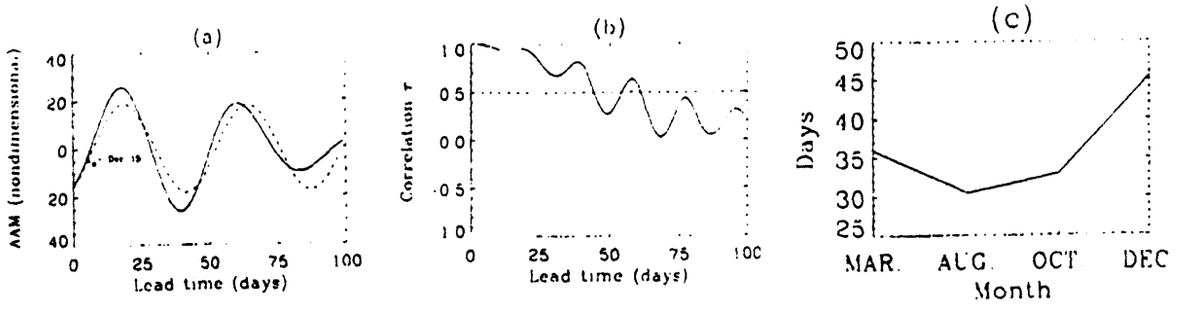

Fig. 3. (a) Results for 100-day forecast with t_0 = December 15 using spectral coefficient data from June 15 - December 14 to determine MEM prediction coefficients; MEM-forecasted AAM for 100 days (dashed line) vs. model AAM for same 100 days (solid line). *x*-axis represents forecast time in days, *y*-axis the magnitude of the nondimensional AAM. (b) Pearson-product-moment correlation coefficient *r* for grid-point streamfunction anomalies, statistical forecast compared to model, for 100 days shown in (a). *x*-axis represents forecast lead time in days, *y*-axis the value of the correlation coefficient *r*. Skill level of $r = 0.5$ indicated by dashed line. (c) Dependence of $r = 0.5$ vs. season for streamfunction-anomaly forecasts. *x*-axis represents month in which forecast was started; *y*-axis the day at which *r* fell below 0.5.

An EPV view of the zonal mean distribution of temperature and wind in the extra-tropical troposphere

De-Zheng Sun
Program in Atmospheric and Oceanic Sciences
Princeton University
Princeton, NJ

Richard S. Lindzen
Center for Meteorology and Physical Oceanography
Massachusetts Institute of Technology
Cambridge, MA

June 9, 1993

1 Introduction.

The uniquely important role of Ertel potential vorticity (EPV) gradient along isentropes in the extra-tropical large scale flow has long been recognized and constantly emphasized (Charney and Stern 1962, Hoskins et al 1985). It has also been proposed that the EPV may be a powerful diagnostic tool for studying the general circulation on a global scale (Hoskins, 1991). However, it appears that no adequate effort has been made to examine temperature and wind distribution of the zonal mean flow as a function of EPV gradient along isentropes.

The need to examine the dependence of the zonal mean flow on the EPV gradient along isentropes was highlighted by Lindzen (1993). He noted a neutral state for the extra-tropical troposphere. In such a state, the EPV gradient along isentropes in the interior troposphere is zero, and the tropopause height is sufficiently large so that the waves with the smallest total wave number is neutral in the sense of the Eady type of instability. Clearly, the relevance of such a neutral state to the real atmosphere is dependent on whether there is a significant difference between the observed distribution of temperature and wind and the one corresponding to a zero EPV gradient along isentropes.

The present paper describes how to calculate the temperature and wind distribution as a function of EPV gradient along isentropes. We are particularly interested in whether the assumption of zero EPV gradient is consistent with observations and its implications for the role of the tropics. In section 2, we show the distribution of EPV of the observed zonal mean flow, whose characteristic structure indeed suggests vigorous mixing in the interior of the extra-tropical troposphere. In section 3, we describe the calculation of the temperature and wind distribution of an extra-tropical troposphere with zero isentropic EPV gradient, and compare the result with the observed. We also investigate the implications of such an efficient EPV mixing for the impact of the tropics. In Section 4, we quantify the sensitivity of the temperature and wind distribution to the changes in the gradient of EPV. Section 5 discusses some implications of the present findings.

2 The characteristic EPV distribution of the observed flow

The expression for the isentropic EPV is

$$P_v = -g(f + \zeta_\theta)\frac{\partial \theta}{\partial p} \tag{1}$$

in which g is the gravity constant, f is the planetary vorticity, θ represents the potential temperature, p is the pressure, and ζ_θ is the relative vorticity evaluated along isentropes

Figure 1 shows the EPV distribution along three representative isentropes of the observed zonal mean flow over the winter season (290 K, 300 K and 275 K respectively). It is apparent from Figure 1 that distribution of EPV along isentropes is characterized by different regimes. The gradient of EPV along the section of the isentropes that falls in the interior of the extra-tropical troposphere is distinguishly smaller than along the section that falls either into the Hadley regime, the immediate region of the ground or the transitional region to the tropopause. This characteristic distribution suggests that there is a vigorous mixing in the interior of the extra-tropical troposphere.

Nevertheless, isentropic gradient of EPV appears to be distinguishable from zero. However, the significance of this difference is dependent on whether the temperature and wind distribution is sensitive to it. Also, one should note that the change of EPV from its surface values or tropical values to its stratospheric values is large. Consequently, low resolution of the data will tend to exaggerate the gradient in between. Observational data used here is only available at the standard pressure levels. An effective way to check how significant the EPV gradient is, is to obtain the temperature and wind distribution which corresponds to a zero gradient of EPV, and then compare this temperature and wind distribution with the observed temperature and wind.

3 Temperature and wind distribution corresponding to a zero isentropic EPV gradient

When the relative vorticity is ignored in the EPV expression, the equation that governs the potential temperature distribution for an extra-tropical troposphere with a zero EPV gradient along isentropes is:

$$f\frac{\partial\theta}{\partial y} - \left(\frac{-gf^2}{P_{as}}\frac{\partial\theta_s}{\partial y} - \frac{df}{dy}(p-p_s)\right)\frac{\partial\theta}{\partial p} = 0 \qquad (2)$$

where $y = a\phi$, a is the radius of the Earth, ϕ represents the latitude, and θ and p represent the potential temperature and pressure respectively. $P_{as} = -gf(\frac{\partial\theta}{\partial p})_s$, which is the potential vorticity distribution at the surface level. Ignoring the relative vorticity turns out to be a good approximation.

Solving equation 2 does not require the knowledge where the troposphere ends. For a given θ_s, P_{as} and a potential temperature distribution at the tropical boundary (the edge of the Hadley cell), the temperature distribution in the extra-tropics is then uniquely determined.

A numerical solution to equation 2 is presented in Figure 2, together with the observed distribution of temperature and wind. The solution appears to define much of the observed distribution with some significant discrepancy near the tropopause level, particularly in the region near the tropical boundary.

Once the temperature distribution is determined, the zonal wind may be estimated from the thermal wind relationship, by assuming the surface level wind is negligible.

When ζ_θ is included in the PV expression, the calculation involves inverting an given EPV distribution under the requirement that mass and momentum are balanced.

In the potential temperature– latitude coordinate, the equation to be solved is in the

following from:

$$\frac{\partial^2 M}{\partial \phi^2} - \frac{2}{sin2\phi}\frac{\partial M}{\partial \phi} + 2\Omega a^2 sin\phi \frac{P_v}{g}\frac{p_0}{R_d}c_p^{-\frac{c_v}{R_d}}(\frac{\partial M}{\partial \theta})^{\frac{c_v}{R_d}}\frac{\partial^2 M}{\partial \theta^2} + (2\Omega a sin\phi)^2 = 0 \qquad (3)$$

$M = c_p T + \Phi$,which is the Montgomery potential. T is the temperature and Φ is the geopotential. c_p and R_d are the specific heat and specific gas constants for dry air respectively. $c_v = c_p - R_d$. Zonal wind and temperature are related to the Montgomery potential through the hydro-static and the geostrophic balance equation.

Equation 3 is a second order elliptic equation for a positive PV distribution, and it requires a closed boundary. Therefore, solving equation 3 requires where the tropopause is and the temperature or wind distribution on the tropopause.

Taken the temperature distribution at the upper boundary as the one given by the approximate solution, the temperature and wind distribution obtained by solving Equation 3 is similar to the approximate solution. However, we have also found that the meridional distribution of zonal wind is very sensitive to changes in the meridional temperature distribution at the tropopause.

Assuming that EPV remains well mixed, we have further found that the temperature and wind distribution in the extra-tropical troposphere are sensitive to changes in the vertical distribution of EPV at the tropical boundary, as well as to the position of the tropical boundary.

4 Temperature and wind distribution corresponding to a finite EPV gradient

Assuming the gradient of EPV along isentropes can be written in the following form

$$(\frac{\partial P_v}{\partial y})_\theta = -g\alpha(y)\frac{\partial \theta}{\partial p} \qquad (4)$$

, we have the following equation that governs the potential temperature distribution,

$$f\frac{\partial\theta}{\partial y} - (\frac{-gf^2}{P_{as}}\frac{\partial\theta_s}{\partial y} + (\alpha - \beta)(p - p_s))\frac{\partial\theta}{\partial p} = 0 \tag{5}$$

$\alpha(y)$ corresponds to the QGPV gradient. When $\frac{\partial\theta}{\partial p}$ can be replaced by a reference value, α is exactly the gradient of QGPV (Charney and Stern 1962). $\beta(y) = \frac{df}{dy}$, the planetary vorticity gradient. We calculated the temperature distributions corresponding to different α. For the same boundary conditions at the surface level and at the tropical side, we found that the larger the EPV gradient along isentropes, the smaller the isentropic slope and the warmer the upper troposphere.

5 Final Remarks

Some important implications of the above results are listed below:

A. The results suggest that an effective way to parameterize the collective effect of baroclinic eddies is to assume that they tend to keep the EPV along isentropes well mixed. This parameterization may offer a better means than models based on the QG theory to examine the maintenance of the vertical stability of the extra-tropical troposphere and the interaction between the Hadley circulation and the baroclinic eddies. Due to the assumptions built in the QG theory, QG models cannot appropriately address the the maintenance of the vertical stability and the role of the tropics. The lapse rate feedback and pole-to equator temperature difference are among the leading factors that determine the climate sensitivity to radiative perturbations.

B. The tendencey for baroclinic eddies to wipe out the EPV gradient along isentropes originating from the tropics will be opposed by the Hadley circulation. The balance between these two opposite effects may be crucial in determining the match of the Hadley circulation regime and the baroclinic eddy regime, and hence the pole-to equator temperature difference.

C. The sensitivity of the balanced wind distribution to changes in the meridional distribution of temperature at the tropopause suggests a negligible role of the requirement of the global momentum balance in determining the thermal structure.

D. The implications for the role of the tropics depend significantly on the extent of the Hadley circulation and the vertical distribution of EPV established at the tropical boundary.

E. Results in section 4 suggest that efficient homogenization of EPV along isentropes does not appear to lead to an efficient heat transport. It is of interest to quantify the relationship between the gradient of EPV and the frictional and diabatic parameters.

References

Charney, J.G. and M.E. Stern, 1962: On the stability of internal baroclinic jets in a rotating atmosphere *J. Atmos. Sci.*, **19**, 159-172.

Hoskins, B.J., 1991: Towards a PV-θ view of the general circulation, *Tellus*, **43 A-B**, 27-35.

Hoskins, B.J., M.E. McIntyre and A.W. Robertson, 1985: On the use and significance of isentropic potential vorticity maps. *Quart. J. R. Met. Soc.*, **111**, 877-946.

Lindzen, R.S., 1993: Baroclinic neutrality and the tropopause. *J. Atmos. Sci.*, **50**, 1148-1151.

Oort, A.H., 1983: *Global Atmospheric Circulation Statistics, 1958-1973.* NOAA Professional Paper 14. NOAA, U.S. Dept. of Commerce, Rockville, MD, 180 pp.

Figure Legends

Figure 1: EPV distribution (in PVU) along three representative isentropic surfaces (Top: 290 K. Bottom left: 275 K. Bottom right 300 K). The 290 K isentrope originates from

the subtropical surface and intersects the tropopause shortly before reaching the pole. The 300 K isentrope originates in the tropics and intersects the tropopause at about 55 N. The 275 K isentrope originates from the extra-tropical surface and passes over the pole without intersecting the tropopause.

Figure 2: Top: temperature distribution obtained through equation 2.In the calculation, we take $p_s = 900mb$. θ_s and P_{ss} are taken from the observed values for the winter. The temperature distribution at the tropical boundary (30N) is assumed to be linear with pressure. The solution is assumed to extend to a specified height which represents the tropopause level. This height is assumed to vary linearly from 200 mb at 30N to 400 mb at 80N. Bottom: observed zonal mean temperature distribution of the winter season (Oort 1983). Contour interval: 10 K.

THE EPV DISTRIBUTION ALONG THREE ISENTROPES

290 K

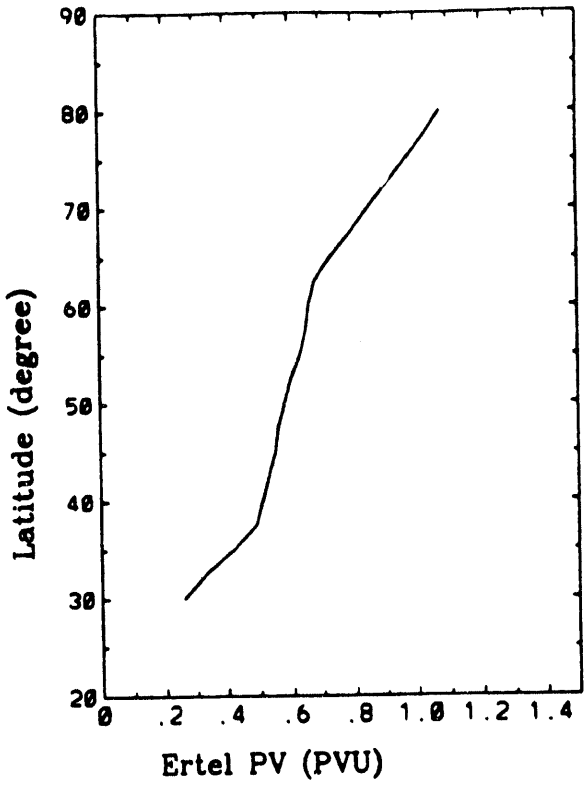

275K

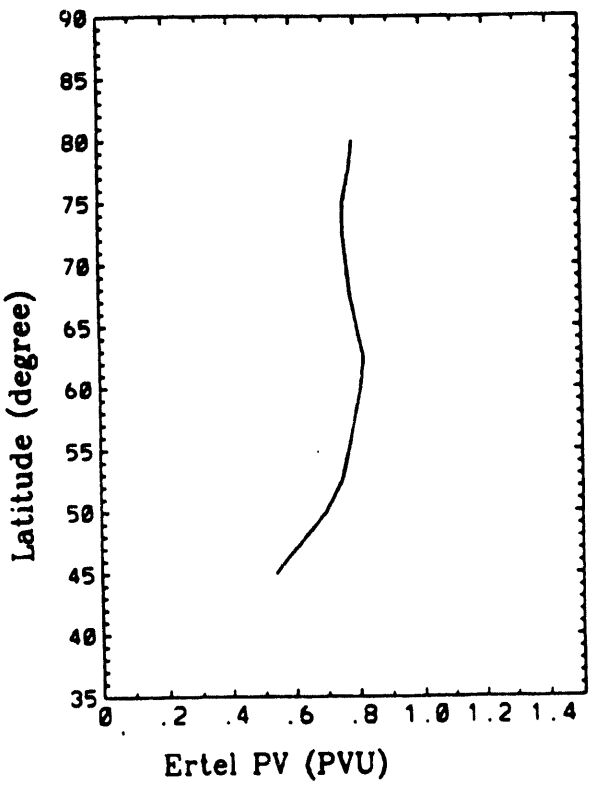

300 K

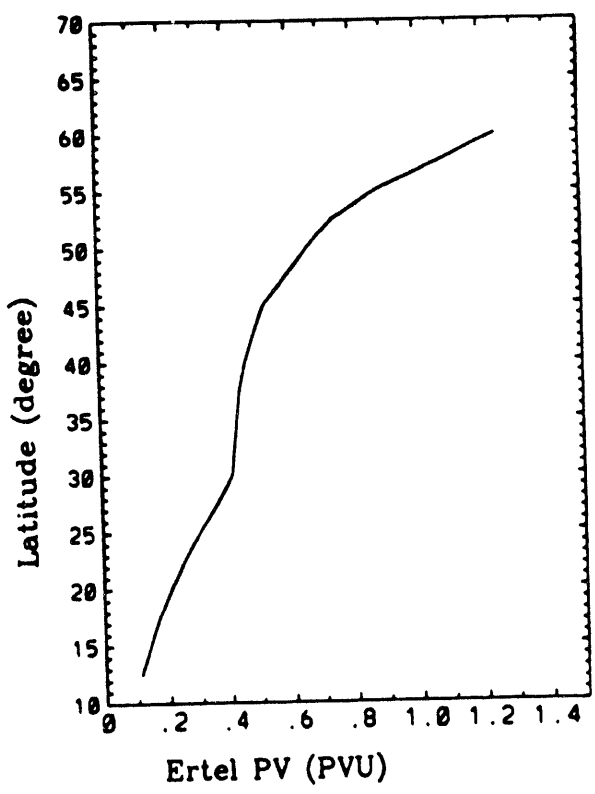

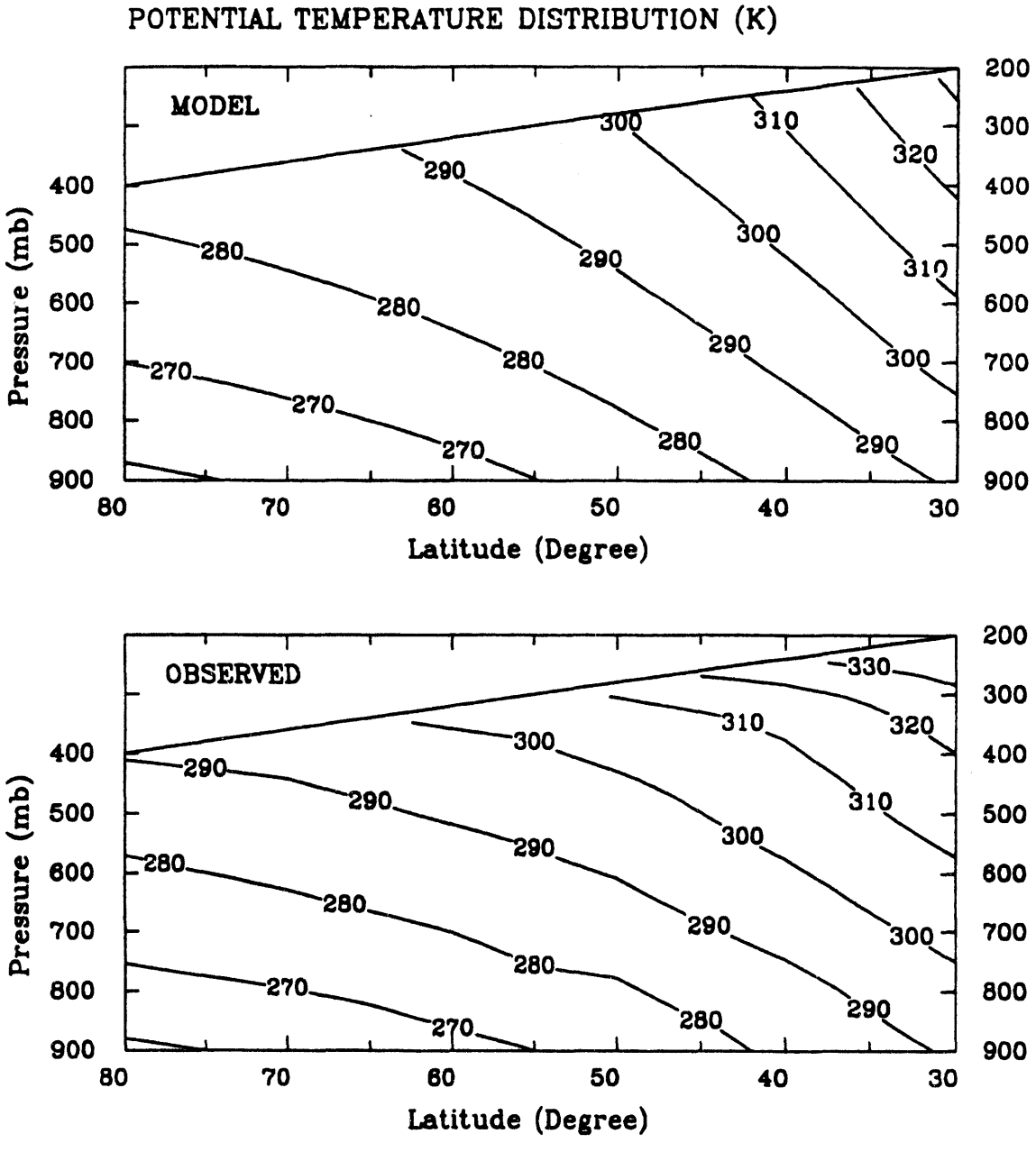
POTENTIAL TEMPERATURE DISTRIBUTION (K)
MODEL
OBSERVED
Pressure (mb)
Latitude (Degree)
200
300
400
500
600
700
800
900
80
70
60
50
40
30
270
280
290
300
310
320
330

Maintenance of Extratropical Low-Frequency Variabilities in the Atmosphere

Mingfang Ting
Department of Atmospheric Sciences
University of Illinois at Urbana-Champaign
Urbana, IL, U.S.A.

1. Introduction

The extratropical low-frequency variability is one of the most important components in extratropical dynamics. While there are some understanding of the high-frequency, synoptic scale storm track eddy development due to baroclinic instability theory, its low-frequency counterpart is poorly understood and the theory for that is slowly evolving. The main difficulty seems to be lying on the fact that the problem is three dimensional in nature.

There have been a number of theories proposed in the past decade which tend to explain the development of low-frequency atmospheric anomalies. Based on observations of the similarity between atmospheric teleconnection patterns in the Pacific/North American sector (Wallace and Gutzler, 1981) and the Rossby wave dispersion from a tropical heat source (Hoskins and Karoly, 1981), Horel and Wallace (1981) argued the role of tropical sea surface temperature (SST) anomalies in inducing the extratropical low-frequency variability. Many subsequent general circulation model (GCM) experiments (Shukla and Wallace, 1981; Blackmon et al, 1983; Lau, 1985; among others) confirm the influence of tropical sea surface temperature anomalies on the extratropical interannual variabilities. It is well accepted that the tropical SST-forced variability constitutes an important part of the total atmospheric low-frequency spectrum.

In a GCM experiment without tropical SST anomalies, Lau (1981) reported that there are just as rich a low-frequency spectrum in the Northern Hemisphere extratropics as

in the observation. Such is found to be the case in Fig.1, which shows the standard deviation of seasonal mean geopotential height at 515 mb in northern winter and spring for the two GCM experiments: one with realistic SST evolution over the global ocean, the other has prescribed climatological SST. The seasonal mean variability in Fig.1 for both winter and spring is quite comparable for the cases with and without non-seasonal SST fluctuations. The difference in Winter over the north Pacific sector is quite significant and interesting, however. This finding invoked the development of three dimensional barotropic instability theory (Simmons et al, 1983). It states that low-frequency extratropical anomalies can grow exponentially by extracting energy from the zonally varying time mean flow. There are less observational evidence which supports the normal mode structure of the barotropic instability theory. The growth rates due to barotropic instability also seem to be small and show large sensitivity when different basic state or horizontal resolution is used.

On the other hand, a large body of evidence is pointing towards the role of high frequency transient vorticity forcing on the maintenance of low-frequency extratropical variabilities. Using a barotropic model, Shutts (1983) demonstrated that high-frequency eddy forcing can reinforce the blocking flow patterns. In an observational and GCM data analysis, Mullen (1987) found that the high-frequency eddy vorticity forcing is to prevent the blocking pattern from blowing away by the time mean flow. Observational studies by Lau (1988) and Lau and Nath (1991) found a general positive reinforcement between the monthly mean anomalies and the storm track eddy vorticity forcing. This latter result was found to be equally valid in a 100-year GCM experiment without any non-seasonal forcing (Ting and Lau, 1993). In the case of tropical SST-forced variability, there are also indications that the extratropical transient eddy vorticity fluxes tend to reinforce the tropically forced signal (Kok and Opsteegh, 1985; Held et al, 1989).

In this presentation, we will examine the effect of high-frequency extratropical transients on both the non-SST and tropical SST-forced low-frequency variabilities in extratropical atmosphere. The main questions to be addressed are:

Why does the seasonal mean variability look so similar in the case with and without non-seasonal SST fluctuations? Are there common dynamical mechanisms for the production of naturally occurring- and externally forced-low-frequency variabilities? To what extent is the three dimensional barotropic instability theory relevant for the generation of low-frequency energy spectrum?

To the extent that low-frequency variabilities can be understood solely through the high-frequency transient vorticity forcing, it becomes extremely important to understand the way high frequency transients are organized by the low-frequency anomaly, as well as what factors are determining the organization of high-frequency transients.

Two examples will be given to shed some lights on possible solutions to the above questions. The first is the maintenance of the monthly mean anomalies in a 100-year GCM experiment without non-seasonal SST forcing. In the second example, the seasonal mean anomalies for the four recent observed El Niño/Southern Oscillation (ENSO) events will be examined. These results will be used to explain the seasonal mean variability shown in Fig.1.

2. Results

The monthly mean anomalies appearing in the 100-year GCM integration are examined using rotated empirical orthogonal function (EOF) analysis. The four most dominant modes of variability are identified. These are similar to the observed North Atlantic Oscillation, the North Pacific Oscillation, the Pacific/North America pattern and the Eurasian pattern, as shown in Fig.2 of Ting and Lau (1993). Using the time coefficients of the first and second EOFs, composite geopotential height anomalies can be obtained, as well as the diabatic heating and transient heat and vorticity fluxes associated with these

EOFs. A baroclinic model linearized about a three dimensional basic state is used to reconstruct the geopotential height anomalies of EOF1 and EOF2, by including the GCM's anomalous forcings. We find that such a linear model is able to successfully simulate the GCM's EOF1 and EOF2 anomaly patterns. When decomposing the total anomaly to that forced by transient vorticity forcing and that by the diabatic heating, we find that the anomaly pattern is largely explained by the transient vorticity forcing. Figures 2a and b illustrate the composite EOF1 and EOF2 geopotential height anomalies at 205 mb level with only the zonally asymmetric component, respectively. The linear model response to the sub-monthly transient vorticity forcing is shown in Figs.2c and d. By comparing Fig.2a with 2c and Fig.2b with 2d, we find that the dominant anomaly patterns of the first two EOFs are largely explained by the higher frequency transient vorticity fluxes. This result provides a quantitative measure of the importance of the high-frequency transients in maintaining the low-frequency anomalies of the extratropical atmosphere.

The third EOF is very similar to the Pacific/North American pattern as defined in Wallace and Gutzler (1981). The maintenance of this internally generated PNA pattern is somewhat more complicated. Not only is the submonthly transient vorticity fluxes playing an important role, the inter-monthly transients also help to maintain the monthly mean anomaly. The nature of this interesting EOF pattern is still under investigation.

One interesting question is whether the mechanism of the tropical SST forced low-frequency variability differs from those generated internally by the internal dynamics of the atmosphere. To the extent the high-frequency transient vorticity flux helps to maintain the naturally occurring low-frequency anomaly pattern in the atmosphere, what is the role of these transients when the anomaly is induced by a tropical SST anomaly? By analyzing a composite El Niño event simulated by a GCM, Held et al (1989) found that the maintenance of the extratropical anomaly is dominated by the transient vorticity forcing, suggesting a similar mechanism is operating for maintaining the forced and naturally occurring low-frequency anomaly.

This idea is further explored here by examining the recent three El Niño and one La Niña events, i.e., 1982/83, 86/87, 91/92 warming, and 88/89 cooling. The extratropical zonally asymmetric stream function anomalies for all four winter seasons show a recurring anomaly pattern with a low (high) over the Gulf of Alaska region, a high (low) over North American Continent, and another low (high) off the east coast of United States for warm (cold) SST anomaly events. The stream function anomalies at σ=.245 level is shown in the upper panels of Fig.3 for 1982/83 and 86/87 El Niño winters. The SST anomaly during these recent events varies from east equatorial Pacific (1982/83) to central Pacific (1986/87), the extratropical flow anomaly seems to be rather insensitive to the logitudinal location of the SST anomaly. Although direct heating data is not available for these anomaly events, anomalous transient vorticity forcing can be obtained from daily observations of the horizontal wind data. Linear baroclinic model is again used to obtain the linear response to transient vorticity forcing. The results are shown in the lower panels of Fig.3. By comparing the observed anomaly patterns with those forced by the transient vorticity fluxes in the linear model, we can conclude that transient vorticity fluxes are the dominant forcing for the tropical SST-forced, seasonal mean anomalies in the extratropical atmosphere. The difference is mainly in the tropics where tropical heating is the dominant forcing.

The role of high-frequency transient vorticity forcing in maintaining the extratropical ENSO-related flow anomalies can be understood by the following chain of interactions. Tropical SST anomaly first induces a tropical diabatic heating anomaly. A tropical anticyclone will be induced by the anomalous heating over the central Pacific. This anticyclone then extend the mid-Pacific jet stream further to the east. The eastward extended jet stream steers the storm track eddy further downstream and cause anomalous transient vorticity flux convergence over the central northern Pacific. These anomalous transient vorticity fluxes then enhance the direct wavetrain from the tropics and cause a much larger extratropical flow anomaly. One necessary ingredient for the tropical heating

to effectively interact with the midlatitude storm track is an extended jet over the mid-Pacific region, so that the heating induced anticyclone is able to interact with the jet stream. In Fig.1, the hatched region shows the 30 m/s climatological mean isotach at 205 mb level for both winter and spring. It is suggestive from Fig.1 that large seasonal mean variance occurs concurrently with the location of the jet exit. During spring, the jet is confined further to the west. Thus anomalous tropical heating over the central and eastern Pacific can not effectively interact with the jet and enhance the extratropical variability. Thus the seasonal mean fluctuations of the geopotential height is quite similar for the case with and without SST anomalies. During wintertime, however, the jet is extended and the anomalous tropical heating induced by tropical SST anomaly contributes largely to the maximum variability over the Gulf of Alaska, through transient vorticity forcing.

In summary, both externally forced and internally generated low-frequency variabilities are largely maintained by the high-frequency transient vorticity forcing. It is not clear how the high-frequency eddies are organized during a low-frequency anomaly episode. But it is hypothesized that tropical heating-induced flow anomaly can interact with the midlatitude jet stream and results large anomalies in transient forcing. The linear model simulation of the low-frequency anomaly also tends to depend very much on the zonal variations of the basic state. Whether this latter conclusion is related to the barotropic instability of the zonally varying flow is still not clear.

References

Blackmon, M. L., J. E. Geisler, and E. J. Pitcher, 1983: A general circulation model study of January climate anomaly patterns associated with interannual variation of equatorial Pacific sea surface temperatures. *J. Atmos. Sci.*, **40**, 1410-1425.

Held, I. M., S. W. Lyons and S. Nigam, 1989: Transients and the extratropical response to El Niño. *J. Atmos. Sci.*, **46**, 163-174.

Horel, J. D., and J. M. Wallace, 1981: Planetary scale atmospheric phenomena associated with the Southern Oscillation. *Mon. Wea. Rev.*, **109**, 813-329.

Hoskins, B., J., and D. J. Karoly, 1981: The steady linear response of a spherical atmosphere to thermal and orographic forcing. *J. Atmos. Sci.*, **38**, 1179-1196.

Kok, C. J., and J. D. Opsteegh, 1985: On the possible causes of anomalies in seasonal mean circulation pattern during the 1982-83 El Niño event. *J. Atmos. Sci.*, **42**, 677-694.

Shukla, J., and J. M. Wallace, 1983: Numerical simulation of the atmospheric response to equatorial Pacific sea surface temperature anomalies. *J. Atmos. Sci.*, **40**, 1613-1630.

Lau, N.-C., 1981: A diagnostic study of recurrent meteorological anomalies appearing in a 15-year simulation with a GFDL general circulation model. *Mon. Wea. Rev.*, **109**, 2287-2311.

Lau, N.-C., 1988: Variability of the observed midlatitude storm tracks in relation to low-frequency changes in the circulation patterns. *J. Atmos. Sci.*, **45**, 2718-2743.

Lau, N.-C., and M. J. Nath, 1991: Variability of the baroclinic and barotropic transient eddy forcing associated with monthly changes in the midlatitude storm tracks. *J. Atmos. Sci.*, **48**, 2589-2613.

Lau, N.-C., 1985: Modeling the seasonal dependence of the atmospheric response to observed El Niños in 1962-76. *Mon. Wea. Rev.*, **113**, 1970-1996.

Mullen, S. L., 1987: Transient eddy forcing of blocking flows. *J. Atmos. Sci.*, **44**, 3-22.

Shutts, G. J., 1983: The propagation of eddies in diffluent jetsttreams: eddy vorticity forcing of 'blocking' flow fields. *Quart. J. R. Met. Soc.*, **109**, 737-761.

Simmons, A. J., J. M. Wallace and G. W. Branstator, 1983: Barotropic wave propagation and instability, and atmospheric teleconnection patterns. *J. Atmos. Sci.*, **40**, 1363-1392.

Ting, M., and N.-C. Lau, 1993: A diagnostic and modeling study of the monthly mean wintertime anomalies appearing in a 100-year GCM experiment. *J. Atmos. Sci.*, **50**, in press.

Wallace, J. M., and D. S. Gutzler, 1981: Teleconnections in the geopotential height field during the Northern Hemisphere winter. *Mon. Wea. Rev.*, **109**, 784-812.

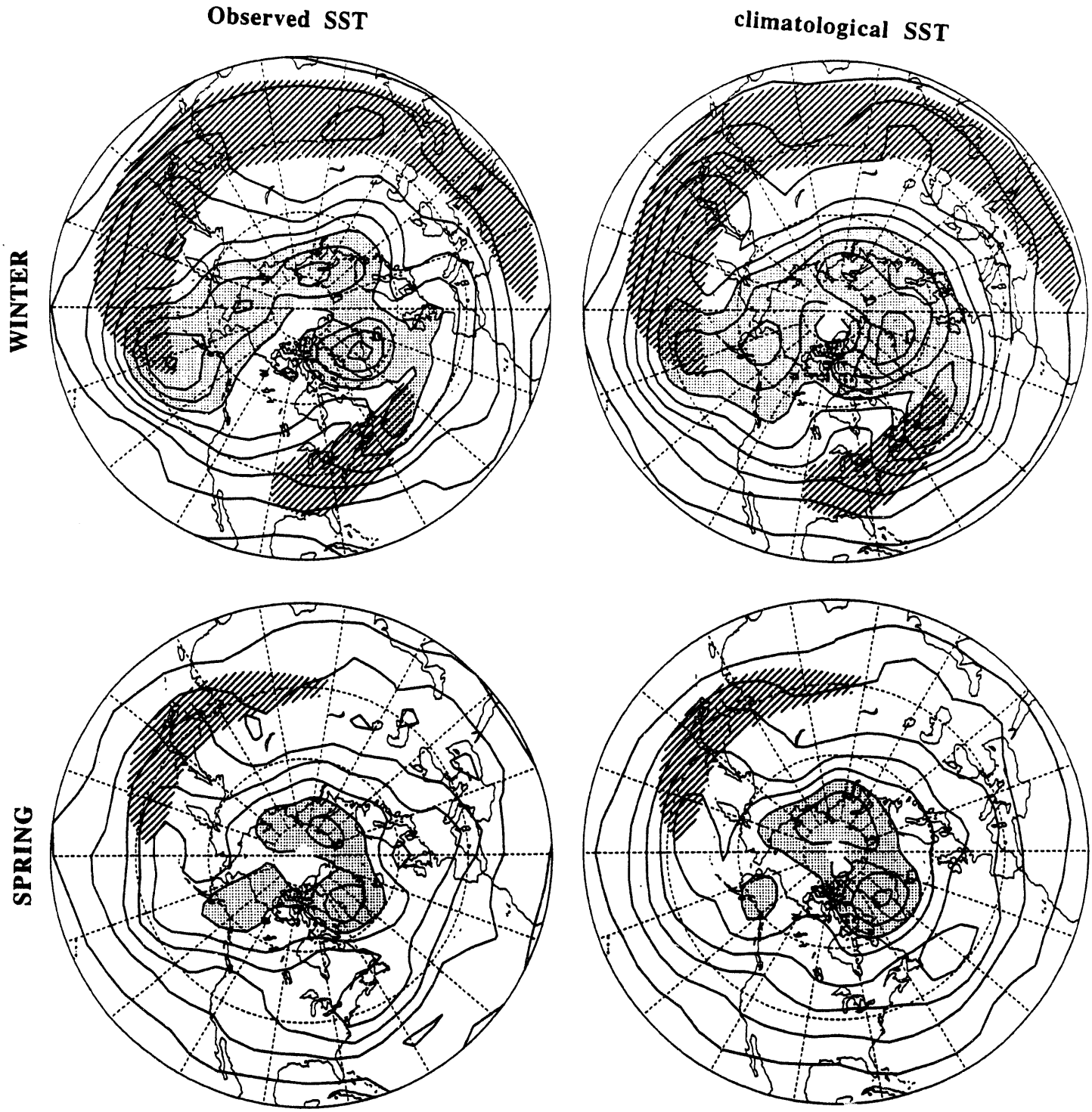

Fig.1 Standard deviation of seasonal mean geopotential height at 515 mb for winter (upper panels) and spring (lower panels). Data obtained from a GCM experiment with prescribed SST over the world oceans with observed fluctuations during the period from 1950 through 1988 (left panels) and with climatological SST (right panels). Contour interval 5 m. Values greater than 35 m stippled. Area of climatological mean isotaches greater than 30 m/s hatched.

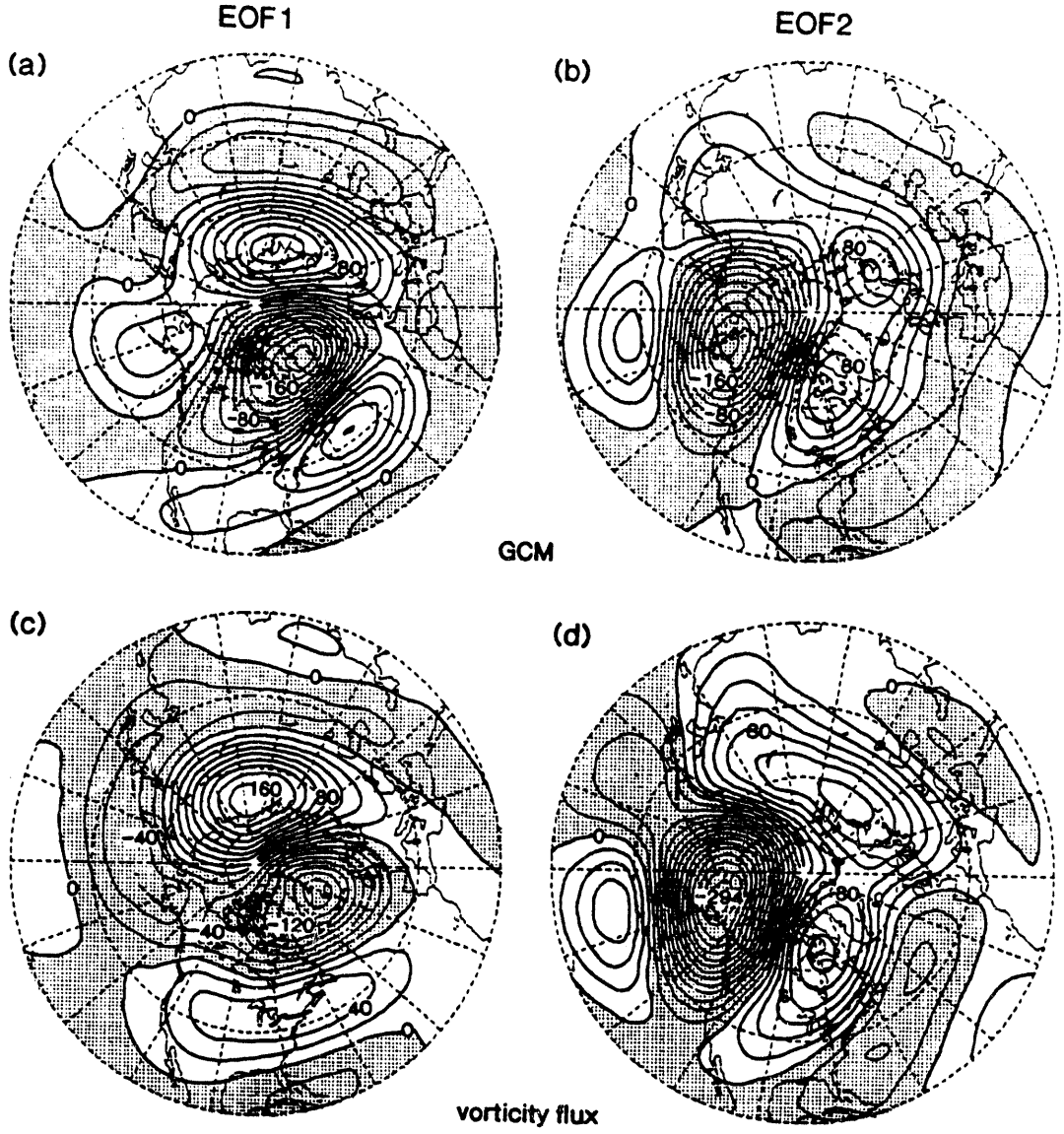

Fig.2 Composite geopotential height anomaly at 205 mb according to the time coefficients of the first (a) and second (b) rotated EOF in a 100-year GCM experiment with climatological seasonally varying SST. The linear model response of geopotential height at 205 mb to the composite transient vorticity forcing for the first (c) and second (d) EOF. Contour interval 20 m and negative contours stippled.

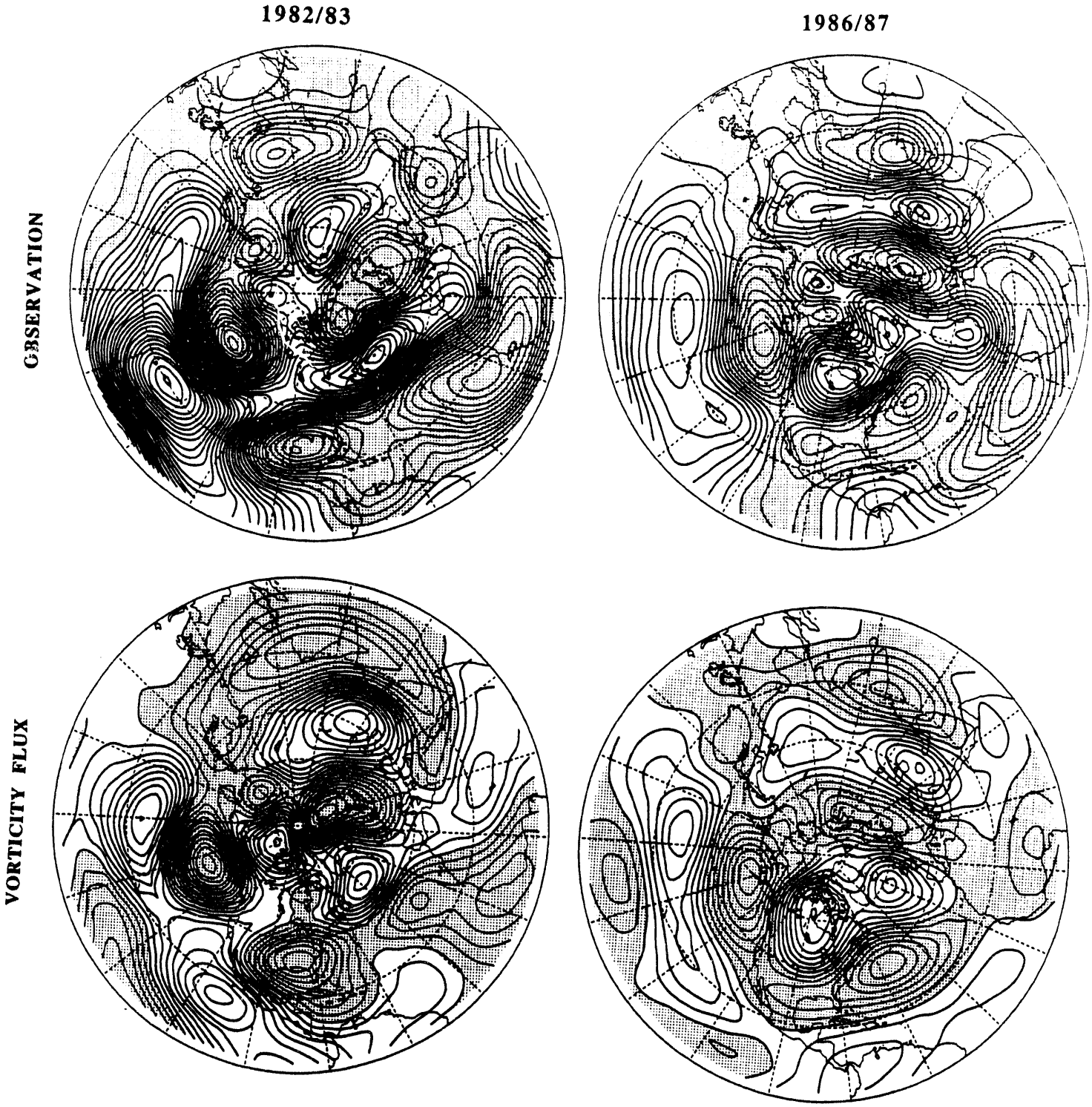

Fig.3 Zonally asymmetric streamfunction anomalies at σ=0.245 for 1982/83 (left panels) and 1986/87 (right panels) El Niño winters, obtained from NMC initialized analysis (upper panels) and linear model response to sub-seasonal transient vorticity forcing (lower panels). Contour interval 1×10^6 m^2 s^{-1} and negative contours stippled.

Predictability of Blocking.

E. Tosi[1], S. Tibaldi[2], , P. Ruti[1] and F. D'Andrea[3]

[1] University of Bologna
Department of Physics, Atmospheric Dynamics Group
Bologna, Italy

[2] University of Camerino
Department of Mathematics and Physics
Camerino, Italy

[3] University of Milano
Department of Physics
Milano, Italy

1. INTRODUCTION

Tibaldi and Molteni (1990, hereafter referred to as TM) had previously investigated operational blocking predictability by the ECMWF model and the possible relationships between model systematic error and blocking in the winter season of the Northern Hemisphere, using seven years of ECMWF operational archives of analyses and day 1 to 10 forecasts. They showed that fewer blocking episodes than in the real atmosphere were generally simulated by the model, and that this deficiency increased with increasing forecast time. As a consequence of this, a major contribution to the systematic error in the winter season was shown to derive from the inability of the model to properly forecast blocking.

The inability shown by forecasting models to properly enter into a blocked state (both in the initial value problem sense and in a climatic sense) and the consequential existence of large systematic errors are limiting factors of paramount importance also for extended range forecasts (*Tracton et al*, 1989; *Tracton*, 1990; *Miyakoda and Sirutis*, 1990; *Tibaldi et al*, 1991; *Branković and Ferranti*, 1992), where the consequences of such errors are amplified by the longer integration time. An improved understanding of the reasons for blocking forecast failures and of the positive relationship between such failures and model systematic errors would therefore have an even larger positive impact on extended range dynamical forecasts, and climate simulation.

In this study, the analysis performed in TM for the first seven winter season of the ECMWF operational model is extended to the subsequent five winters, during which model development, reflecting in both resolution increases and parametrisation modifications, continued unabated. In addition the objective blocking index developed by TM has been applied to the observed data to study the natural low frequency variablity of blocking. The ability to simulate blocking of some climate models (developed at the Deutsches Klimarechenzentrum, Hamburg,FRG) as also been tested.

2. DESCRIPTION OF THE DATA SET AND OF THE ANALYSIS PROCEDURES

The database for the study of the performance of the operational ECMWF model consists of daily Northern Hemisphere winter 500 hPa geopotential heights analyses and the corresponding day 1 to day 10 forecasts. Winter is here defined as the 90-day period spanning the months of December, January and February (DJF period). For each winter day, eleven fields are then available: analysis and day one to day ten forecasts, all verifying on the same day but started from progressively lagging initial conditions. Such an arrangement of analysis and forecast fields is commonly known as a "Lorenz files" dataset (*Lorenz*, 1982). The total set includes twelve complete winters, from DJF 1980-81 to DJF19 91-92.

The database for the study of the natural low frequency variablity of blocking consists of daily Northern Hemisphere winter 500 hPa geopotential heights analyses, from the NMC and ECMWF archives, from the winter 1949-50 to the winter 1991-92.

For the climate models 5 different runs with two different models have been analyzed. The models are ECHAM2 and ECHAM3 (developed starting from the ECMWF model at the Deutsches Klimarechenzentrum) which differ for the physical package and for the fact that ECHAM2 can run only with orizontal resolution of T21 (both models are spectral and T21 stands for triangular truncation at the 21st spherical harmonic). Climatic or observed sea surface temperatures (SSTs) have been used. The main characterisic of the runs are reported in Table 1.

The TM blocking index has been used on the different data sets. The geopotential height gradients GHGS and GHGN are computed for each longitude

$$GHGS = \frac{Z(\phi_0) - Z(\phi_s)}{(\phi_0 - \phi_s)},$$

$$GHGN = \frac{Z(\phi_n) - Z(\phi_0)}{(\phi_n - \phi_0)},$$

where

$\phi_n = 80°N+\Delta$

$\phi_0 = 60°N+\Delta$

$\phi_s = 40°N+\Delta$

$\Delta = -4°, 0°, +4°$

A given longitude is defined as blocked at a specific day if the following condition are satisfied for at least one value of Δ:
(1) GHGS> 0,
(2) GHGN < -10 m/deg lat.
Similarly to TM, the two main NH sectors are then identified and defined, with the following longitudinal limits:

Euro-Atlantic:	25.5° W	33.5° E
Pacific:	110.0° E	170.0° W

A sector is then considered to be blocked if three or more adjacent longitudes contained in it are blocked according to the local and instantaneous TM index definition.

3. OBSERVED AND PREDICTED BLOCKING

Figure 1 shows the longitudinal dependency of blocking frequency as measured by the index applied on subsets of ten years of the observaed winters (1949-50 to 91-92) of 500 hPa geopotential height, and is shown here only to give a measure of the different behaviour of the atmosphere, that shows appreciable intradecadal variability. This behaviour is of particular interest when the performance of climate models has to be assessed.

The four panels of Figure 2 show the blocking frequency relative to the first seven winters of ECMWF operations. Panel (a) shows observations alone, while in panels (b) to (d) forecast day 3, 6 and 10 respectively are superimposed on the observed longitudinal frequency. The disruption of the observed maxima in correspondence of both the Pacific and the Atlantic sectors is quite evident

already at day 6 and is almost complete by day 10. Figure 3 has the same layout of Figure 2, but refers to the last five ECMWF operational winters, 1987-88 to 91-92. Now the picture is quite different and shows a marked improvement in model climatology of blocking, with the model-produced frequency profile becoming measurably different from observations only by day 10.

Figure 4 summarizes the analysis performed on the climate models. The two top panels show the longitudinal dependence of the blocking frequiency used for comparison, the right panel is relative to the years for which observed SSTs where used in the simulation. The improvements in the phisical parametrizations from ECHAM2 T21 to ECHAM3 T21 do not produce relevant changes in the simulation of blocking. The increase of resolution from ECHAM3 T21 to ECHAM3 T42 has a positive effect on the simulation of Euro-Atlantic blocking, but does not affect Pacific blocking. The use of observed SSts seemes again to have better effects on the Euro-Atlantic blocking. The lack of an ECHAM2 T42 makes impossible a valutation of the effects of increasing resolution without changing the physical parametrizations.

4. CONCLUSIONS

Measurable improvements have been achieved by the ECMWF operational forecasting system in modelling blocking. Such improvements range from a better overall model blocking climatology to an improved deterministic predictability of the phenomenon. Such improvements make it more realistic to plan for extended range forecasts. Unfortunately, the practical set-up of operational forecasting and the related model development efforts make it impossible to ascribe such improvements to a precise cause, be it model resolution (horizontal or vertical) or improvements in the physical parametrisation package.

Blocking diagnostics in climate models show that improvements in resolution and in the physical parametrisation package produce a better blocking climatology, but also in this case a clear distinction between the effects of resolution and physics are impossible.

Acknowledgements

Dr. E. Roeckner of Max Plank Institute, Hamburg, and Dr. U. Cubash of Deutsches Klimarechenzentrum, Hamburg, are gratefully acknoledged for giving us the opprtunity of analysing the runs of their climate models.

References

Branković, Č. and L. Ferranti, 1992: Seasonal integrations with realistic boundary forcing. ECMWF Workshop on "New developments in predictability", 305-333.

Lorenz E.N., 1982: Atmospheric predictability with a large numerical model. Tellus, **34**, 505-513.

Miyakoda K. and J. Sirutis, 1990: Subgrid Scale Physics in 1-Month Forecasts. Part II: Systematic Error and Blocking Forecasts. J. Atmos. Sci., **118**, 1065-1081.

Tibaldi S. and F. Molteni, 1990 (TM): On the Operational Predictability of Blocking. Tellus, **42A**, 343-365.

Tibaldi S., T.N. Palmer, C. Brankovic and U. Cubasch, 1991: Extended-Range Predictions with ECMWF Models: Influence of Horizontal Resolution on Systematic Error and Forecast Skill. Q.J.R. Meteor. Soc., **116**, 835-866.

Tracton M.S., 1990: Predictability and its relationship to scale interaction processes in blocking. Mon. Wea. Rev., **118**, 1666-1695.

Tracton M.S., K. Mo, W. Chen, E. Kalnay, R. Klister and G. White, 1989: Dynamical extended range forecasting (DERF) at the National Meteorological Center. Mon. Wea. Rev., **117**, 1604-1635.

Table and Figure Captions

Table 1. Main characteristics of the five climatic runs analyzed.

Figure 1 Longitudinal distribution of winter (DJF) blocking frequency for differen decades. a) 1949-50 to 1958-59, b) 1959-60 to 1968-69, c) 1969-70 to 1978-79, d) 1979-80 to 1991-92.

Figure 2 TM blocking index applied to the first seven ECMWF operational winters (80/81 to 86/87). (a) analyzed data; (b) forecast day 3 and analysis (dashed); (c) forecast day 6 and analysis (dashed); (d) forecast day 10 and analysis (dashed).

Figure 3 As Figure 2, but for the last five ECMWF operational winters (87/88 to 91/92).

Figure 4 Longitudinal distribution of winter (DJF) blocking frequency for observations and climate models runs. a) for the complete data set available, b) for the ten winters from 1979-80 to 1987-88. panels c to e for 20 years runs of ECHAM2 T21, ECHAM3 T21 and ECHAM3 T42, all with climatic SSTs. Panels f and g for 10 years runs of ECHAM3 T21 and ECHAM3 T42, with observed SSTs. The dotted line on panels c to g are the observed frequencies.

Tabl 1

MODEL	HORIZONTAL REPRESENTATION	VERTICAL LEVELS	SSTs	GWD	Length of integration
ECHAM2	T21	19	Climatological	No	20 years
ECHAM3	T21	19	Climatological	No	33(20) years
ECHAM3 GAGO	T21	19	Observed	No	10 years
ECHAM3	T42	19	Climatological	Yes	20 years
ECHAM3 GAGO	T42	19	Observed	Yes	10 years

DJF

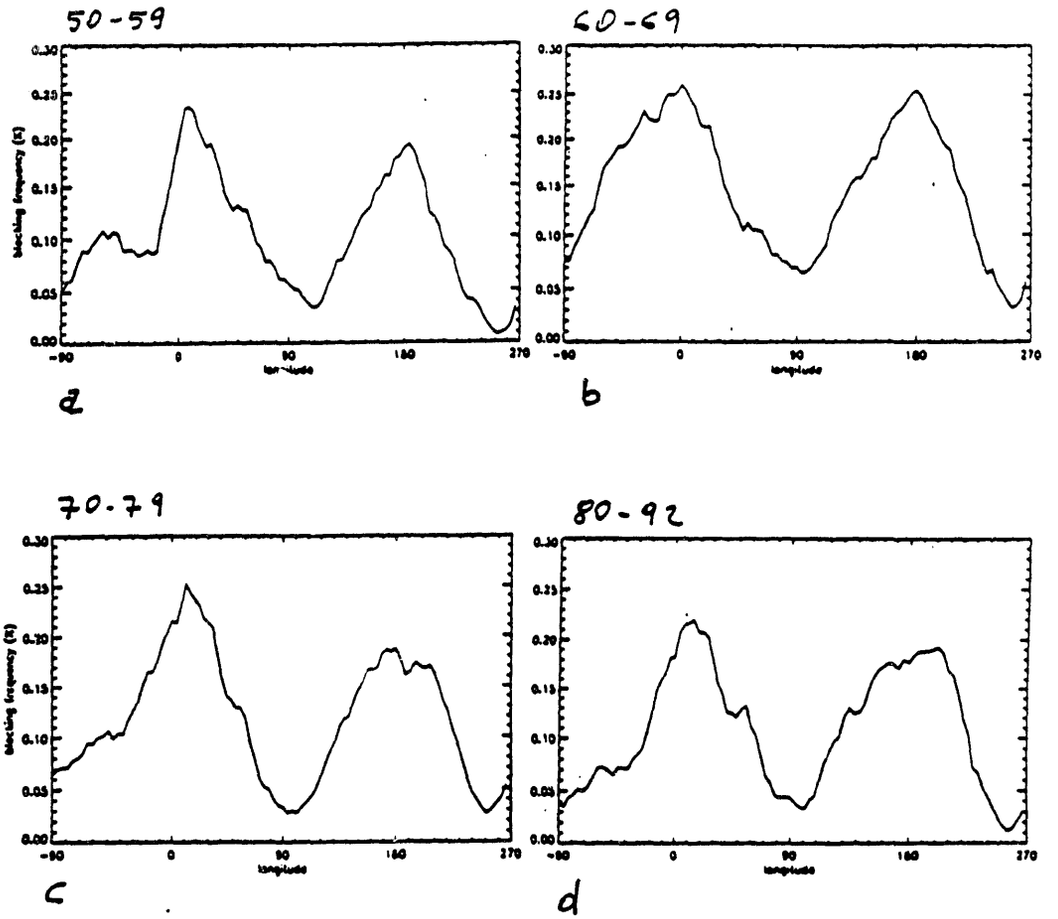

Fig 1

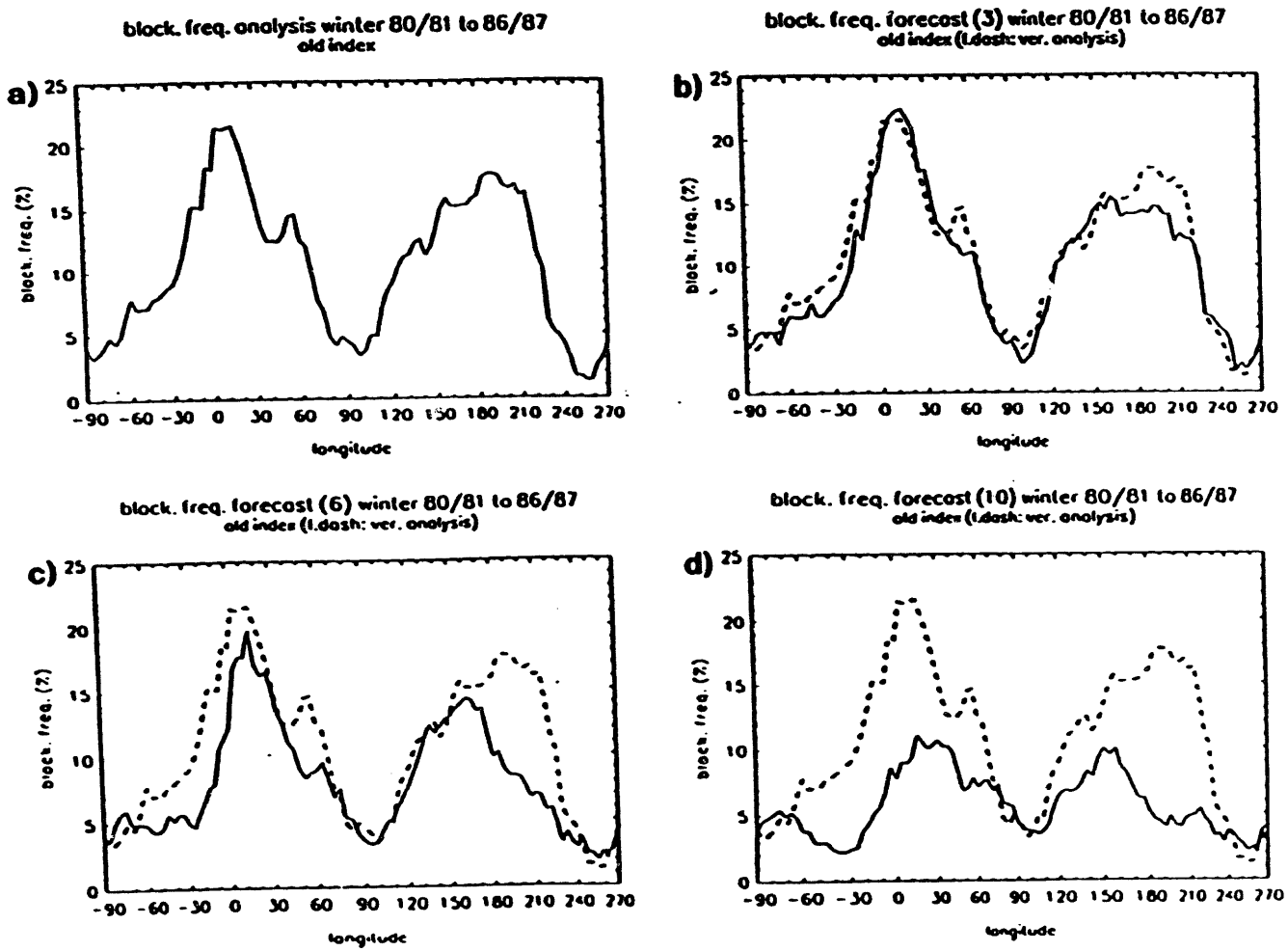
block. freq. analysis winter 80/81 to 86/87
old index
a)
block. freq. (%)
longitude
block. freq. forecast (3) winter 80/81 to 86/87
old index (l.dash: ver. analysis)
b)
block. freq. (%)
longitude
block. freq. forecast (6) winter 80/81 to 86/87
old index (l.dash: ver. analysis)
c)
block. freq. (%)
longitude
block. freq. forecast (10) winter 80/81 to 86/87
old index (l.dash: ver. analysis)
d)
block. freq. (%)
longitude

Fig 2

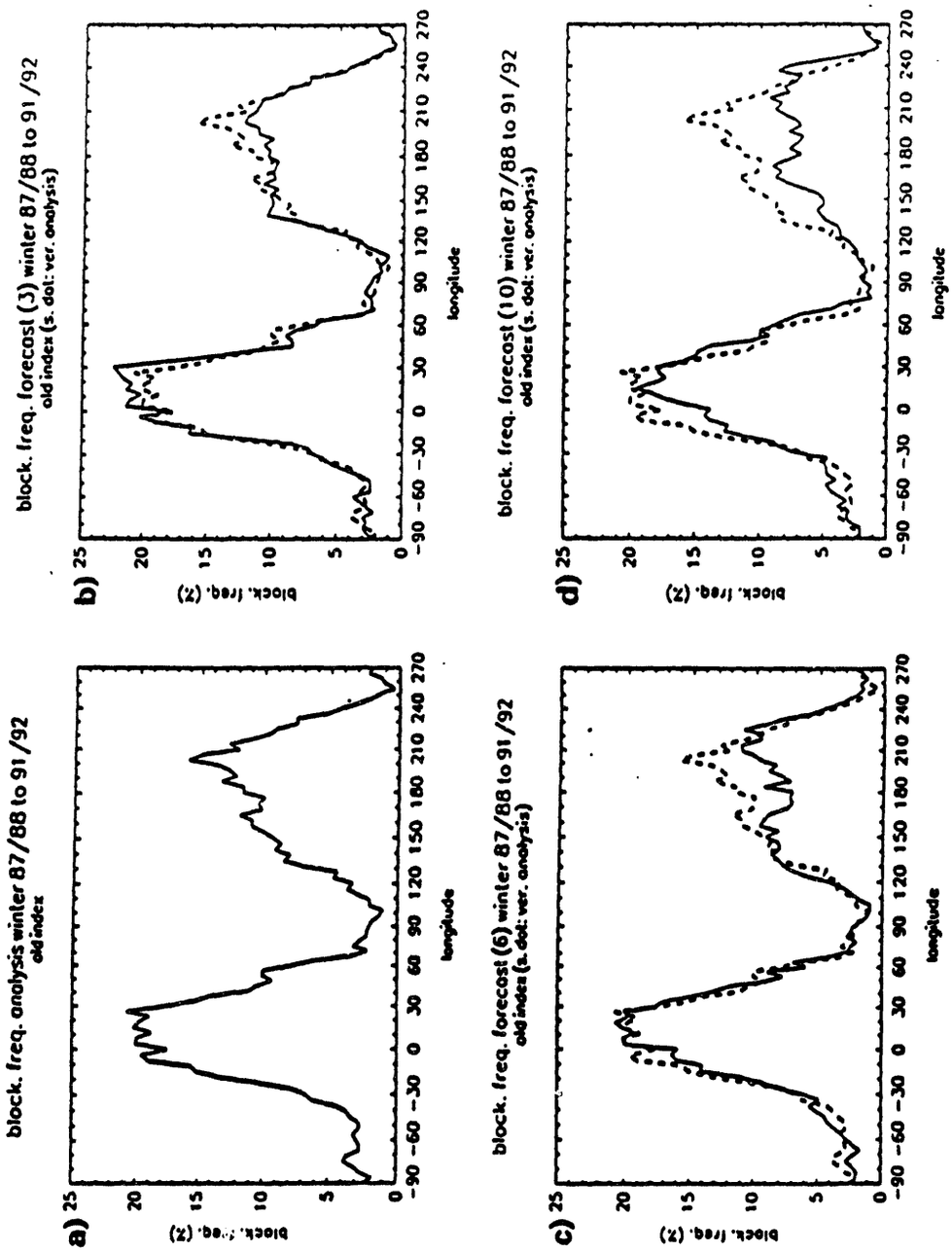
a)
block. freq. analysis winter 87/88 to 91/92
old index
block. freq. (%)
longitude
b)
block. freq. forecast (3) winter 87/88 to 91/92
old index (s. dot: ver. analysis)
block. freq. (%)
longitude
c)
block. freq. forecast (6) winter 87/88 to 91/92
old index (s. dot: ver. analysis)
block. freq. (%)
longitude
d)
block. freq. forecast (10) winter 87/88 to 91/92
old index (s. dot: ver. analysis)
block. freq. (%)
longitude

Fig 3

Winters 49/50 – 91/92. Analysys
old index

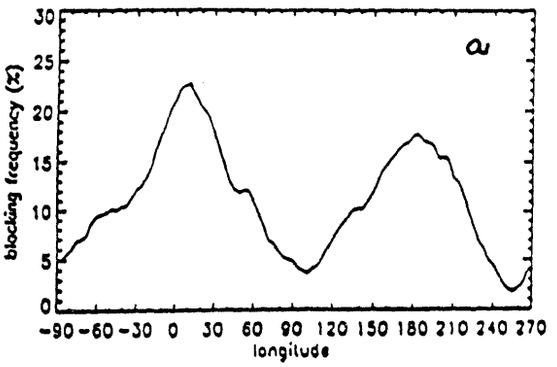

Winters 79/80 – 87/88. Analysys
old index

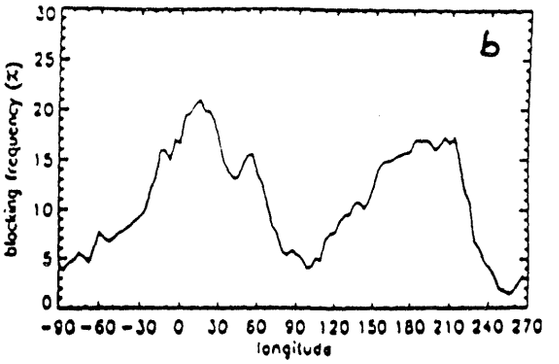

20 winters. ECHAM2 T21
old index

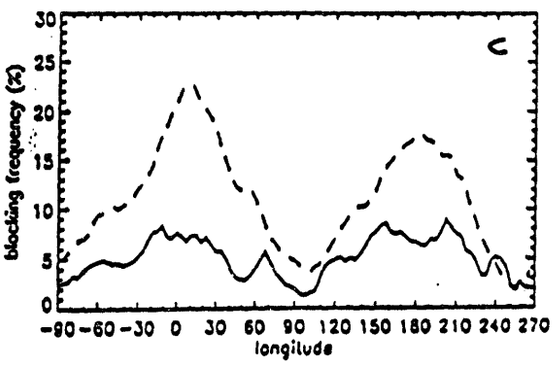

20 winters. ECHAM3 T21
old index

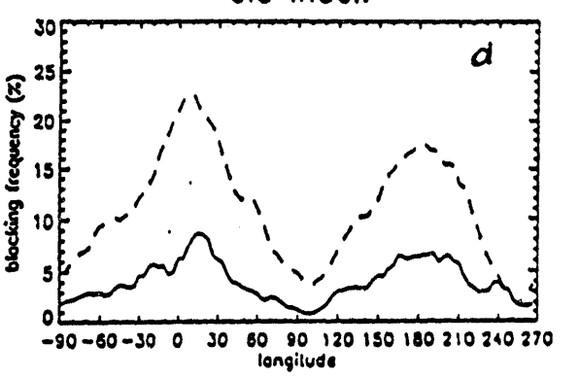

winters 79/80 – 87/88
ECHAM3 T21 GAGO – old index

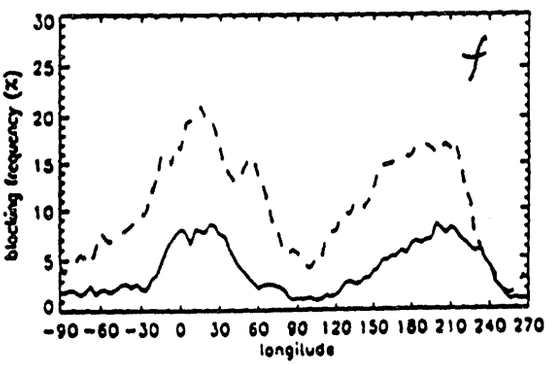

20 Winters. ECHAM3 T42
– old index

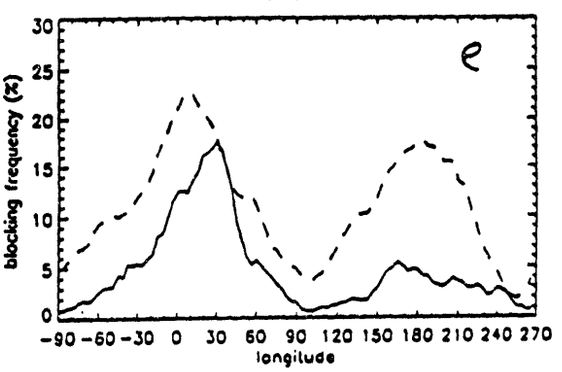

Winters 79/80–87/88
ECHAM3 T42 GAGO – old index

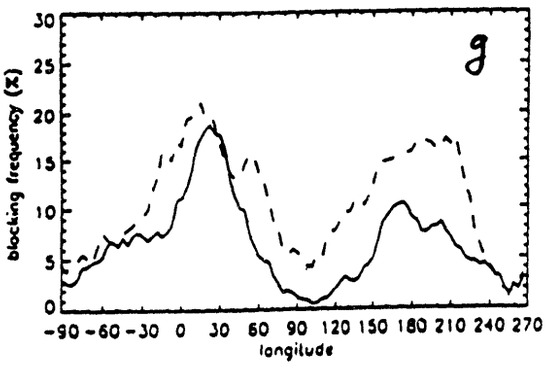

Fig 4

PANEL SUMMARY

The 17th Stanstead Seminar concluded with a panel discussion consisting of four invited speakers (Peter Stone, Isaac Held, Ray Pierrehumbert, and George Boer) and seminar co-organizer Bill Gutowski of Iowa State, who acted as the moderator. The panel addressed several questions put forward by Seminar organizers to stimulate discussion.

Question 1. How good are GCMs at simulating eddy dynamics in the *present* climate? What could account for known systematic errors, e.g., realistic momentum fluxes but weak eddy amplitudes (i.e., weak eddy kinetic energy)? What other important errors occur in modeling large-scale extratropical dynamics? How can we correct them?

In response to this question, I. Held commented that existing CO_2 climate change experiments with GCMs have suffered from inadequate horizontal resolution, leading to errors in large-scale eddy dynamics and transports. However, he noted that systematic errors in numerical weather prediction models do not change much beyond a resolution of about T42-63. Therefore, he expects diminishing returns in the improvement of eddy dynamics in GCM climate simulations as the GCMs move toward higher horizontal resolution. He suggested that improvements in the representation of physical processes are more likely to generate overall model improvement, including improvements in eddy dynamics.

I. Held also commented that much of the dissipation at small scales is enstrophy dissipation, not energy dissipation, so that moderate GCM resolution of about R30 (or slightly more) may adequately represent global energy cycles. R. Pierrehumbert commented that R30-40 may be adequate to represent the potential enstrophy cascade to smaller scales, but that smaller unresolved scales may affect how well moisture dynamics and dissipation at the surface are simulated.

P. Stone commented that better vertical resolution in GCMs is also very important because of the static stability adjustment that occurs in baroclinic eddy life cycles. Most of the adjustment of both vertical and meridional temperature gradients by baroclinic eddies occurs in the lower troposphere. Accurate simulation of this adjustment may require significant increases in GCM vertical resolution in the lower troposphere. P. Stone also suggested that large-scale eddy dynamics in GCMs may be affected substantially by how subgrid-scale physical processes, esp. dissipation in the PBL and moist convection, are parameterized. He noted that most of the poleward eddy heat transport occurs in

the lower troposphere so that large-scale eddy feedbacks in GCMs are likely to be affected by surface flux parameterizations.

P. Stone also noted that in climatic equilibrium all processes must balance, so that surface parameterizations will inevitably influence time-mean eddy dynamics. Following up on that comment, R. Pierrehumbert suggested that eddies may equilibrate at the wrong amplitude if the dissipation is incorrectly modeled. He proposed that GCMs be tested over a wide range of adjustable parameters to see how eddy processes and time-mean climatic conditions are affected by model parameters. Later, R. Pierrehumbert returned to this topic and suggested that GCMs should be subjected to much bigger climate perturbations than a doubling of CO_2 in order to evaluate their ability to represent dynamical and physical processes and global climate change. He also recommended experiments with simplified versions of GCMs so that the effects of specific processes can be studied in isolation.

G. Boer stated that GCM modelers are very active in improving resolution and testing surface parameterizations. However, he noted that validating parameterizations is difficult. P. Stone commented that validation is difficult in part because of sparsity of data over the oceans and the Southern Hemisphere. Currently, data is adjusted and validated through model analysis which has inherent limitations and uncertainities. In response, G. Boer stated that there is some consistency in data analysis between GCMs. P. Stone commented that surface moisture flux varies between GCMs, and that further effort is needed to validate parameterizations related to precipitation and evaporation, but that the data may not be readily available.

Brian Farrell from Harvard suggested that GCMs do poorly at simulating individual synoptic-scale events such as rapid cyclone development and that GCM validation should partly depend on how well the models simulate such events as judged by experts in synoptic meteorology (termed by Farrell as the "Bosart test"). G. Boer questioned if much detail in "weather" events is needed to adequately simulate climate dynamics. P. Stone commented that small differences in individual events that cannot be measured or recognized by subjective evaluation may accumulate to larger relative errors over long-term means. R. Pierrehumbert stated that a GCM with R30 resolution will likely fail the Bosart test since this resolution does not adequately represent frontal scale dynamics, but may successfully simulate larger scale transports and motions that contribute to a realistic climate. For example, he noted that transient eddy sensible heat flux peaks at planetary zonal wavenumber 5.

Question 2. What is a satisfactory level of confidence (or error range) in projecting global climate change? Can "accurate" greenhouse climate change projections be made before the change actually occurs?

I. Held suggested the use of paleoclimatological conditions as a measure of a GCM's ability to model climate change, although he noted that our understanding of paleoclimate is evolving as new data becomes available or old data is re-interpreted. Generally speaking, I. Held was pessimitic about our ability to predict climate change since validation with observations is so difficult. Later, G. Boer commented that paleoclimate may provide a good test for GCMs, but also wondered if we would ever know enough about climatic conditions to achieve successful model validations.

R. Pierrehumbert commented that GCMs have "training wheels" at the present time, e.g., sea surface temperatures are often specified. He urged that GCMs must be able to represent the present climate accurately and must do so with coupled models (i.e., fully coupled atmospheric and oceanic GCMs). P. Stone seconded that recommendation.

I. Held proposed that errors in cloud modeling are the basis for many problems in simulating climate with GCMs. P. Stone indicated that with the ISCCP data set, some solutions to issues involving cloud parameterizations and model validation may be attainable.

From the audience, Enda O'Brien from the University of Miami suggested that GCMs should certainly be able to simulate the seasonal cycle if climate change projection is to be successful.

R. Pierrehumbert pointed to uncertainties in modeling evaporation and the water cycle in general. He also said that the endeavor to model climate is important, but the primary objective should be understanding, perhaps not specific projections. He noted ironically that politicians frequently complain about uncertainties in climate prediction, yet rely on econometric models that are probably much worse than GCMs as reliable predictive tools.

P. Stone urged that we redouble our effort to understand how the coupled atmospheric-oceanic system works. Considering whether or not climate is predictable, he noted that ocean models indicate extreme sensitivity in their climatic state. The noise level or natural internal variability on a 100-year time scale may be fairly large, making detailed predictions on that time scale difficult, esp. given the lack of data on the current climatic state of the oceans.

Question 3. What value do GCMs have over more simplified models (e.g., low-order models, zonally symmetric models with parameterized eddy fluxes) in understanding the role of eddy dynamics in the maintenance of extratropical climate?

P. Stone endorsed I. Held's suggestions (made during Held's invited talk) that all levels of model complexity are needed to understand climatic processes. I. Held commented that scientists must be able to move back and forth between model levels. G. Boer urged better application of the inductive method for identifying the behavior of simple systems in the complex systems of GCMs. From the audience, Ted Shepherd of the University of Toronto encouraged closer connections between theoretical models and GCMs. P. Stone also urged that closer links between simpler models and GCMs and stated that GCM research centers need to have staff who are knowledgeable in both areas.

R. Pierrehumbert urged that GCM output needs to be more readily available and conveniently formatted for analysis and interpretation by the broad scientific community. G. Boer commented that GCMs are becoming less proprietary, and I. Held commented public domain models are becoming more common. P. Stone urged better documentation of GCMs and Bill Gutowski argued in favor of more extensive standard GCM diagnostic calculations.

R. Pierrehumbert stated that low-order models with just a few wave modes have lost much of their value as climate models, since they lack useful geographic variations. On the other hand, I. Held commented that 3-D steady-state models have considerable value in interpreting GCM results and understanding climate processes.

Question 4. How good is the observational record for observing possible responses of extratropical dynamics to climate change? How long does it need to be? Are the dynamics observed as well as (or better than) the temperature structure? Could dynamical signatures of greenhouse warming show up more readily than some thermal signatures?

P. Stone commented that the adequacy of the observational record needs to be examined. He also noted that observations to deter-mine if model feedbacks are correct are very difficult to obtain. Referring back to Question 2, he thought that we may have to wait until significant climate change occurs before we can adequately understand the host of feedbacks in the system.

R. Pierrehumbert suggested field studies could be performed to enhance our observational database, but that the results are likely to be region-dependent. He reiterated the urgent need for

more data over the oceans and better moisture data in the middle and upper troposphere. He suggested that remotely piloted vehicles could provide a low-cost alternative to expensive satellite programs for collecting data in remote regions.

G. Boer commented that climatic changes in temperature are most significant, while dynamical responses are expected to be less so.

Question 5. What is the role of eddies on different spatial and temporal sales in maintaining climate? In particular, how much of a role is played by small cyclone-scale eddies (zonal wavenumber > 10) in climate variability and maintenance?

P. Stone recommended more attention be given to diagnostics such as moisture transport spectra to ascertain the impact of cyclone scales on climate maintenance. R. Pierrehumbert commented that wavenumber decomposition does not make sense at the cyclone scale and that improved diagnostic methods are required to answer this question. I. Held noted that vertical heat flux is probably concentrated at smaller scales. P. Stone wondered where such fluxes peak in wavenumber space and urged further study of this question.

From the audience, Brian Farrell argued that extreme cyclone events are important in characterizing and simulating climate change. Phil Smith of Purdue proposed that changes in intense cyclones will, at least, affect regional climate and, furthermore, that cyclone intensity is an important climate parameter. R. Pierrehumbert noted that, while hurricanes are important as weather events, they are responsible for only about 2% of total global evaporation. Thus, it is not evident that extreme events make a significant contribution to the maintenance of the global climate.

R. Pierrehumbert suggested that regional-scale models will be driven by GCM output to examine the response of cyclones and smaller scale motions to climate change. I. Held expected that full climate models will eventually resolve cyclone scales in any case. He commented that, in the future, coupled ocean-atmosphere models at T42 resolution and atmospheric GCMs at T100 will assess changes in cyclone behavior.

Question 6. What plays a more important role in determining regional climate change - large-scale dynamics or regional surface processes?

P. Stone stated that surface processes will generally be more important at smaller scales. Norm MacFarlane of the Canadian Climate Centre suggested that the answer to this question is

highly region-dependent. R. Pierrehumbert commented that land surface changes such as deforestation can compete on a regional scale with climate changes due to large-scale dynamics.

Brian Farrell commented that climate models should be capable of determining what causes regional drought, either dynamics or regional land-surface changes. Walter Robinson of the University of Illinois suggested that drought may be initiated by anomalous dynamical patterns, but it is often maintained through positive feedbacks in local surface processes.

Shilling Peng of McGill commented that the answer to the question depends on what time scale of variation is considered. P. Stone commented that surface processes can vary over long time scales.

Final Remarks. Following the discussion of the questions, the panel made a few final comments regarding areas of climate research that need special attention.

R. Pierrehumbert stated that cloud feedbacks in the extra-tropics are a very important, but often overlooked, component of the climate system. He stated that the components of cloud radiative forcing are most out of balance in mid-latitudes. Additional work in the theory of cloud cover, cloud height and fluctuations and their relationship to large-scale eddy dynamics and transports needs to be undertaken.

I. Held also targeted cloud feedback as a major uncertainty in climate modeling. He also urged intensive modeling and observation of certain critical regions such as the "warm pool" region of the western Pacific.

P. Stone mentioned air-sea interaction as a major unknown in climate research, esp. considering the importance of the interaction of large-scale eddies with the surface fluxes that force ocean circulations.

G. Boer concluded that better physical parameterizations are a more critical need than higher resolution in GCM climate simulations. He urged closer cooperation between theoreticians, observationalists, and GCM modelers so that improvements can be made in parameterizations. From the audience, Norm MacFarlane commented that changes or improvements in individual parameterizations sometimes lead to deterioration of model climate, which may indicate the existence of other deficiencies in the model. He encouraged the development of parameterizations that are coupled together in a physically consistent fashion, such as the planetary boundary layer and convective schemes.

L.E. Branscome

DATE
FILMED
10/26/94
END